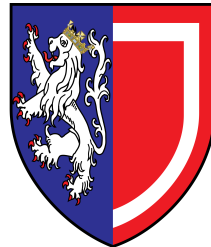


Future Searches for Rare Astrophysical Signals and Detector Commissioning in SNO+

Christopher R. Jones

Balliol College, Oxford



Thesis submitted in partial fulfilment of the requirements for the
degree of Doctor of Philosophy at the University of Oxford

Trinity Term, 2016

Future Searches for Rare Astrophysical Signals and Detector Commissioning in SNO+

Christopher R. Jones
Balliol College, Oxford

Thesis submitted in partial fulfilment of the requirements for the degree of
Doctor of Philosophy at the University of Oxford

Trinity Term, 2016

Abstract

SNO+ is a 780 kTonne liquid scintillator experiment, situated 2km underground in the Creighton mine near Sudbury, Ontario and primarily designed to study neutrinoless double beta decay, but also has several other physics goals such as solar neutrinos, reactor and geo-neutrinos and supernova neutrinos. SNO+ may also be sensitive to rare astrophysics signals, such as Axion-Like Particles (ALPs) originating from the Sun. This thesis predicts a limit on the ALP-electron coupling, $|g_{Ae} \times g_{3AN}| < 0.7 \times 10^{-11}$ via the axio-electric effect and a limit on the ALP-photon coupling of $|g_{A\gamma} \times g_{3AN}| < 2.9 \times 10^{-11} \text{ GeV}^{-1}$ via the inverse Primakoff interaction, which could be achieved with 5 years of Te-loaded scintillator phase of SNO+. Both of these upper limits are an order of magnitude improvement on the current published limits on ALP couplings.

SNO+ should also be sensitive to another rare astrophysics signal: a burst of neutrinos from a supernova, originating from our Galaxy, via proton elastic scattering (PES) and inverse beta decay (IBD) interactions within the scintillator. The ratio of PES/IBD interactions, due to supernova neutrinos, is determined by the ν_x/ν_e flux ratio. This ratio could indicate a preference for the inverted neutrino mass hierarchy, due to a proposed dramatic ‘spectral swapping’ between ν_x and ν_e flux distributions caused by neutrino-neutrino interactions from the core-collapse of a supernova. The initial commissioning of the data acquisition (DAQ) and scattering calibration (SMELLIE) systems, during SNO+ data commissioning runs taken in December 2014, is also evaluated in this thesis.

Acknowledgements

Firstly I'd like to thank Steve Biller and Armin Reichold for their support and guidance over the past four years. From the first day, I have learnt so much from both of them and they have helped me grow as a physicist. They have not just been fantastic mentors, but good friends too. I would like to thank all of the Oxford SNO+ group for their amazing level of camaraderie including: Krish Majumdar, Ian Coulter, Jack Dunger, Jeff Lidgard, Luca Cavalli, Laura Segui, Alex Rollings, Esther Turner & Jeff Tseng. I will dearly miss working with all of you and our array of eccentric activities from soviet Fridays to office cricket and the endless amount of laughter and debate. I have truly made friends for life and will always reflect joyfully upon this period of my life!

I would also like to thank other members of the Oxford physics department. Farrukh Azfar has been a wonderful friend and mentor but also Will Kalderon, Mark Pickering and all of the students at Oxford. A special thanks should also go to my dear friends at Balliol college, especially Elwyn Davies and his willingness to take random trips to Morocco! I would also like to thank the SNO+ collaboration for all the interesting discussions and especially the young SNO+ members. They managed to turn months in the frozen depths of Northern Ontario into one of the warmest places I've ever been! I would like to thank the STFC and the Oxford physics department for funding my thesis.

Finally, thank you to my family and my parents: Helen and Andrew. It is both humbling and scary, in equal measure, to think how much support and help I have needed throughout my life to be able to write a PhD in Physics.

Contents

1	SNO+ experiment	1
1.1	The Sudbury neutrino observatory	1
1.2	Introduction to SNO+	3
1.3	ELLIE system	4
1.4	Calibration in SNO+	5
1.5	Simulation software	7
1.6	Experimental phases	8
1.6.1	Water phase	8
1.6.2	Scintillator phase	9
1.6.3	Te-loaded scintillator phase	9
1.7	SNO+ physics goals	10
1.7.1	Neutrinoless double beta decay	10
1.7.2	Supernova neutrinos	14
1.7.3	Solar neutrinos	14
1.7.4	Reactor and geo-neutrinos	15
1.7.5	Exotic searches: nucleon decay and ALPs	15
2	The physics of neutrinos	17
2.1	Neutrinos in the Standard Model	18
2.2	Sources of neutrinos	19
2.3	Neutrino oscillations in vacuum	20

2.4	Neutrino oscillations in matter	23
2.5	Neutrino oscillations in supernovae	24
2.6	Neutrino mass hierarchy	26
2.7	Neutrinoless double beta decay	27
2.7.1	Current experimental limits	31
3	Commissioning the SNO+ DAQ software	33
3.1	Introduction to SNO+ DAQ	34
3.2	Implementation of run & configuration files	41
3.3	SNO+ DAQ software	43
3.4	Upgrades to control/monitoring	44
3.4.1	GT monitoring	45
3.4.2	Automatic shutdown of SNO+	46
3.4.3	Multi-threading in SNO+	47
3.5	Implementing the channel hardware status	48
3.5.1	What is a ‘Channel’?	49
3.5.2	PMT status DB	49
3.5.3	PMT resistor status DB	49
4	Commissioning of the SMELLIE system	52
4.1	Purpose of the SMELLIE system	52
4.2	Overview of the SMELLIE hardware	53
4.2.1	SNO+ PMT safety considerations	58
4.3	Logic of a SMELLIE run	58
4.4	Integration of SMELLIE into ORCA	61
4.5	Commissioning of SMELLIE	65
4.5.1	SNO+ run 9044	65
4.5.2	SMELLIE monitoring PMT	69
4.5.3	SMELLIE triggers	74

4.6	Conclusion	75
5	ALP theory	77
5.1	Introduction to ALPs	77
5.2	ALP Interactions	80
5.2.1	Compton conversion of ALPs (CCA)	81
5.2.2	Axio-electric effect	83
5.2.3	Inverse Primakoff effect (IP)	85
5.2.4	ALP Decay	86
5.3	Theoretical Limits	86
5.3.1	Decay Limits on ALP searches	86
5.3.2	Limitation of Solar ALP production	87
6	ALP detection with neutrino experiments	90
6.1	Validation of ALPs in SNO+	91
6.2	External backgrounds in SNO+	93
6.3	Timing discrimination for ALPs in SNO+	95
6.4	ALPs in SNO+ unloaded phase	101
6.4.1	Limits on the inverse Primakoff effect	101
6.5	ALPs in SNO+ Te-loaded phase	107
6.5.1	Limits on the Compton conversion of ALPs	107
6.5.2	Limits on the inverse Primakoff effect	110
6.5.3	Limits on the Axio-electric effect	112
6.6	Systematic uncertainties for ALPs in SNO+	115
6.7	LUN experiments	117
6.7.1	Sensitivity to $ g_{3AN} \times g_{Ae} $	117
6.7.2	$ g_{3AN} \times g_{Ae} $ sensitivity with CCA	117
6.7.3	$ g_{3AN} \times g_{Ae} $ sensitivity with AE	120
6.8	Sensitivity to $ g_{3AN} \times g_{A\gamma} $	121

6.9	Borexino	121
6.10	SNO (all phases)	123
6.11	Super Kamiokande	127
6.12	Hyper Kamiokande	130
6.13	Other ALP searches	131
6.14	Conclusion	134
6.14.1	Limits for $ g_{3AN} \times g_{Ae} $	134
6.14.2	Limits for $ g_{3AN} \times g_{A\gamma} $	138
7	Supernova neutrinos in SNO+	141
7.1	The physics of supernovae	142
7.1.1	Type Ia	143
7.1.2	Type Ib/c	143
7.1.3	Type II	143
7.1.4	Core collapse supernovae	144
7.2	Neutrino mass hierarchy with SN	145
7.3	Supernova neutrinos in SNO+	147
7.3.1	Inverse beta decay (IBD)	148
7.3.2	Inelastic scattering off ^{12}C	149
7.3.3	Electron elastic scattering (νES)	149
7.3.4	Proton-neutrino elastic scattering (PES)	149
7.4	PES flux in SNO+	150
7.5	Backgrounds to PES events	152
7.5.1	Internal backgrounds to PES events	153
7.5.2	External backgrounds to PES signal	155
7.6	PES signal extraction	158
7.6.1	Verification of PES extraction	166
7.6.2	Ratio of PES to IBD events	168

7.6.3	Systematic uncertainties	170
7.6.4	Supernova model uncertainties	172
7.7	Conclusion	173
8	Conclusion	174
A	Statistical limit setting technique for ALPs	178
B	ALP detection in SNO+ water phase	180
C	$g_{Ae} \times g_{3AN}$ in SNO+ scintillator phase	186
D	Distinct ALP signals in SNO+ water phase	190
E	$\Delta\mathcal{L}$ cut for ALPs	194
	Bibliography	196

List of Figures

1.1	Schematic of SNO+ detector	2
1.2	Schematic of the ELLIE system	4
1.3	Deployment of calibration sources in SNO+	7
1.4	SNO+ phase I backgrounds	11
1.5	SNO+ $0\nu\beta\beta$ sensitivity	13
2.1	Energy spectrum of neutrino sources	20
2.2	Neutrino-neutrino forward scattering	25
2.3	Neutrino mass hierarchy	27
2.4	Feynman diagram of double beta decay	28
2.5	Feynman diagram of neutrinoless double beta decay	29
2.6	$0\nu\beta\beta$ Sensitivity for all experiments	31
3.1	Overview of SNO+ electronics flow	37
3.2	SNO+ DAQ control & data flow	41
3.3	Screenshot of SNO+ DAQ	43
3.4	Screenshot of MTC/D GUI	45
3.5	Schematic of automatic emergency shutdown for SNO+	46
3.6	Multithreading logic for remote shutdown	48
3.7	Resistor DB GUI	51
4.1	Layout of the SMELLIE hardware	55

4.2	SMELLIE run-flow diagram	59
4.3	SMELLIE run builder	62
4.4	SMELLIE run GUI	63
4.5	SMELLIE configuration builder	64
4.6	Average Nhit on SNO+ run 9044	67
4.7	SMELLIE occupancies	68
4.8	Example CAEN trace from SMELLIE	70
4.9	CAEN height traces on run 9044	71
4.10	NHIT100 trigger stealing	72
4.11	Average CAEN height on SNO+ run 9044	73
4.12	SMELLIE triggers for run 9044	74
5.1	ALP Interactions	81
5.2	Compton conversion of ALPs	82
6.1	ALP direction diagram	91
6.2	Direction of e^-/γ from CCA interaction	92
6.3	Energy of e^-/γ from CCA interaction	92
6.4	^{208}Tl external backgrounds	94
6.5	Light emission profile of ^{208}Tl event	96
6.6	Time residual PDF for CCA	97
6.7	Distributions of $\Delta\mathcal{L}$ for AE	99
6.8	Backgrounds to ALP (IP) signal for SNO+ scintillator phase	102
6.9	Distribution of $ g_{A\gamma} \times g_{3AN} $ limits for SNO+ Scintillator Phase	105
6.10	Backgrounds to ALP (CCA) signal for SNO+ Te Phase	109
6.11	Backgrounds to ALP (IP) signal for SNO+ Te Phase	111
6.12	Axio-electric effect in SNO+ Te Phase	113
6.13	ALPs in water Cherenkov detectors	119
6.14	ALPs in liquid scintillator detectors	120

6.15	Schematic of the Borexino experiment	122
6.16	Energy spectrum from SNO phase I data	125
6.17	Schematic of the Super Kamiokande experiment	128
6.18	Super Kamiokande (SK-I) directional distribution at 5.0 - 20.0 MeV	129
6.19	Schematic of the Hyper Kamiokande experiment	130
6.20	Image of the CAST experiment	132
6.21	ALP interaction in CAST	133
6.22	Summary of ALP limits	137
6.23	Summary to Axio-electric effect	138
6.24	Summary of ALP limits	140
7.1	Massive star before collapse	144
7.2	Spectral swapping of a supernova	146
7.3	Diagram of the IBD Interaction	148
7.4	Source of external backgrounds	154
7.5	AV ^{210}Bi decays in 10s	156
7.6	2D histogram of ^{210}Po decays in 10s	157
7.7	PES PDFs	158
7.8	Marginalised likelihood	162
7.9	Extracted PES events	165
7.10	Mean bias for PES events	167
7.11	Mean pull for PES events	168
7.12	Extracted ratio of IBD to PES	169
7.13	Expected number of SN neutrinos in SNO+	173
B.1	ALP background energy spectrum	182
B.2	Distribution of $ g_{Ae} \times g_{3AN} $ limits for SNO+ water phase	185
C.1	Backgrounds to ALP (CC) signal for SNO+ scintillator phase	187

C.2	Distribution of $ g_{Ae} \times g_{3AN} $ limits for SNO+ scintillator phase . . .	188
D.1	Double Cherenkov cone diagram	191
D.2	Double Cherenkov cone analysis	192
D.3	Energy reconstruction performance for Compton conversion	193
E.1	Distributions of $\Delta\mathcal{L}$	194
E.2	Distributions of $\Delta\mathcal{L}$	195

List of Tables

1.1	SNO+ Background count	12
4.1	SMELLIE hardware components	54
4.2	SMELLIE connections	56
4.3	Sub-run information for SNO+ run 9044	66
5.1	Axio-electric effect with SNO+ at different Te-loadings	84
5.2	Inverse Primakoff with SNO+ at different Te-loadings	85
6.1	Table of external ^{208}Tl backgrounds	93
6.2	$\Delta\mathcal{L}$ cuts for ALPs	100
6.3	LAB molecules in SNO+	103
6.4	Expected Backgrounds in SNO+ scintillator phase	104
6.5	Median limits for $ g_{A\gamma} \times g_{3AN} $ in SNO+ Scintillator Phase	105
6.6	U/Th Purity in SNO+ Te phase	107
6.7	Expected Backgrounds in SNO+ Te-loaded scintillator	108
6.8	Median limits for $ g_{3AN} \times g_{Ae} $ in SNO+ Te-Scintillator Phase	109
6.9	Median limits for $ g_{A\gamma} \times g_{3AN} $ in SNO+ Te-Scintillator Phase	112
6.10	Median limits for $ g_{3AN} \times g_{Ae} $ (no CC)	114
6.11	SNO phase I backgrounds	125
6.12	SNO phase II backgrounds	126
6.13	SK-I Summary	129

6.14	HK Summary	131
6.15	Summary of $ g_{3AN} \times g_{Ae} $ limits	136
6.16	Summary of $ g_{A\gamma} \times g_{3AN} $ limits	139
7.1	Estimated supernova events in SNO+	147
7.2	Internal backgrounds to PES events	153
7.3	External backgrounds to PES events	155
B.1	Expected backgrounds in SNO+ water phase	181
B.2	Expected water backgrounds to ALPs	183
B.3	Median limits for $ g_{Ae} \times g_{3AN} $ in SNO+ water phase	185
C.1	Median limits for $ g_{Ae} \times g_{3AN} $ in SNO+ scintillator phase	187

1

SNO+ experiment

“SNO was nicknamed ‘Still Not Operational’, as it took so long to start. But when it did, it won a Nobel Prize”

– Member of the SNO collaboration

1.1 The Sudbury neutrino observatory

The Sudbury neutrino observatory (SNO) was built almost 25 years ago with an overburden of approximately 2km of rock in Sudbury, Canada. SNO, which was operational until 2006, observed solar neutrino oscillations using heavy water for which the leader of the experiment, Arthur McDonald, was a recipient of the 2015 Nobel Prize. SNO+ is the successor experiment to SNO, building upon the SNO infrastructure, using liquid scintillator loaded with ^{130}Te , and therefore requires the installation of hold-down ropes, commissioning of the scintillation plant and development of Te-loading techniques.

The SNO+ detector (see figure 1.1) consists of a spherical acrylic vessel (AV) with a radius of 6.005 m and placed within an approximately cylindrical cavity with a height of $\sim 40\text{m}$ and a radius of $\sim 20\text{m}$. Approximately 9,300 Hamamatsu

R1408 photomultiplier tubes (PMTs) are mounted onto a PMT support structure (PSUP), which (almost entirely) face inwards towards the centre of the detector[1]. Around 30 PMTs are facing outwards into the surrounding light water - these outward looking PMTs (OWLs) are used as a muon veto. The entire cavity is filled with over 7,000 tonnes of ultra pure light water, and the AV is filled with either water, scintillator or tellurium-loaded scintillator during the different phases of the SNO+ experiment.

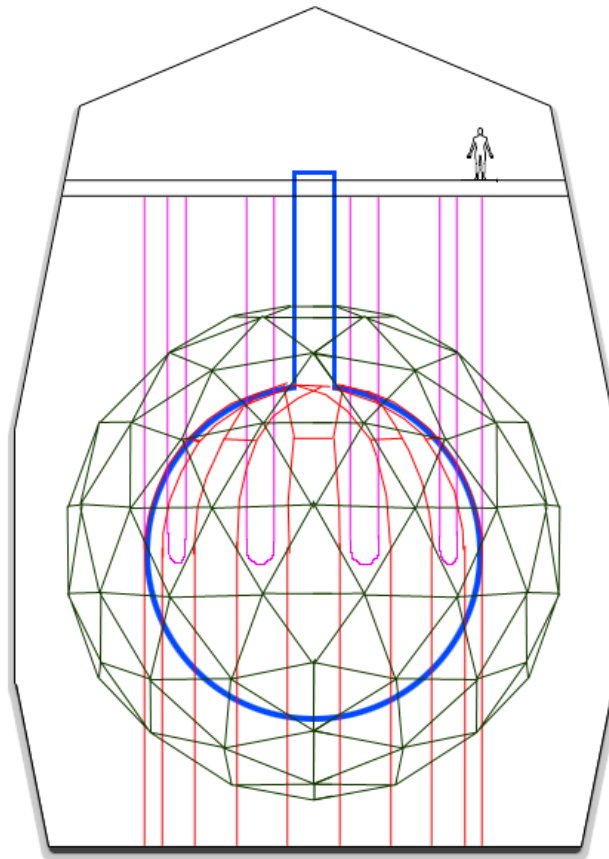


Figure 1.1: Schematic of the SNO+ Detector. The PSUP is shown in dark green, hold-up/hold-down ropes are shown in pink and red respectively and the AV is shown in blue [2].

1.2 Introduction to SNO+

The primary goals of SNO+ are to observe neutrinoless double beta decay ($0\nu\beta\beta$) and demonstrate the potential of scaleable loaded liquid scintillators for observations of $0\nu\beta\beta$. Due to the relatively low muon flux and large active volume of SNO+, it is also sensitive to neutrinos from the Sun, neutrinos originating from the uranium and thorium radioactive chains within the Earth's crust and mantle and beyond-the-standard-model physics, such as searches for nucleon decay. SNO+ should also be sensitive to rare astrophysical signals, such as axion like particles (ALPs), originating from the Sun. An ALP is a proposed particle, which could explain a fraction of the observed dark matter in the Universe. SNO+ may also provide the best measurement on the non-electron supernova neutrino flux, which could be a probe for the fundamental properties of supernova explosions and the intrinsic nature of neutrinos[3][4]. These two signals form the main 'rare' astrophysical signals explored throughout this thesis.

1.3 ELLIE system

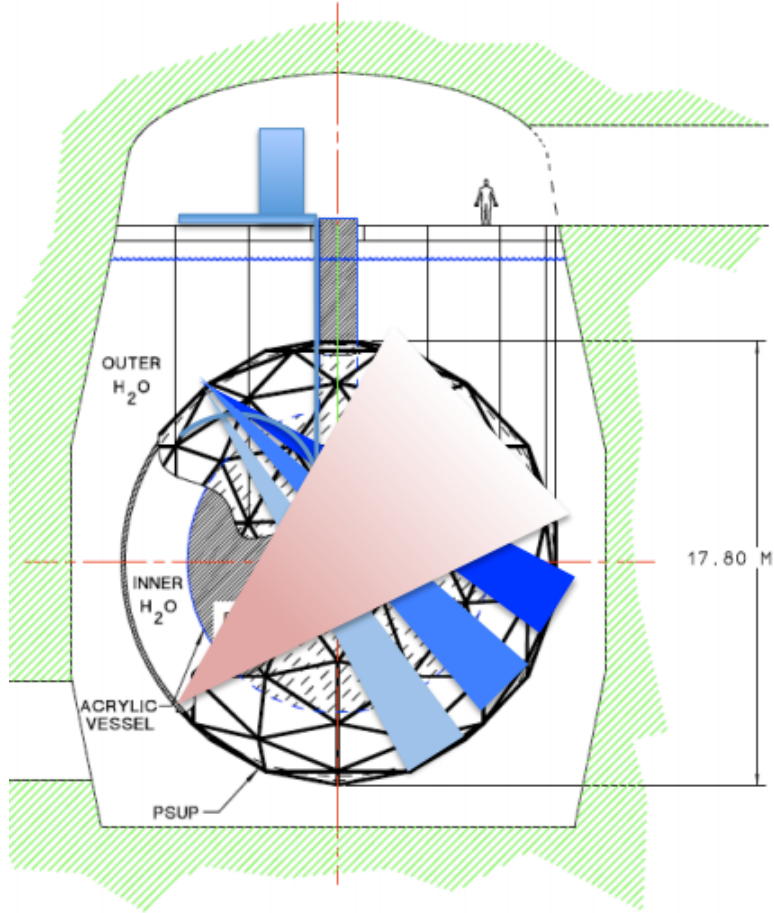


Figure 1.2: Schematic of the ELLIE system, ELLIE is controlled from the deck and the fibres are placed onto the PSUP at different locations. The blue beams represent SMELLIE and the red beam is the TELLIE system. The TELLIE beams have a wider angular profile compared to SMELLIE.

The ELLIE (Embedded LED/Laser light Injection Entity) system is an *in-situ* multi-purpose calibration system to measure the timing (TELLIE), the scattering (SMELLIE) of light across the detector and the stability of scintillator properties (AMELLIE).

The TELLIE system has 91 injection points at different locations on the PSUP, giving coverage of every inward pointing PMT, which allows for the PCA cali-

bration (PMT timing and charge calibration). By minimising the introduction of external calibration sources into the AV, the radio-purity of the scintillator can be improved [5]. Another advantage of the TELLIE system is that the PCA calibration can be interspersed within a normal physics run, effectively increasing the physics running time whilst constantly monitoring the performance of PMTs.

The SMELLIE system has 4 injection points with three emission angles of 0, 10, 20 degrees with respect to the centre of the AV [6]. The system has 5 different lasers: 375nm, 405nm, 440nm, 500nm and a super continuum laser that can produce a wide wavelength range of laser light (400-700 nm) [6]. SMELLIE investigates the angular and wavelength dependence of optical scattering during different SNO+ phases. The commissioning of the SMELLIE system is explored in further detail in chapter 4.

The AMELLIE system has 4 injection points and uses a wide angled fibres [6] to monitor the scintillator's properties over time. AMELLIE uses the same electronics as the TELLIE system, whereas the SMELLIE hardware is operated as an independent system. The optical calibration of SNO+ is critical for the position and energy reconstruction in the SNO+ experiment.

1.4 Calibration in SNO+

In addition to the optical calibration sources associated with the ELLIE system, a laserball system, refurbished from SNO, is deployed to calibrate the TELLIE system and measure several properties of the optical model such as the angular response of the PMTs and scintillator attenuation length. The laserball consists of a spherical quartz flask with a diameter of 109mm and coupled to a nitrogen dye laser, which produces diffuse, isotropic light across a range of wavelengths.

Several other energy calibration sources will be deployed, which can be ‘tagged’ either from an associated PMT in the source or a coincidence tag of radioactive decays. These include a ^{48}Sc source (untagged) producing a 3.3 MeV γ -ray, a ^{24}Na source with a 4.1 MeV γ -ray and a ^{16}N source which produces a 6.1 MeV γ -ray.

The laserball, tagged and untagged calibration sources are deployed internally into the inner volume of the AV (as seen in figure 1.3). It is crucial to maintain the radiopurity of the nitrogen exposed to the scintillator within the AV, otherwise this may increase the radioactivity levels within the scintillator. Thus, sources are contained within a sealed ‘glove box’ on the deck clean room just above the neck of the AV.

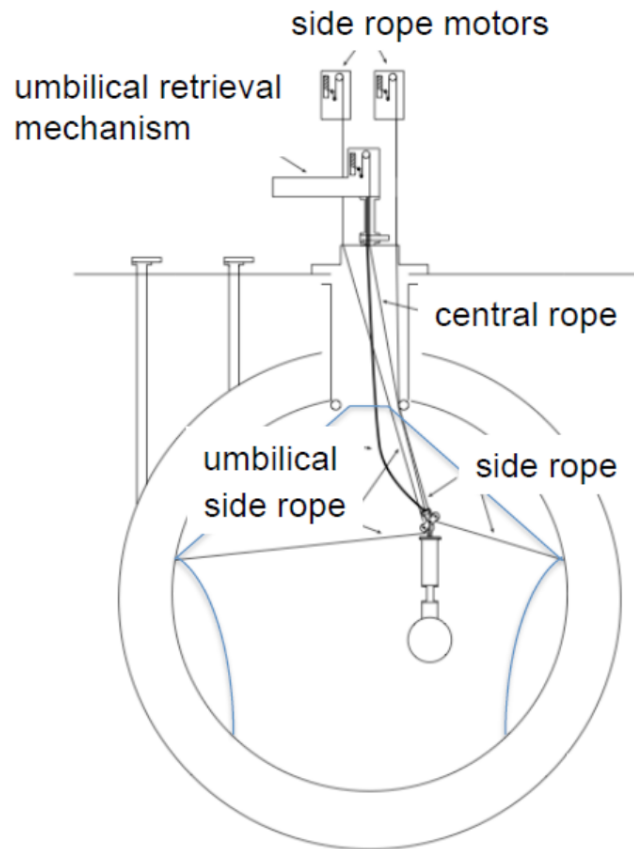


Figure 1.3: Layout of calibration source deployments for SNO+. A central rope and umbilical side ropes are controlled by motors on the SNO+ deck. These enable the calibration source to be placed into different locations. This figure is taken from [2].

Sources are deployed using the central rope to place them in the scintillator and side ropes to move the source in different locations. These ropes are controlled by motors in the deck clean room. In order to meet the radiopurity requirements for deployment in scintillator, the side ropes have been made of terylon and the umbilical is made out of tygothane [7].

1.5 Simulation software

SNO+ uses a software framework called RAT for Monte-Carlo simulation, which is derived from Geant4 [8]. It is a C++ package originally developed for the Braidwood collaboration by Stan Seibert for simulating generic liquid scintillator

experiments. This framework is currently the basis for software used on several experiments including DEAP/CLEAN, mini-CLEAN and DEAP 3600. RAT makes use of ROOT for its optimised storage and analysis of data. SNO+ RAT v5.3.1 is the basis for all the work completed in this thesis, and any deviation from this is explicitly specified.

1.6 Experimental phases

The SNO+ experiment will consist of three primary phases: the water phase (due to start autumn 2016 and run for ~ 6 months), the scintillator phase (due to start at the beginning of 2017 and run for ~ 6 months) and the Tellurium loaded scintillator phase (due to start in 2017 and run for ~ 3 -5 years). There will also be transitional phases, such as the replacement of water with scintillator in the AV, which will take several months to complete.

1.6.1 Water phase

The SNO+ AV will initially be filled with light water for an estimated period of 6 months (including a transitional period with a partially water filled detector). This phase will be used to commission upgrades to the DAQ and to verify the performance of ELLIE. The primary physics aims of the water phase are to calibrate the PMT timing and charge, and estimate the build-up of Radon gas on the inner surface of the AV from exposure to mine air for several years. The water phase is also expected to set an improved upper limit on invisible nucleon decay modes [9]. The SNO+ water phase is expected to be too short for an improved limit on ALP couplings, but an ALP analysis could be performed in order to determine the ALP detection potential in water Cherenkov detectors.

1.6.2 Scintillator phase

During this phase, the AV will be filled with about 780 tonnes of linear alkyl benzene (LAB) in combination with a primary fluor of 2,5 Diphenyloxazole (known as PPO) at a concentration of 2g/L of LAB. This phase will be used: to further verify the performance of SNO+ upgrades to the electronics, to verify the optical model of SNO+ and to measure the rate of internal and external backgrounds from radioactive sources [10]. The rate of radioactive backgrounds will determine the ability to make precision measurements on the solar neutrino-related *pep* flux and low energy ^8B spectrum, as a probe for new physics such as flavour changing neutral currents or mass-varying neutrinos [10]. This phase is sensitive to rare astrophysical signals and could improve upon the current ALP coupling measurements.

1.6.3 Te-loaded scintillator phase

The Te-loaded phase of SNO+ (also referred to as SNO+ phase I) involves the loading of a chemical complex of Telluric acid ($\text{Te}(\text{OH})_6$) and 1,2 butane diol (referred to as Te-diol) into the scintillator. The loading level for SNO+ phase I is 0.5% by weight of natural Tellurium. The Te-diol is transparent and miscible in LAB, with chemical components that are easy to purify and cheap to implement in large quantities. The detected light yield is projected to be 360 PMT hits per MeV at 0.5% loading at 4 °C, but the mixture does quench fluorescence light at higher loading levels [11]. This mixture is used for all Te-loaded scintillator analysis and simulation throughout this thesis. This mixture has been chosen, based on comparisons against several other surfactant based loading methods at 0.3% loading, which typically have light yields between 200-300 PMT hits per MeV [11].

1.7 SNO+ physics goals

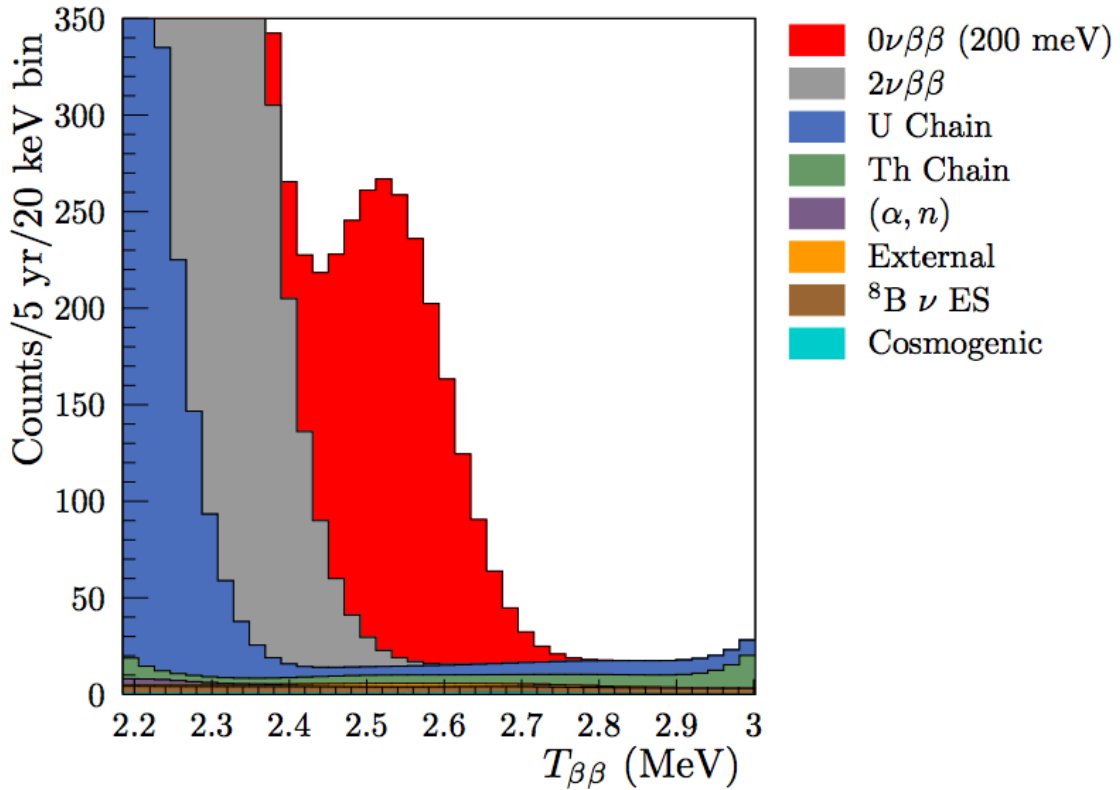
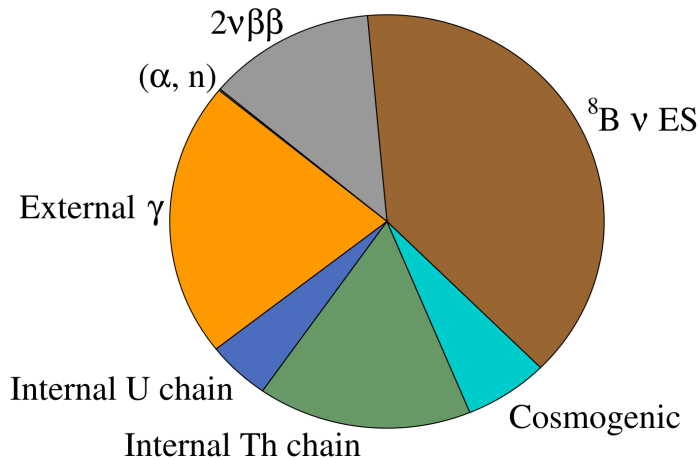
This section contains a brief outline of the different SNO+ physics goals with further discussions on neutrino theory presented in chapter 2 and supernova neutrinos in chapter 7.

1.7.1 Neutrinoless double beta decay

The primary goal of SNO+ is to further the search for neutrinoless double beta decay ($0\nu\beta\beta$), which could usher an entirely new age of our understanding of the Universe. If neutrinos were Majorana particles, or their own anti-particle as required for $0\nu\beta\beta$, this would be a clear demonstration of lepton number violation and could help explain the matter-antimatter asymmetry in the early Universe.

Tellurium is a good choice for observing $0\nu\beta\beta$, because of the large natural abundance of ^{130}Te ($\sim 34\%$) and a long $2\nu\beta\beta$ half-life of $\sim 7 \times 10^{20}$ years (the $0\nu\beta\beta$ decay mechanism is described in chapter 2). Throughout this thesis, the effective Majorana mass is assumed to be 200-400meV with a half life on the order 10^{26} years [10]. There is also the potential to load Te to levels $> 5\%$, using Tellurium diol based compounds, whilst maintaining a sufficiently light yield [10]. The proposed $0\nu\beta\beta$ of ^{130}Te is two electrons with an effective visible energy of 2.527 MeV (see figure 1.4a).

The major backgrounds to a $0\nu\beta\beta$ signal, within the SNO+ detector, are given in figure 1.4b. The $2\nu\beta\beta$ background is a dominant component, which can only be reduced by improving the energy resolution. ^8B neutrinos, produced in the Sun, are detected in SNO+ via the elastic scattering off electrons in the scintillator. The energy spectrum of ^8B is flat between 1.0 and 10.0 MeV (see figure 1.4a), which is irreducible in SNO+ phase I.

(a) SNO+ phase I backgrounds with $0\nu\beta\beta$ signal at 200 meV [10]

(b) Pie chart of SNO+ phase I backgrounds (after one year) within the energy region of interest for SNO+ [10]

Figure 1.4: SNO+ phase I backgrounds for neutrinoless double beta decay that reconstruct within a 3.5m fiducial volume centred on the centre of the AV. Assuming 4.5% energy resolution at 2.5MeV (360 p.e. per MeV) with 0.5% Te loading and 100% ${}^{212}\text{Bi-Po}$ timing based rejection [10].

Background	Count per 5 years
$2\nu\beta\beta$	31.6
${}^8B\nu$ ES	36.3
Uranium Chain	10.4
Thorium Chain	8.7
External γ	18.1
Cosmogenic	6.0
(α , n)	0.8

Table 1.1: Background counts within the region of interest in 5 years of SNO+ Te-loaded phase [10]

Backgrounds from external γ 's, originating from detector materials, such as the PMT glass, AV, hold down ropes, can be reduced by taking a smaller fiducial radius. Internal backgrounds of Uranium and Thorium are reduced significantly by considering the timing profile of Bi-Po *pile-up* events, where two or more decays occur within the same SNO+ event window. For ${}^{214}\text{Bi}$ -Po events almost always occur in separate event windows, whereas a fraction of ${}^{212}\text{Bi}$ -Po events occur within the same event window. By identifying distortions in this timing distribution, the number of ${}^{212}\text{Bi}$ -Po background events can be reduced by a factor of 50 with negligible signal sacrifice [10]. The rate of cosmogenic activation is less relevant in SNO+, compared to similar loaded liquid scintillator experiments such as KamLand-Zen, due to the significantly lower muon flux. However, even a small amount of certain isotopes (produced via cosmogenic activation) can have an impact upon the SNO+ sensitivity to $0\nu\beta\beta$. For example, the decay of ${}^{60}\text{Co}$ is a $\beta - \gamma$ decay, typically deposits an effective visible energy of 2.81 MeV in scintillator; almost indistinguishable from a $0\nu\beta\beta$ decay.

SNO+ has several advantages over others experiments. The loading of ${}^{130}\text{Te}$ isotope, directly into liquid scintillator, is a significantly cheaper method to scale to large active volumes, compared to manufacturing high purity isotope loaded crystals (such as with CUORE) or using liquid Xenon in a time projection chamber

(as in EXO-200). Despite the higher background level, the increase in the number of signal events, ultimately, provides a better sensitivity to $0\nu\beta\beta$. Figure 1.5 shows the sensitivity to $0\nu\beta\beta$ lifetime and effective Majorana mass for SNO+ phase I and a proposed higher Te loading phase (referred to as SNO+ phase II) with 3% loading and a light yield of 500 nhits per MeV.

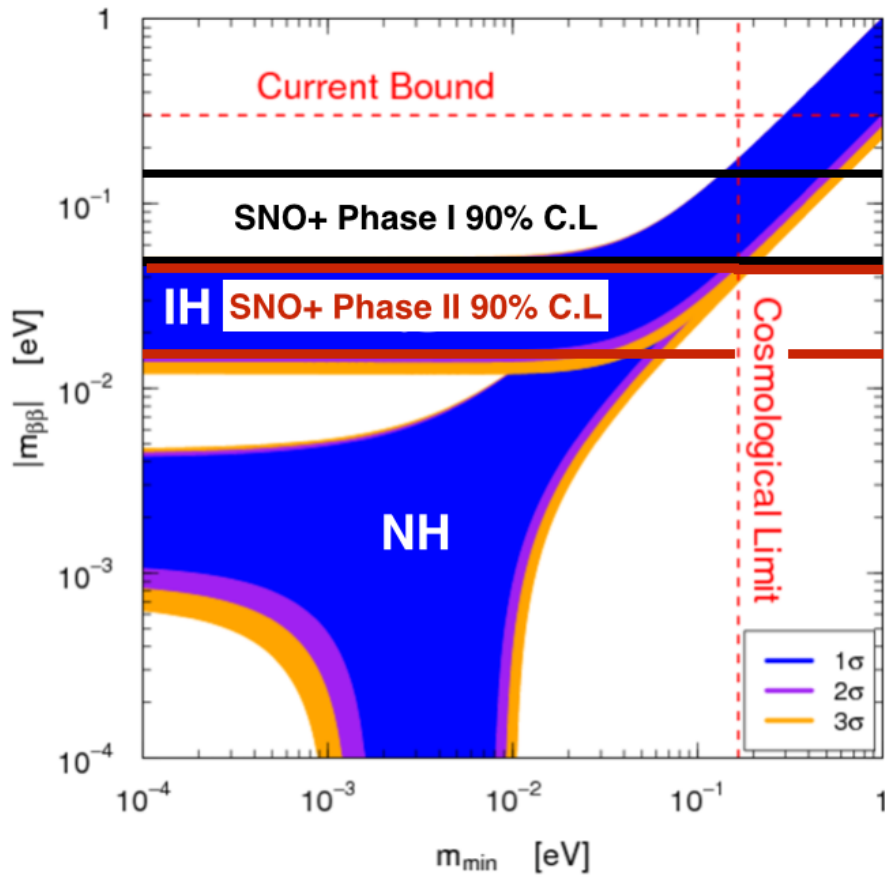


Figure 1.5: $0\nu\beta\beta$ sensitivity in phase space represented by $|m_{\beta\beta}|$, the Majorana neutrino mass against the mass of the lightest neutrino m_{min} . The inverted hierarchy (IH) and normal hierarchy (NH) are separate bands that merge as the neutrino mass eigenstates become degenerate: $m_1 \sim m_2 \sim m_3$. The current bound is taken from CUORE with a ^{130}Te $0\nu\beta\beta$ half-life $> 2.7 \times 10^{24}$ yr at 90% C.L. [12] and compared against a SNO+ phase I with 5 yrs of 0.5% Te-loaded scintillator with 360 p.e. per MeV and SNO+ phase II, which is a proposed upgrade to SNO+ running for 5 yrs with 3% Te-loaded scintillator and > 500 nhits per MeV. This figure is adapted from [13].

1.7.2 Supernova neutrinos

Supernova neutrinos constitute one of the rare astrophysical signals, which could be observed in SNO+ via inverse beta decay and proton elastic scattering interactions, and are further discussed in chapter 7. The core collapse of a supernova generates an incredible number of neutrinos, with around 99% of the gravitational energy converted into neutrinos of all flavours [14]. The production of neutrinos is so great that a supernova, at a distance of 10 kPc away from Earth, is expected to produce $\sim 1,000$ events during the SNO+ scintillator phases[4]. It is also possible that SNO+ would be sensitive to a neutrino burst from stellar collapse into a white dwarf, via the neutrinos produced from electron-proton fusion in a process called neutronisation [15].

The last detected galactic supernova SN1987A, occurred at a distance of 50 kPc in the Large Magellanic Cloud (a satellite Galaxy around the Milky Way). It was observed by several experiments, which saw a total of 24 events[3] and it was noted that the neutrino signal arrived several hours earlier than visible light. This observation is highly advantageous to astronomical measurements of a galactic supernova and forms the basis of an advanced warning system of neutrino experiments called SNEWS. SNO+ will be a member of SNEWS and hopes to alert astronomers to an imminent supernova explosion.

1.7.3 Solar neutrinos

The Sun is a very prodigious source of neutrinos, and these offer an insight into the internal dynamics of the Sun. Measuring the CNO, pep and low energy ^8B neutrino flux would improve our understanding of the Sun's metallicity and MSW effects[10]. The sensitivity to this type of physics is determined by the energy trigger threshold. The relatively low muon flux, in SNO+, means that the cosmo-

genic activation isn't the dominant background at low energies near the trigger threshold. The trigger threshold will be limited by the level of ^{14}C present in the scintillator, where ^{14}C beta decays with an endpoint of 0.170 MeV, which can reconstruct to a ~ 0.5 MeV, and is intrinsically present within the scintillator cocktail. Higher than expected rates of ^{222}Rn leaching from the inner AV into the scintillator [16] could also swamp a measurement of the ^8B flux in SNO+. The frequency of *pile-up* against other backgrounds will also determine the energy trigger threshold.

1.7.4 Reactor and geo-neutrinos

Nuclear reactors (within $\sim 500\text{km}$ of the SNO+ detector) and naturally occurring radioactive decays of ^{238}U and ^{232}Th chain, within the Earth's crust and mantle, can generate a measurable anti-neutrino flux in SNO+. These types of events are expected to produce ~ 90 events a year in the detector [10]. In collaboration with several other physics experiments, identification of these types of neutrinos may lead to an improved measurement of the radiogenic heat flow, within the Earth's crust and mantle, and an improved understanding of mantle dynamics [10].

1.7.5 Exotic searches: nucleon decay and ALPs

Many theories predict baryon and lepton non-conservation, and a measurement of invisible nucleon decay would provide a hint of such new physics [10]. Invisible nuclear decay modes, such as $n \rightarrow 3\nu$, could be observed. Other experiments have searched for nucleon decay with ^{16}O decays (SNO [17]) and ^{12}C decays (KamLAND [18] and Borexino [19]). The initial water phase of SNO+ will also search for ^{16}O decays, where the resulting ^{15}O nuclei de-excites by emitting a 6.18 MeV γ particle [10]. SNO+ is expected to measure the lifetimes of the invisible nucleon decay for neutrons τ_n and for protons τ_p with 6 months of water running, with

a predicted 90% (Bayesian) C.L. of $\tau_n > 1.25 \times 10^{30}$ and $\tau_p > 1.38 \times 10^{30}$ years [10]. This is an improvement upon the current limit from KamLAND, a liquid scintillator experiment, with $\tau_{n,p} > 5.8 \times 10^{29}$.

SNO+ will be sensitive to Axion Like Particles (ALPs) produced within the Sun. An ALP is defined as a neutral pseudoscalar particle that exists as a potential dark matter constituent. ALPs could be produced via proton-deuterium fusion with a total energy of 5.5 MeV and a rest mass of < 1 MeV. There are several channels for detecting ALPs, with different phases of SNO+ being sensitive to different channels. ALPs are explored throughout this thesis; the physics of ALPs is described in chapter 5 and ALP detection in neutrino experiments is discussed in chapter 6.

2

The physics of neutrinos

“Neutrinos have mass? I didn’t know they were Catholic”

– Adapted from Woody Allen

The neutrino was first postulated by Wolfgang Pauli in 1930, in his famous letter to the Physical Institute of the Federal Institute of Technology, Zürich, in which he speculated that the continuous beta decay spectrum could be explained by a new neutral particle. But the neutrino was only directly observed in 1956, when a scintillator experiment performed by Clyde Cowan Jr. and Frederick Reines at the Savannah River reactor [20], observed inverse β decay and confirmed the existence of the electron anti-neutrino $\bar{\nu}_e$.

The Homestake experiment, performed by Raymond Davis Jr. *et al.* from the late 1960s onwards [21], measured the flux of solar neutrinos by observing ν_e capture on ^{35}Cl . They discovered that the ν_e flux was $\sim 1/3$ of the expected flux of solar neutrinos, which marked the emergence of the ‘solar neutrino problem’. The confirmation of the solar neutrino flux from [21] resulted in the 2002 Nobel prize in Physics. The solar neutrino problem can be explained by neutrino oscillations between flavour eigenstates (see section 2.3) and was first conclusively confirmed by the combination of Super Kamiokande [22] and SNO [23].

2.1 Neutrinos in the Standard Model

The Standard Model is the theoretical framework that describes the nature of fundamental particles. Particles are divided into spin-1/2 fermions, which respect the Pauli exclusion principle, and integer spin bosons that are not subject to this principle. The Pauli exclusion principle states that two identical fermions cannot occupy the same quantum state simultaneously. Fermions with a spin-1/2 are divided into ‘coloured’ quarks and ‘colourless’ leptons. Bosons with integer spin are responsible for mediating the fundamental forces through which particles interact: the electromagnetic force is mediated by massless photons, the strong force is mediated by gluons, the weak force is mediated by W^\pm and Z^0 bosons.

The neutrino is a fundamental spin-1/2 fermion with neutral charge and is built into the Standard Model as a massless particle. The neutrino only interacts via the weak force as it does not have any colour or electrical charge. Measurements of the width of Z^0 boson taken at CERN have confirmed that there are three active neutrino states with masses less than half the mass of the Z^0 mass [24] at $91.1876 \pm 0.0021 \text{ GeV}/c^2$ [25].

In the Standard Model, elementary particles obtain mass through their coupling to the Higgs boson, which specifically requires non-zero terms for both couplings to the right and left handed fields of each particle. However, in the case of neutrinos, there is no right handed field and this mechanism doesn’t yield a mass. This observation is in direct contrast to strong experimental evidence of neutrino oscillation, which requires at least two neutrinos to have non-zero mass.

2.2 Sources of neutrinos

There are many different sources of neutrinos. Figure 2.1 depicts the different energy spectra of neutrinos including relic neutrinos that decoupled from baryonic matter in the early Universe, which have very low energies $< 10^{-3}$ eV, solar neutrinos that are produced by fusion reactions within the Sun, with energies between 1-10 MeV, and supernova neutrinos produced by a supernova burst 1987A and a relic background from old supernovae at energies between 1-30 MeV. Figure 2.1 also includes neutrinos produced by man-made nuclear reactors and naturally occurring nuclear reactions taking place within the Earth. Neutrinos produced by extra-galactic sources [26], which have been detected at energies > 1 PeV [27] are also included. Figure 2.1 also shows how SNO+ fits into this context, given that it will have an energy threshold of 0.1 MeV and is sensitive to terrestrial, solar, supernova and reactor neutrinos [10].

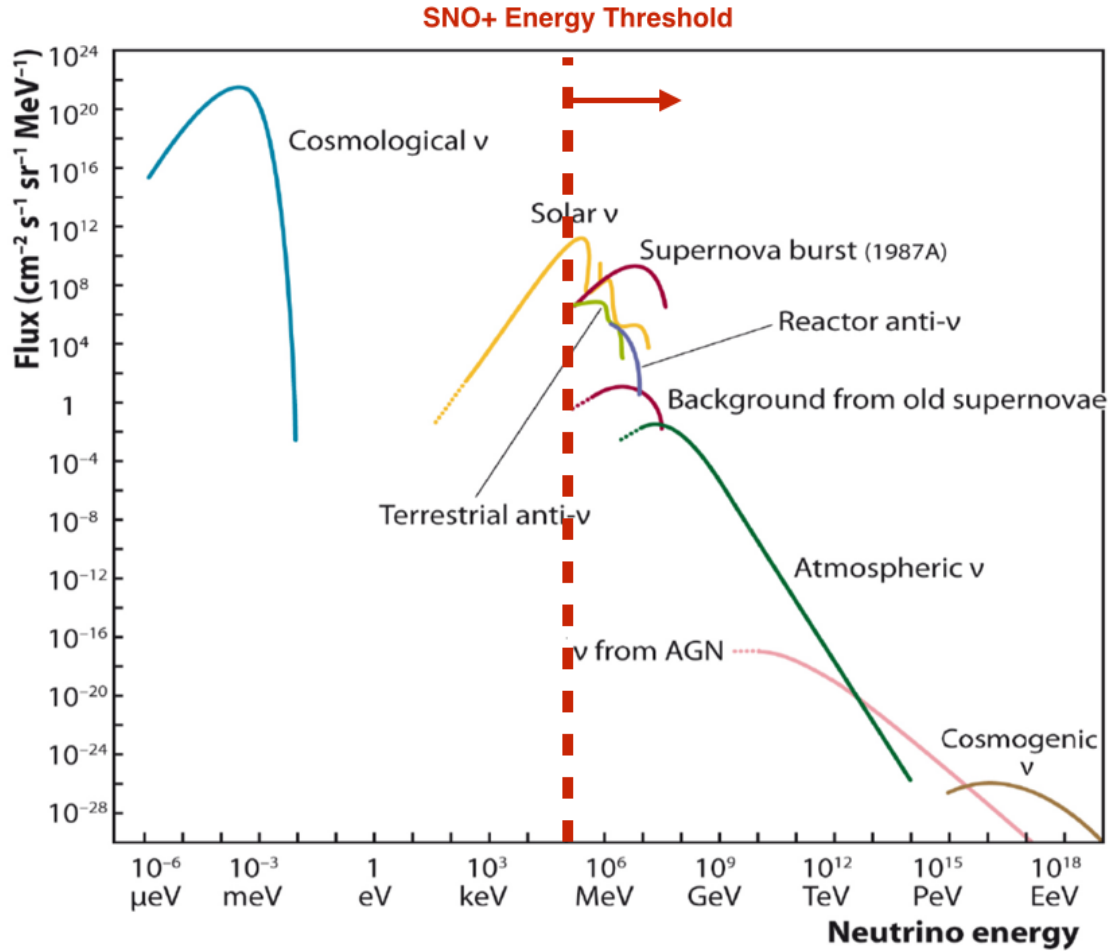


Figure 2.1: Energy spectra of different neutrino sources. Proposed cosmological ν 's originate from the early Universe, solar ν 's refer to neutrinos originating from nuclear processes in our local Sun, supernova burst ν 's use SN 1987A, terrestrial ν 's come from radioactivity within the Earth's core, and reactor anti- ν 's are a by-product of artificial nuclear reactors. This figure is adapted from [28].

2.3 Neutrino oscillations in vacuum

Neutrinos are produced in one of three flavour eigenstates: electron, muon or tau, via the weak interaction. The neutrino propagates in mass eigenstates, but interacts in flavour eigenstates. If the two sets of eigenstates are rotated relative to each other, then as the neutrino propagates, the relative phase of each mass eigenstate changes. This affects the composition of the neutrino and gives a non-negligible probability that a different flavour of neutrino is observed, after travelling a finite distance. The Pontecorvo-Maki-Nakagawa-Sakata (PMNS) uni-

tary matrix, U_{lj} describes the mixing between the mass and flavour eigenstates of the neutrino:

$$\begin{aligned} |\nu_l\rangle &= \sum_{j=1}^3 U_{lj} |\nu_j\rangle \\ |\bar{\nu}_l\rangle &= \sum_{j=1}^3 U_{lj}^* |\bar{\nu}_j\rangle \end{aligned} \quad (2.1)$$

$$l \in \{e, \mu, \tau\}, \quad j \in \{1, 2, 3\}$$

where the flavour eigenstate, $|\nu_l\rangle$ is given as a superposition of the mass eigenstates, $|\nu_j\rangle$ and U_{lj} is given as:

$$U_{lj} = \begin{pmatrix} U_{e1} & U_{e2} & U_{e3} \\ U_{\mu1} & U_{\mu2} & U_{\mu3} \\ U_{\tau1} & U_{\tau2} & U_{\tau3} \end{pmatrix} \quad (2.2)$$

$$U_{lj} = \begin{pmatrix} 1 & 0 & 0 \\ 0 & c_{23} & s_{23} \\ 0 & -s_{23} & c_{23} \end{pmatrix} \begin{pmatrix} c_{13} & 0 & s_{13}e^{-i\delta} \\ 0 & 1 & 0 \\ -s_{13}e^{-i\delta} & 0 & c_{13} \end{pmatrix} \begin{pmatrix} c_{12} & s_{12} & 0 \\ -s_{12} & c_{12} & 0 \\ 0 & 0 & 1 \end{pmatrix} \begin{pmatrix} e^{i\alpha_1/2} & 0 & 0 \\ 0 & e^{i\alpha_2/2} & 0 \\ 0 & 0 & 1 \end{pmatrix} \quad (2.3)$$

where $c_{jk} = \cos\theta_{jk}$ and $s_{jk} = \sin\theta_{jk}$. θ_{jk} is the mixing angle between mass eigenstates j and k , δ is the CP violating phase and α_M are the Majorana phases where $M \in \{1, 2\}$. If neutrinos are Dirac particles, they have distinct anti-particles and the last matrix in equation 2.3 reduces to the identity matrix.

In order to illustrate the effects of neutrino oscillations, the rest of this chapter will assume a two-neutrino mixing case between ν_e and ν_μ and use natural units. The time evolution of eigenstates is described by the time-dependent Schrödinger equation:

$$i\frac{\partial}{\partial t} \begin{pmatrix} |\nu_1\rangle \\ |\nu_2\rangle \end{pmatrix} = H \begin{pmatrix} |\nu_1\rangle \\ |\nu_2\rangle \end{pmatrix} \quad (2.4)$$

where H is hamiltonian in the mass basis giving

$$i\frac{\partial}{\partial t} \begin{pmatrix} |\nu_1\rangle \\ |\nu_2\rangle \end{pmatrix} = \begin{pmatrix} E_1 & 0 \\ 0 & E_2 \end{pmatrix} \begin{pmatrix} |\nu_1\rangle \\ |\nu_2\rangle \end{pmatrix} \approx \begin{pmatrix} m_1^2/2p & 0 \\ 0 & m_2^2/2p \end{pmatrix} \begin{pmatrix} |\nu_1\rangle \\ |\nu_2\rangle \end{pmatrix} + \begin{pmatrix} p & 0 \\ 0 & p \end{pmatrix} \begin{pmatrix} |\nu_1\rangle \\ |\nu_2\rangle \end{pmatrix} \quad (2.5)$$

The mixing between flavour and mass eigenstates can be expressed as:

$$\begin{pmatrix} |\nu_e\rangle \\ |\nu_\mu\rangle \end{pmatrix} = \begin{pmatrix} \cos\theta_{12} & \sin\theta_{12} \\ -\sin\theta_{12} & \cos\theta_{12} \end{pmatrix} \begin{pmatrix} |\nu_1\rangle \\ |\nu_2\rangle \end{pmatrix} \quad (2.6)$$

and the mixing angles θ_{12} between the two flavour and mass eigenstates. It is helpful to re-write the Hamiltonian for a vacuum H_{VAC} into the neutrino flavour basis, as we can directly observe flavour eigenstates. This can be achieved by combining equations 2.5 and 2.6 giving:

$$i\frac{\partial}{\partial t} \begin{pmatrix} |\nu_e\rangle \\ |\nu_\mu\rangle \end{pmatrix} = H_{\text{VAC}} \begin{pmatrix} |\nu_e\rangle \\ |\nu_\mu\rangle \end{pmatrix} \quad (2.7)$$

where H_{VAC} is:

$$H_{\text{VAC}} = \left(\frac{\Delta m_{12}^2}{4E} \right) \begin{pmatrix} -\cos 2\theta_{12} & \sin 2\theta_{12} \\ \sin 2\theta_{12} & \cos 2\theta_{12} \end{pmatrix} \quad (2.8)$$

where E is the energy of the neutrino in GeV. After having travelled a distance L , the survival probability of an electron neutrino $P(\nu_e \rightarrow \nu_e)$ is given as:

$$P(\nu_e \rightarrow \nu_e) = 1 - \sin^2 2\theta_{12} \sin^2 \left(\frac{\Delta m_{12}^2 L}{4E} \right) \quad (2.9)$$

$$\Delta m_{12}^2 = m_2^2 - m_1^2$$

where Δm_{12}^2 is the difference between the two mass eigenstates in natural units. A key feature of this equation is that if the difference in mass is zero, then neutrino oscillations cannot take place. Thus, the experimental observation of neutrino

oscillation indicates that the mass of at least one neutrino mass eigenstate must be greater than zero. The distance over which a neutrino oscillates back into its original state, when travelling through a vacuum, L_{VAC} can be parameterised as:

$$L_{\text{VAC}} = \frac{4\pi E}{\Delta m_{12}^2} \quad (2.10)$$

where equation 2.9 can be re-written using L_{VAC} to give:

$$P(\nu_e \rightarrow \nu_e) = 1 - \sin^2 2\theta_{12} \sin^2 \left(\frac{\pi L}{L_{\text{VAC}}} \right) \quad (2.11)$$

If L is smaller than L_{VAC} , then $\sin^2 \left(\frac{\pi L}{L_{\text{VAC}}} \right) \rightarrow 0$ and the neutrino will not have propagated long enough for oscillations to develop. However, if L is greater than L_{VAC} , there is a non-negligible probability of ν_e disappearance and the reduction of the average ν_e flux. There are several different experiments, which are sensitive to θ_{12} and Δm_{12}^2 , and also to one or more of the other 3-neutrino-flavour mixing parameters: θ_{13} , θ_{32} , Δm_{32}^2 and Δm_{31}^2 .

2.4 Neutrino oscillations in matter

In matter, all flavours of neutrinos undergo coherent, forward scattering with electrons via a ‘neutral current’ interaction mediated by the Z^0 boson. But, the electron neutrino also undergoes a charged current interaction (mediated by a W boson). This enhances the forward scattering amplitude for ν_e and affects the relative propagation of different mass eigenstates. This effect is known as the ‘MSW’ effect [29][30], and can lead to large neutrino mixing even if the mixing angles in a vacuum are small.

When including the effect of the charged current interaction of ν_e , the time evolution of the flavour eigenstates changes to give an adjusted Hamiltonian for matter,

H_{MAT} :

$$H_{\text{MAT}} = H_{\text{VAC}} \pm \sqrt{2}G_F \begin{pmatrix} N_e & 0 \\ 0 & 0 \end{pmatrix} \quad (2.12)$$

where G_F is the Fermi constant and N_e is the number density of electrons. The original mixing angle, θ_{12} then becomes θ_{12}^* where:

$$\sin^2 2\theta_{12}^* = \frac{\sin^2 2\theta_{12}}{(\cos 2\theta_{12} - \frac{L_{\text{VAC}}}{L_M})^2 + \sin^2 2\theta_{12}} \quad (2.13)$$

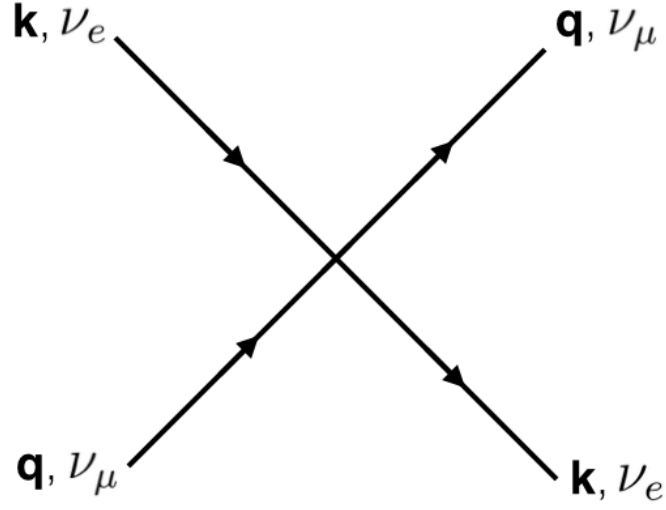
where L_M is the effective scattering length of the electron:

$$L_M = \frac{\sqrt{2}\pi}{G_F N_e} \quad (2.14)$$

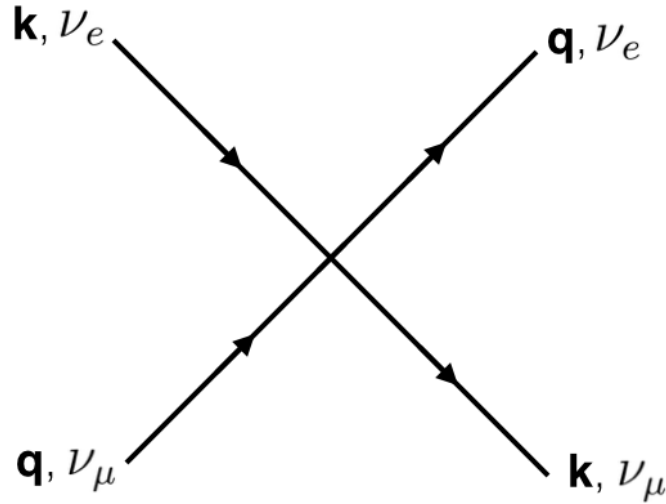
High densities of electrons in matter have a significant effect upon neutrino oscillations, but the extreme conditions of a core-collapse supernova can further distort the flavour composition.

2.5 Neutrino oscillations in supernovae

During a supernova explosion, the iron core of a massive star becomes unstable, it collapses on itself and rebounds producing regions of ultra-high densities and a shockwave that propagates through the star. At these ultra-high densities of $\sim 10^{14}$ g cm⁻³, neutrino-neutrino forward scattering becomes non-negligible and strongly affects the flavour composition of supernova neutrinos [31][14][3][32]. In the two neutrino case, figure 2.2 depicts the Feynman diagrams for neutrino-neutrino forward scattering, where the ν_e and ν_μ have initial momenta \mathbf{k} and \mathbf{q} respectively [33].



(a) Diagonal terms



(b) Off-diagonal terms

Figure 2.2: Feynman diagrams for neutrino-neutrino forward scattering.

By including these effects, the Hamiltonian for neutrino flavour propagation in a core-collapse supernova, H_{SN} becomes [33]:

$$H_{\text{SN}} = H_{\text{MAT}} \pm \sqrt{2}G_F \begin{pmatrix} N_{\nu_e} & N_{\langle\nu_e|\nu_\mu\rangle} \\ N_{\langle\nu_e|\nu_\mu\rangle} & N_{\nu_\mu} \end{pmatrix} \quad (2.15)$$

where N_{ν_e} and N_{ν_μ} are the number densities of electron and muon neutrinos arising from interaction given in figure 2.2a. $N_{\langle\nu_e|\nu_\mu\rangle}$ and $N_{\langle\nu_e|\nu_\mu\rangle}$ represent the off-diagonal potential, which arises from the interaction given in figure 2.2b.

These effects occur for supernova neutrinos as they propagate within core-collapse supernova. The oscillation mixing is highly dependent upon the collapse model, the size of the collapsing star and initial neutrino flux just before the collapse. In certain models [31][3], the effect of neutrino-neutrino interactions can produce a distinct swapping of the ν_x and ν_e energy spectra in the inverted hierarchy of neutrino, but not in the normal hierarchy (see section 2.6). SNO+ is sensitive to the flux of all neutrino flavours (ν_x) via proton neutrino elastic scattering and the flux of $\bar{\nu}_e$ via inverse β -decay. A supernova at ~ 10 kPc away would create ~ 100 s of events in the SNO+ detector and it may be possible to distinguish a difference between the inverted and normal mass hierarchies from the ν_x/ν_e flux ratio. The potential for making this measurement is discussed extensively in chapter 7.

2.6 Neutrino mass hierarchy

Neutrino oscillations do not give a direct measurement of the mass eigenstates, but can measure the square difference of mass eigenstates. The current best values of these from global fits of data from various experiments are [25]:

$$\Delta m_{12}^2 = 7.58 \times 10^{-3} \text{ eV}^2 \text{ - solar}$$

$$\Delta m_{23}^2 = 2.53 \times 10^{-5} \text{ eV}^2 \text{ - atm.}$$

However, the mass differences alone do not indicate the ordering of the mass eigenstates and leaves two possibilities:

$$\text{Normal hierarchy: } m_1 < m_2 < m_3$$

$$\text{Inverted hierarchy: } m_3 < m_1 < m_2$$

as shown with the flavour compositions for different mass hierarchies in figure 2.3. There are several next-generation experiments such as DUNE, PINGU, INO,

ORCA and Hyper-Kamiokande that may be able to determine the mass hierarchy [34].

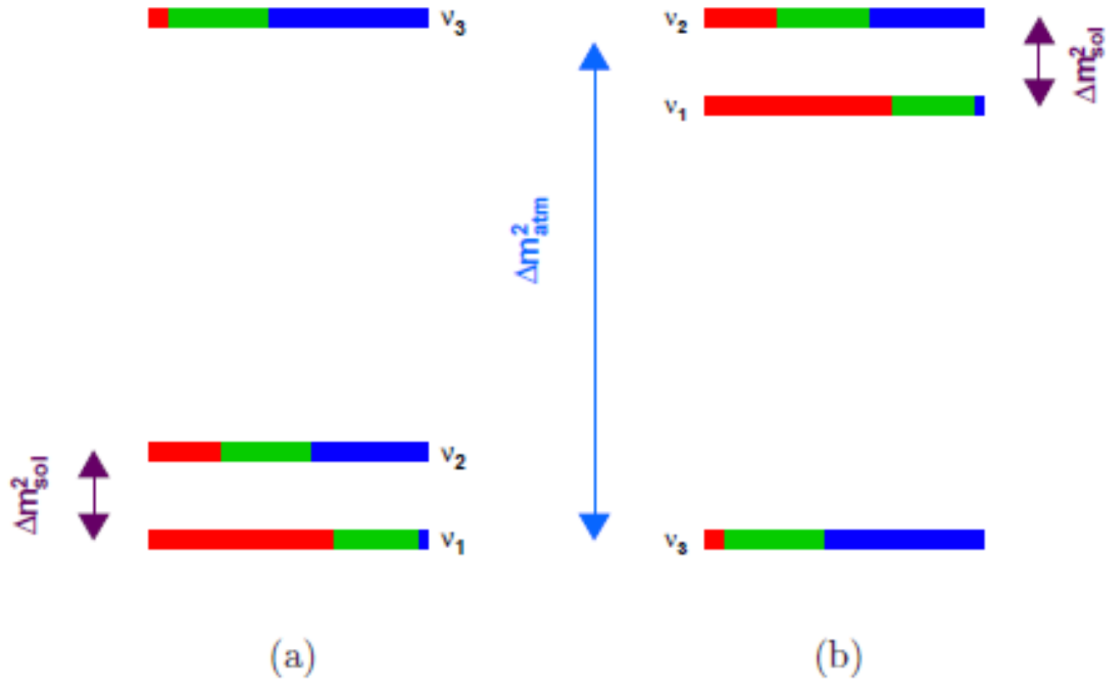


Figure 2.3: Possible neutrino mass orderings for the (a) normal hierarchy and the (b) inverted hierarchy. The colours represent the flavour eigenstate contribution to each mass eigenstate: red (electron neutrino), green (muon neutrino) and blue (tau neutrino). Δm_{12} is often called Δm_{solar} , because solar neutrino experiments are sensitive to its value. This figure is taken from [34].

2.7 Neutrinoless double beta decay

A key question in neutrino physics still remains unanswered: are neutrinos their own anti-particles? In 1937, Majorana proposed that the neutrino may not necessarily have a distinct anti-particle, as is the case for Dirac particles, but instead be its own anti-particle [35], a Majorana particle. If neutrinos are Dirac particles, they have four states from a combination of particle or anti-particle with either left or right handedness. In the Majorana theory, neutrinos are either left handed or right handed, such that an anti-neutrino is in fact a right handed state of the

neutrino. Neutrinoless double beta decay ($0\nu\beta\beta$) is a fascinating process that violates lepton number conservation and provides a mechanism for leptogenesis [36].

In order to understand the mechanism behind $0\nu\beta\beta$, we must first understand the process of double β decay ($2\nu\beta\beta$) as a concept. Double β decay is a rare radioactive process, whereby two neutrons simultaneously transform into two protons within an atomic nucleus. This transformation emits two electrons and two anti-electron neutrinos as seen in figure 2.4.

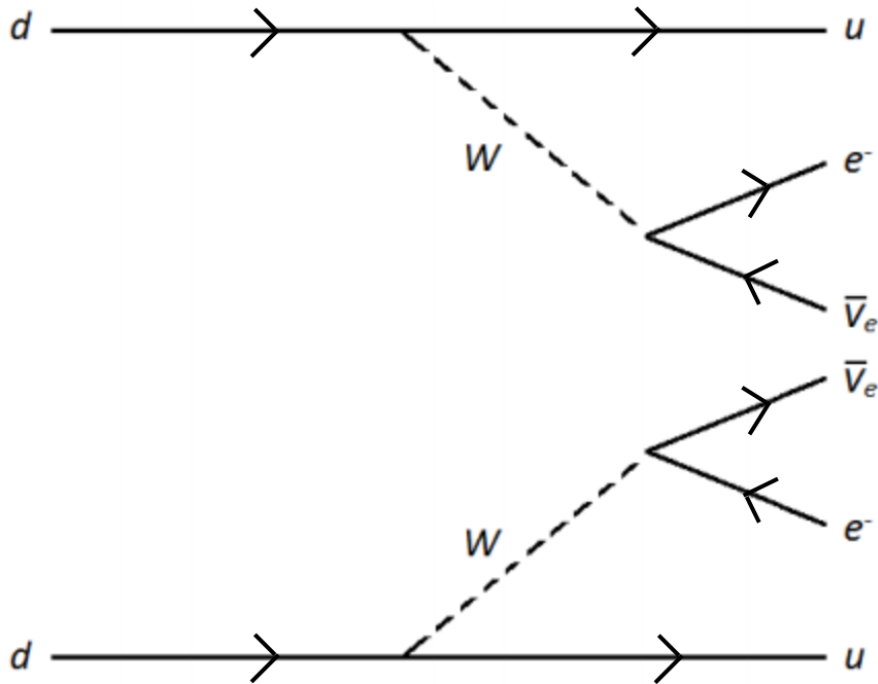


Figure 2.4: Feynman diagram of double β decay with the two electrons and two anti-neutrinos emitted.

Double β decay can only occur in certain nuclei with mass $m(Z, A)$ that meet the following criteria [37]:

$$\begin{aligned} m(Z, A) &> m(Z + 2, A) + 2m_e \\ m(Z, A) &< m(Z + 1, A) + m_e \end{aligned} \tag{2.16}$$

where Z is the atomic number and A is the total number of nucleons in the nu-

cleus. The total energy released by this reaction is the difference between the rest mass energies of the parent and daughter nuclei. This type of decay occurs when normal beta decay is forbidden, because the latter is energetically disfavoured or strongly suppressed by angular momentum conservation. This opens the opportunity for a nucleus to favour double beta decay and is most common in ‘even-even’ nuclei [38]. In double beta decay, the neutrons undergo beta decay, emitting right handed anti-neutrinos (which we know are coupled to the weak force) with a positive helicity.

$0\nu\beta\beta$ decay occurs when the $\bar{\nu}_e$ emitted, from one of the β -decays in $2\nu\beta\beta$, is absorbed as a ν_e by the W boson in the other β -decay (see figure 2.5). If the neutrino is massive and a Majorana particle, one of the anti-neutrinos can flip its helicity (such that it is negative). The helicity flip of the anti-neutrino is proportional to the neutrino mass, and therefore would be responsible for significantly suppressing the $0\nu\beta\beta$ decay relative to the $2\nu\beta\beta$ decay.

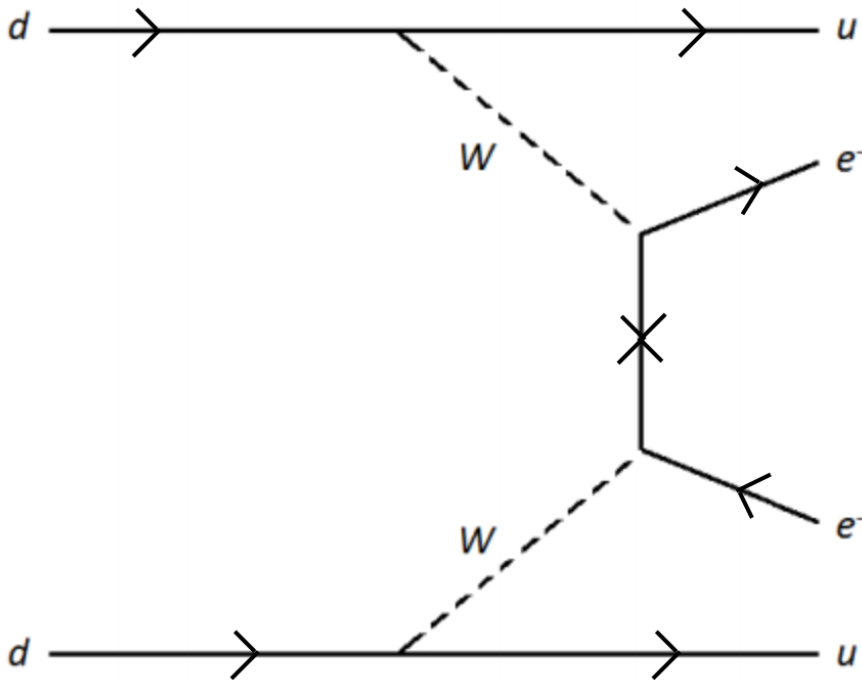


Figure 2.5: Feynman diagram of $0\nu\beta\beta$ with the two electrons emitted.

The measurement of $0\nu\beta\beta$ is also a direct probe of the Majorana mass, as the rate of $0\nu\beta\beta$ decay is proportional to $m_{\beta\beta}^2$ [34] giving:

$$\frac{1}{T_{1/2}^{0\nu\beta\beta}} = G^{0\nu}(Q, Z) \times |M^{0\nu}|^2 \times \frac{m_{\beta\beta}^2}{m_e^2} \quad (2.17)$$

$$m_{\beta\beta} = \Sigma_{i=1}^3 m_i U_{ei}$$

where $G^{0\nu}(Q, Z)$ is the phase factor determined by the Q-value of a particular transition for a nuclei with associated nuclear charge Z , $M^{0\nu}$ is the nuclear matrix element and $m_{\beta\beta}$ is the effective Majorana mass and defined as the sum over the neutrino mass eigenstates. Figure 2.6 shows the effect of using different nuclear matrix models of $T_{1/2}^{0\nu\beta\beta}/m_{\beta\beta}$ for several $0\nu\beta\beta$ experiments. For example, SNO+ Phase I with a $0\nu\beta\beta$ rate measurement of $T_{1/2}^{0\nu\beta\beta} = 2.0 \times 10^{26}$ yrs is sensitive to $m_{\beta\beta}$ masses between 35 - 100 meV depending on the choice of nuclear matrix model.

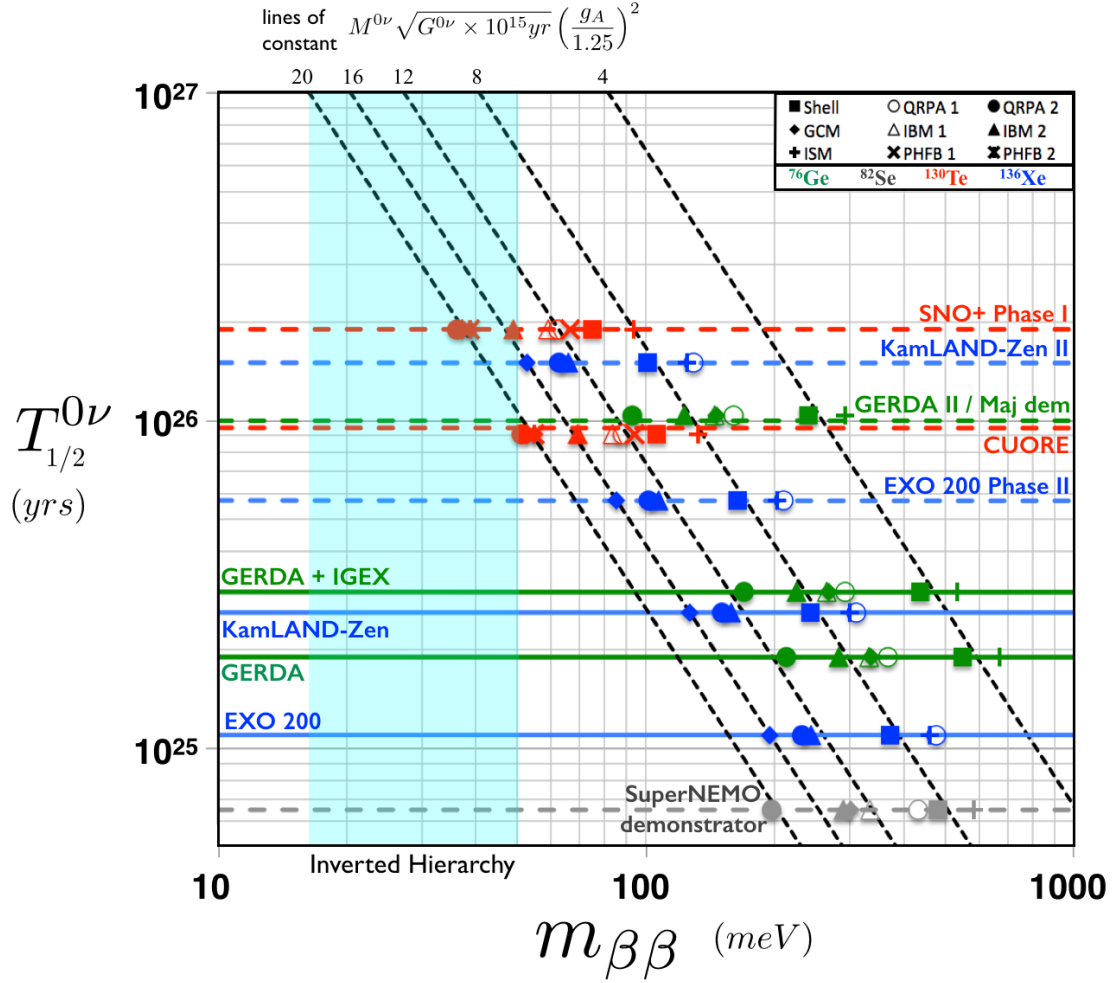


Figure 2.6: $0\nu\beta\beta$ sensitivity for all current $0\nu\beta\beta$ experiments (solid) and proposed/upgrading experiments (dashed). Different shapes (per experiment) represent different nuclear matrix element models used to calculate the Majorana mass. This is taken from [39]

2.7.1 Current experimental limits

The best limit for $0\nu\beta\beta$ in ^{130}Te is from CUORE-0 and CUORICINO (combined), with a result of $T_{\frac{1}{2}}^{0\nu\beta\beta} > 4.0 \times 10^{24}$ yrs at 90% C.L., corresponding to an effective Majorana mass $m_{\beta\beta}$ of 270 - 760 meV [40]. The first phase of CUORE, CUORE-0 consists of TeO_2 bolometers, shielded from external radioactive backgrounds and themselves contained within a highly radio-pure material with almost zero backgrounds. As more bolometric towers are added to CUORE, this will gradually improve the sensitivity to the point where CUORE will be close to probing

part of the inverted hierarchy (see figure 2.6) and ultimately, reaching down to $T_{\frac{1}{2}}^{0\nu\beta\beta} > 9.0 \times 10^{25}$ yrs once the CUORE experiment is fully commissioned.

The KamLand-Zen [41] and EXO-200 [42] experiments both use ^{136}Xe as their double beta isotope. KamLand-Zen is the upgraded version of KamLand, a large liquid scintillator based experiment similar to SNO+. KamLand-Zen deployed a highly radio-pure bag filled with liquid scintillator enriched with 320kg of ^{136}Xe [41]. EXO-200 is a 200kg liquid TPC detector loaded with liquid Xenon and using ^{136}Xe isotope enriched to 80%. Its aim is to observe the $0\nu\beta\beta$ of ^{136}Xe and to demonstrate the potential of observing $0\nu\beta\beta$ in an upgraded version of EXO [42] called nEXO. nEXO is different from other $0\nu\beta\beta$ experiments, because it may be possible to measure the amount of ^{136}Ba -ions produced from the neutrinoless double beta decay of ^{136}Xe [43]. The absorption and remission spectra of the Ba^+ ion, using laser beams, as a secondary confirmation of $0\nu\beta\beta$, along side the energy spectrum of the electrons produced in the main detector.

The limits from the KamLand-Zen experiment[44] and EXO-200 experiment [42] are respectively $T_{\frac{1}{2}}^{0\nu\beta\beta} > 2.4 \times 10^{25}$ at 90% C.L., and $T_{\frac{1}{2}}^{0\nu\beta\beta} > 1.1 \times 10^{25}$ at 90% C.L. and correspond to an effective upper limit on the Majorana neutrino mass of 120 - 250 meV.

3

Commissioning the SNO+ DAQ software

The SNO+ data acquisition system (DAQ) and associated software is responsible for: controlling the detector, diagnosing the health of the detector and taking quality physics data that can be used for a variety of physics goals of the SNO+ experiment. Searches for ALPs and supernova neutrinos are two such analyses that are highly dependent upon the performance of the DAQ. Neutrinos from a supernova explosion (in the Galaxy) are thought to produce a burst of events over a 10s period [10], but only occur at a rate of ~ 3 per century [14]. In order to maximise the chance of capturing this signal, SNO+ needs to be fully operational for as long as possible. If the DAQ can be easily controlled and reliably reports the detector health, a SNO+ operator can more effectively respond to malfunctions and reduce the probability of having to repair the detector and ultimately increase the operation time.

The partial commissioning of the SNO+ DAQ took place over a series of data runs in December 2014. A significant amount of hardware has been inherited from the SNO experiment, but several upgrades, such as the XL3s and ELLIE system, are

required in order to meet the physics goals of SNO+. Thus, the SNO+ DAQ has also had a significant overhaul in its software systems. This chapter will discuss the implementation of software upgrades to SNO+ that I have completed with the DAQ, with a discussion on the SMELLIE system in chapter 4 .

This chapter is organised as follows with: an introduction to the SNO+ DAQ given in section 3.1, the implementation of the run/configuration files given in section 3.2, an overview of the SNO+ DAQ software given in section 3.3 and the implementation of the control and monitoring of the DAQ given in section 3.4.

3.1 Introduction to SNO+ DAQ

The basic function of the SNO+ DAQ is to control the detector hardware and collect data from the front end electronics associated with each PMT. Understanding the SNO+ trigger system offers a useful insight into understanding how SNO+ DAQ controls the overall detector.

The basic idea of a SNO+ trigger is simple: if a pre-determined number of PMTs ‘fire’ in coincidence, the front end electronics (FECs) are signalled to save any data taken from all PMTs. PMTs ‘fire’ when a photon lands on the photocathode and creates a primary electron¹. The PMT focusses this electron, uses it to produce a cascade of electrons. If the charge exceeds a pre-determined threshold, the PMT is considered to ‘fire’ . This is called a NHIT trigger², which is detected by the SNO+ electronics and leads to the issuance of a global trigger.

The SNO+ electronics can be described by considering the processes, which follow

¹via the photoelectric effect

²There are other types of trigger, such as the EXTA (External Async.) trigger, which signal a readout of the FECs regardless of the number of PMTs firing in coincidence.

the detection of photons from a physics event (such as a nuclear decay) inside the AV. Once the charge on a particular PMT exceeds a calibrated threshold (above a noise level specified per PMT), several processes occur:

- a small trigger pulse is sent to the Master analogue board (MTC/A), which sums the analogue triggers from all the PMTs in that crate
- a 12-bit time-to-amplitude convertor (TAC) determines the hit time of a PMT relative to the physics event
- the PMT charge is integrated with a ‘high’ gain factor across the PMT over a ‘short’ time period (~ 40 ns), known as QHS.
- the PMT charge is integrated with a ‘high’ gain factor across the PMT over a ‘long’ time period (~ 120 ns), known as QHL
- the PMT charge is integrated with a ‘low’ gain factor across the PMT configured with either a ‘short’ or ‘long’ integration window, known as QLX

Any PMT measurements are temporarily cached into cells on the front end cards (FECs). If more than a pre-specified number of PMTs cross their respective discriminator thresholds within a 100 ns window (called the NHIT100 Trigger), the master trigger card (MTC/D) issues a global trigger (GT), which has several effects upon the SNO+ detector:

- For all functioning PMTs, the cached QHS, QHL and QLX information is readout from the FECs and bundled into a ‘SNO+ event’.
- Other types of trigger are blocked out for a 440 ns time window (known as the ‘GTValid’ window).

The QHS, QHL, QLX and TAC from each PMT are bunched into physical crates by the XL3s - one of the major upgrades on SNO+, which enables the detector to

readout cached information at a much quicker rate than SNO. The SNO+ event builder is responsible for collating trigger information and the XL3 data bundles into specifically formatted files called ZDAB files. The appropriate run and sub-run boundaries are injected into ZDAB files from the SNO+ DAQ software called ORCA via the SNO+ event builder.

There are several different types of electrical signals, which can cause the issuance of a GT, if the measurement of any of these signals exceeds a pre-defined value, and leads to a readout of the SNO+ detector[45]:

- NHIT100 - measurement of the analogue trigger sum for the entire SNO+ detector over a 100 ns window. This is the nominal trigger expected for taking physics data in SNO+.
- NHIT20 - similar to the NHIT100, but with a width of 20 ns. The arrival of this trigger can be delayed on a per PMT basis, in order to move the in-window coincidence to different locations in the detector. This is used to study backgrounds in the centre of the detector.
- ESUMHI - a copy of the raw charge of all PMT pulses with a high voltage gain applied across them. This can be useful for determining broken crate trigger cards that are producing very large charges and determining the location of high voltage breakdown events (on-the-fly) during the operation of the SNO+ detector.
- ESUMLO - same as the ESUMHI trigger, but with a lower gain applied across the PMTs.
- EXTA - an external asynchronous trigger that is received from another source into the MTC/D and causes the issuance of a global trigger. This is

used by several different calibration systems to force a readout of the SNO+ detector.

- OWLN - similar to the NHIT100 signal but only for the outward looking PMTs.
- OWLEHI - similar to the ESUMHI signal but for the outward looking PMTs.
- OWLELO - similar to the ESUMLO signal but for the outward looking PMTs.

Each SNO+ event associated with a GT also contains the number of PMTs for which there was a ‘channel’ trigger, also known as the ‘Nhits’ of an event. Figure 3.1 gives an overview of the electronics within SNO+ where each PMT is connected to an electronics motherboard with 31 other PMTs. For each SNO+ crate, there are 16 motherboards connected to a single crate trigger card (CTC) and 512 PMTs in total. There also are 19 crates and 7 MTCAs within the SNO+ experiment.

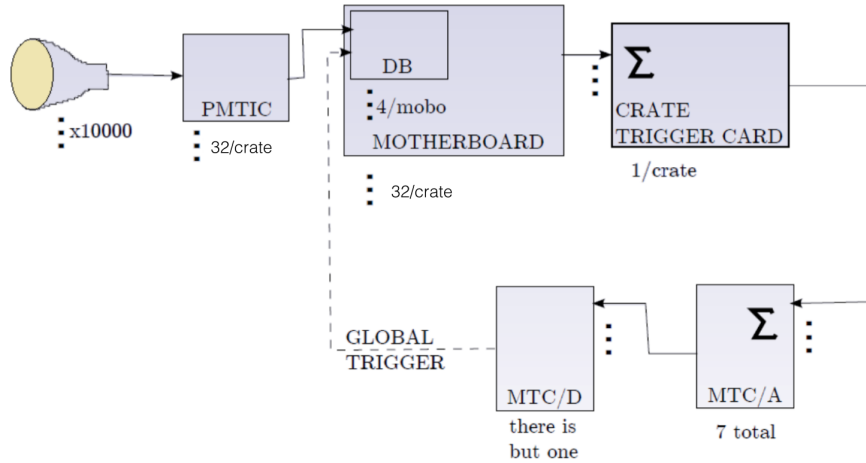


Figure 3.1: Schematic of the SNO+ detector electronics from PMT to MTC/D. This figure is taken from [46].

Definition: Global Trigger (GT)

The Global trigger (GT) is the name given to the electrical signal sent to all the SNO+ electronics, which instructs the detector to read out charge and timing information.

A global trigger causes the readout of the SNO+ PMTs and this information is collected into an SNO+ event. It is also the unique identifier for a SNO+ event.

Definition: Global Trigger ID (GTID)

Each global trigger is given a unique ID per run, which is called the GTID.

SNO+ events are divided into runs and sub-runs with run boundaries injected on-the-fly by the DAQ. Runs are helpful as they provide a logical boundary between different activities, such as a normal physics run or a calibration run, as different types of SNO+ run require different detector configurations.

Definition: SNO+ Event

A SNO+ event represents the readout of the SNO+ detector within a ~ 400 ns window.

The key pieces of hardware in SNO+ are defined as:

- **SNO+ Crate:** A crate is a collection of 31 FECs and 1 XL3. There are 19 crates in SNO+ (in total).
- **Daughter Board (DB):** The DB is responsible for setting the discrimination threshold for firing each of its 8 PMTs. Each SNO+ PMT is associated with 16 ADC (12-bit) cells on the DB, which temporarily store the data until the arrival of a detector trigger. Each cell stores charge and hit time information. A specific run type called Electronic calibration (ECA), is performed to find the zero charge value on a PMT and calibrate the conversion

of the hit time from ADC counts to nanoseconds for each PMT. The SNO+ DAQ loads the current calibration constants for each PMTs and is also responsible for managing ECA runs. Each DB also controls one HV power switch for all its 8 PMTs, but can disable the digitisation of data for each PMT separately.

- **Front End Card (FEC):** The FEC digitises and buffers the data for each of its 4 DBs. The FEC is also responsible for the analogue trigger sum from each DB.
- **XL3:** The XL3 is responsible for the read-out and buffering of FEC data. It also controls and monitors its electronics crate, which includes monitoring the temperature of the electronics crate, monitoring the current powering the PMTs and controlling the HV power supply to the PMTs.
- **Master Trigger Card (MTC/D):** The MTC/D is responsible for the issuance of global triggers based on a trigger mask. It also issues triggers, their GTID and time of an event.
- **Crate Trigger Card (CTC):** The CTC is responsible for the analogue sum of trigger pulses from each FEC to produce a crate-wide analogue trigger sum.
- **MTC/A+:** The MTC/A+ is responsible for summing the different trigger signals such as the NHIT100, NHIT20 etc. from all the crates. If any trigger sum passes its current threshold, a trigger signal is sent to the MTC/D.
- **CAEN:** The CAEN digitises the trigger waveforms, produced by the MTC/A+, and has several different channels that can simultaneously digitise the trigger waveforms.
- **TUBii:** TUBii is a trigger utility board, which provides general tools for

the issuance of triggers in SNO+. It will also provide the 100MHz reference clock for the SNO+ detector.

- **SNO+ Event Builder (EB):** The SNO+ Event Builder (EB) is a computer that collects PMT data from the XL3s, trigger information from the MTC/D and digitised waveforms from the CAEN. This data is synchronously combined into a run file and converted into a ROOT file for analysis.

The SNO+ DAQ builds upon a general purpose Data Acquisition software ‘ORCA’ built by John Wilkerson, Frank McGirt and Mark Howe and used by several experiments (Majorana, Halo and Katrin)¹.

Definition: ORCA

ORCA is the SNO+ DAQ software that controls the detector hardware, shipping of data to the EB and the issuance of runs/sub-runs.

ORCA loads almost all of the possible settings to different pieces of hardware and has low level control on all hardware given in figure 3.2, which depicts the flow of information from the FECs to ORCA. The EB is responsible for collecting the shipped data, organising this information into physics events (asynchronously) and creating run files. Run files are ultimately stored on the GRID. The GRID is a network of computers, which are used to store and process data across many different particle physics experiments.

¹full accreditation for this software can found at <http://orca.physics.unc.edu/>

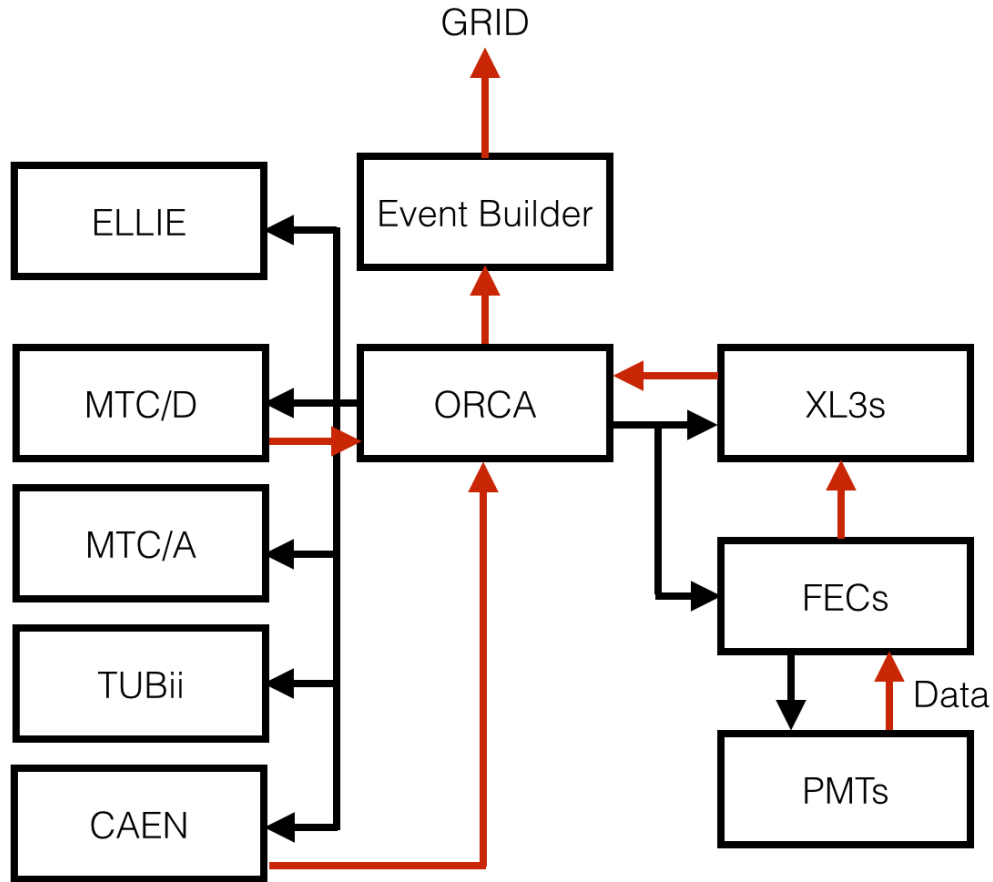


Figure 3.2: Simplified view of the SNO+ DAQ control & data flow. **Black arrows** represent the control flow and **red arrows** represent the data flow.

3.2 Implementation of run & configuration files

The configuration and runs files are crucial for quality physics analysis, as they describe the conditions of a SNO+ run and how to replicate those conditions in simulation. The configuration file is a document, which is ~ 2 MB and completely describes all of the settings of SNO+ detector, the majority of which are set by ORCA and is **only** created with the issuance of a new run. The configuration file also includes a pointer to its associated run file.

Definition: SNO+ configuration file

A SNO+ configuration file is a JSON formatted document that includes: a pointer to the associated run file, all the configurable settings of the SNO+ detector and a timestamp.

A significant amount of software development has been completed, to include nearly every setting from every piece of hardware in the configuration file (including all objects listed in section 3.1). SNO+ maintenance runs are runs that occur when the detector configuration is changed, an example would be changing the trigger mask on the MTC/D or adjusting the gain across a specific PMT. These runs are not designed for physics analysis, but are designed to change the detector state. In any SNO+ run, which isn't a maintenance run, the settings of the detector should not be changed other than in an emergency situation.

Definition: SNO+ run file

A SNO+ run file is a JSON formatted document that includes: the run number, the type of run, a pointer to the associated configuration file, a timestamp and pointers to any run specific description files.

SNO+ run files contain meta-information of the type of run that was performed (e.g. maintenance run or physics run), a pointer to the configuration file, a unique run number and a timestamp. These run files are crucial for analysis of data, because it provides a boundary between data that is optimal for the core physics analysis (such as the $0\nu\beta\beta$ analysis) and calibration analysis. Both the configuration file and run files are produced at the beginning of the run. These are stored locally as JSON documents in a no-SQL database and also pushed to GRID. Run types are a label used for data quality and run selection. Run type is a 32-bit mask, where each bit represents a specific run condition, for example if the "physics" and "scintillator" bits are set then is a physics run with a scintillator filled detector.

Run types are set by the operator in the SNO+ operator, converted into a 32-bit mask and stored as part of the run document.

3.3 SNO+ DAQ software

The SNO+ DAQ has been developed using Mac OS X and takes advantage of the MVC (Model-View-Controller) Software design philosophy [47] with Objective-C, Xcode and the Cocoa Foundation Libraries [48]. The MVC software approach provides the tools to make a robust and intuitive GUI (Graphical User Interface) to the control the SNO+ Detector. This is critical because a well-built GUI that is easy to use for SNO+ operators, facilitates taking better quality data. Objective-C and the Cocoa Foundation Libraries were chosen because they have been optimised to manage memory and threading.

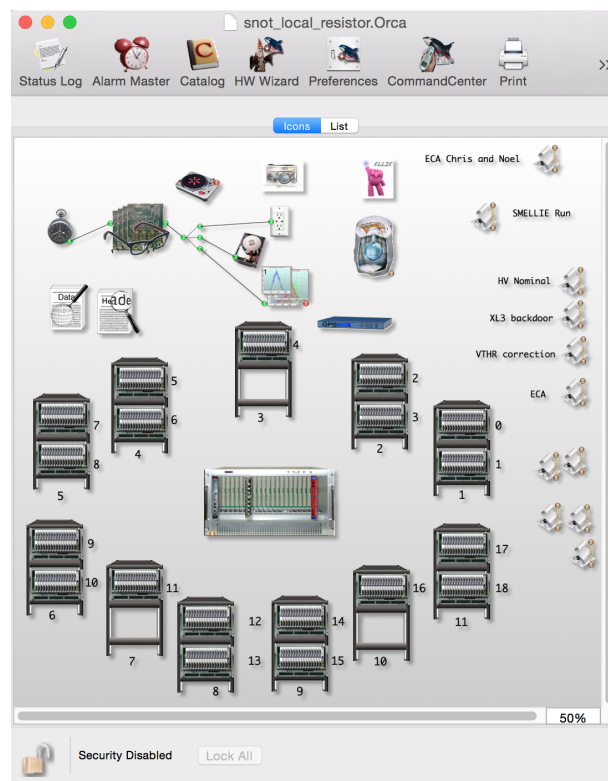


Figure 3.3: Screenshot of the operator interface for SNO+ DAQ. This is a replica of the physical layout of electronics on the SNO+ Deck and provides low and high level control for different SNO+ detector components.

3.4 Upgrades to control/monitoring

The SNO+ experiment is housed deep within a working mine and access can be limited by the mine company due to external factors. Thus, the SNO+ DAQ must be able to operate for long periods of time, without detector expert access, and respond appropriately if connection to the mine is lost. From the experience of running the SNO experiment, it is better to avoid power cycling the PMTs, because the ramping up/down of PMTs degrades both PMTs and their associated electronics [49]. Accounting for these factors, one of the core aims of the SNO+ DAQ system is to be able to remotely monitor and control the detector, whilst minimising the risk of damage.

The operation of SNO+ makes use of XSNOED, a piece of software that visualises the data from the EB, giving the topology of individual SNO+ events. XSNOED relies upon data from MTC/D and the XL3s being shipped from ORCA to the EB. Sudden increases in the GT rate from instrumental effects, such as a high voltage discharge from a submerged PMT, referred to as ‘wet-end breakdowns’ (WEBs), affect the quality of physics data and could damage the detector [50]. Such sudden increases to data rates greater than ~ 10 kHz are unexpected, but not uncommon [50], and the EB cannot reliably dispatch data at this rate. In this instance, operators can no longer observe events in XSNOED, which relies upon the data from the EB. Ideally, the procedure in this situation, is to raise the trigger thresholds to reduce the data rate such that operators can determine the source of the high data rate. It is possible to poll the MTC/D directly in ORCA and monitoring tools are given below, which report the GT rate directly to the operator in ORCA.

3.4.1 GT monitoring

The MTC/D has a circular buffer that can hold $\sim 200,000$ SNO+ events before the buffer is full and events are overwritten. Thus, a low level monitor of the GT rate has been added that directly ‘polls’ the size of current memory in the buffer of the MTC/D. The number of events is dependent upon the average number of PMT hits per event; bigger events require more memory in the MTC/D. In figure 3.4, the ‘events in memory’ is calculated by taking the difference between the read and write pointers and updated after every $1 \mu\text{s}$ (every 10 counts of the 10MHz clock). If the write pointer overtakes the read pointer, then events will start to be deleted. The ‘GTID rate’ is also calculated by dividing the number of events in memory by the time elapsed. The GTID rate gives a measurement directly from the hardware, rather than through monitoring systems that rely upon the EB.

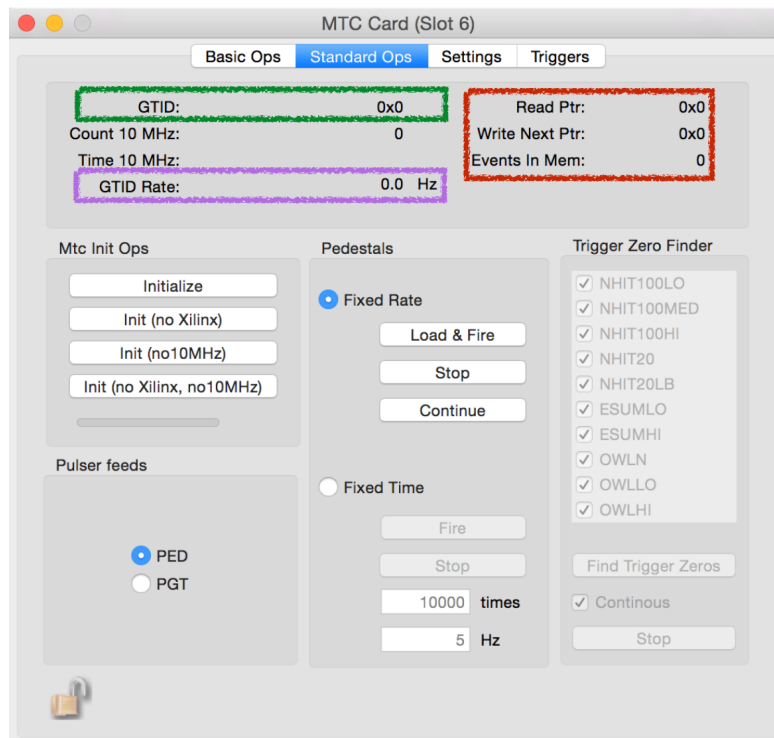


Figure 3.4: MTC/D Interface for ORCA with GTID monitoring. Green: Current GTID number in hexadecimal, Red: the current read and write pointer on the MTC/D memory, Purple: Calculated GTID rate from the rate of global triggers being issued by the MTC/D.

3.4.2 Automatic shutdown of SNO+

Power to the surrounding, active mine can be lost due to external factors (weather, accidental damage) and the SNO+ detector is provided with an uninterruptible power supply (UPS) that can operate for several hours. If certain conditions are met, outlined in figure 3.5, ORCA will initiate an automatic shutdown of the SNO+ detector without any external control.

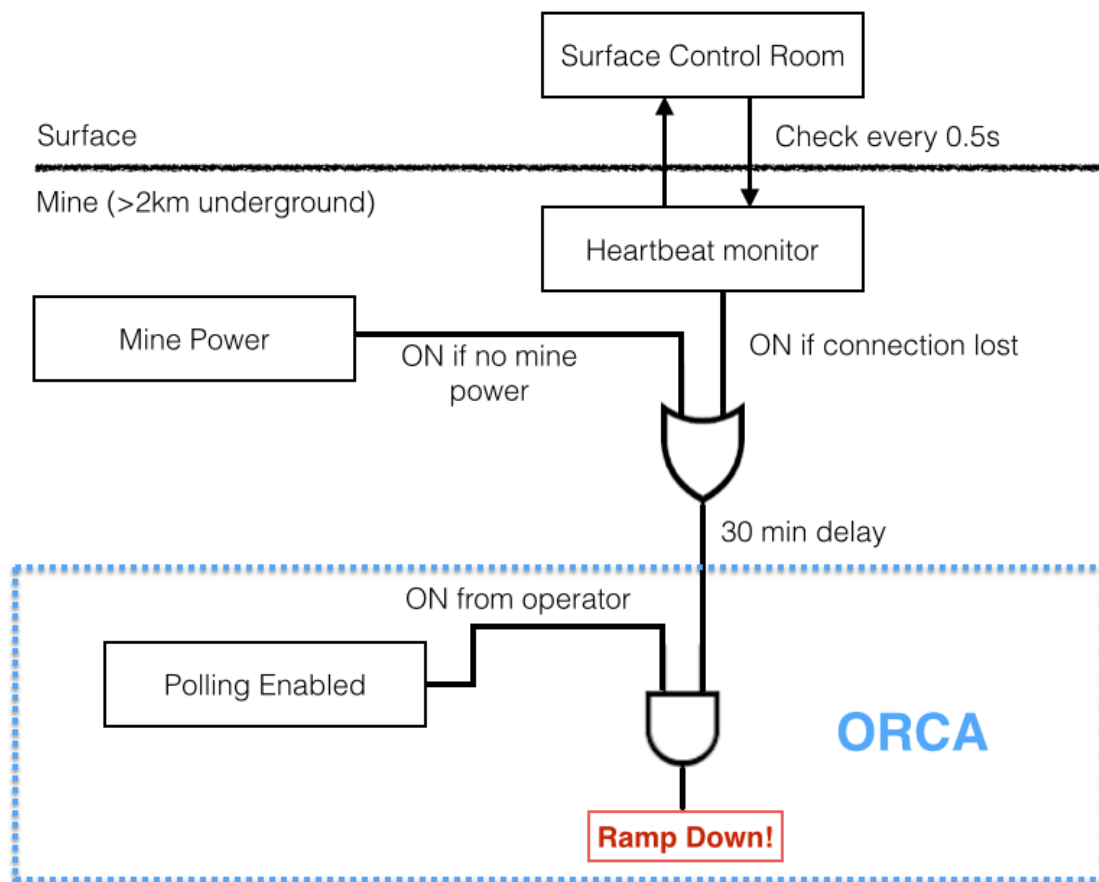


Figure 3.5: Schematic of the logic for an automatic emergency shutdown. A heartbeat monitor checks every 0.5s to see if there is a connection from surface. The SNO+ operator needs to enable polling of the automatic shutdown in order to enable the entire process.

The connection to the surface control room is checked, every 0.5 seconds, by a heartbeat signal that is sent to the SNO+ Detector. This prevents the detector from running without operator control for an extended period of time. If either the mine power or the surface control room heartbeat are lost, ORCA will wait 30

minutes before commencing an automatic ramp-down of the detector. The ramp-down is performed in voltage steps of 50V per second, for all PMTs (from 2100V to 0V nominal voltage). This system was in operation during the December 2014 commissioning runs and tested with four SNO+ crates simultaneously at 500V. The crates correctly responded to the ramp down signal and ramped down in steps of 50V. During the ramp-down procedure, XL3 data packets are being sent to the EB and the FECs are being polled. Thus, several different processes were being managed, at the same time by ORCA, and careful consideration needs to be given to how these are multi-threaded.

3.4.3 Multi-threading in SNO+

In order to reliably respond to a ramp down signal, without delay and without waiting for other ORCA controlled hardware, careful consideration needs to be given to the multi-threading logic. Objective-C and Mac OSX use the Grand Central Dispatch (GCD) libraries [48] for managing multiple threads, and the highest priority thread is called the ‘main’ thread. This thread has the ability to stop other functionality being managed by the Orca (e.g. polling the XL3 data). If the emergency shutdown is initiated, the ramping down process takes priority over other queued processes (including any data taking threads) as illustrated in figure 3.6.

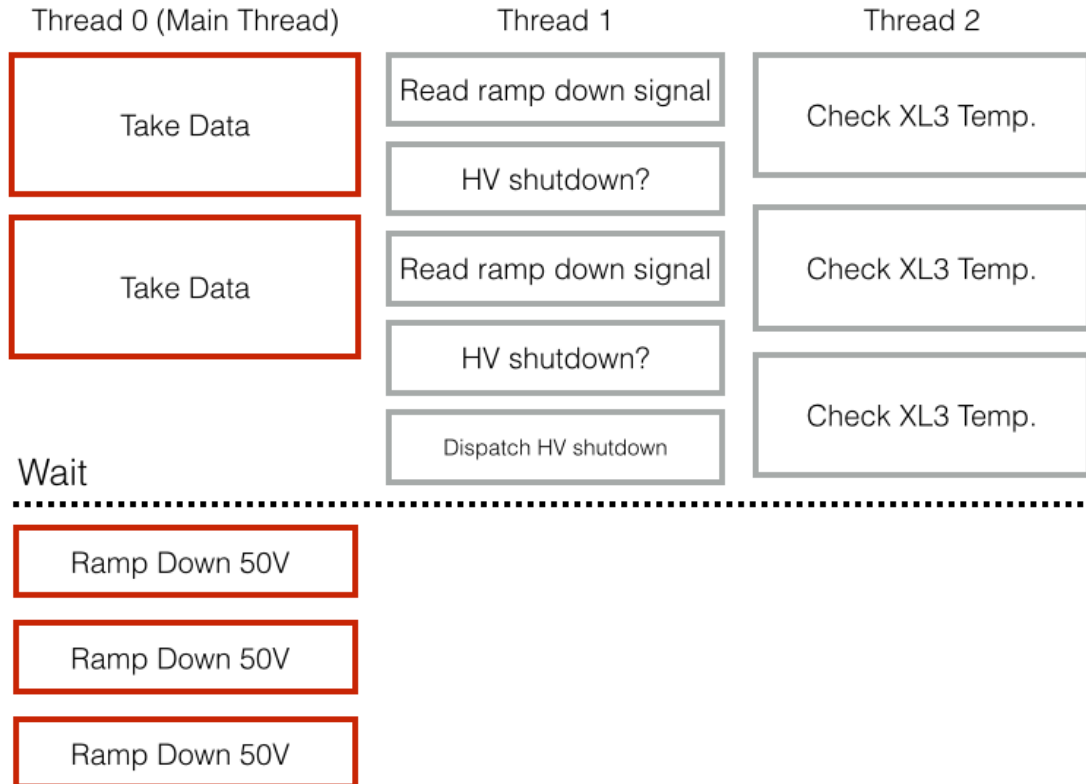


Figure 3.6: An illustration of the multithreading logic for the remote emergency shutdown. The main thread (Thread 0) is the only blocking thread in ORCA, but other threads can asynchronously send commands to the main thread to initiate a shutdown of the detector.

3.5 Implementing the channel hardware status

The channel hardware status provides the status of a SNO+ PMT and the electronics associated with that PMT. Each PMT channel reports information about the charge measured and the time at which its discriminator threshold was crossed.

Definition: SNO+ channel

A SNO+ channel is defined by each PMT in SNO+ with its associated readout electronics. This is a hardware definition that includes the PMT and the FEC, DB and CTC which are connected to that PMT.

The channel hardware status aims to provide sufficient information, to decide whether or not to include a particular PMT in a physics analysis and to disable

any broken channels, which may cause instrumental noise.

3.5.1 What is a ‘Channel’?

The SNO+ detector consists of 18 electronics crates, with each crate containing 31 FECs (Front End Cards) and one crate trigger card (CTC). Each FEC contains 32 front end amplifiers and 2 shaper circuits, one for each PMT. Each PMT is also connected to its high voltage supply via a 75 Ohm resistor. A ‘channel’ is defined for each PMT and any associated electronics (FEC and DB) that is used to place the information from that PMT into a SNO+ event.

3.5.2 PMT status DB

Currently, SNO+ is still undergoing a refurbishment (as of July 2016). One aspect of this refurbishment is to replace PMTs that are broken or malfunctioning, from more than 10 years of operation of the SNO experiment. Throughout the refurbishment of the SNO Detector for SNO+, a record has been kept of PMTs that have been replaced by new PMTs or PMTs that have been refurbished. The history of the PMT is helpful as a given type of PMT (e.g. refurbished PMTs) may systematically have a particular problem (e.g. overestimating charge compared to a different type of PMT). This record also keeps track of the type and location of cable connections from the PMT to its power supply. All PMT status records are stored on a no-SQL couchDB database in the PMT status DB.

3.5.3 PMT resistor status DB

Each PMT has a corresponding 75 Ohm load resistor, which regulates the voltage across the PMT and is accessible on the SNO+ deck. These resistors are accessible to SNO+ detector operators and will be accessible during detector running. Each PMT shares its power supply with seven other PMTs, if a particular PMT

is very noisy or broken, the resistor can be removed from that PMT without removing an entire set of ‘well-behaved’ PMTs. It is also important to keep track of which PMTs are enabled (as part of the channel hardware status) for later physics analysis. There may be a systematic problem with the detector, such as a significant amount of electrical breakdown between a submerged PMT and its connecting cable (known as Wet End Breakdown) [50]. The PMT resistor status DB stores the current information about the PMT resistor status and an expert operator will be able to update the database through an interface in ORCA. This information is accessible to ORCA, because it can be automatically used to enable ‘operational’ channels, reduces the overall detector noise and improves the quality of physics data. An illustration of the GUI for querying and updating the PMT resistor database is given in figure 3.7.

The screenshot shows a window titled "Resistor DB" with a standard macOS-style title bar (red, yellow, green buttons). The window is divided into several sections:

- Query Resistor DB:** Contains a "Query DB" button and three dropdown menus for "Crate:", "Card:", and "Channel:".
- Current Status:** A section with a light gray background containing:
 - Resistor Status: Query DB
 - SNO Low Occ. : Query DB
 - PMT removed: Query DB
 - PMT reinstalled: Query DB
 - Pulled Cable: Query DB
 - Bad Cable: Query DB
 - Reason: None (text input field)
 - Info: None (text input field)
- Update PMT Resistor:** A section with a light gray background containing:
 - Resistor Status: [dropdown]
 - SNO Low Occ. : [dropdown]
 - PMT removed: [dropdown]
 - PMT reinstalled: [dropdown]
 - Pulled Cable: [dropdown]
 - Bad Cable: [dropdown]
 - Reason: [dropdown]
 - Other (If Specified): [text input]
 - Info: [text input]
- PMT Database:** A section at the bottom containing two buttons: "Update Resistor Database" and "Update PMT Database".

Figure 3.7: GUI for the SNO+ PMT resistor DB.

4

Commissioning of the SMELLIE system

*“SMELLIE, it **still** does not stink”*

– Several SNO+ presentations on SMELLIE

4.1 Purpose of the SMELLIE system

SMELLIE is the Scattering Module of the Embedded Laser/LED light Injection Entity (ELLIE). It has been developed to measure the scattering properties of the detector media for all SNO+ phases, but crucially, to monitor changes in the optical scattering during the Te-loaded phase. SMELLIE consists of 5 different lasers, whose light can be injected at 12 different locations on the PSUP. Four lasers have fixed wavelengths and a fifth super-continuum laser has been added to access a wider continuous range of wavelengths. The super-continuum laser is not yet fully implemented and not included in this thesis. Laser light, from any one of these lasers, can be injected into any of the 12 detector fibres via a micro-mechanical fibre switch.

The optical properties of the SNO+ scintillator (unloaded and Te-loaded), such as the light yield, the average scattering and absorption lengths affect the position and energy reconstruction of physics events. In turn, this affects the ability to distinguish between $0\nu\beta\beta$ and $2\nu\beta\beta$ decays, solar neutrinos and other SNO+ events. SMELLIE is designed to measure and monitor the scattering properties across the SNO+ detector.

This chapter focusses on two aspects: firstly, the software that I have written to control the SMELLIE hardware (described in section 4.2), to communicate between ORCA and the SMELLIE system and secondly, the logic of a SMELLIE run, which is given in section 4.3. Additionally, integrated a SMELLIE control interface into ORCA (see section 4.2) and implemented the graphical user interface (GUI) for building and automatically performing SMELLIE runs. SNO+ run 9044 was a dedicated SMELLIE run (taken after the integration of SMELLIE into ORCA was completed) and is used to evaluate the commissioning of the SMELLIE system in section 4.5.

4.2 Overview of the SMELLIE hardware

The different pieces of SMELLIE hardware are described in table 4.1 and the SNO+ hardware, used by SMELLIE, is described in section 3.1. Figure 4.1 depicts the layout of the SMELLIE hardware, with enumerations given in table 4.2.

Component	Description
SNODROP	Control PC for SMELLIE - controls SMELLIE hardware, provides a heartbeat to laser interlock and communicates with ORCA via a TCP/IP connection
NI Unit	National Instruments NI-DAQmx Unit [51] used to generate triggers for the SMELLIE system in master mode.
SEPIA II Laser Driver (SEPIA)	Laser driver unit built by Picoquant [52] for all lasers in SMELLIE. This unit controls the intensity set point of a laser, trigger rate and trigger mode. The intensity set point is chosen between 0% - 100%. SEPIA can trigger on an external or internal trigger (up to 20 MHz). It also has a software operated soft-lock, which disarms the laser.
Laser Switch (LS)	The laser switch is a set of relays, which asserts that only one laser, at a time, is connected to the SEPIA. This has been built to save the cost of buying a larger SEPIA unit, which could control all 5 lasers.
Fibre Switch (FS)	The fibre switch is a micro mechanical fibre switch with 5 input channels and 14 output channels [53]. The input channels are connected to different laser heads and the output channels are connected to detector fibres.
Monitoring PMT Unit (MPU)	Multipurpose electronics unit with an internal PMT. It is used for converting trigger signals and sampling the SMELLIE monitoring PMT voltage. This PMT is a high quantum efficiency PMT [54] used to measure the energy of each laser shot.
SMELLIE monitoring PMT	The SMELLIE monitoring PMT sits within the MPU and is a Hamamatsu H10721-210 photosensor module with a 10 mm-diameter face [55].
Beam Splitters	The beam splitters are fused fibre taper splitters [56], which send a fraction of the laser light into the detector and to the MPU.
Attenuators	The attenuators are used to reduce the energy of each laser shot, before it reaches the detector. They are variable fibre optic in-line attenuators manufactured by Fibredyne [57].
Laser heads	There are 4 laser heads (at wavelengths 375nm, 405nm, 440nm and 500nm) connected to the LS via a 12-pin LEMO B-series [58] connection.

Table 4.1: Description of the hardware components in the SMELLIE system

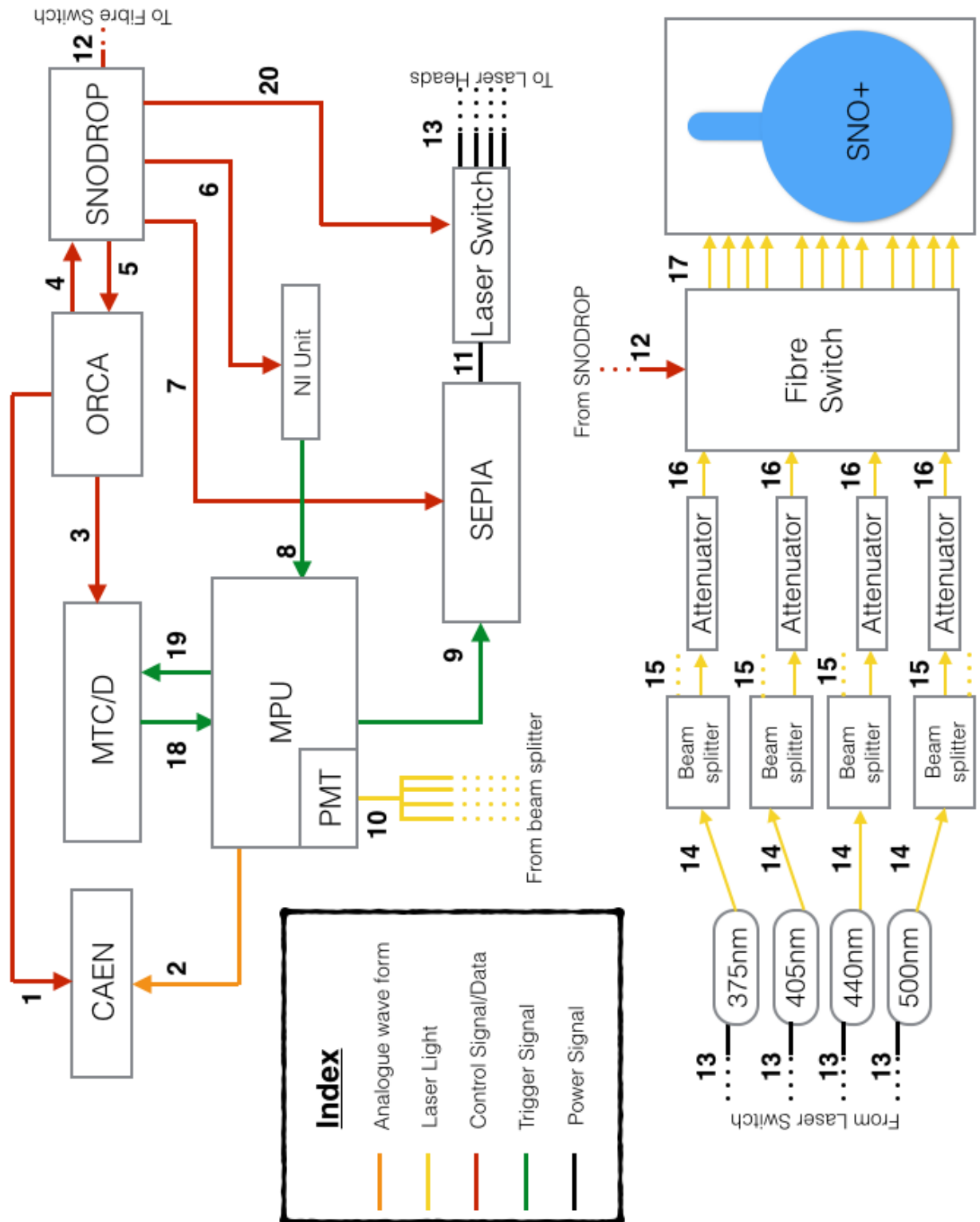


Figure 4.1: Layout of the SMELLIE hardware. The connections are described in table 4.2 and the hardware is described in table 4.1. There is also a laser interlock system, controlled by SNODROP, which is not included here.

No.	Description
1	Control of the CAEN from ORCA via TCP/IP
2	SMELLIE monitoring PMT waveforms
3	Control of the MTC/D from ORCA via TCP/IP
4	TCP/IP connection between ORCA and SNODROP
5	TCP/IP connection between ORCA and SNODROP
6	SNODROP control of the NI Unit via USB
7	SNODROP control of the SEPIA via USB
8	NI trigger (in master mode) into the MPU
9	Trigger from MPU to SEPIA
10	Laser light to the SMELLIE monitoring PMT
11	12-pin LEMO B-series connection from the SEPIA to the LS
12	SNODROP control of the FS
13	Same as 11 but from the LS to the laser heads
14	Laser light from the laser heads into a beam splitter
15	Laser light from the beam splitters to both the attenuator and SMELLIE monitoring PMT
16	Laser light from the attenuator into the fibre switch
17	Laser light from the FS to the SNO+ detector
18	Trigger from MTC/D to MPU (slave mode) via 50Ω co-axial cable
19	Trigger from the MPU to MTC/D (master mode) via 50Ω co-axial cable
20	SNODROP control of the laser switch via USB

Table 4.2: Enumeration of all SMELLIE connections in figure 4.1.

Red lines in figure 4.1 show the control paths for the hardware used in the SMELLIE system. ORCA directly controls both the CAEN and MTC/D, as these are pieces of general SNO+ hardware, whereas SNODROP controls the NI Unit, laser switch, fibre switch and SEPIA laser driver. Any commands for the SMELLIE system are issued from ORCA and sent to SNODROP over a TCP/IP socket.

A trigger must first be given to the SMELLIE system in order to produce laser

light. There are two triggering modes with the SMELLIE system: slave and master mode. In master mode, the NI Unit, under control of the SNODROP computer, produces a TTL (Transistor-transistor Logic signal with a low voltage level of +0V and a high voltage level of +5V) signal that is sent to the MPU. The MPU converts this to a SEPIA specific electrical ‘trigger’ signal, which is 200 ns wide with voltage levels between -0.2V and +1.0V [54], and responsible for triggering the SEPIA to fire one of the lasers. The MPU also converts the original TTL signal into a single-ended ECL (Emitter-Coupled Logic signal with a low voltage of -1.75V and a high voltage of 0.9V) [54], and sends this signal to the external asynchronous input of the MTC/D, which subsequently issues a global trigger (GT).

In slave mode, the MTC/D sends an ECL trigger signal from its PED output, which arrives at the MPU and is converted to the correct trigger signal for the SEPIA and causes the laser to fire. The MTC/D also issues a GT, delayed by ~ 250 ns, such that the laser light is correctly timed for the SNO+ detector to be readout.

When a laser pulse is produced, the light is sent into the detector (via the fibre switch and attenuator) and the SMELLIE monitoring PMT. This PMT sits within the MPU and its waveform is digitised by the CAEN. When a GT is issued, any waveforms on the CAEN are recorded into a SNO+ event. The SMELLIE monitoring PMT is used as an independent measure of the amount of laser light produced and timing for each shot.

4.2.1 SNO+ PMT safety considerations

SNO+ uses around 10,000 PMTs, which are each designed to measure single photoelectrons incident on the photocathode. Each SMELLIE laser is ‘dialled’ down from $\sim 10^8$ photons per shot to $\sim 10^4 - 10^5$ photons per shot. This is achieved through: attenuation in the transmission fibres (over $\sim 40\text{m}$ of fibre optics), beam splitters and variable attenuators attached to each laser head. In order to protect the SNO+ detector from stray laser light or a malfunction in the SMELLIE system. A set of SMELLIE safe states are asserted at the start and end of a SMELLIE run. The SMELLIE safe states involve setting:

- the laser intensity set point to 0 %
- the fibre switch to an empty output channel (with no detector fibre connected)
- the laser switch to channel 0, which has no laser heads connected
- the SEPIA triggering mode to external triggering
- the SEPIA soft-lock to disarm the lasers (i.e. they cannot generate laser light)

As an additional precaution, there are several interlock systems with:

- a keep alive pulse, issued every 0.5s by SNODROP, which is required to arm the laser.
- a physical interlock button is placed within the SNO+ control room, such that an operator can instantly disarm the laser in hardware.

4.3 Logic of a SMELLIE run

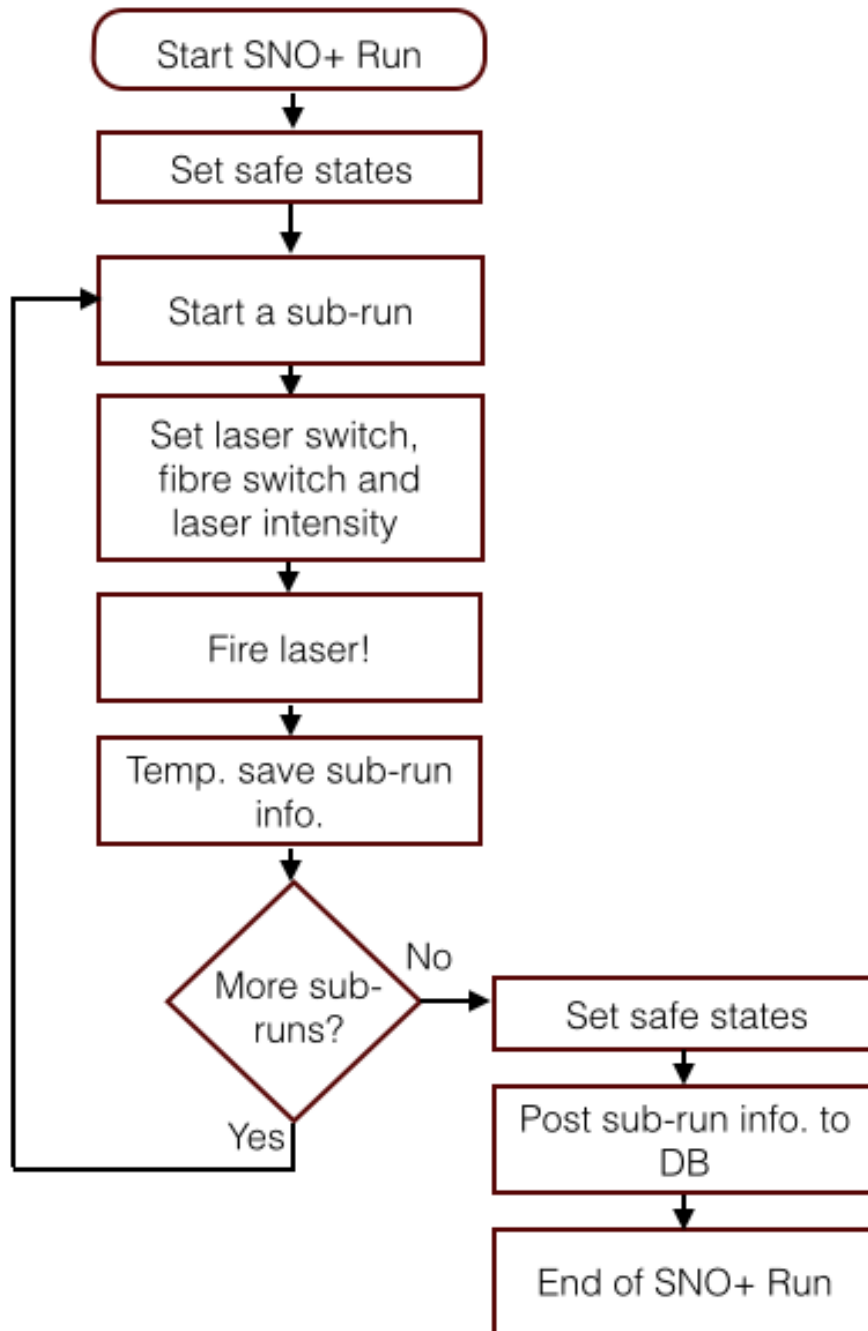


Figure 4.2: Flow diagram of a SMELLIE run. These commands are controlled by ORCA and sent to SNODROP. Handshaking over the TCP/IP socket takes place at each stage, if any command fails or is rejected, the SMELLIE run is cancelled and ORCA automatically goes into a maintenance run.

A SMELLIE run is a type of SNO+ run. Starting a SNO+ run (of any kind), causes the issuance of SNO+ configuration and run files, which are posted to the SNO+ database. However for a SMELLIE run, the SNO+ run file also contains

a pointer to two additional files: a SMELLIE run description and SMELLIE configuration file. These files describe the nature of the SMELLIE run (e.g. which fibre(s) and laser(s) to use and how the SMELLIE system was configured (e.g. the mapping of fibre switch outputs to detector fibres). I implemented these files and the SMELLIE run logic as part of the SMELLIE integration into ORCA.

Definition: SMELLIE run description file

A SMELLIE run description file includes the fibre(s), laser(s) and intensity set point(s) combinations, which are expected to be used during a SMELLIE run. This also includes the number of events and the trigger rate. This file describes how a run is going to be completed (e.g. which laser channel to pick and which fibre channel to pick).

Definition: SMELLIE configuration file

A SMELLIE configuration file provides complete information about the connections in the SMELLIE hardware, such as the mapping of the fibre switch to detector fibres and the mapping of laser heads to laser switch channel. This file describes how SMELLIE is physically connected.

The logical flow of a SMELLIE run is given in figure 4.2. Once a SMELLIE run is started and the safe states are set, a SNO+ sub-run is started. When a new SNO+ sub-run is commenced, the EB (Event Builder) sends a marker into the data stream, which indicates the start of a sub-run for offline analysis purposes. For SMELLIE, a sub-run is designed to encapsulate data taken using one combination of fibre, laser and intensity set point. ORCA parses a SMELLIE run description file chosen by the operator. This determines the sub-run combination, which should be included in the run. ORCA also uses this file to determine the number and frequency of triggers for a sub-run and the estimated length of the run.

As the sub-runs are completed, they are recorded into a temporary SMELLIE run file. When all sub-runs have been completed, the SMELLIE system is set back to its safe states and the SMELLIE run file is permanently stored to the SMELLIE couchDB database.

Definition: SMELLIE run file

A SMELLIE run file includes a pointer to a SNO+ run, SNO+ configuration, SMELLIE run description and configuration files. The SMELLIE run file includes the fibre/laser/intensity combination for all completed sub-runs in a SMELLIE run. It also includes the trigger frequency and the number of triggers per sub-run.

4.4 Integration of SMELLIE into ORCA

SMELLIE run description files are created through the SMELLIE run builder GUI in ORCA. Figure 4.3 gives the GUI where SNO+ operators can build a SMELLIE run by choosing: the trigger rate (< 1 kHz), the combination of laser(s), fibre(s) and the range of intensities. The SMELLIE run builder also completes on-the-fly sanity checks such as: a run has intensity set points less than 100%, a trigger frequency less than 1 kHz and valid entries for each option. If these checks are passed, the new SMELLIE run description file is saved to the SMELLIE couchDB database and can be easily loaded by SNO+ operators using the SNO+ run GUI (given in figure 4.4). This makes it very easy for SNO+ operators to take high quality SMELLIE runs with a limited knowledge of the SMELLIE system.

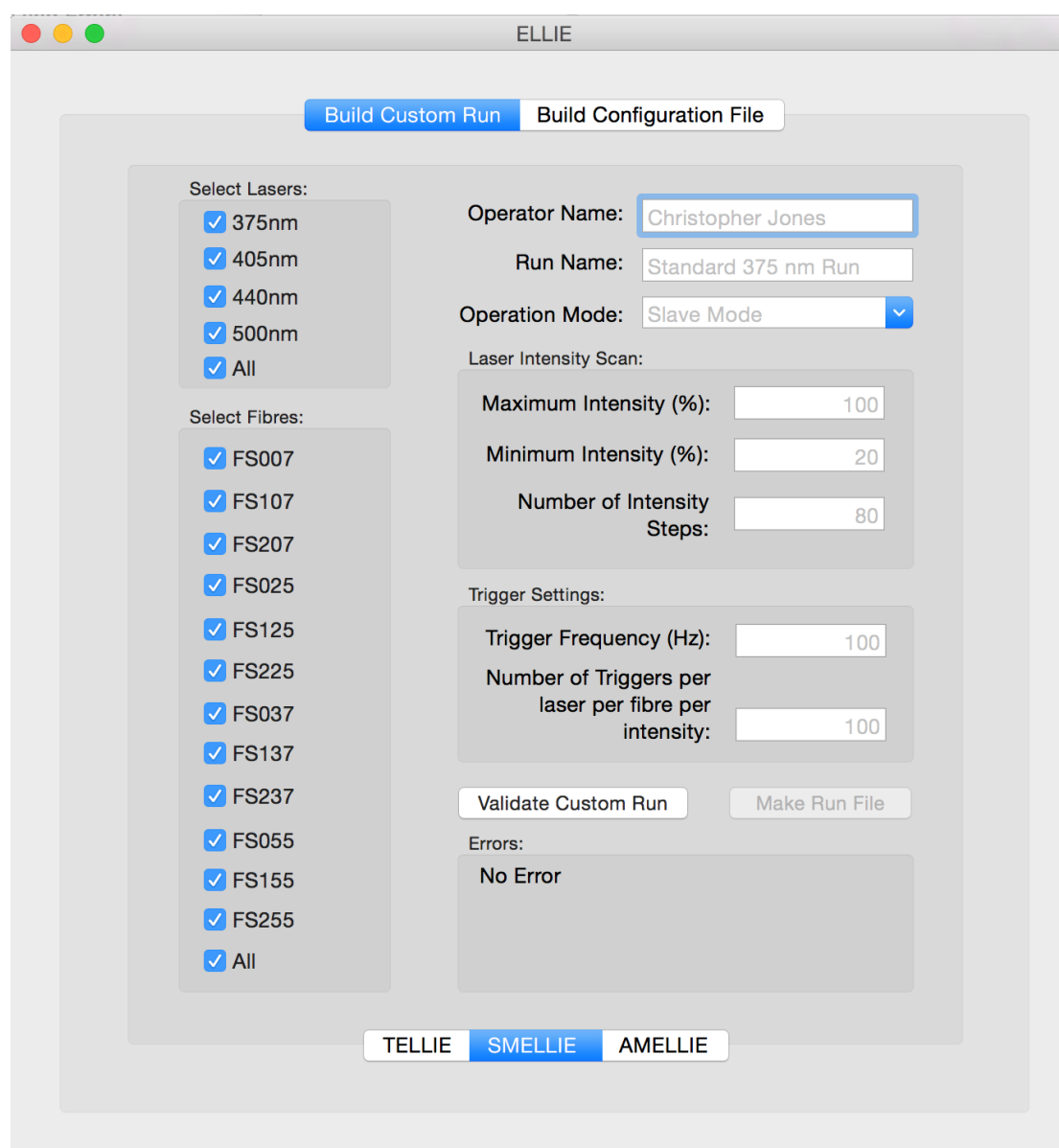


Figure 4.3: The SMELLIE run builder (in ORCA) helps an operator build custom runs for later use. A custom run is stored as a SMELLIE run description file.

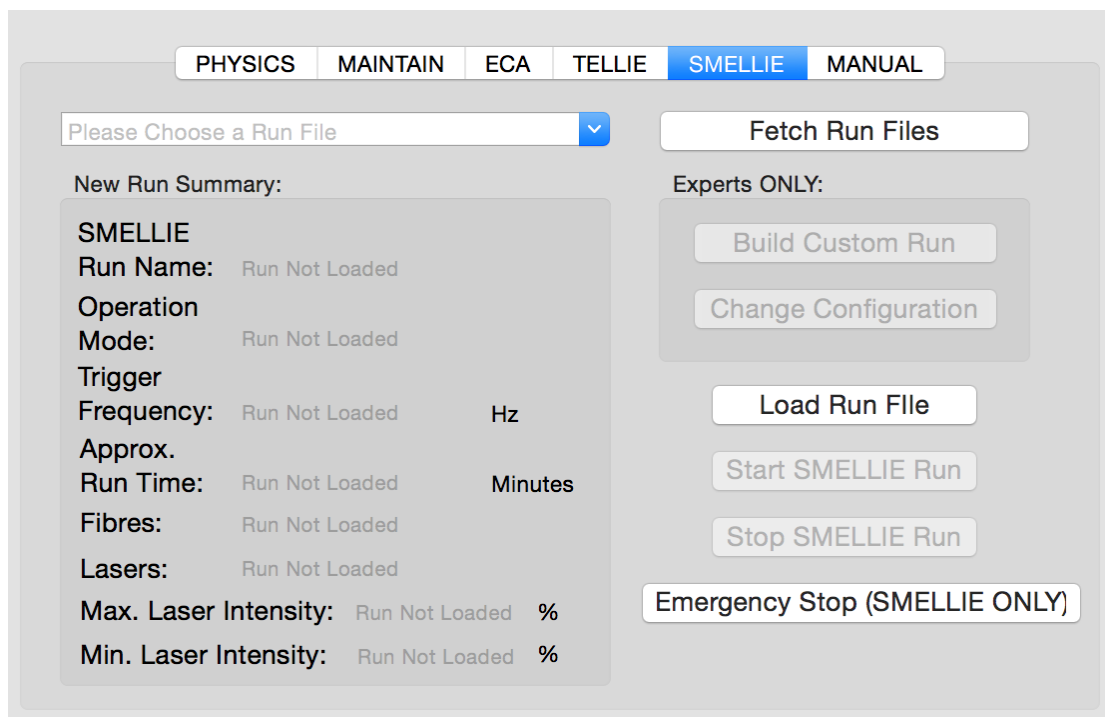


Figure 4.4: The SMELLIE run GUI is embedded within the SNO+ run GUI. The operator can select specific SMELLIE run description files from a list of such files found in the SMELLIE couchDB database. An estimate of time of a SMELLIE run is given as a cross check for SNO+ operators.

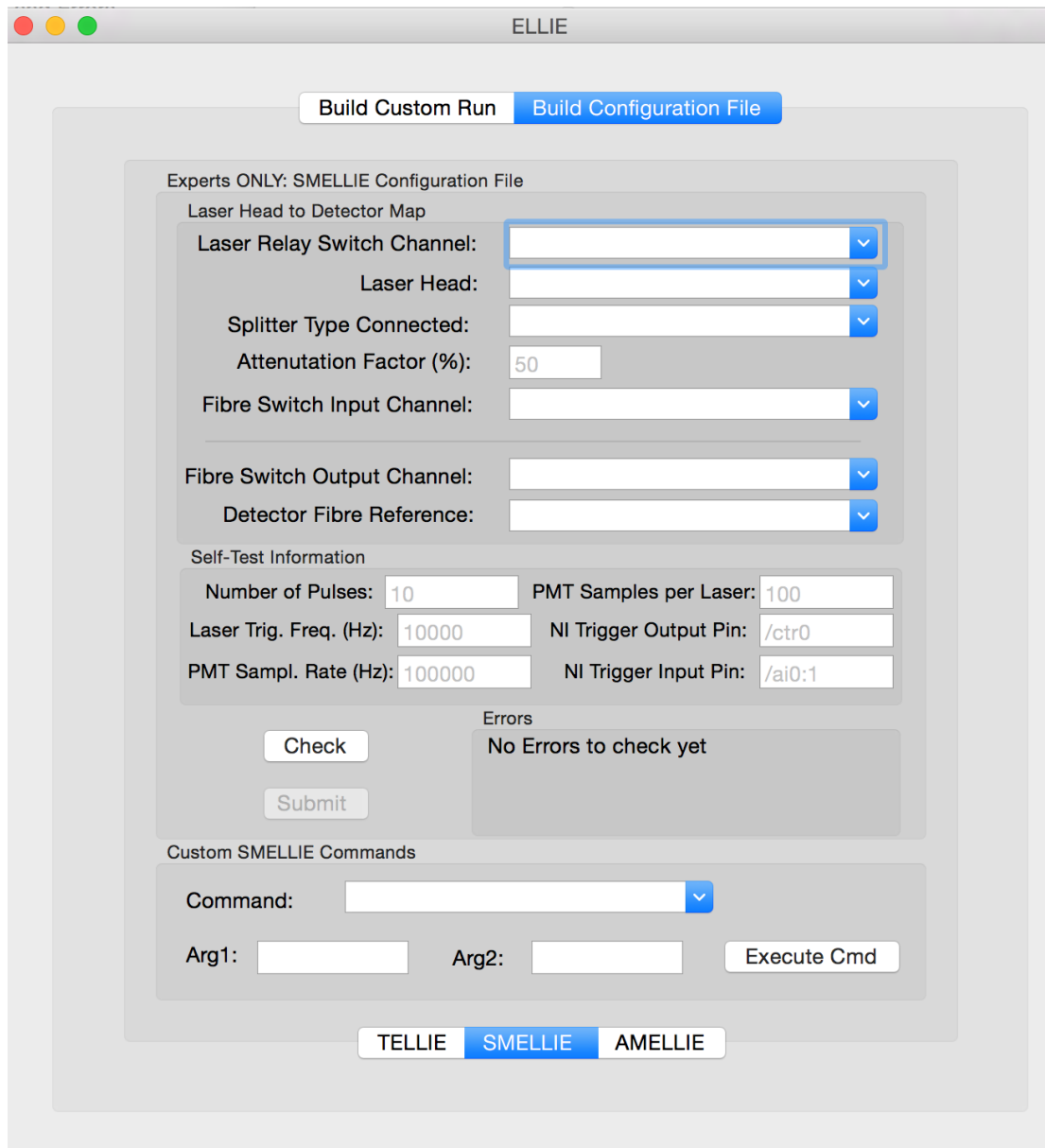


Figure 4.5: The SMELLIE configuration builder is used to build SMELLIE configuration files. It stores the fibre mapping/laser mapping for the SMELLIE system and is parsed by ORCA during a SMELLIE run. In the GUI, the ‘self-test’ section includes the configuration of NI DAQ and the ‘custom SMELLIE commands’ are used for testing individual commands, e.g. set the laser switch, during the commissioning of SMELLIE and will be removed during the operation of SNO+.

I have also implemented a simple way for the SMELLIE configuration to be updated within ORCA. Figure 4.5 depicts the GUI, which can be used by SMELLIE experts to update the hardware configuration of the SMELLIE system. This requires a SMELLIE expert, because they need to physically change the hardware

configuration and update this information. If the configuration is updated incorrectly, ORCA could have the wrong mapping of laser head to laser switch, or fibre switch to detector fibre and fire the incorrect laser or detector fibre. Thus, whenever the configuration file is updated, detector operators will need to verify the mapping of fibre switch channel to detector fibre.

4.5 Commissioning of SMELLIE

The commissioning of the SMELLIE system was largely completed with several underground shifts in December 2014. At this time, the SNO+ detector was partially filled with water, up to a level of ~ 30 ft from the base of the SNO+ cavity. At this time, only six SMELLIE fibres were installed into the detector. The other fibres will be installed, from boats, during the water filling of SNO+. The SMELLIE system was commissioned with all SMELLIE fibres submerged, but only a fraction of the SNO+ PMTs were submerged.

4.5.1 SNO+ run 9044

SNO+ run 9044 was performed specifically for evaluating the integration of SMELLIE into ORCA. All analysis, presented in the following section, for SNO+ run 9044 has been completed by extracting sub-run/run level information from the SMELLE and SNO+ files posted automatically by ORCA and recorded event data. Thus, any analysis for these runs directly relies upon the DAQ upgrades implemented in chapter 3 and also acts as a verification for these upgrades. For SNO+ run 9044, the interfaces described in this chapter, were used in ORCA to:

- make a SMELLIE run description file with the SMELLIE run builder (before the run).
- make a SMELLIE configuration file with the SMELLIE configuration builder

(before the run).

- execute a SMELLIE run using the corresponding SMELLIE run description and configuration files.

SNO+ run 9044 consisted of 36 sub-runs and cycled through all 6 installed SMELLIE fibres with intensity set points of 95% - 100% in 1% steps, using the 375 nm wavelength laser (see table 4.3). Each sub-run is expected to contain 50,000 laser shots, fired at a frequency of 500 Hz in slave mode.

Sub-run number	SMELLIE Fibre	Intensity (%)
1, 2, 3, 4, 5, 6	FS255	95, 96, 97, 98, 99, 100
7, 8, 9, 10, 11, 12	FS155	95, 96, 97, 98, 99, 100
13, 14, 15, 16, 17, 18	FS055	95, 96, 97, 98, 99, 100
19, 20, 21, 22, 23, 24	FS237	95, 96, 97, 98, 99, 100
25, 26, 27, 28, 29, 30	FS137	95, 96, 97, 98, 99, 100
31, 32, 33, 34, 35, 36	FS037	95, 96, 97, 98, 99, 100

Table 4.3: Sub-run information for SNO+ run 9044

Slave mode uses the pedestal or ‘PED’ trigger, which is a forced readout of the SNO+ detector and originates from the MTC/D. The PED is also assigned bit 12 in the SNO+ trigger word, a 32-bit trigger word assigned to each SNO+ event and describes the associated triggers. If the PED bit is TRUE, within a SMELLIE run such as SNO+ run 9044, the event is recorded for analysis as a SMELLIE event in slave mode. It is important to note that the PED trigger is used for electronics calibration runs and events with the PED bit can only be strictly considered SMELLIE events within a SMELLIE run. It is important to note that some of the SMELLIE fibres were submerged below water in SNO+ run 9044 and this will affect the beam profile.

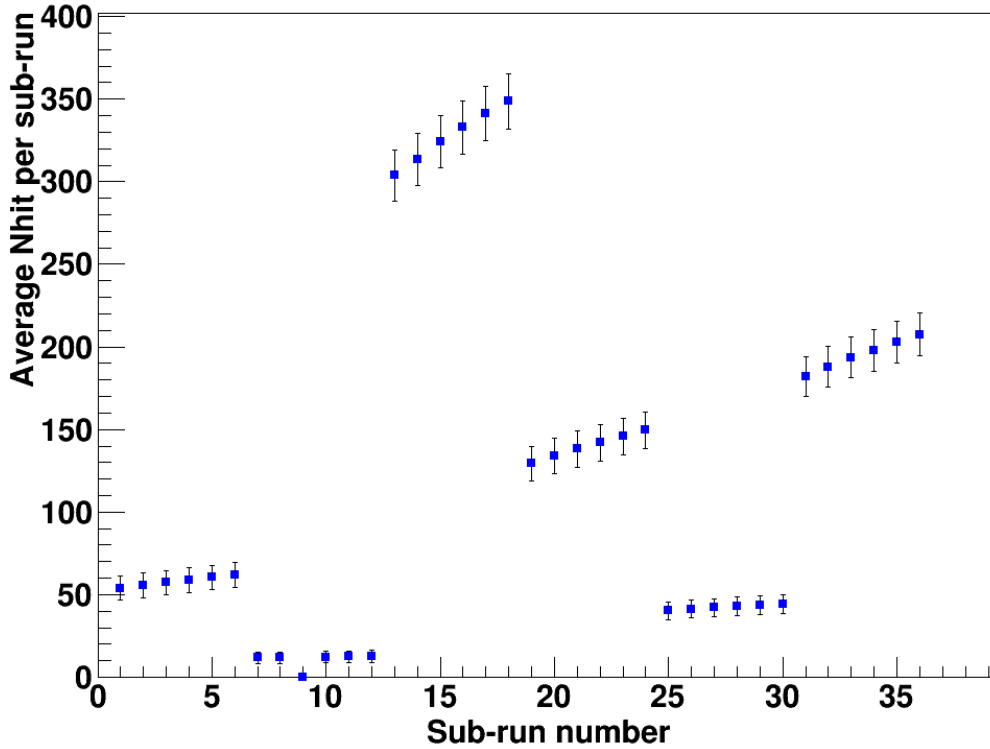


Figure 4.6: Average Nhit per sub-run for SMELLIE events in SNO+ run 9044. All sub-runs use the 375nm laser but cycle through all 6 fibres and 6 intensity set point combinations (see table 4.3 for the exact sub-run information). The error bars are the standard deviation of a Gaussian fit to the Nhits distribution of all events within the sub-run.

Definition: Nhit

Nhit is the number of PMTs, within a SNO+ event, which observe a charge above a calibrated threshold equivalent to a calibrated expected value of $1/4$ of a photo-electron.

Figure 4.6 depicts the average Nhit per sub-run for SMELLIE events in SNO+ run 9044. Each sub-run represents a different fibre/intensity set point combination and all sub-runs use the 375 nm laser (as outlined in table 4.3). An abrupt change in the Nhit corresponds to a change in fibre. No events were recorded for sub-run 9, because no PED triggers were issued from the MTC/D during that sub-run.

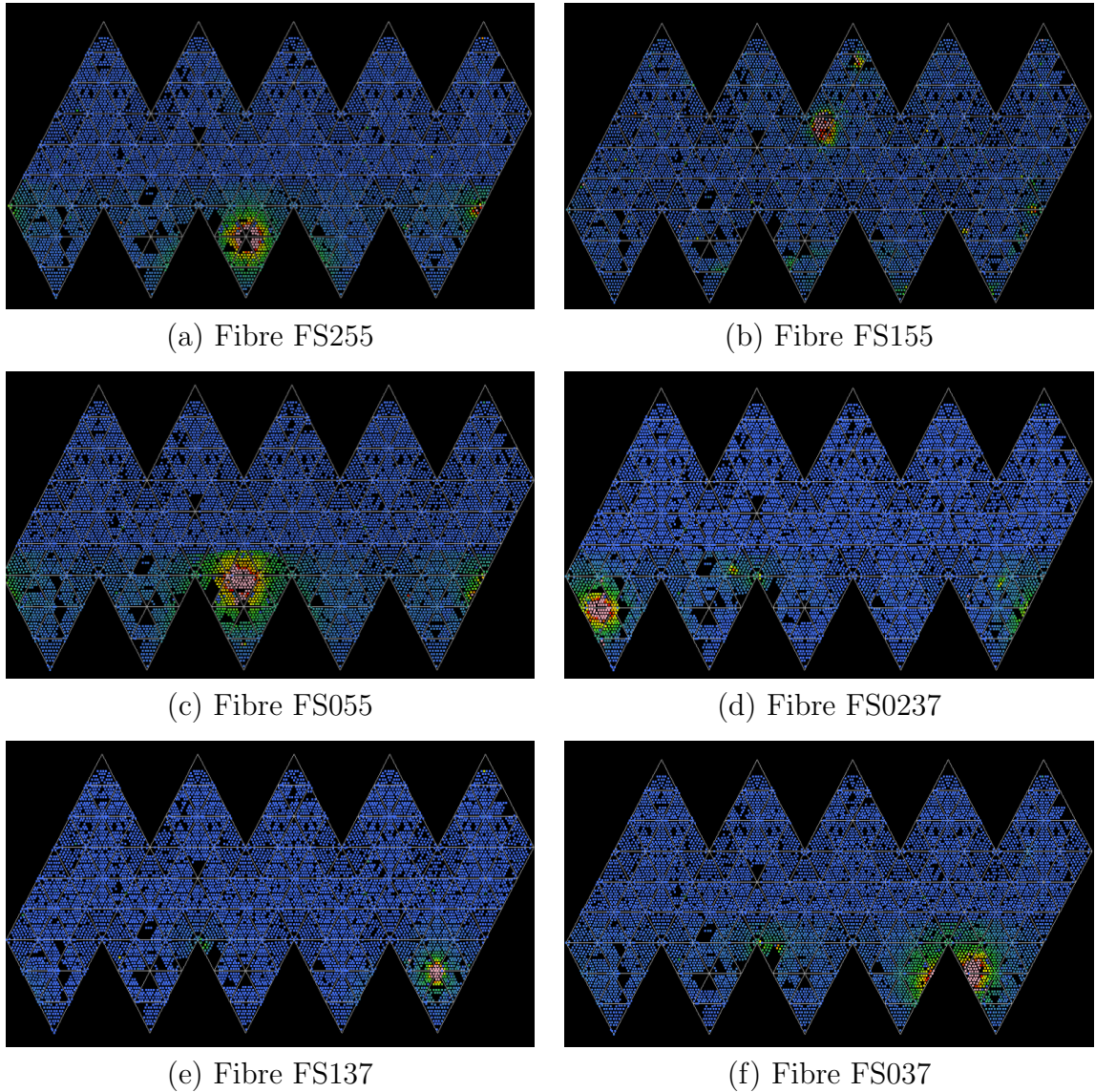


Figure 4.7: Projection of the average occupancies for SMELLIE fibres. These projections contain the occupancies for all PMTs in the SNO+ experiment. Pink corresponds to approximately $> 80\%$ occupancy, red is between $20\% < \text{occupancy} < 80\%$ yellow is between $10\% < \text{occupancy} < 20\%$, green is between $1\% < \text{occupancy} < 10\%$ and blue is less than 1% occupancy. Each point corresponds to one PMT and holes in the projection correspond to a non-operational or disabled PMT.

For each fibre, the laser light is directed onto a different set of PMTs. It is expected that the average N_{hits} are similar for each fibre, but the average N_{hit} is significantly smaller for fibres FS255, FS155 and FS137, despite using the same laser, intensity and frequency combinations. The average occupancy for all SNO+

PMTs over each fibre combination, given in figure 4.7, can be simply explain the lower average Nhits:

- For fibre FS255 (subfigure (a) in figure 4.7): a central beam spot hits a large number of disabled PMTs (~ 70 disabled PMTs), despite a wide beam profile projection in the occupancy space.
- For fibres FS137 has and fibre FS155, a very small number of PMTs with occupancies greater than $>10\%$, which significantly reduces the average Nhits for these fibres.

The larger than expected variation between fibres is due to a combination of the specific locations of each fibre, the beam width of each fibre and coincidentally disabled PMTs where the laser light is incident on the PSUP.

4.5.2 SMELLIE monitoring PMT

Each laser shot is sent to the detector and the SMELLIE monitoring PMT simultaneously via the fibre splitters. The direct waveform from the SMELLIE monitoring PMT is digitised by the CAEN and associated with a SMELLIE event. Figure 4.8 depicts an example of a direct CAEN waveform from the SMELLIE monitoring PMT.

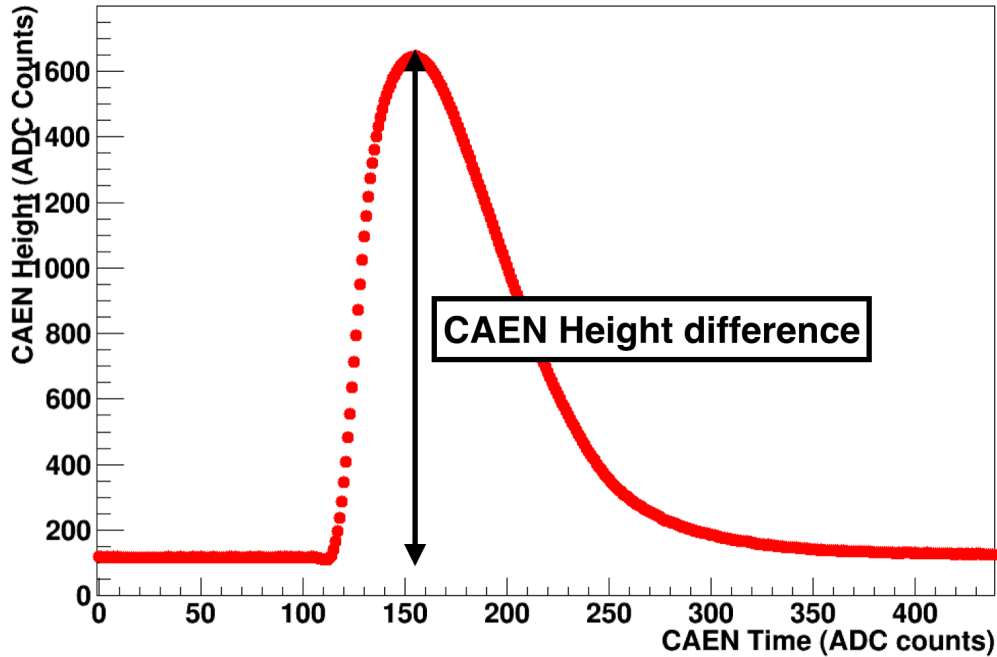


Figure 4.8: This is an example CAEN trace from the SMELLIE monitoring PMT. 1 ADC count is equal to 4 ns.

The CAEN height corresponds to the voltage across the PMT and the CAEN time is measured from the beginning of the SNO+ event. The CAEN height difference in figure 4.8 corresponds to the intensity of the laser shot, measured by the SMELLIE monitoring PMT and is the difference between the smallest non-zero value and the largest value of the CAEN trace. The CAEN height difference for all triggers, with and without a PED trigger, across all sub-runs in run 9044 is given in figure 4.9. SNO+ events with a PED trigger, in a SMELLIE run, correspond to a SMELLIE event that was issued in slave mode.

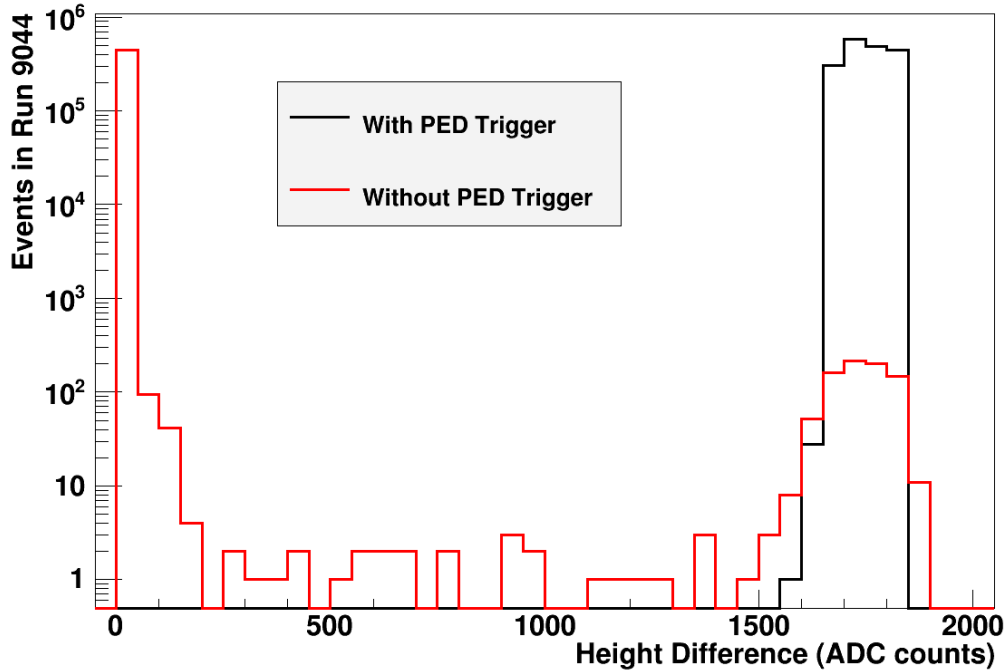


Figure 4.9: CAEN height differences on run 9044 for events with (black) and without (red) the PED trigger.

The PED trigger is used to trigger the laser to fire (in run 9044). Events without a PED trigger should have a very small height differences (as they are measuring noise on the SMELLIE monitoring PMT without laser light present). In figure 4.9, for events with a PED trigger, there is a clean population of events that all have a height difference $> 1,500$ ADC counts. This indicates that SMELLIE events with a PED trigger, were sending light to the monitoring PMT, this light was being recorded by the CAEN and placed into a SNO+ event.

For events without a PED trigger, the vast majority of CAEN traces have very low height differences (< 100 ADC counts) and this is due to noise on the digitisation of the SMELLIE monitoring PMT. The trigger in this case is generated by one of the other physics triggers in SNO+ such as the NHIT100. There are around 4,000 events (out of nearly 2 million events) that have a large height difference, indicative of being a SMELLIE event, but with no PED trigger. It is possible that these triggers are being stolen. The SMELLIE system can send enough light into

the detector to generate a physics trigger, such as the NHIT100 trigger and issue a GT.

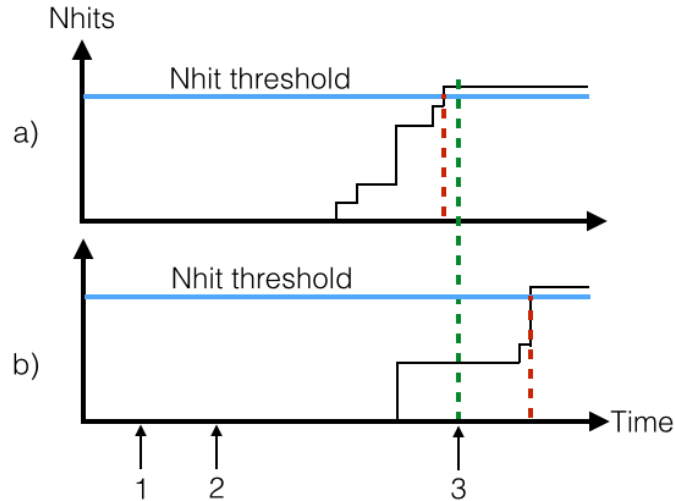


Figure 4.10: Diagram of NHIT100 trigger stealing with two plots of Nhits against time. In case a) the NHIT100 GT is issued before the GT associated with the PED (and SMELLIE) and in b) the PED arrives before the NHIT100 GT is issued.

1 - the time of a PED trigger being sent, 2 - arrival of the PED trigger at the SMELLIE system and 3 - the timed issuance of a GT (after the PED). The blue line represents the Nhit trigger threshold that leads to the issuance of a GT (at a time specified by the red dashed line).

If the GT from the NHIT100 trigger is issued, before the arrival of a GT associated with the PED trigger, as in figure 4.10 a), then the GT will not have the 'PED' bit in the trigger word. The SMELLIE monitoring PMT waveform is read from the CAEN regardless of the trigger word, thus SNO+ events with SMELLIE light exist without the PED bit in the trigger word. The NHIT100 trigger does not always steal the trigger from the SMELLIE, it is issued when the analogue trigger sum for all SNO+ PMTs exceeds a specified voltage threshold. This isn't a common occurrence, as the relative timing of an NHIT100 crossing the Nhit threshold, depends on the PMT trigger time, the number of PMTs within the event and differences in the time delays of associated electronics of each PMT.

Figure 4.11 shows the average CAEN height differences and standard deviation

for each sub-run.

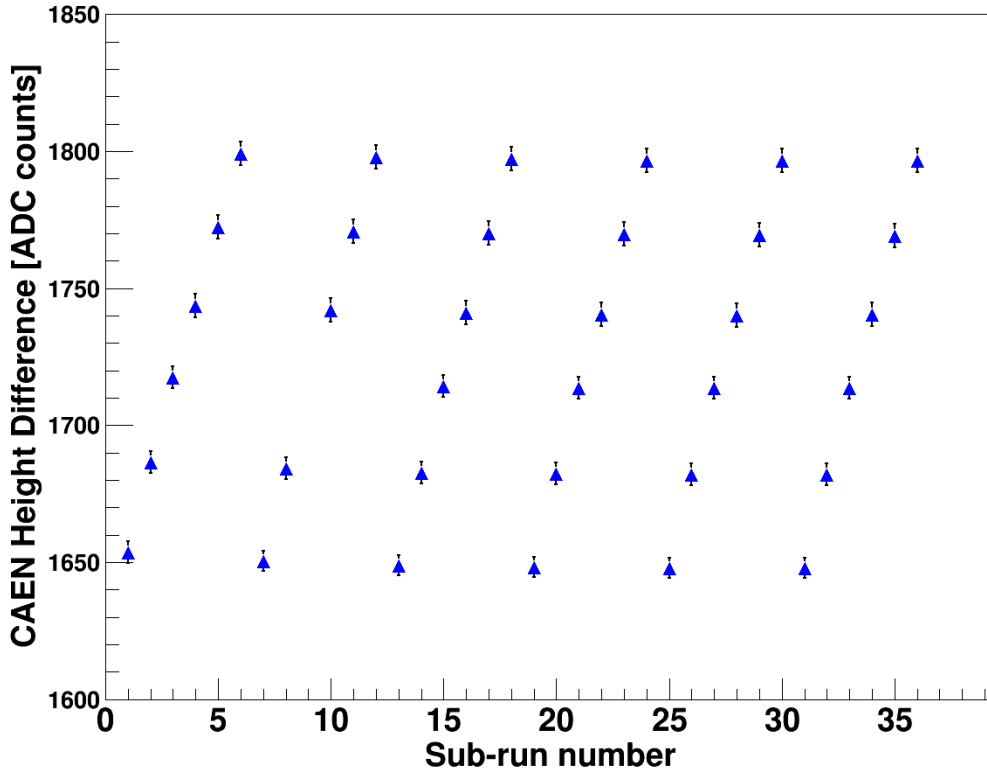


Figure 4.11: Average CAEN height against sub-run on Run 9044

The CAEN height difference is proportional to the laser intensity of light that is directed onto the SMELLIE monitoring PMT. It shows that the intensity of laser light is increasing, as the intensity set point is increased for a particular fibre. Laser light is ‘tapped off’ before the fibre switch, such that the response should be the same regardless of the fibre used to send light into the detector. The relative intensity (in CAEN height difference) in figure 4.11, clearly depicts that the light intensity for each sub-run is consistent, as this is the same regardless of detector fibre choice. However the relative intensity (in terms of Nhits), in figure 4.6, from the SNO+ detector varies significantly from for different fibre choices. This indicates that the light intensity is the same for all sub-runs, but the choice of detector fibre can significantly effect the relative light intensity measurement with the SNO+ detector. This doesn’t have a significant impact upon the scattering calibration as long as the intensity profile is calculated on a detector fibre basis.

4.5.3 SMELLIE triggers

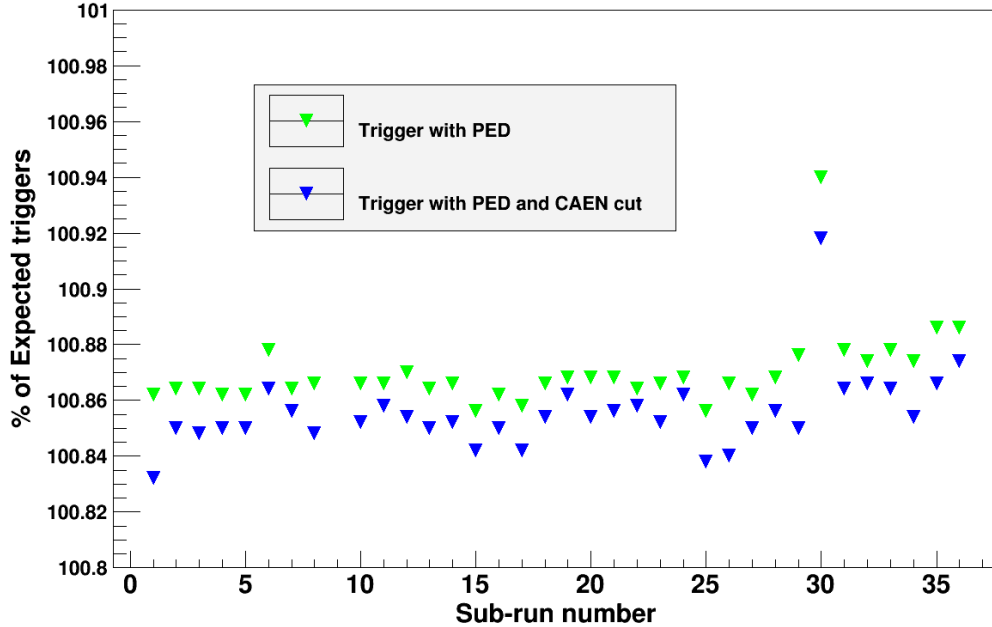


Figure 4.12: % of expected triggers against sub-run number, after a PED trigger cut and a combined PED trigger and CAEN height difference cut for SNO+ run 9044

The SMELLIE run description file expected to send 50,000 SMELLIE shots at a 500 Hz frequency per sub-run. Figure 4.12 shows the % of expected events relative to observed events, after only PED events are included and after PED events with a CAEN cut. The CAEN cut includes events that both have a CAEN trace of the SMELLIE monitoring PMT and a CAEN height difference > 1500.0 ADC counts.

In figure 4.12, the number of events is consistently greater than expected because there was a rounding error in the code that causes a jitter in the number of PED events. The MTC/D is currently only capable of sending PED triggers at a certain rate. Thus the PED triggers are enabled for a certain amount of time at a pre-specified frequency. ORCA calculates the time (in seconds) required by dividing the number of triggers per sub-run by the frequency rate. A mistake (in the ORCA code) causes a rounding error, whereby the time is rounded-up, which

consistently produces more PED triggers than expected.

There are also ~ 6 events in each sub-run, which pass the PED cut but do not pass the CAEN cut. This could indicate that there are some PED events with small CAEN height differences, but figure 4.9 has no CAEN height differences less than 1500.0 ADC counts for PED events. Thus, these are missing SMELLIE events, which do not have a CAEN trace recorded. This could be due to the EB not correctly associating the CAEN trace with a SMELLIE event or that the CAEN was not recorded for a small number of GTs. This effect is less than 0.01%, but should be double checked for future SMELLIE runs.

4.6 Conclusion

SNO+ run 9044 demonstrated that the SMELLIE software can send laser pulses into different fibres, with different intensities, using a PED trigger from the MTC/D. Since SNO+ run 9044 was completed using a pre-built run file, it demonstrates that SMELLIE runs can be pre-built (using the SMELLIE configuration tool in ORCA) and executed using the SMELLIE run control GUI in ORCA. This also demonstrates that the SMELLIE software, controlled by SNODROP and integrated into ORCA, can execute SMELLIE runs and automatically store the run/sub-run level information for offline analysis.

There are still several issues with the SMELLIE system such as PED triggers missing in sub-run 9, rounding errors with the expected number of SMELLIE triggers and SMELLIE triggers being stolen. Some of these problems are associated with SMELLIE, but there are still many non-SMELLIE systems (used by SMELLIE), which are not yet fully commissioned (as of July 2016). Once these systems are commissioned, a further session of SMELLIE commissioning is required, in order

to isolate any problem intrinsic to the SMELLIE system. Overall, the SMELLIE system was able to reliably take data and the success of taking data via ORCA also validates the DAQ upgrades described in chapter 3

5

ALP theory

*“Let’s name our new particle after Axion [a brand of laundry detergent]
to ‘clean up’ this problem in physics!”*

– Frank Wilczek

5.1 Introduction to ALPs

Dark matter is a proposed form of matter that does not absorb or emit a significant amount of electromagnetic radiation. It has been inferred via the rotation curves of the Galaxy, the gravitational lensing of galaxy clusters and anisotropies in the cosmic microwave background radiation [59]. It is estimated to constitute up to around 25% of the Universe [59] and remains one of the open scientific mysteries of our time. There are many proposed solutions to the dark matter problem, but this thesis will focus on how neutrino detectors are sensitive to a dark matter candidate called Axion Like Particles (ALPs).

An ALP is defined as a neutral pseudoscalar particle and given as an extension to the QCD Lagrangian. One of the aims of this thesis is to explore detection techniques for such a neutral pseudoscalar particle. The original formulation of

axions started with Peccei & Quinn [60], who first proposed a solution to the strong CP problem - the observation that there is no violation of CP Symmetry with the strong interaction. They proposed an extension to the QCD Lagrangian, which included a dynamic CP-violating term, θ with Weinberg [61] and Wilczek [62] demonstrating that this leads to the existence of a neutral pseudoscalar particle. The potential of the θ field is tuned to cancel out any CP violating term that arises in the QCD Lagrangian and leads to a new particle called an ‘axion’. The original ‘Weinberg-Wilczek-Peccei-Quinn’ axion model has since been disproved by accelerator, reactor and radioactive source experiments [63].

Despite the failings of the ‘Weinberg-Wilczek-Peccei-Quinn’ axion model, the general principle of an ALP has been extended with two theoretical models: a hadronic model from Kim-Shifman-Vainstein-Zakharov (KSVZ) [64] [65] and a Grand Unified Theory (GUT) model from Dine-Fischler-Srednicki-Zhi (DFSZ) [66] [67]. Throughout this thesis, the DFSZ and KSVZ models are both considered as a possible model for ALPs.

At this point in the discussion, it is important to clarify two different definitions:

- **an axion** - is defined as a specific solution to cold dark matter, whose mass and couplings are highly model dependent and constrained by several different models inferred from cold dark matter. The axion mass is dependent upon the coupling to matter.
- **an ALP** - is a generalised pseudo-scalar particle(s), where the ALP coupling constants and mass are not necessarily dependent. Cold dark matter could be explained by several manifestations of ALPs.

Possible examples of such an ALP include light CP-odd Higgs bosons [68] [69] and light spin 1 particles known as hidden sector photons [69], with a wide range of

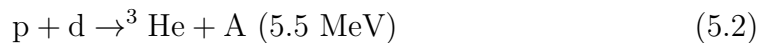
potential particles explored in [70].

Using either the KSVZ or DFSZ models, the ALP mass m_A is given as [71]:

$$m_A \approx (f_\pi m_\pi / f_A) (\sqrt{z} / (1 + z)) \quad (5.1)$$

where m_π and f_π are the mass and decay constant of the neutral π meson respectively, f_A is the decay constant of an ALP and $z = m_u/m_d$ is the quark mass ratio. This can be reduced to $m_A(\text{eV}) \sim 6.0 \times 10^6 / f_A(\text{GeV})$, which relates the mass of an ALP directly to its decay constant and the scale of Peccei-Quinn symmetry violation. The lack of observational evidence for ALPs arises, because the ALP-hadron and ALP-lepton interaction probability are both proportional to m_A and thus significantly suppressed. The majority of experimental searches are for axions between 10^{-6} - 10^{-2} eV, as relic axions with these masses are considered a favourable cold dark matter candidate[71] with experiments such as ADMX haloscope[72]. There are also direct searches for solar axions with CAST [73], which are explored further in section 6.13.

Throughout this thesis, the Sun is assumed to be the main source of ALP production via proton-deuterium fusion via:



The production of ALPs is dependent upon the couplings of ALPs to nucleons g_{AN} . The ALP-nucleon coupling is split into an isoscalar g_{0AN} and isovector g_{3AN} component. The proton capture from the S state in equation 5.2, corresponds to an isovector transition and thus the isoscalar component is negligible. The ratio

of ALP production (ω_A) and photon production (ω_γ) via normal p-p fusion:

$$\frac{\omega_A}{\omega_\gamma} = 0.54(g_{3AN})^2 \left(\frac{p_A}{p_\gamma}\right)^3 \quad (5.3)$$

where p_A and p_γ are the axion and photon momenta respectively [71]. The hadronic (KSVZ) and grand unified (DFSZ) models both predict comparable ratios of ALP production to normal pp fusion [71]. It is important to emphasise that both models predict that $\frac{p_A}{p_\gamma} \approx 1.0$.

This thesis will focus on a specific class of experiments: Large Underground Neutrino (LUN) experiments. A LUN experiment refers to any large water Cherenkov or liquid scintillator experiment such as SNO+ and Super Kamiokande. LUN experiments have to be: large such that they can observe a sufficient ALP signal, deep underground experiments such that any low energy signal isn't drowned out by cosmogenically activated isotopes and neutrino experiments as these typically have low radioactive backgrounds. There also could be sensitivity to relic ALPs [74] but this thesis only considers ALPs originating from the Sun. Thus, if the coupling of ALPs to matter is too strong, they would rarely escape from the Sun. However, a coupling of ALPs to matter, which is too weak would make any potential detection of ALPs almost impossible. This provides some natural theoretical limits on the ALP couplings to matter, which are further explored in section 5.3.

5.2 ALP Interactions

There are several different interactions that could be observed with LUN experiments (see figure 5.1) [71]:

- Compton conversion of ALPs, $A + e^- \rightarrow e^- + \gamma$
- Axio-electric effect $A + e^- + Z \rightarrow e^- + Z$

- ALP decay to two photons, $A \rightarrow \gamma + \gamma$
- Inverse Primakoff effect, $A + Z \rightarrow \gamma + Z$

where Z is a nucleus target and A is the solar ALP.

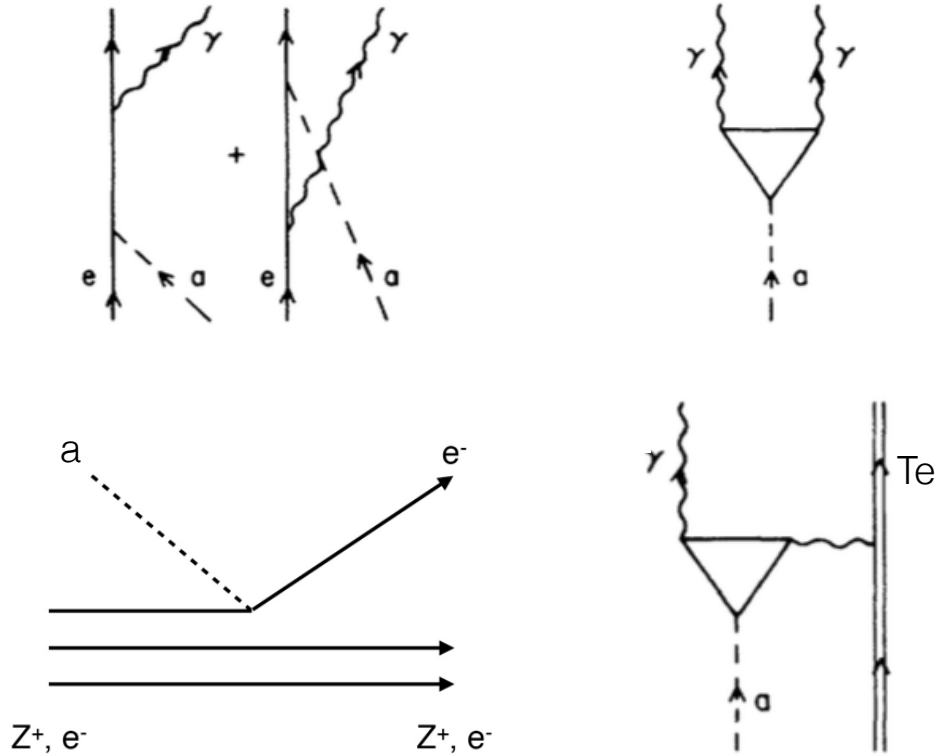


Figure 5.1: **Top Left:** Compton conversion of ALPs, **top right:** ALP decay to two γ 's, **bottom left:** Axio-electric effect and **bottom right:** inverse Primakoff with Tellurium (as an example nucleus)

5.2.1 Compton conversion of ALPs (CCA)

Compton conversion of ALPs (CCA) typically produces an electron with ~ 2.5 MeV and a γ -ray with ~ 3 MeV. The differential cross section of CCA, given in figure 5.2, shows a forward peaked distribution relative to the incoming direction of the ALP. The majority of CCA interaction events have electrons with energies > 3 MeV and γ -rays with energies < 2 MeV. The reconstructed direction of solar ALPs, in a water Cherenkov detector, is also forward peaked with respect

to the Sun, because Cherenkov light maintains directional information. This is advantageous because the majority of internal backgrounds to an ALP signal, such as U/Th impurities, are isotropic. By applying a directional cut, backgrounds to ALP events in water can be reduced by an order of magnitude (see appendix B), whilst maintaining 80% of the ALP signal.

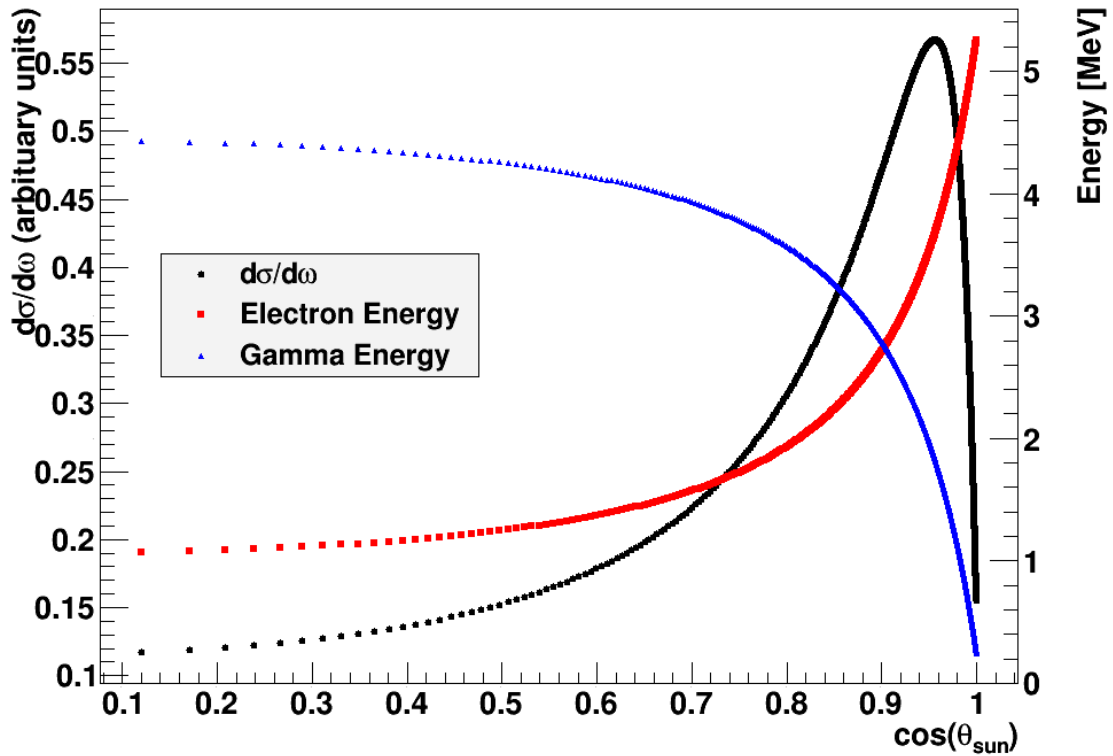


Figure 5.2: Differential cross section of CCA with the corresponding electron and γ particle energies in MeV.

In liquid scintillator based experiments, the directionality of the Compton conversion is lost, as scintillation light is isotropic. However, in liquid scintillators the light yield per MeV is greater than in water Cherenkov detectors, which improves the energy resolution.

The integrated cross section for Compton conversion σ_{CCA} is [75][74][76]:

$$\begin{aligned} \sigma_{CCA} = & \frac{g_{Ae}^2 \alpha}{8m^2 p_A} \left[\frac{2m^2(m + E_A)y}{(m^2 + y)^2} \right. \\ & + \frac{4m(m_A^4 + 2m_A^2 m^2 - 4m^2 E_A^2)}{y(m^2 + y)} \\ & \left. + \frac{4m^2 p_A^2 + m^4}{p_A y} \ln \frac{m - E_A + p_A}{m + E_A - p_A} \right] \end{aligned} \quad (5.4)$$

where p_A and E_A are the momentum and energy of the ALP respectively and $y = 2mE_A + m_A^2$. The number of Compton conversion events observed in a given detector, S_{CC} :

$$S_{CCA} = \Phi_{\nu pp} \left(\frac{\omega_A}{\omega_A + \omega_\gamma} \right) \sigma_{CC} N_e T \epsilon \quad (5.5)$$

where $\Phi_{\nu pp}$ is the pp neutrino flux, N_e is the number of electron targets, T is the exposure time (in seconds) and ϵ is the detector efficiency for observing ALPs via Compton conversion. Using equation 5.3, equation 5.5 and approximating $(p_A/p_\gamma)^3 \approx 1$ for $m_A \leq 1$ MeV, the expected number of Compton conversion events becomes:

$$\begin{aligned} S_{CCA} = & g_{Ae}^2 \times g_{3AN}^2 \times 1.4 \times 10^{-14} N_e T \epsilon \\ |g_{3AN} \times g_{Ae}| \leq & \left(\frac{S_{CCA}}{1.4 \times 10^{-14} N_e T \epsilon} \right)^{\frac{1}{2}} \end{aligned} \quad (5.6)$$

5.2.2 Axio-electric effect

The axio-electric effect is another proposed mechanism for ALP detection and can also be used to probe the ALP coupling to electrons. During the reaction of the axio-electric effect, an electron of the target atom is given a kinetic energy equivalent to the total energy of the ALP (E_A), less the binding energy of the electron (E_b). Assuming that $E_A \gg E_b$ and the atomic number $Z < 137$, then the

cross section for the axio-electric effect σ_{Ae} is [74]:

$$\sigma_{Ae} = 2(Z\alpha m_e)^5 \frac{g_{Ae}^2 p_e}{m_e^2 p_A} \left[\frac{4E_A(E_A^2 + m_A^2)}{(p_A^2 - p_e^2)^4} - \frac{2E_A}{(p_A^2 - p_e^2)^3} - \frac{64}{3} p_e^2 p_A^2 m_e \frac{m_A^2}{(p_A^2 - p_e^2)^6} - \frac{16m_A^2 p_A^2 E_e}{(p_A^2 - p_e^2)^5} - \frac{E_A}{p_e p_A} \frac{1}{(p_A^2 - p_e^2)^6} \ln \frac{p_e + p_A}{p_e - p_A} \right] \quad (5.7)$$

where p_A and p_E are the momenta of the ALP and electron respectively, E_e is the energy of the outgoing electron, m_e is the mass of the electron and α is the fine structure constant.

A key feature of the axio-electric effect is that its cross section is proportional to Z^5 , where Z is the atomic number of the nucleus. Table 5.1 depicts the event rate for the Te-loaded scintillator, after a fiducial volume cut of $R < 5500$ mm and an energy cut between 5.0 - 5.7 MeV. Higher loadings of Tellurium improve the event rate for AE interaction by two orders of magnitude, when the Te-loading is increased from 0.1% to 10%.

Te-loading level (% by mass)	Event rate (per yr)
0.1	109.4
0.3	172.0
0.5	234.6
1.0	391.1
3.0	1,017.3
10.0	2,308.8

Table 5.1: Axio-electric effect with SNO+ at different Te-loadings. The event rate is calculated using $|g_{Ae} \times g_{3AN}| < 1.9 \times 10^{-10}$ set by BGO [77] after a fiducial volume cut of $R < 5500$ mm and an energy cut between 5.0 - 5.7 MeV.

5.2.3 Inverse Primakoff effect (IP)

The inverse Primakoff effect can help probe the ALP coupling to photon and occurs off atoms within the detector medium. The signal is typically a 5 MeV γ particle. The inverse Primakoff cross section is proportional to Z^2 , which is slightly advantageous for isotope loaded detectors such as SNO+ ($Z=52$ for tellurium) and Kamland-Zen ($Z=54$ for Xenon). The integrated cross section for the inverse Primakoff effect (σ_{IP}) is [75]:

$$\sigma_{IP} = g_{A\gamma}^2 \frac{Z^2 \alpha}{2} \left[\frac{1 + \beta^2}{2\beta^2} \ln\left(\frac{1 + \beta}{1 - \beta}\right) - \frac{1}{\beta} \right] \quad (5.8)$$

where $\beta = p_A/E_A$. For SNO+, the sensitivity to ALPs is slightly improved because the inverse primakoff interaction cross section off Tellurium is greater than off Carbon. The event rate as a function of Te-loading (% by mass) is given in table 5.2, where the event rate marginally increases as higher loadings are used.

Te-loading level (% by mass)	Event rate (per yr)
0.1	118.2
0.3	119.2
0.5	120.1
1.0	122.5
3.0	131.7
10.0	164.2

Table 5.2: Inverse Primakoff with SNO+ at different Te-loadings. The event rate is calculated using $|g_{3AN} \times g_{A\gamma}| < 4.6 \times 10^{-11} \text{GeV}^{-1}$ set by Borexino [71].

The differential cross section for the IP interaction is [78]:

$$\frac{d\sigma}{d\omega} \propto \frac{1 + \cos(\theta)}{1 - \cos(\theta)} \quad (5.9)$$

where θ is the scattering angle in the nuclear rest frame. In water Cherenkov

detectors, directional information cannot be used to discriminate ALP events from other backgrounds. The γ particle is detected via its Compton scatter off electrons in the detector medium. Compton scattering has a differential cross section $\frac{d\sigma}{d\omega} \propto 1 + \cos(\theta)^2$, which is doesn't preserve directional information of the γ particle produced in the IP interaction.

5.2.4 ALP Decay

For ALPs with a mass above $2m_e$, the dominant decay mode is $A \rightarrow e^+ + e^-$. The lifetime of an ALP above $2m_e$ ($\tau_{e^+e^-}$) in the lab frame is given as [71]:

$$\tau_{e^+e^-} = \frac{8\pi}{g_{Ae}^2 \sqrt{m_A^2 - 4m_e^2}} \quad (5.10)$$

For ALPs with a mass less than $2m_e$, $A \rightarrow e^+ + e^-$ decay is forbidden[71], and the dominant decay mode is $A \rightarrow \gamma + \gamma$ is possible. The probability of decay depends on $g_{A\gamma}$ and the lifetime of an ALP below $2m_e$ ($\tau_{2\gamma}$) [71]:

$$\tau_{2\gamma} = \frac{64\pi}{g_{A\gamma}^2 m_A^3} \quad (5.11)$$

ALP decays are not calculated for SNO+, because the inverse Primakoff interaction provides a much tighter constraint on the limit setting potential for $|g_{3AN} \times g_{A\gamma}|$.

5.3 Theoretical Limits

5.3.1 Decay Limits on ALP searches

Assuming the Sun is the predominant source of detectable ALPs, they have to reach the Earth in sufficient quantities before decaying in order to be detected.

The probability, $P(p_A, m_A)$ that an ALP will survive to reach Earth is:

$$P(p_A, m_A) = \exp(-\tau_f/\tau_{e^+e^-}) \quad (5.12)$$

where τ_f , the time of flight in the ALP frame is given as

$$\tau_f = \frac{Lm_A}{cp_A} = \frac{m_A}{E_A} \frac{L}{\beta c} \quad (5.13)$$

where $L = 1.5 \times 10^{13}$ is the distance from Sun to the Earth. If ALPs decay before reaching the Earth, they will not be detectable by SNO+, thus providing a constraint on the decay rate for ALPs. where the mass of an ALP $m_A < 2m_e$ with $g_{Ae} < 10^{-11}$ [79]. For ALP decay to 2γ , using equations 5.12 and 5.13, the flux of ALPs reaching the Earth is:

$$\Phi_A = \exp(-\tau_f/\tau_{2\gamma})\Phi_{A0} = \exp(-\tau_f g_{A\gamma}^2 m_A^3 / 64\pi)\Phi_{A0} \quad (5.14)$$

where Φ_{A0} is the ALP flux at the Sun. This limits the sensitivity to ALP decays to 2γ with $m_A < 2m_e$ at SNO+ and similar experiments, as the sensitivity falls off rapidly with large values of $g_{A\gamma}^2 m_A^3$.

5.3.2 Limitation of Solar ALP production

Since solar ALPs have to pass through the Sun itself, they can't have an interaction cross section that is too large otherwise they would not be able to escape. However, they can't have a cross section that is too small, otherwise they it will be too hard to detect. If ALPs exist and are produced in the Sun, they would have been produced throughout the evolution of the Universe, whilst rarely interacting with other matter due to their low interaction cross section of ALPs. Assuming that ALPs have a very long lifetime before they decay, they could be considered

a candidate to explain the observed dark matter in the Universe.

ALPs produced in the Sun have to pass through high number densities of electrons (n'_e) and $n'_e = 6.8 \times 10^{35}$ electrons/cm² within the Sun [71]. Assuming the Compton conversion of ALPs occurs, the Compton conversion cross section multiplied by the number density of electrons $\sigma_{CC}n'_e$ is required to be less than 1 so that ALPs can escape in sufficient quantities. From equation 5.7, the Compton conversion cross section is given as $\sigma_{CC} \sim g_{Ae}^2 \times 4.3 \times 10^{-25}$ cm² and with $n'_e = 6.8 \times 10^{35}$ electrons/cm²:

$$\begin{aligned} 4.3g_{Ae}^2 n'_e \times 10^{25} &< 1 \\ g_{Ae} &< 1.8 \times 10^{-6} \end{aligned} \tag{5.15}$$

If ALPs interact via the axioelectric effect, the maximum cross section for the axioelectric effect is $\sigma_{Ae} = g_{Ae}^2 Z^2 \times 1.9 \times 10^{-29}$ cm² [71]. Assuming a dominance of hydrogen within the Sun and a relative abundance of elements with $Z > 50$ of 10^{-9} , then the ALP flux does not change by more than 10% if $g_{Ae} < 10^{-3}$ [71].

Theoretical restrictions on $g_{A\gamma}$ can be placed by looking at the inverse Primakoff interaction. The cross section of this reaction is $\sigma_{PC} \approx g_{A\gamma}^2 Z^2 \times 1.8 \times 10^{-29}$ cm². Again assuming a dominance of hydrogen in the Sun, $g_{A\gamma} < 10^{-4}$ GeV⁻¹. There is a possibility of axiodissociation:

$$A + Z \rightarrow Z_1 + Z_2 \tag{5.16}$$

where a nucleus Z is dissociated into two separate daughter nuclei, Z_1 and Z_2 via an interaction with the ALP and is analogous to photodissociation [80]. For ALPs

with 5.5 MeV energy, this effect is only relevant for a few nuclei: ^{17}O , ^{13}C and ^2H and it has been shown that axiodissociation cannot substantially reduce the ALP flux for couplings to nucleons, $g_{AN} < 10^{-3}$ [80].

6

ALP detection with neutrino experiments

This chapter is divided into two parts: the ALP detection potential of SNO+ specifically and the ALP detection potential for Large Underground Neutrino (LUN) experiments, which are similar to SNO+. In the first part of this chapter, the validation of ALPs in SNO+ is given in section 6.1, the external backgrounds to an ALP signal and the potential for timing based cuts for ALPs are given in sections 6.2 and 6.3 respectively. The sensitivity to $|g_{3AN} \times g_{Ae}|$ and $|g_{3AN} \times g_{A\gamma}|$ in unloaded and Te-loaded scintillator are given in sections 6.4 and 6.5 respectively.

In the second part of this chapter, the sensitivity to $|g_{3AN} \times g_{Ae}|$ and $|g_{3AN} \times g_{A\gamma}|$ for Large Underground Neutrino (LUN) experiments is discussed. In lieu of access to the data and simulation, the sensitivity of LUN experiments to ALPs is estimated, relative to Borexino, using a simple scaling law. Other non-LUN experimental searches for ALPs are also considered in section 6.13. This chapter is concluded with a comparison between the ALP sensitivity in SNO+, LUN and non-LUN experiments.

6.1 Validation of ALPs in SNO+

The simulation of ALPs in the SNO+ detector is dependent upon the resultant kinetic energy and direction of the outgoing particle from the interaction. Geant4 [8] is used within the SNO+ simulation, RAT to create an ALP vertex, which produces daughter particles with a kinetic energy and outgoing direction (relative to the Sun) distributions. The simulation of ALPs via the AE/IP interactions is trivial, because a mono-energetic e^- (for AE) or γ (for IP) have a momentum equal to the momentum of the original ALP. The direction of the produced e^-/γ is neglected for analysis in scintillator, because these particles are detected via the scintillation light produces, which is intrinsically isotropic.

The CCA interaction is non-trivial because the e^- is produced at an angle relative to the Sun, θ_{Sun} and the γ -ray at a corresponding angle (see figure 6.1). The angle θ_{Sun} is related to the energy of the e^- and γ -ray (see section 5.2.1). The directional information cannot be used in scintillator, but is useful in water Cherenkov detectors and SNO+ water phase.

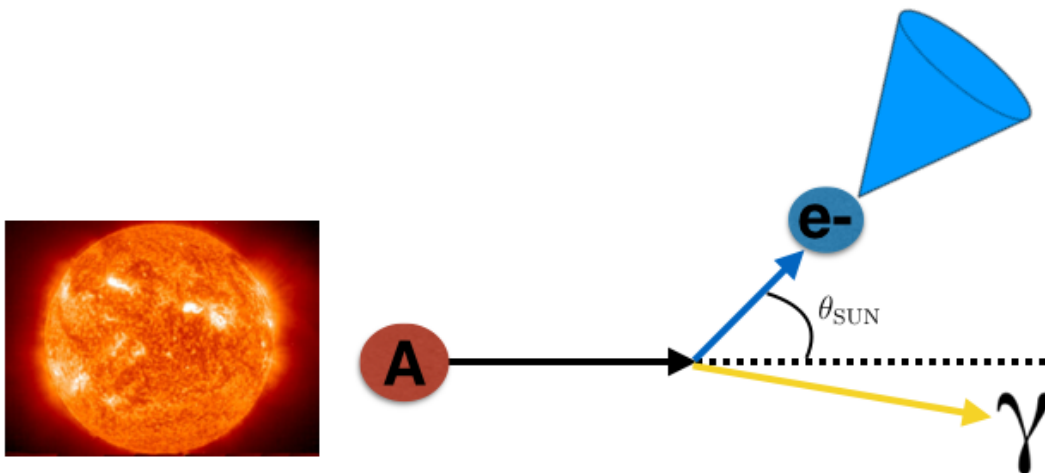


Figure 6.1: Diagram of the angle θ_{SUN} between the incoming ALP and outgoing electron.

The theoretical distribution of the angle of the e^-/γ particles, with respect to the

incoming ALP, is plotted against the simulated (measured) MC distribution in figure 6.2. The simulated and theoretical distributions are in good agreement, as the $\tilde{\chi}^2$ divided by the degrees of freedom (DOF) for both particles is between $0.75 < \tilde{\chi}^2/\text{DOF} < 1.25$.

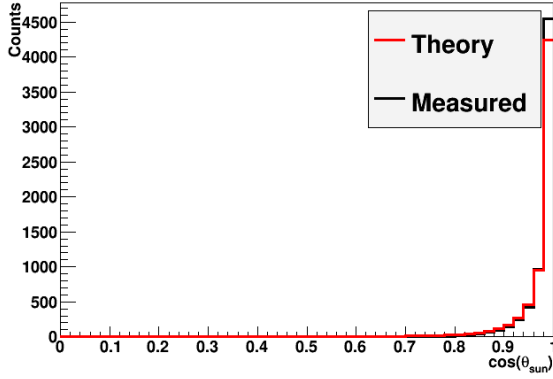
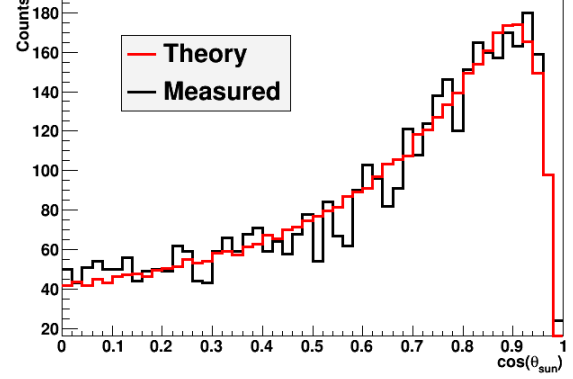
(a) Direction of γ 's ($\tilde{\chi}^2/\text{DOF} = 0.75$)(b) Direction of electrons ($\tilde{\chi}^2/\text{DOF} = 1.17$)

Figure 6.2: Theoretical direction distribution compared to the simulated (measured) direction of e^-/γ from CCA interaction

The theoretical distribution of energy of the e^-/γ particles for CCA are given in figure 6.3, with the simulated energy of the e^-/γ particles. The distributions are also in good agreement, as the $\tilde{\chi}^2$ divided by the degrees of freedom (DOF) for both particles is between $0.75 < \tilde{\chi}^2/\text{DOF} < 1.25$.

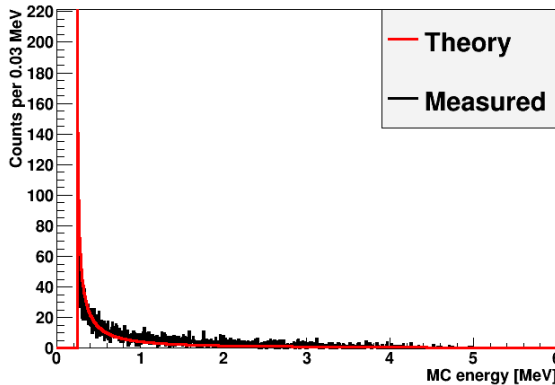
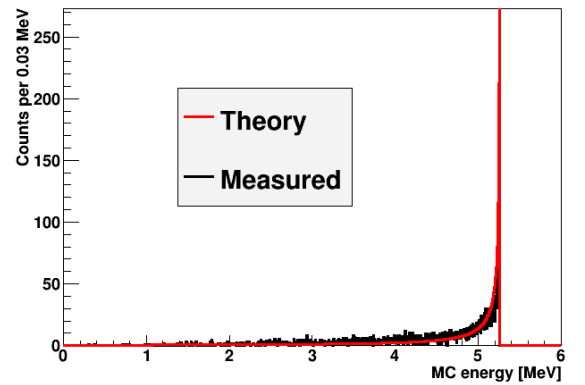
(a) Kinetic energy of γ 's ($\tilde{\chi}^2/\text{DOF} = 0.98$)(b) Kinetic energy of electrons ($\tilde{\chi}^2/\text{DOF} = 0.92$)

Figure 6.3: Theoretical energy distribution compared to the simulated (measured) energy of e^-/γ from CCA interaction

6.2 External backgrounds in SNO+

The external backgrounds to ALPs determine the choice of fiducial volume used for an ALP analysis. For all ALP interactions, the energy deposited within the scintillator is ~ 5.0 MeV. ^{208}Tl is the only type of reducible background decay that is near this energy with a sufficient rate. It is present (internally) within the scintillator, but also externally in the AV, the hold-up/down ropes, the external water and the PMTs. ^{208}Tl is a daughter nuclei of the Thorium chain, and consists of a β -decay with an endpoint of ~ 2.4 MeV with associated γ 's produced at ~ 2.6 MeV. The ^{208}Tl decay has a Q-value of 5.004 MeV, just below the region of interest for ALPs. The expected rate of decays within different detector components given in table 6.1.

^{208}Tl external backgrounds	Decays per year [16]
Hold down ropes	2.32×10^6
Hold up ropes	4.78×10^5
AV	1.50×10^6
External water	3.92×10^6
PMTs	4.4×10^{10}

Table 6.1: Table of external ^{208}Tl from the hold down ropes, hold up ropes, external water and PMTs. Note that these are the number of expected decays in the SNO+ detector in one year [16].

Thorium impurities from the PMTs (themselves) are the most numerous source of ^{208}Tl decays. However, the PMTs are approximately 3 meters away from the AV and 8 meters away from the centre of the AV. The average scattering distance of a 2.6 MeV γ is $\sim 30\text{cm}$, thus any ^{208}Tl γ 's from the PMTs are almost 10 scattering lengths away from the AV and thus, suppressed by a factor $(\frac{1}{e})^{10} \sim 10^{-5}$.

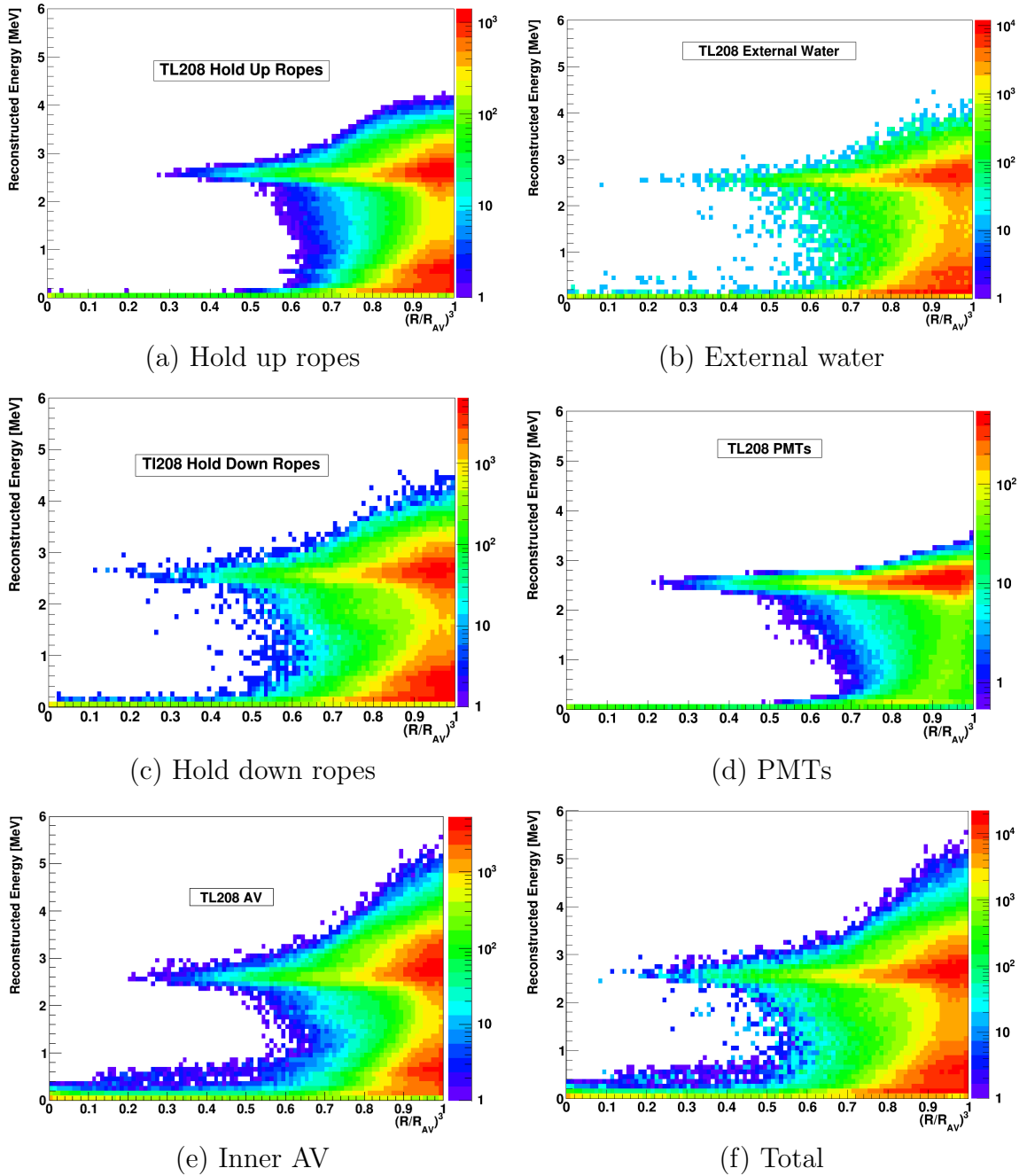


Figure 6.4: 2D histogram of the reconstructed energy against the R/R_{AV} for ^{208}Tl external backgrounds per year for SNO+. The background rates for different external backgrounds are given in table 6.1.

Figure 6.4 depicts the 2D histograms of (R/R_{AV}) against reconstructed energy (MeV) for ^{208}Tl originating from different detector components, where $R_{AV} = 6005$ mm is the radius of the AV. Each subfigure in figure 6.4, has a significant number of events, which reconstruct to low radii ($R/R_{AV} < 0.3$) within the de-

detector at ~ 2.6 MeV. This occurs, when a γ travels close towards the centre of the detector, before depositing energy within the scintillator. This effect is particularly prominent at 2.6 MeV, because every ^{208}Tl event has an associated γ with 2.6 MeV of energy. In every subfigure, expect subfigure (d) for the ^{208}Tl from PMTs, there is a large population of events with energies between 0.1 - 1.0 MeV of energy, which reach values of R/R_{AV} up to ~ 0.8 . These events are associated with the intermediate γ 's produced during the ^{208}Tl decay.

The total of all external backgrounds is given in subfigure (f) of figure 6.4 for one year of running SNO+. ALPs have an observed at energies between 4.5 and 6.0 MeV, thus an energy window of 4.5 - 6.0 MeV indicates that a choice of $R/R_{AV} < 0.7$, equivalent to a fiducial volume of $R < 5500$ mm, would include no contribution from ^{208}Tl external backgrounds. Thus, external backgrounds are considered negligible for an ALP analysis in SNO+.

Internal ^{208}Tl decays could be a considerable background to an ALP analysis. Around 250 events of internal ^{208}Tl decays per year are expected in the unloaded scintillator and around 17,780 ^{208}Tl decays per year in Te-diol 0.5% loaded scintillator [16]. Section 6.3 described how the scintillation timing profile of ^{208}Tl decay-like events can be distinguished from ALP-like events.

6.3 Timing discrimination for ALPs in SNO+

Internal ^{208}Tl event could form a large background to an ALP analysis, if the concentration of Thorium is significantly higher than expected. The following section explores possible timing discrimination cuts that could be applied, in order to mitigate a larger concentration of Thorium in SNO+. ^{208}Tl consists of the emission of early light via the electron (from the decay), followed by the Compton

scattering of the γ -ray (at a slightly different location), which produces electron(s) that scintillate at a slightly later time (see figure 6.5). The scintillation emission profile for an ALP event, via the axioelectric effect, is purely an electron with early scintillation light with a small amount of Cherenkov light.

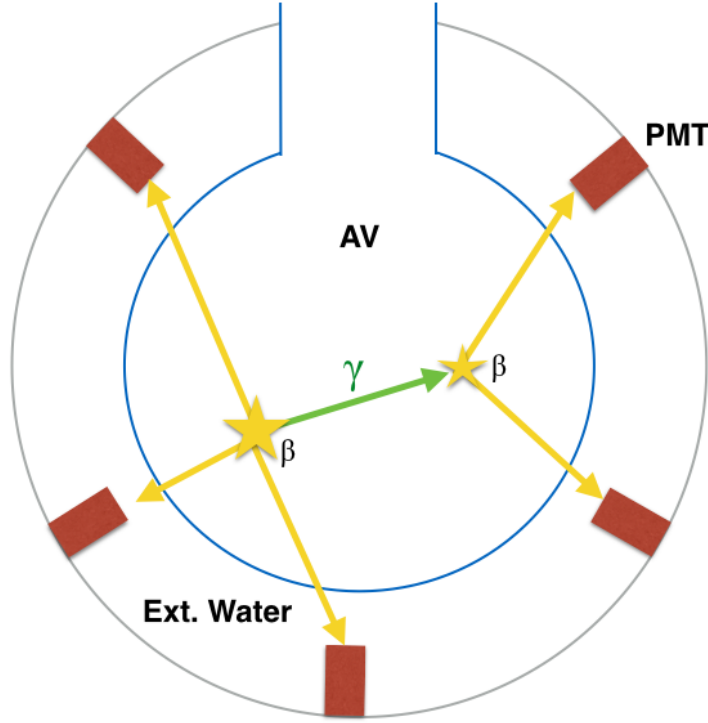


Figure 6.5: Light emission profile of ^{208}Tl event. The initial decay occurs with the emission of an e^- , which can produce Cherenkov light and scintillation light immediately. Whereas the 2.6 MeV γ -ray travels a small distance, before Compton scattering off several electrons.

In SNO+ the light emission profile is captured by the time residuals across all PMTs within the detector. The time residual t_{res}^i of the i -th PMT in an event is given by:

$$t_{res}^i = t_{PMT}^i - t_{flight}^i - t_{rec} \quad (6.1)$$

where t_{PMT}^i is the time at which the i -th PMT was triggered, t_{rec} is the reconstructed time at which the event occurred and t_{flight}^i is flight time of the photon from the reconstructed position to the i -th PMT. The time of flight, t_{flight}^i is calculated using a straight line path between the reconstructed position and the i -th

PMT, taking into account the different velocities of light in the different materials due to their refractive indices. It is possible to have negative times, because the beginning of a SNO+ event is defined by the time at which a GT was issued. PMTs can detect light before the issuance of a GT, store this information and placed it into a SNO+ event.

Figure 6.6 is an example of time residual PDFs for Te-loaded and unloaded scintillator, which include time residuals from PMTs in events that reconstruct with energies between 4.5 and 5.5 MeV at $R < 5500$ mm. The PDF for ^{208}Tl events has a marginally larger fraction of later light compared to AE of ALPs, as the light emission from γ 's is marginally later.

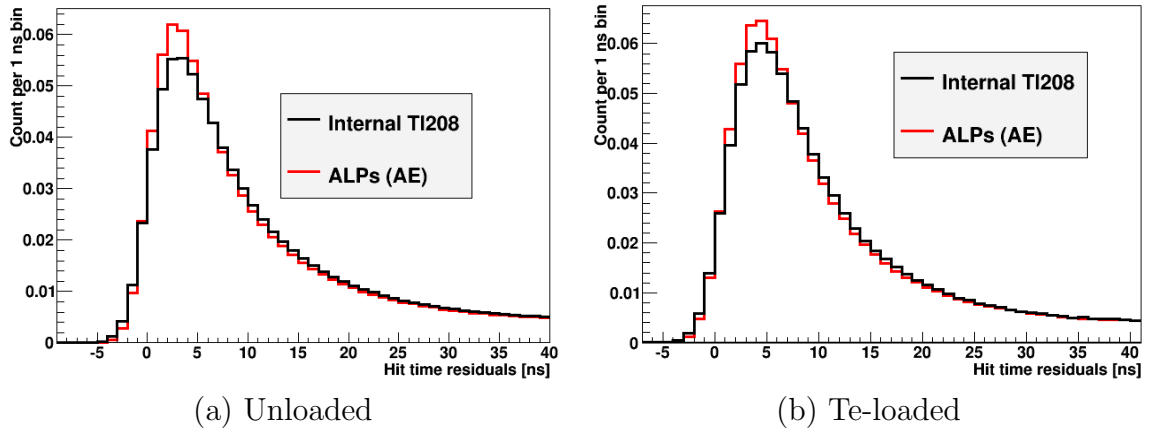


Figure 6.6: Time residual PDF for AE/ ^{208}Tl over 10,000 events for unloaded and Te-loaded scintillator, which reconstruct with energies between 4.5 and 5.5 MeV and with $R < 5500$ mm.

A likelihood ratio test can be applied as the most powerful statistical test to differentiate between " ^{208}Tl -like" and "ALP-like" events (for each type of ALP interaction). The difference in likelihood ratio ($\Delta\mathcal{L}$) is equivalent to the likelihood ratio test, and equal to:

$$\Delta\mathcal{L} = \mathcal{L}_{^{208}\text{Tl}} - \mathcal{L}_{\text{ALP}} \quad (6.2)$$

where $\mathcal{L}_{^{208}\text{Tl}}$ and \mathcal{L}_{ALP} are the likelihood values of ^{208}Tl and ALP events respec-

tively. The likelihood is given as:

$$\mathcal{L}_k = \prod_{i=1}^{N_{\text{PMTs}}} P(t_{res}^i/k) \quad (6.3)$$

$$k \in [{}^{208}\text{Tl}, \text{ALP}]$$

where N_{PMTs} is the number of PMTs that were hit in an event and assuming the time residual on each PMT are independent. The PDFs (such as the PDFs given in figure 6.6) are used for calculating $\Delta\mathcal{L}$. Additionally, only events that reconstruct within a $R < 5500$ mm and within an energy window are included in building the PDFs and calculating $\Delta\mathcal{L}$. It is also important to note that a different set of simulated data is used for building the PDFs and constructing $\Delta\mathcal{L}$.

Figure 6.7 gives the $\Delta\mathcal{L}$ for the AE ALP interaction against ${}^{208}\text{Tl}$ events. The calculation of the time residuals is very sensitive to the types of events being chosen. For ${}^{208}\text{Tl}$ events, it is a very specific population $< 1\%$ of the total events that reconstruct with the ALP window, thus two energy windows are chosen to investigate the sensitivity to different energy window choices for building time residuals. It is important to note that $\Delta\mathcal{L}$ is a statistical separation and the absolute value of $\Delta\mathcal{L}$ has no direct physical meaning.

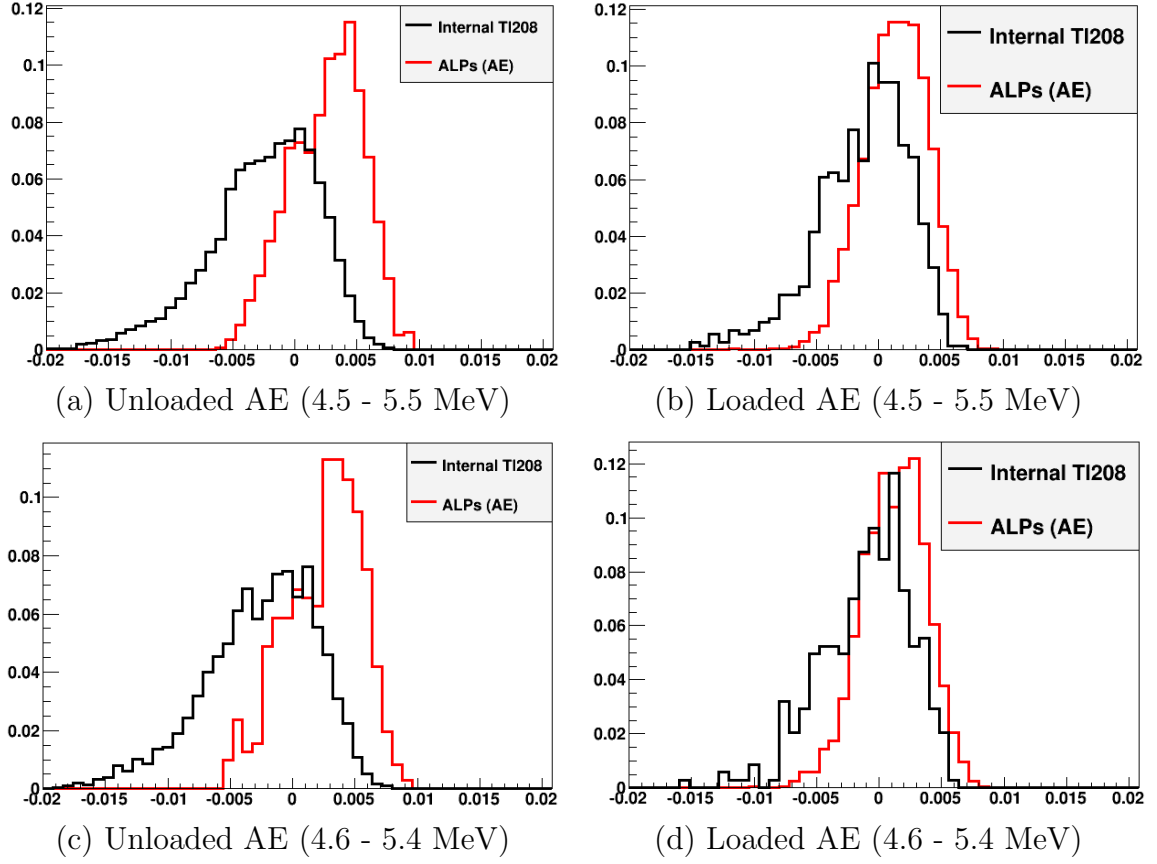


Figure 6.7: Distributions of $\Delta\mathcal{L}$ for AE interaction of ALPs in unloaded and Te-loaded scintillator with different energy windows.

Figure 6.7 shows the difference in $\Delta\mathcal{L}$ for unloaded and loaded scintillator. The separation between AE/ ^{208}Tl is smaller in the loaded scintillator compared to the unloaded scintillator in figure 6.7. This effect arises as $\Delta\mathcal{L}$ is calculated using the time residual PDFs and the time residual, which is sensitive to both the energy and position reconstruction. The loading of Tellurium into the scintillator cocktail, reduces the light yield per MeV and thus reduces the resolution of both position and energy reconstruction [9]. This reduction in resolution leads to a smearing of the time residual and a reduction in separation between different types of event.

The optimal likelihood cut, $\Delta\mathcal{L}_{\text{cut}}$ is chosen by maximising the amount of ALP signal divided by the square root of ^{208}Tl events. The optimal choice for differ-

ent combinations of ALP interaction, energy window and scintillator cocktail are given in table 6.2.

Energy (MeV)	Interaction	$\Delta\mathcal{L}_{\text{cut}}$	Signal (%)	Background (%)
4.5 - 5.5	AE (Te-loaded)	-0.0012	87.0	58.4
4.6 - 5.4	AE (Te-loaded)	-0.0028	95.2	73.8
4.5 - 5.5	CCA (Te-loaded)	-0.002	94.3	80.1
4.6 - 5.4	CCA (Te-loaded)	-0.002	94.4	81.3
4.5 - 5.5	IP (Te-loaded)	-0.0028	96.6	92.7
4.6 - 5.4	IP (Te-loaded)	-0.0084	98.0	96.0
4.5 - 5.5	AE (unloaded)	0.0044	36.0	3.6
4.6 - 5.4	AE (unloaded)	0.0052	24.3	1.9
4.5 - 5.5	CCA (unloaded)	0.0036	27.0	4.7
4.6 - 5.4	CCA (unloaded)	-0.0004	80.4	48.4
4.5 - 5.5	IP (unloaded)	0.0012	58.8	28.7
4.6 - 5.4	IP (unloaded)	-0.0004	78.7	53.8

Table 6.2: $\Delta\mathcal{L}$ cuts for different ALP interactions against ^{208}Tl . Different energy windows are used for both unloaded and Te-loaded scintillator. Appendix E has the corresponding graphs of likelihood separation.

AE has the best separation against ^{208}Tl events, because the 5.5 MeV e^- has an light emission profile the most distinct from $e^-\gamma$ of a ^{208}Tl decay. However, even a $\Delta\mathcal{L}_{\text{cut}}$ with the AE interaction in unloaded scintillator only keeps 36% of signal, whilst removing most of the ^{208}Tl events. Additionally, table 6.2 assumes an equal rate of ALP events to ^{208}Tl events within the ALP energy region of interest.

The timing cuts described in this section **are not** applied in this thesis, because the number of ^{208}Tl events, which reconstruct at energies > 4.5 MeV is expected to be less than 10 events per year [81]. These timing cuts are presented as a possible strategy to employ, if the rate of Thorium is significantly higher than expected

in SNO+. Assuming the Thorium rate is equivalent to Borexino, the dominant background to ALPs is the solar neutrino background, which is an irreducible background for this analysis.

6.4 ALPs in SNO+ unloaded phase

The ALP analysis procedure for SNO+ is relatively simple and applied to all ALP interactions in both the unloaded and Te-loaded scintillator phases. A fiducial volume is defined by the rate, energy and position distributions for external backgrounds. An energy window, for each type of ALP interaction, is defined by the detector response of different ALP interactions. The number of events within that energy window and fiducial volume are counted, with an upper bound placed on a specific ALP interaction rate set using the procedure described in appendix A. For the water phase, a similar analysis is performed but a direction cut with respect to the direction of the Sun, is also applied.

The SNO+ scintillator phase consists of LAB + 2g/L of PPO with a radio-purity assumed to be the same as Borexino: Thorium level of 10^{-18} g/g and Uranium level of 10^{-17} g/g. The energy spectra for inverse Primakoff interaction of ALPs, after a fiducial volume cut of 5.5 m with 1 year of SNO+ scintillator phase, are given in figure 6.8. This figure includes the internal backgrounds but also external backgrounds from γ -rays from the AV, PSUP, outer water and PMTs. Solar neutrinos form the majority of the background to an IP signal in SNO+. Reactor neutrinos can be reduced by delayed neutron tagging [10], but this is not included in this study.

6.4.1 Limits on the inverse Primakoff effect

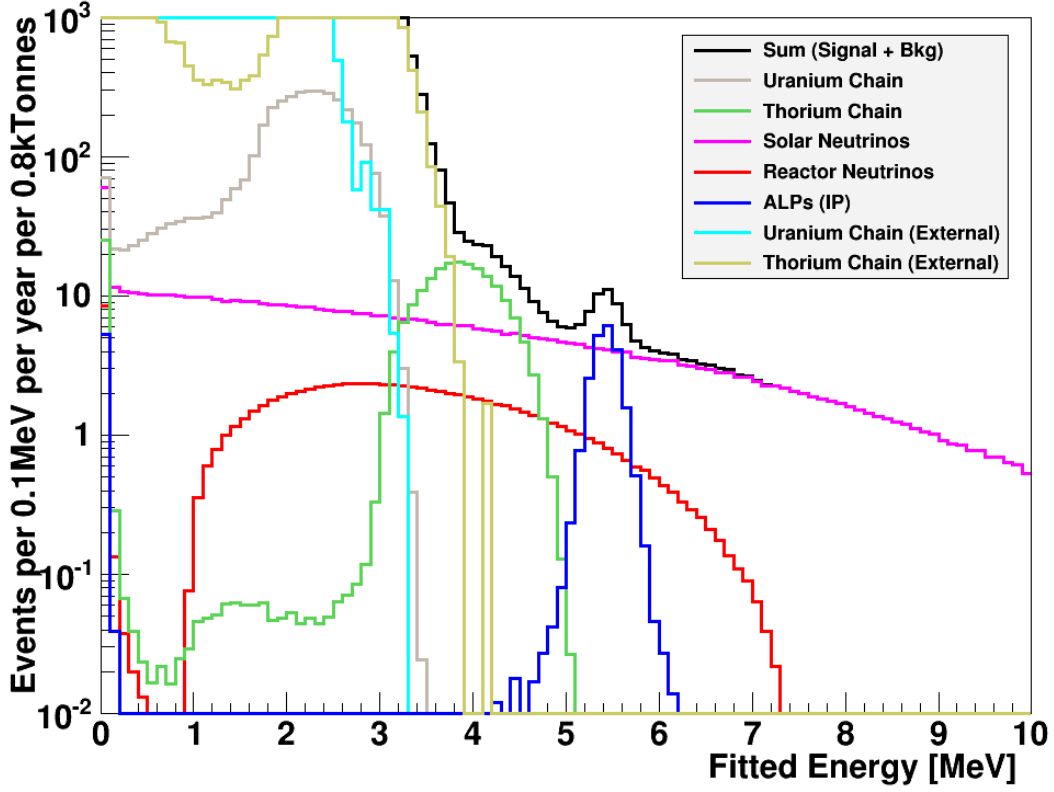


Figure 6.8: Estimated event rate for SNO+ in scintillator phase after 1 year and a fiducial volume cut of 5.5m.

Figure 6.8 shows the energy distribution of simulated events, which reconstruct at $R < 5500$ mm for 1 year of unloaded scintillator. The IP interaction has an energy distribution centred at around 5.2 MeV, where the dominant background to ALPs are solar neutrinos. The same concentration of Thorium as Borexino is assumed for SNO+ unloaded scintillator phase. The IP interaction rate in SNO+ is given by:

$$S_{IP} = \Phi_A \sigma_{IP} N_C T \epsilon_{IP} \quad (6.4)$$

where S_{IP} is the rate of IP interactions (in s), Φ_A is the ALP flux, σ_{IP} is the cross section between a carbon nucleus and an ALP, N_C is the number of carbon atoms and ϵ_{IP} is the efficiency of detecting ALPs in SNO+ via inverse primakoff

conversion. Using the following equations from [71]:

$$\begin{aligned}\Phi_A &= 3.23 \times 10^{10} \times g_{3AN}^2 \\ \sigma_{IP} &= g_{A\gamma}^2 Z^2 \times 1.8 \times 10^{-29}\end{aligned}\tag{6.5}$$

where Z is the atomic number and equation 6.4 can be reduced to:

$$S_{IP} = |g_{A\gamma}^2 \times g_{3AN}^2| \times 6.3 \times 10^{-19} \times Z_C^2 N_C T \epsilon_{IP}\tag{6.6}$$

for the scintillator phase of SNO+. The number of Carbon atoms within a SNO+ fiducial volume of 5.5m can be calculated from the amount of LAB placed into the AV. LAB is a mixture of several different hydrocarbon compounds, such as $C_{15}H_{24}$, with different relative abundancies:

Molecule	Fraction	RAM	No. of C atoms
$C_{15}H_{24}$	0.012	204	3.2×10^{29}
$C_{16}H_{26}$	0.204	218	5.5×10^{30}
$C_{17}H_{28}$	0.432	232	1.2×10^{31}
$C_{18}H_{30}$	0.334	246	8.9×10^{30}
$C_{19}H_{32}$	0.018	260	4.8×10^{29}
		Total	2.68×10^{31}

Table 6.3: The relative fraction of different types of molecules within LAB and the total number of carbon atoms from each of these molecules. A fiducial mass of 0.7 kTonnes of LAB is assumed (the mass of LAB after a fiducial volume cut of $R < 5.5m$ has been taken. The total number of carbon atoms within a fiducial volume is taken as 2.68×10^{31} throughout this thesis.

Using equation 6.6 and the number of carbon atoms (N_C) in the scintillator with:

- $N_C = 2.68 \times 10^{31}$ atoms
- $T(6 \text{ Months}) = 1.58 \times 10^7$ s
- $Z = 6$ for Carbon atoms

the 90% confident limit on the inverse Primakoff effect, $S_{IP}^{90\%}$ for SNO+ scintillator phase is:

$$|g_{3AN} \times g_{A\gamma}| \leq \left(\frac{S_{IP}^{90\%}}{8.9 \times 10^{21} \times \epsilon_{IP}} \right)^{\frac{1}{2}} \quad (6.7)$$

where ϵ_{IP} depends on the detector efficiency for the inverse Primakoff effect and is a function of the chosen energy window. $S_{IP}^{90\%}$ is calculated using the method described in appendix A and the background rates for one year of SNO+ scintillator are given in table 6.4.

Backgrounds	Interactions per year	Source
Solar (after oscillations)	678	SNO B8 Paper
Bi214 (Internal)	4,897	SNO+ Backgrounds [81]
Bi214 (HDR)	4.06×10^7	SNO+ Backgrounds [81]
Bi214 (AV)	1.28×10^6	SNO+ Backgrounds [81]
Tl208 (Internal)	246	SNO+ Backgrounds [81]
Tl208 (HDR)	2.32×10^6	SNO+ Backgrounds [81]
Tl208 (AV)	1.50×10^6	SNO+ Backgrounds [81]
Reactor (after oscillations)	110	I.Coulter PhD Thesis [2]

Table 6.4: Estimated background count after 1 year of SNO+ scintillator phase with a fiducial volume cut of $R < 5.5\text{m}$.

Since this is simulated data for a counting experiment, figure 6.9 shows the statistical ensembles of 1,000 potential experiments with three different energy windows. Since each of the distribution of limits from many different experiments are skewed, their median value is reported for each energy window. This is repeated throughout all the ALP limit setting analysis in this chapter.

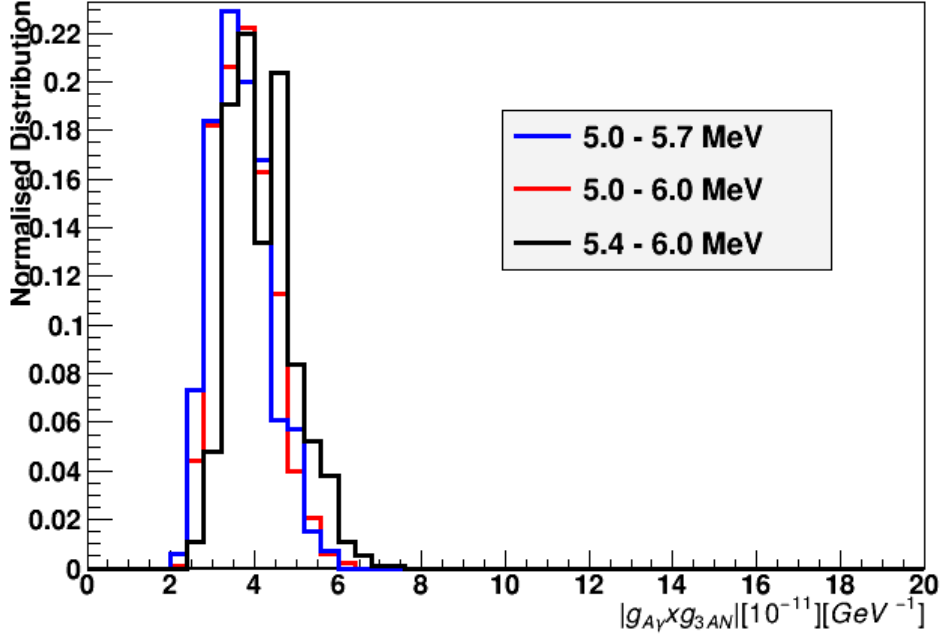


Figure 6.9: Statistical ensemble of 1,000 different potential measurements of $|g_{3AN} \times g_{Ae}|$. This is a Poisson fluctuation of the expected total rate after 6 months of scintillator data.

Energy Window [MeV]	ϵ_{IP}	Exp. Bkg.	$S_{IP}^{90\%}$	$ g_{A\gamma} \times g_{3AN} $
5.0 - 5.7	0.86	46.9	13.4	4.2
5.0 - 6.0	0.87	53.0	19.9	5.1
5.4 - 6.0	0.51	26.0	9.8	4.6

Table 6.5: Summary of the sensitivity to $|g_{A\gamma} \times g_{3AN}|$ with different energy windows. Median values taken from figure 6.9. $|g_{A\gamma} \times g_{3AN}|$ is in units of 10^{-11}GeV^{-1} .

In order to find the optimal energy window, $|g_{A\gamma} \times g_{3AN}|$ is calculated for different energy windows between 4.5 and 6.0 MeV in steps of 0.1 MeV. Table 6.5 shows the best energy window between 5.4 - 6.0 MeV and two energy windows for comparison. The energy window between 5.0 - 6.0 MeV has a higher signal count, but also a higher background count and thus the ALP limit is larger than the window between 5.4 - 6.0 MeV limit. The choice of energy window is biased towards higher energy because the Thorium chain increases the background to an ALP event at lower energies. Using equation 6.7, the upper limit on $|g_{A\gamma} \times g_{3AN}|$

after 6 months of SNO+ scintillator phase with an energy window between 5.0 - 5.7 MeV is:

$$|g_{3AN} \times g_{A\gamma}| \leq 4.2 \times 10^{-11} \text{ GeV}^{-1} \text{ (90\% c.l.)} \quad (6.8)$$

Specifically taking the hadronic (KSVZ) model gives:

$$m_A \times |g_{A\gamma}| \leq 1.5 \times 10^{-12} \quad (6.9)$$

This is only a small improvement against the limits set by Borexino. But this measurement, with only 6 months of SNO+ scintillator phase, would demonstrate that a deeper and larger scintillator experiment can match the current best limits in a shorter time.

The sensitivity to $|g_{A\gamma} \times g_{3AN}|$ is a only small improvement on Borexino, which is potentially due to a slightly different scintillation response of γ -rays in LAB compared to PC used in Borexino. The limit for CCA is calculated in appendix C and tables 6.15 and 6.16 give the ALP limit setting potential for 6 months of SNO+ unloaded scintillator for both $|g_{3AN} \times g_{Ae}|$ and $|g_{A\gamma} \times g_{3AN}|$ respectively. The energy resolution and bias are the dominant systematic uncertainties in this analysis and are discussed in section 6.6.

6.5 ALPs in SNO+ Te-loaded phase

SNO+ is proposed to run in Te-loaded phase for up to 5 years. The primary objective of SNO+ is to search for neutrinoless double beta decay by loading 0.5% (by mass) of natural Tellurium into the scintillator. The loading of Tellurium into the scintillator cocktail increases the amount of quenching and scattering [11], which reduces the energy resolution of the detector. Current simulation estimates of the light yield are ~ 600 Nhits per MeV for pure scintillator and ~ 360 Nhits per MeV for 0.5% Te-loaded scintillator. The radio-purity of different components of the SNO+ Te phase are given in table 6.6.

Component	^{232}Th (g/g)	^{238}U (g/g)
LAB + PPO	6.8×10^{-18}	1.6×10^{-17}
TeA	5.0×10^{-14}	1.0×10^{-13}
BD	3.5×10^{-15}	3.5×10^{-14}

Table 6.6: Purity of U/Th for different components of the scintillator cocktail with 0.5% Te loading taken from [81]. TeA is Telluric acid and BD is butane diol.

6.5.1 Limits on the Compton conversion of ALPs

Figure 6.10 depicts the energy spectrum per year of SNO+ Te-loaded phase, includes the normalisation on CCA events set by Borexino and a fiducial volume cut of 5.5 m has been applied. The rate of ^{208}Tl is greater for SNO+ Te-loaded phase, compared to pure scintillator, because the loading of Tellurium introduces a higher level of Thorium impurities. The CCA signal sits at the end of the ^{208}Tl spectrum, which has a steep gradient at ~ 5 MeV. This could be problematic to an observation of CCA because any further reduction in the energy resolution would lead to a significant reduction in sensitivity to CCA as more ^{208}Tl are ‘smeared’ into the CCA spectrum. Table 6.7 gives the expected background counts per year

for SNO+ Te phase (with 0.5% loading) and are the normalisations in figure 6.10. A fiducial volume cut of 5.5 m is taken, because there are γ -rays from the ^{208}Tl decays from the AV acrylic. It is important to note that the $0\nu\beta\beta$ analysis uses a smaller fiducial volume, because the background rate of ^{208}Tl γ 's at ~ 2.5 MeV (the end point of $0\nu\beta\beta$) is higher and reducing the fiducial volume reduces the background rate of γ 's in the energy window.

Backgrounds	Interactions per year	Source
Solar (after oscillations)	678	SNO B8 Paper
Bi214 (Internal)	390,232	SNO+ Backgrounds [81]
Bi214 (HDR)	4.06×10^7	SNO+ Backgrounds [81]
Bi214 (AV)	1.28×10^6	SNO+ Backgrounds [81]
Tl208 (Internal)	17,780	SNO+ Backgrounds [81]
Tl208 (HDR)	2.32×10^6	SNO+ Backgrounds [81]
Tl208 (AV)	1.50×10^6	SNO+ Backgrounds [81]
Reactor (after oscillations)	110	I.Coulter PhD Thesis [2]

Table 6.7: Estimated backgrounds counts per year of SNO+ Te-loaded scintillator phase including external backgrounds and internal backgrounds for SNO+ experiment. Oscillations have been applied to both reactor and solar neutrinos.

Figure 6.10 depicts the energy distribution for 1 year of Te-loaded scintillator after a fiducial volume cut of $R < 5500$ mm. The main background to the CCA interaction are solar neutrinos, but the tail from the Thorium chain (^{208}Tl decays) overlaps with ALP events, which reconstruct at lower energies.

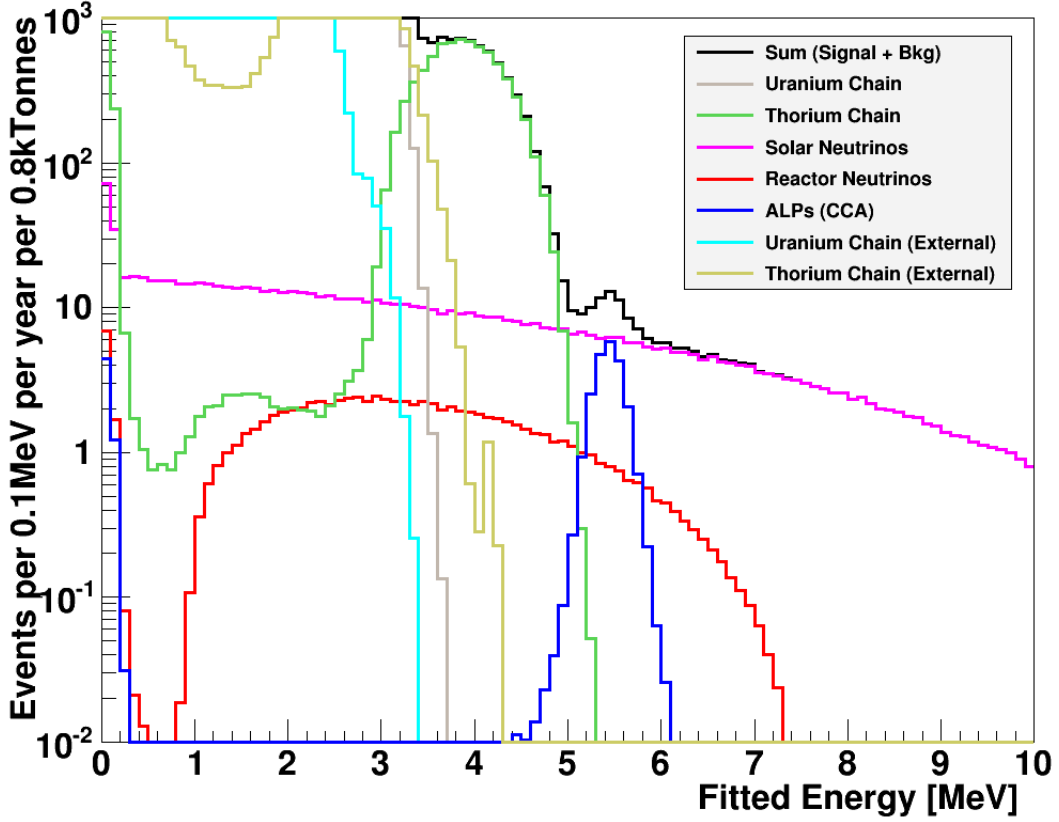


Figure 6.10: Energy spectrum from 0.5% Te-loaded scintillator for one year of SNO+ Te phase. The CCA normalisation is from [71]. A fiducial volume of $R = 5.5\text{m}$ has been applied. No coincidence timing cuts have been applied.

Using equation 5.6 with the CCA interaction and the statistical method described in appendix A, the limit for the optimal energy window (and two comparative energy windows) is given in table 6.8.

Energy Window [MeV]	Efficiency	Exp. Bkg.	$S_{CC}^{90\%}$	$ g_{3AN} \times g_{Ae} $
5.0 - 5.7	0.72	365.4	61.6	5.1
5.0 - 6.0	0.73	375.6	148.3	5.3
5.4 - 6.0	0.44	160.9	83.1	3.4

Table 6.8: Summary of the sensitivity to $|g_{3AN} \times g_{Ae}|$ with CCA in different energy windows for 5 years of Te-loaded scintillator. Median values are taken from figure 6.10

The optimal energy window choice from 5.4 - 6.0 MeV gives a limit of $|g_{3AN} \times g_{Ae}|$

$< 3.4 \times 10^{-13}$ and is slightly smaller and higher in energy than the CCA interaction in pure scintillator (see appendix C). This is due to the loading of Tellurium into the SNO+ detector, which increases the concentration of Thorium by an order of magnitude. If the concentration of Thorium was much higher than expected in [81], timing cuts considered in section 6.3 could be used to statistically separate ALP-like from ^{208}Tl -like events.

6.5.2 Limits on the inverse Primakoff effect

The same analysis can be applied to the inverse Primakoff effect for Te-loaded scintillator and the energy distributions after a fiducial volume cut of $R < 5500$ mm is given in figure 6.11. The energy distribution of IP (in Te-loaded scintillator) has a marginally larger tail at lower energies, but has a very similar distribution to the CCA interaction. The rate of inverse primakoff interactions in Te-loaded scintillator can be calculated by adapting equations 6.4 and 6.5:

$$S_{IP} = |g_{A\gamma}^2 \times g_{3AN}^2| \times 6.3 \times 10^{-19} \times T\epsilon_{IP} \times (Z_C^2 N_C + Z_{Te}^2 N_{Te}) \quad (6.10)$$

Taking a fiducial volume of $R < 5.5\text{m}$ and with a 0.3% loading (by mass) of Tellurium into the scintillator:

- Mass of Te in SNO+ (within the fiducial volume of $R < 5.5\text{m}$ at 0.3% loading by mass) = 3.1×10^6 g
- Number of Te atoms = 1.5×10^{28} atoms
- Number of C atoms = 2.68×10^{31} atoms (see table 6.3)
- $T(5 \text{ years}) = 1.9 \times 10^8$ s

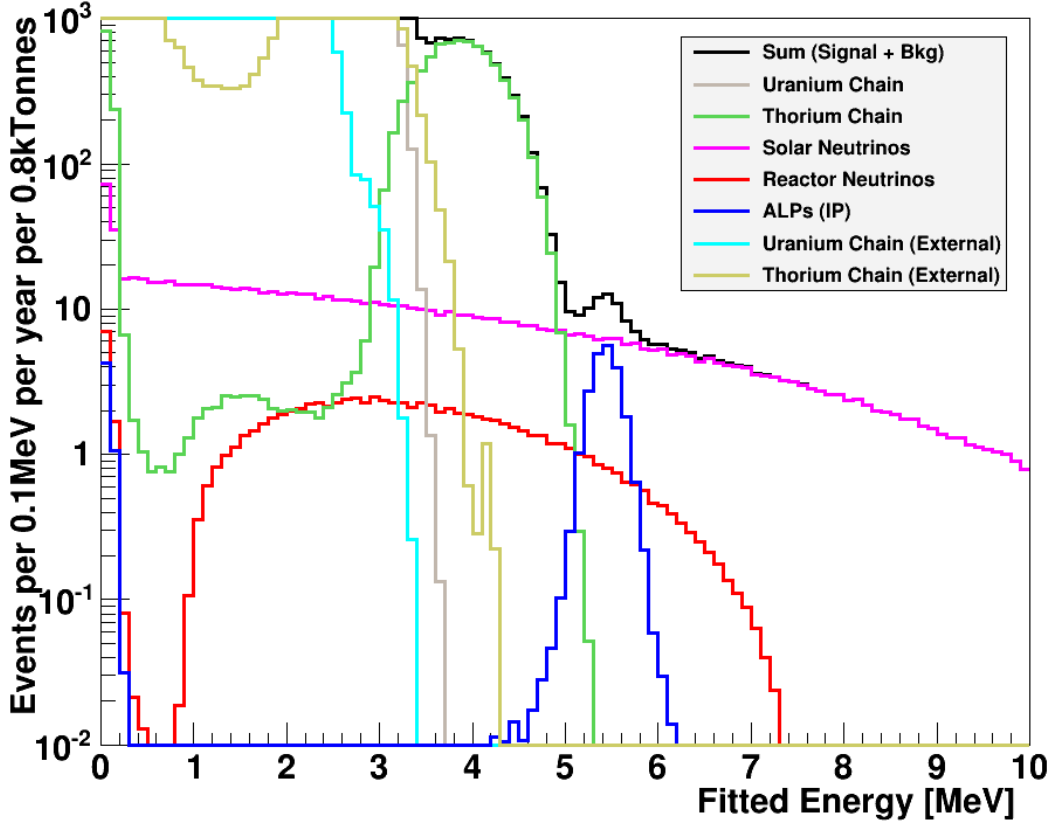


Figure 6.11: Energy spectrum from one year of SNO+ Te phase. The IP signal is normalised to the current limits set by [71]. A fiducial volume of $R=5.5\text{m}$ has been applied. No coincidence timing cuts have been applied.

Using equation 6.10 and setting a 90% Bayesian confident limit on the inverse Primakoff effect gives:

$$|g_{3AN} \times g_{A\gamma}| \leq \left(\frac{S_{IP}^{90\%}}{1.2 \times 10^{23} \times \epsilon_{IP}} \right)^{\frac{1}{2}} \quad (6.11)$$

where ϵ_{IP} depends on the detector efficiency for the inverse Primakoff effect. $S_{IP}^{90\%}$ is calculated using the analysis described in appendix A and the normalisation of backgrounds given in figure 6.11 (but scaled to 5 years of SNO+ Te Phase).

Energy Window [MeV]	Efficiency	Exp. Bkg.	$S_{IP}^{90\%}$	$ g_{A\gamma} \times g_{3AN} $
5.0 - 6.0	0.71	369.7	71.2	2.9
5.4 - 6.0	0.41	162.7	75.9	3.9
5.0 - 6.1	0.71	378.9	75.1	3.0

Table 6.9: Median values taken from the statistical ensemble of the inverse primakoff interaction of ALPs, given in figure 6.11. The units of $|g_{A\gamma} \times g_{3AN}|$ are 10^{-11}GeV^{-1} .

Table 6.9 gives best limits from 5 years of SNO+ Te-loaded scintillator phase with energy window between 5.0 - 6.0 MeV:

$$|g_{3AN} \times g_{A\gamma}| \leq 2.9 \times 10^{-11} \text{ GeV}^{-1} \text{ (90\% c.l.)} \quad (6.12)$$

Specifically taking the hadronic (KSVZ) model gives:

$$m_A \times |g_{A\gamma}| \leq 1.6 \times 10^{-11} \text{ (90\% c.l.)} \quad (6.13)$$

6.5.3 Limits on the Axio-electric effect

This section outlines the sensitivity of SNO+ to $|g_{Ae} \times g_{3AN}|$ with the AE effect. This current limit is given by BGO [77], which is a small bolometer experiment using around 8kg of Bismuth crystals. The AE signal in one year of SNO+ Te phase is given in figure 6.12 and is clearly a significant improvement over the current limits. BGO is a much smaller experiment, which comes at the expense of signal detection but has almost no background to an AE signal [77]. Additionally, the AE effect has a Z^5 dependence that also favours higher loadings of Tellurium into SNO+ (see table 5.1).

Figure 6.12 shows an AE signal that is large and shifted slightly to high ener-

gies. The AE effect deposits energy in the scintillator via one electron, whereas CCA deposits energy via an electron and a γ -ray. There is a slightly higher light yield per MeV in the AE interaction, as electrons have a slightly higher light yield than γ -rays in scintillator. This pushes the AE signal further away from the ^{208}Tl spectrum.

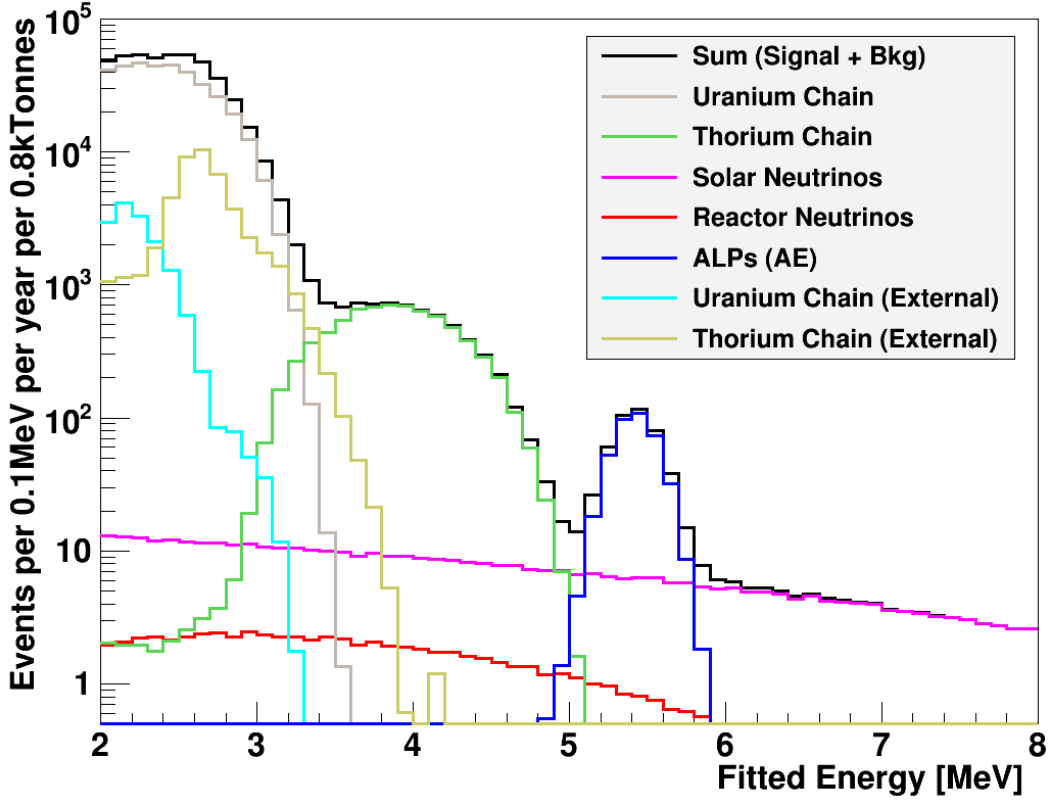


Figure 6.12: Energy spectrum from one year of SNO+ Te phase. The ALP signal is due to the axioelectric effect with the upper coupling limits given in [77]. A fiducial volume of $R = 5.5\text{m}$ has been applied. No coincidence timing cuts have been applied.

The equation for the Axioelectric effect is given by:

$$S_{AE} = \Phi_A \sigma_{AE}(N_C, N_{Te}) T \epsilon_{AE} \quad (6.14)$$

where Φ_A is given in equation 6.5 and σ_{AE} written as :

$$\sigma_{AE} = 1.6 \times 10^{-32} \times g_{Ac}^2 Z^5 \quad (6.15)$$

using equation 2 from [82] where the ALP mass is assumed to be less than 1eV.

The 90% Bayesian confident limit on the axio-electric effect, $S_{AE}^{90\%}$ is:

$$S_{AE}^{90\%} = 5.1 \times 10^{-22} \times g_{Ae}^2 \times g_{3AN}^2 \times [N_C Z_C^5 + N_{Te} Z_{Te}^5] T \epsilon_{AE} \quad (6.16)$$

and given that 0.5% loading of SNO+ Te phase has:

- $N_C = 2.68 \times 10^{31}$ atoms
- $N_{Te} = 1.5 \times 10^{28}$ atoms
- $T(5 \text{ Years}) = 1.58 \times 10^8$ s

can be combined to give:

$$|g_{Ae} \times g_{3AN}| \leq \left(\frac{S_{AE}^{90\%}}{1.0 \times 10^{24} \times \epsilon_{AE}} \right)^{\frac{1}{2}} \quad (6.17)$$

where ϵ_{AE} depends on the detector efficiency for the axio-electric effect.

Energy Window [MeV]	Efficiency	Exp. Total.	$S_{AE}^{90\%}$	$ g_{3AN} \times g_{Ae} $
5.0 - 6.0	0.73	1,877	126.9	1.3
5.4 - 6.0	0.41	550	35.8	0.9
5.0 - 5.7	0.72	1,710	38.2	0.7

Table 6.10: Median values of each distribution in for an ensemble of 1,000 experiments. The units of $|g_{3AN} \times g_{Ae}|$ are 10^{-11} .

Using table 6.10, the best limit for the ALP coupling with AE is:

$$|g_{Ae} \times g_{3AN}| \leq 0.7 \times 10^{-11} \text{ (90\% c.l.)} \quad (6.18)$$

6.6 Systematic uncertainties for ALPs in SNO+

The signal for ALPs is predicted to be between 4.5 - 6.0 MeV of visible energy, depending on ALP interaction, during both the unloaded and Te-loaded scintillator phases of SNO+. The following section discusses several systematic uncertainties that could affect the limit setting potential for ALPs and proposes actions to take during the operation of SNO+.

Energy resolution

^{208}Tl decays from the Thorium chain have a Q-value of 5.0 MeV, whilst very few events reconstruct with an energy greater than 5.0 MeV, a poor energy resolution can increase the number of events that reconstruct within the ALP energy window. This is due to the steep energy distribution of ^{208}Tl decays at 5 MeV, in both unloaded and Te-loaded scintillator, which can ‘smear’ a significant number of events to higher energies when the energy resolution is reduced. This can overlap onto the ALP signal and could reduce the limit setting potential of SNO+. The solar neutrino energy spectrum is flat at ~ 5.0 MeV, thus a reduction of the energy resolution has little impact upon the number of events at ~ 5.0 MeV. The energy resolution can be measured at around $\sim 4.5 - 6.0$ MeV by using the ^{16}N calibration source. ^{16}N decay produces a mono-energetic γ -ray at 6.1 MeV and is a tagged source. The energy resolution at 6.1 MeV can be extracted by fitting a Gaussian curve to the energy distribution of tagged ^{16}N events and extracting the sigma of the distribution. The energy distribution of ^{16}N decays should also be centred on 6.1 MeV as a cross-check for any biases in the energy reconstruction. This analysis will also have to be performed separately for the water, unloaded and Te-loaded scintillator phases separately.

Position resolution

The position resolution is important for an ALP analysis, because it is used to reconstruct the energy of an event. The reconstructed position can also be verified at 6 MeV, by comparing the reconstructed position of ^{16}N decays against the deployed ^{16}N source. The position reconstruction should also be verified, as a check that external backgrounds have not reconstructed within the fiducial volume.

6.7 LUN experiments

The latter half of this chapter explores the detection of ALPs with other Large Underground Neutrino (LUN) experiments. These are explored to reinforce the ALP detection potential of SNO+, but also to explore the wider potential of detecting ALPs with LUN experiments. Two classes of LUN experiment are explored: water Cherenkov and liquid scintillator detectors. The following sections estimate the sensitivity of different LUN experiments, using a simple scaling law described in appendix A, for: Borexino in section 6.9, SNO in section 6.10, Super Kamiokande in section 6.11 and Hyper Kamiokande in section 6.12.

6.7.1 Sensitivity to $|g_{3AN} \times g_{Ae}|$

LUN experiments are sensitive to g_{3AN} via the production of ALPs in the Sun and g_{Ae} via their interaction in a detector. Both liquid scintillator and water Cherenkov detectors are sensitive to ALP coupling to electrons. This section considers the best limit on $|g_{3AN} \times g_{Ae}|$ for Compton conversion of ALPs (CCA) and for the axio-electric effect (AE). The number of events due to Compton conversion of ALPs (S_{CCA}):

$$S_{CCA} = g_{Ae}^2 \times g_{3AN}^2 \times 1.4 \times 10^{-14} T \epsilon_{CCA} N_C \quad (6.19)$$

6.7.2 $|g_{3AN} \times g_{Ae}|$ sensitivity with CCA

Figure 5.2 shows the energy distribution and differential cross section of the electron and γ -ray from CCA. The differential cross section is larger between ~ 0.8 - 0.98 in $\cos(\theta_{SUN})$, where the angle θ_{SUN} is the angle between the incoming solar ALP and outgoing electron (see figure 6.1). This corresponds to an electron with between 2.5 - 4.5 MeV of energy and a γ particle with between 1 - 3 MeV of energy. The energy deposition for CCA is different in different types of LUN experiment:

- in a water Cherenkov detection:

- the electron is observed within water as it produces a Cherenkov cone, which helps determine its outgoing direction.
- the γ -ray is observed within water by Compton scattering off an electron (or several electrons). This produces a lower relative light yield per MeV (compared to an electron) and gives a downwards bias on the energy reconstruction of these events.
- in a liquid scintillator detector:
 - the isotropic scintillation light produced by the electron and the γ particle both Compton scatter within the scintillator. Thus, the light yield per MeV is much higher than in water, there is no intrinsic downwards bias in the energy reconstruction and the energy resolution is comparatively higher.

The electron from CCA determines the direction reconstruction of the Cherenkov cone. The resolution of the direction reconstruction of the electron determines how well CCA events can be separated from isotropic backgrounds. In SNO+ water phase, this reduces isotropic backgrounds by almost an order of magnitude, whilst keeping $\sim 80\%$ of signal events (see appendix B). On the other hand, the γ -ray Compton scatters off an electron giving it ~ 1 -2 MeV of kinetic energy. This secondary electron can produce a small Cherenkov cone, but is a challenging signal to observe (see appendix D).

For any LUN experiment, the sensitivity to ALPs is improved with a better energy (or direction) resolution, larger fiducial volume or lower background levels. In both water Cherenkov and liquid scintillator LUN experiments, higher levels of ^{208}Tl from the Thorium chain and ^{214}Bi from the Uranium chain can reduce the sensitivity to ALP couplings. Figures 6.14 and 6.13 depict the number of scintillation and Cherenkov photons for a general 1kTonne liquid scintillator and water

Cherenkov experiment respectively after 1 year of running. These figures make no assumptions about the detector geometry, external backgrounds, photocathode coverage, optical properties or event reconstruction. These provide a general approach to considering LUN experiments and considering detector properties that might give high levels of sensitivity to ALP couplings.

The energy distribution of CCA for a liquid scintillator detector in figure 6.14 has much narrower peak than in figure 6.13, due to the higher energy resolution in liquid scintillator. In both cases, solar neutrinos are the dominant background but ^{214}Bi is a large background in only water detectors. ^{208}Tl is a background in both types of detector, as it has a relatively large Q-value of 5 MeV compared against ~ 5.5 MeV of CCA.

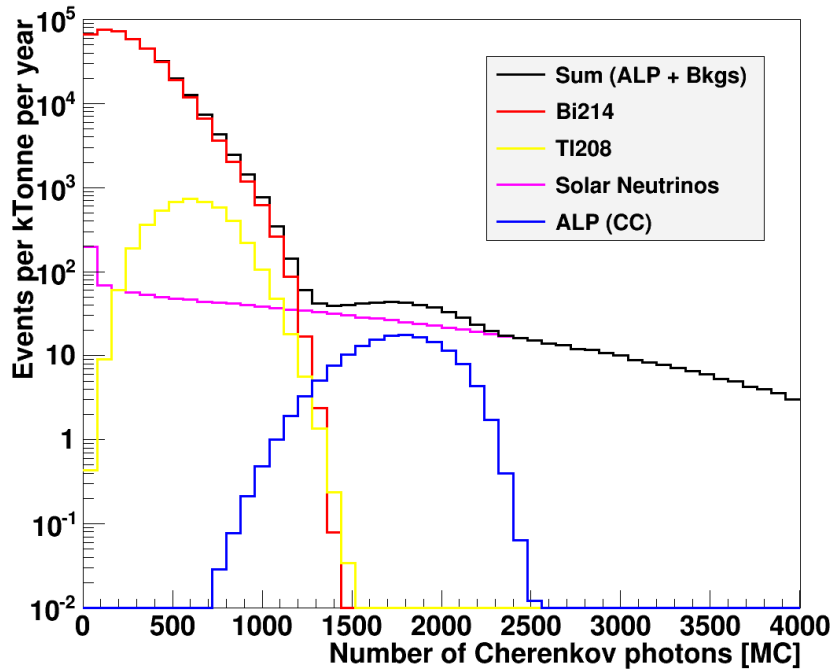


Figure 6.13: Number of (MC) Cherenkov photons produced in a water Cherenkov detector for Compton conversion of ALPs and internal backgrounds. The radio-purity: Thorium level of 10^{-16} g/g and Uranium level of 10^{-15} g/g is the same as SNO [83]. No external backgrounds are included.

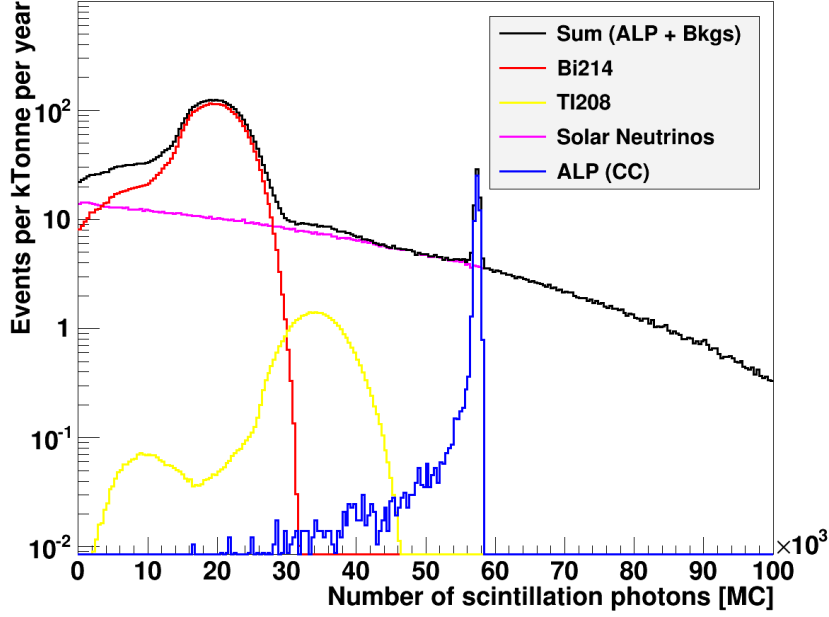


Figure 6.14: Number of (MC) scintillation photons produced in a liquid scintillator detector for CC with only internal backgrounds included. The radio-purity: Thorium level of 10^{-18} g/g and Uranium level of 10^{-17} g/g is the same as Borexino [71]. No external backgrounds are included.

6.7.3 $|g_{3AN} \times g_{Ae}|$ sensitivity with AE

The current best limit on $|g_{3AN} \times g_{Ae}|$ with the axio-electric effect is set by BGO [77]. The axio-electric effect has a cross section that is proportional to Z^5 , which strongly amplifies the cross section with high- Z nuclei such as Bi ($Z=83$) and Tellurium ($Z=52$). SNO+ will load Tellurium into its scintillator cocktail and can substantially improve the current limit due to the larger fiducial volume of SNO+ in the Te-loaded phase. The increase in event rate per year for different % Te-loadings for SNO+ are given in table 5.1. The proposed Gadolinium ($Z=64$) loading into Super Kamiokande [84] could also improve upon the BGO limit. However, the axio-electric effect doesn't conserve directional information and might be swamped by a significant number of backgrounds within the optimal energy window in Super Kamiokande. This isn't true for CCA as the directional information can be used to reduce the background level by an order of magnitude.

6.8 Sensitivity to $|g_{3AN} \times g_{A\gamma}|$

This section will show how liquid scintillator LUN experiments are sensitive to $|g_{3AN} \times g_{A\gamma}|$. Water Cherenkov LUN experiments are not sensitive to this interaction because both the inverse Primakoff (IP) effect and ALP decay produce γ -ray's, which do not conserve directional information and have a lower light yield per MeV than in scintillator. IP converts an ALP into a γ particle with 5.5 MeV, in the presence of a nucleus with an atomic number Z . The number of events from inverse primakoff S_{PC} [71]:

$$S_{IP} = \Phi_A \sum_i \sigma_{IP}(Z_i) N_i T \epsilon_{IP} \quad (6.20)$$

$$S_{IP} = g_{A\gamma}^2 \times g_{3AN}^2 \times 6.3 \times 10^{-19} \times T \epsilon_{IP} \times \sum_i Z_i^2 N_i$$

where $\sigma_{IP}(Z_i)$ is the inverse primakoff cross section for a nucleon of species i with atomic number Z_i , N_i is the number of nucleon species i , T is the time of exposure in seconds and ϵ_{IP} is the detection efficiency for inverse Primakoff effect. This interaction has a Z^2 dependence, which can be favourable to high- Z loaded scintillators such as SNO+.

6.9 Borexino

Borexino is a large scintillation experiment with an active mass of 278 tons of pseudocumene (C_9H_{12}), housed in an inner nylon vessel uniformly surrounded by over 2,212 8-inch PMTs. It is situated within the LNGS lab, which is placed within a mountain at Gran Sasso underneath 1.4 km of rock [71]. Borexino also has a muon veto consisting of an outer volume of water with 208 outward looking PMTs, which is depicted in figure 6.15. Borexino used 1,2,4-Trimethylbenzene (PC) as the main scintillator with 1.5g/L of PPO as the primary fluor and has an

active volume of 278 tonnes.

The primary goal of Borexino was to observe solar neutrinos from ${}^7\text{Be}$ neutrinos via the reaction:



which has a mono-energetic peak of 0.86 MeV [85].

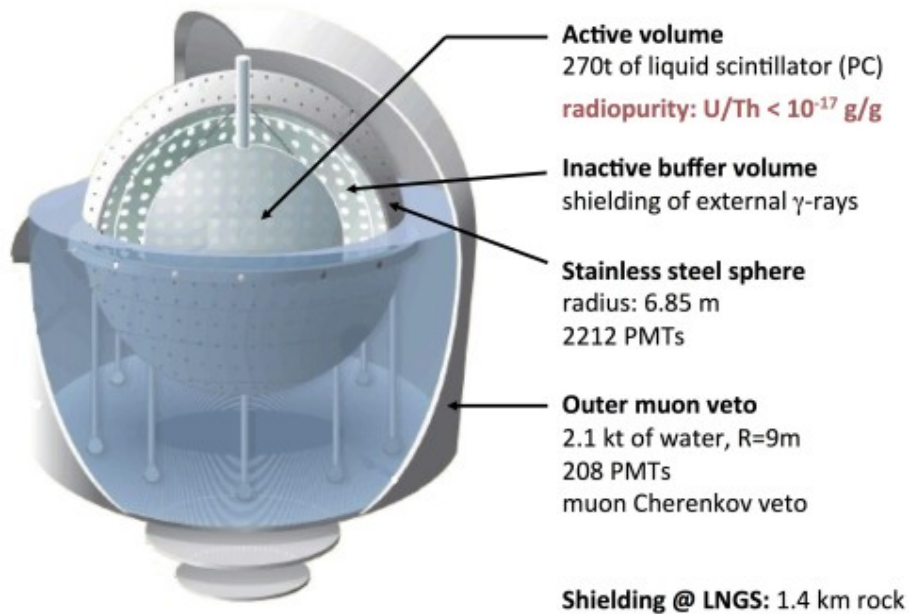


Figure 6.15: Diagram of the Borexino experiment. The active volume consists of liquid scintillator within a nylon vessel with inactive buffer shielding and over 2000 PMTs. Borexino is contained within a stainless steel vessel and surrounded by a outer muon veto. This image is taken directly from <http://www.staff.uni-mainz.de/wurmm/borexino.html>

Borexino analysis cuts included[71]:

- A cut of 2.2ms applied from muon events observed in the external water shielding. The majority of muons passing through Borexino, deposit some energy in the external water as Cherenkov photons. These are observed by the outward looking PMTs.
- A cut of 6.5s after a muon crossing of the active volume. Muons can activate

short lived radioactive isotopes, such as ${}^8\text{B}$ with a half-life of 1.1s and ${}^8\text{Li}$ with a half life of 1.2s.

- A fiducial volume cut (of a sphere with radius 3.02 m) is applied to reduce the number of 2.6 MeV γ 's from the radioactive decay of ${}^{208}\text{Tl}$ within the PMTs.

The dominant background against ALP detection for Borexino is from the internal Thorium within the scintillator. ${}^{208}\text{Tl}$ decays to ${}^{208}\text{Pb}$ via a beta-decay with an endpoint of 2.4 MeV and a total energy released of 4.99 MeV with associated gammas.

Borexino placed 90% confidence on the Compton conversion of ALPs, $S_{90\%} \sim 0.013$ counts/(100t day) [71]. Borexino has a number of electron targets, $N_e = 9.17 \times 10^{31}$ in its fiducial volume, a detector live-time of $T = 4.63 \times 10^7\text{s}$ and a CCA detection efficiency $\epsilon = 0.358$ [71]. Using equation 5.6 and assuming $(p_A/p_\gamma)^3 \approx 1$ and $m_A < 1$ MeV gives [71]:

$$|g_{Ae} \times g_{3AN}| \leq 5.5 \times 10^{-13} \text{ (90\% c.l.)} \quad (6.22)$$

Borexino also placed a limit on the coupling of ALPs to photons using the Inverse Primakoff (IP) interaction. Using equations 5.3 and 6.20 gives a limit of $|g_{3AN} \times g_{A\gamma}|$ [71]:

$$|g_{3AN} \times g_{A\gamma}| \leq 4.6 \times 10^{-11} \text{ GeV}^{-1} \text{ (90\% c.l.)} \quad (6.23)$$

6.10 SNO (all phases)

SNO is the parent experiment to SNO+ and shares almost all of its geometric features, except the hold down ropes. The primary goal of SNO was to understand the solar neutrino problem and detected solar neutrinos through three interactions

[83]:

$$\begin{aligned}
 \nu_x + e^- &\longrightarrow \nu_x + e^- \quad (\text{ES}) \\
 \nu_e + d &\longrightarrow p + p + e^- \quad (\text{CC}) \\
 \nu_x + d &\longrightarrow p + n + \nu'_x \quad (\text{NC})
 \end{aligned} \tag{6.24}$$

For both the elastic scattering (ES) and charged current (CC) interactions, the electrons are detected directly through the Cherenkov light produced in water. The neutrons from the neutral current (NC) interaction are detected through the de-excitation of γ 's as a result of their capture on another nucleus. SNO Phase I was dominated by neutron captures on deuterium which releases a 6.25 MeV γ [83] and indirectly detected via electrons in the cascade. The detection efficiency of the neutral current interaction was significantly increased in SNO Phase II as 2 tonnes of NaCl was added to the D₂O. ³⁵Cl nuclei have a much higher cross section than deuterium and release a γ at 8.6MeV [83]. SNO Phase III had an energy threshold above 6.0 MeV, which significantly reduces any sensitivity to ALPs and is not considered in this thesis.

Figures 6.16 show the fitted energy spectra for SNO Phase I. These plots have been taken from publicly available data in [23] and [83] respectively. Using the SNO+ water simulation, as a proxy, the efficiency of detecting ALPs in SNO, ϵ_{SNOI} with an 4.5 - 6.0 MeV is 0.384. A directional cut of $\cos(\theta_{\text{sun}}) > 0.8$, can also reduce isotropic backgrounds by an order of magnitude, whilst only keeping $\sim 80\%$ of the ALP signal (and solar neutrino signal). This energy cut is applied because it represents an approximate 1σ fluctuation about 5.5 MeV. The energy spectrum for Compton conversion of ALPs is given in Appendix B.1.

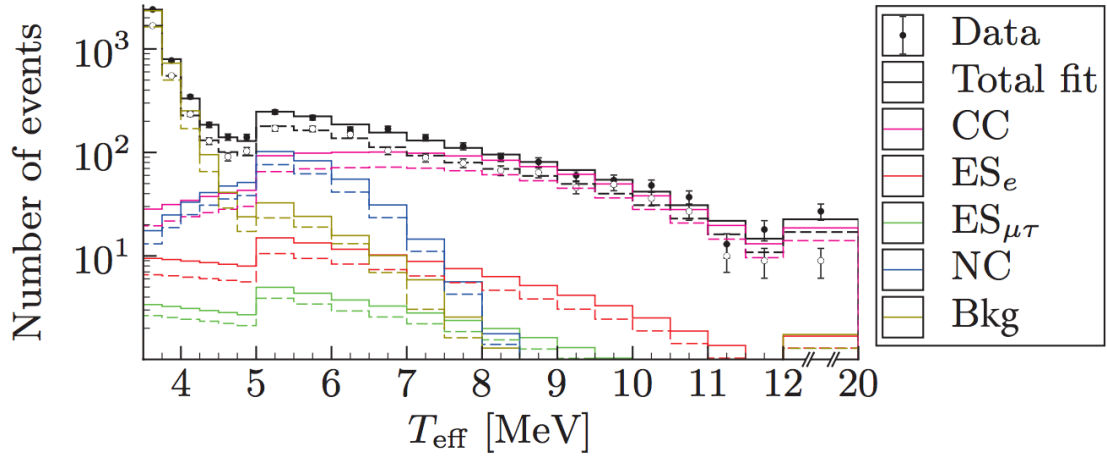


Figure 6.16: Energy spectrum of SNO phase I fitted for different components of the energy spectrum. ES_e and $ES_{\mu,\tau}$ are the elastic scattering events from solar neutrinos, CC events are the charged current events from solar neutrinos, NC are the neutral current events from solar neutrinos, Bkg events are the summation of external and internal backgrounds in the detector such as ^{208}Tl . The solid lines are measured during the night and dashed lines are from measured during the day. This figure is figure 11 of [23].

Background	Extracted Count	Count (after cuts)
Internal & External Bkgs	6,162	83
CC	982	59
NC	963	59
ES	259	137
Total	8,365	337

Table 6.11: SNO phase I backgrounds extracted from figure 12 of [23]. The event count is manually extracted from the figure 6.16. The count is given as the number of background events, after an estimated energy cut between 4.5-6.0 MeV and directional cut with $\cos(\theta) > 0.8$, where θ is the angle between the direction of the Sun and the reconstructed direction of the event. The background count is taken over the entirety of SNO Phase I, which had a lifetime of 312.9 days [83] and equates to a 0.6kTonne-yr exposure.

The SNO Phase I data had a live-time of 312.9 days [83], which equates to a 0.6kTonne-yr exposure with 337 background counts. Borexino had an exposure of 0.146 kTonne-yrs with ~ 10 background counts in the same region of interest and an efficiency of 0.358 [71]. Using equation A.6, an estimated sensitivity relative to

Borexino is:

$$\frac{\text{SNO Phase I}}{\text{Borexino}} = \sqrt{\frac{\epsilon_{SNOI}}{\epsilon_{BOR}} \times \frac{\rho_{SNOI}}{\rho_{BOR}} \times \sqrt{\frac{B_{BOR}}{B_{SNOI}}}} \quad (6.25)$$

$$\frac{\text{SNO Phase I}}{\text{Borexino}} \sim \sqrt{\frac{0.384}{0.385} \times \frac{0.6}{0.146} \times \sqrt{\frac{10.0}{337.0}}} = \sqrt{0.76} = 0.89$$

Background	Extracted count	Event count (after cuts)
Internal & External Bkgs	12,594	144
CC	2,322	137
NC	1,413	86
ES	376	199
Total	16,705	566

Table 6.12: SNO Phase II backgrounds extracted manually from figure 12 of [23]. The count is given as the number of background events after an estimated energy cut between 4.5-6.0 MeV and directional cut with $\cos(\theta) > 0.8$. The background count is taken over the entirety of SNO Phase II, which had a lifetime of 398.6 days [83] and equates to a 0.76kTonne-yr exposure.

The backgrounds to ALPs in SNO are similar to Borexino with internal backgrounds from Uranium/Thorium, solar neutrinos and external sources of Uranium/Thorium (from the AV, the hold up ropes, the PSUB and from the PMTs themselves). SNO also observes neutral current events in both Phase I and Phase II, which contribute a background to the ALP signal that is not present in Borexino. Applying the same analysis for SNO Phase II data, which has a live-time of 398.6 days [83] and equate to a 0.76kTonne-yr exposure with 566 background counts (after analysis cuts). Using equation A.6 the estimated sensitivity relative

to Borexino is:

$$\begin{aligned} \frac{\text{SNO Phase II}}{\text{Borexino}} &= \sqrt{\frac{\epsilon_{\text{SNOII}}}{\epsilon_{\text{BOR}}} \times \frac{\rho_{\text{SNOII}}}{\rho_{\text{BOR}}} \times \sqrt{\frac{B_{\text{BOR}}}{B_{\text{SNOII}}}}} \\ \frac{\text{SNO Phase II}}{\text{Borexino}} &= \sqrt{\frac{0.384}{0.385} \times \frac{0.76}{0.146} \times \sqrt{\frac{10.0}{566.0}}} = \sqrt{0.74} = 0.86 \end{aligned} \quad (6.26)$$

Combining SNO Phase I & Phase II data gives:

$$\begin{aligned} \frac{\text{SNO Phase I \& II}}{\text{Borexino}} &\sim \sqrt{\sqrt{\left(\frac{\text{SNO Phase I}}{\text{Borexino}}\right)^2 + \left(\frac{\text{SNO Phase II}}{\text{Borexino}}\right)^2}} \\ &= \sqrt{0.76^2 + 0.74^2} = \sqrt{1.06} = 1.03 \end{aligned} \quad (6.27)$$

The combination of SNO Phase I & SNO Phase II gives a sensitivity that is comparable to the current limit set by Borexino. SNO Phase I & II had higher background levels (to an ALP signal), due to elastic scattering events of D₂O and ³⁵Cl targets. However, this is offset by the increased exposure of these phases and the directional cut that can be applied in SNO as a water Cherenkov detector.

6.11 Super Kamiokande

Super-Kamiokande (SK) is a 50 kTonne water Cherenkov detector, in a stainless steel tank, situated in Kamioka Observatory below the peak of Mt. Okenoyama near Kamioka, Japan with around 1km of an overburden of rock. The tank is a cylinder that is 41.6 m high, 39.3 m in diameter and divided into the inner detector (ID) and the outer detector (OD)[22]. The inner surface of the ID (32.5 kTon) is lined with over 11,000 inward facing 20 inch Hamamatsu R3600 PMTs with over 40% cathode coverage[22]. The remainder of the ID surface is covered with an opaque sheet, to reduce photo reflection and provide an optical separation between the ID and the OD. The OD is lined with over 1,800 outward facing 8

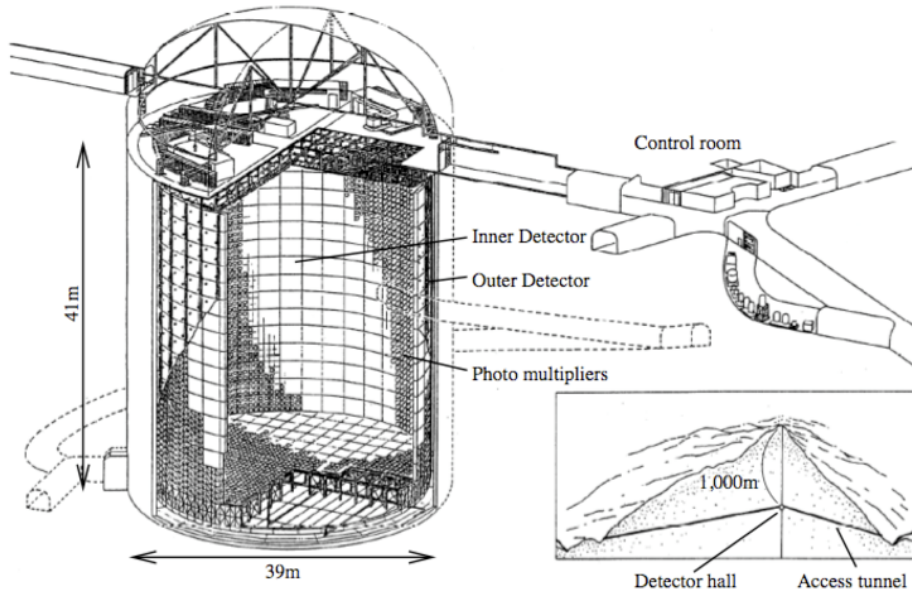


Figure 6.17: Schematic of the Super Kamiokande experiment.

inch PMTs, and operates as a muon veto for events entering from the OD into the ID [22]. One of the main aims of SK was to measure the deficit in solar (electron) neutrinos.

There are many similarities between the backgrounds to an ALP signal in SK and in SNO. In both experiments, there are a significant amount of γ particles from the PMTs, which determine the trigger threshold and data rate. Both of these backgrounds can be removed by applying a directional cut with respect to the direction of the Sun. The event count per day is give by the SK collaboration in [22] (see figure 6.18).

Extracting the number of events with $\cos(\theta_{Sun}) > 0.8$, is equivalent to the performing an ALP directional cut (with a slightly larger than desired energy window). The extracted number of backgrounds as well as information about SK-I is given in table 6.13. Assuming a similar energy distribution to SNO+ water phase for

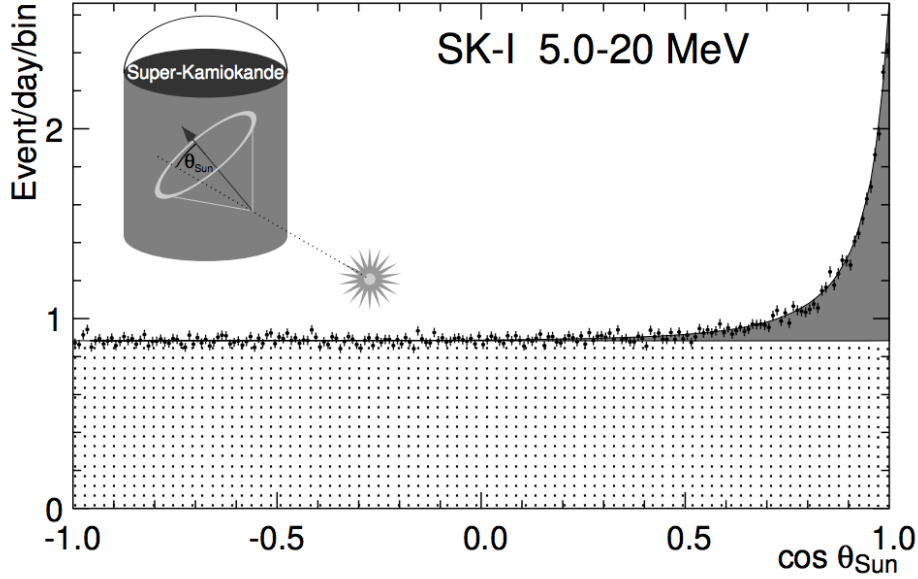


Figure 6.18: Super Kamiokande directional distribution at 5.0 - 20.0 MeV, this includes all the events observed per day at different angles of θ_{SUN} . This figure is taken directly from figure 40 of [22].

SK-I Live time (days) [taken from [22]]	1,488.6
SK-I Fiducial Vol. (ktonnes) [taken from [22]] [ρ_{SK}]	22.5
Background count per day (after cuts)	28.7
Efficiency of detecting ALPs [ϵ_{SK}]	0.243
SK-I background count (after cuts) [B_{SK}]	42,700

Table 6.13: Summary of the information for SK-I that is used to estimate the ALP sensitivity in SK-I. The number of backgrounds (after cuts) is extracted from figure 6.18, where this is an energy cut of 5.0 - 20.0 MeV combined with a directional cut of $\cos(\theta_{\text{sun}}) > 0.8$

Compton conversion of ALPs (see appendix B.1), the efficiency between 5.0-20.0 MeV is 0.243 (after analysis cuts). Thus, using equation A.6 the estimated sensitivity of Super Kamiokande from SK-I is given as:

$$\frac{\text{SK}}{\text{Borexino}} = \sqrt{\frac{\epsilon_{SK}}{\epsilon_{\text{BOR}}} \times \frac{\rho_{SK}}{\rho_{\text{BOR}}} \times \sqrt{\frac{B_{\text{BOR}}}{B_{SK}}}} \quad (6.28)$$

$$\frac{\text{SK-I}}{\text{Borexino}} = \sqrt{\frac{0.243}{0.385} \times \frac{22.5}{0.146} \times \sqrt{\frac{10.0}{42700.0}}} = \sqrt{6.52} = 2.6$$

It is important to stress that this is an estimated sensitivity and it has been assumed that the efficiency of SK-I is similar to SNO+ water phase with an energy cut between 5.0 - 6.0 MeV. It appears that using only the data from SK-I is sufficient for setting a limit that is a noticeable improvement compared to Borexino. This analysis could easily be improved by using the original SK-I data and choosing a tighter energy window or including other phases of SK. The SK-II data could also be used to perform a similar analysis, but the publicly data has a threshold of energies > 7.0 MeV.

The efficiency of detecting an ALP signal (in SK) between 5.0-20.0 MeV could have been overestimated by using the efficiency from SNO+ Water Phase. However, it is unlikely that SK is an order of magnitude worst at detecting ALPs compared to SNO+ Water Phase.

6.12 Hyper Kamiokande

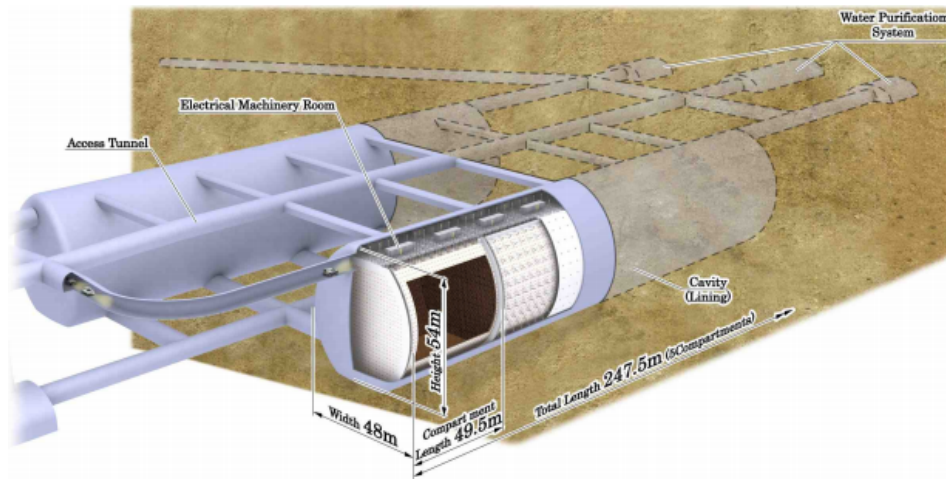


Figure 6.19: Schematic of the Hyper Kamiokande experiment

Hyper Kamiokande (HK) is the proposed next generation experiment to Super Kamiokande. It consists of two cylindrical tanks, in a similar design to Super

Kamiokande, with a total (fiducial) mass of 0.99 (0.56) Mtonnes of ultra pure water [86]. It is proposed to be located beneath 648m of rock (1750m of equivalent water). The inner detector is proposed to have over 99,000 20-inch PMTs with a photocathode coverage of around 20% [86].

Assuming the number of background events scale linearly (with size) from SK to HK, the total expected number of backgrounds for Hyper-K can be estimated as 1,304,173 events over a 5 year period. The HK detector is expected to have half the photocathode coverage of SK, thus its estimated ALP detection efficiency at > 5.0 MeV is taken as 0.122 . Running HK with a live-time of 5 years, a 5.0 MeV energy threshold and an exposure of 2800.0 kTonne-yrs would set a sensitivity relative to Borexino:

$$\frac{\text{HK}}{\text{Borexino}} = \sqrt{\frac{\epsilon_{HK}}{\epsilon_{\text{BOR}}} \times \frac{\rho_{HK}}{\rho_{\text{BOR}}} \times \sqrt{\frac{B_{\text{BOR}}}{B_{HK}}}} \quad (6.29)$$

$$\frac{\text{HK}}{\text{Borexino}} = \sqrt{\frac{0.122}{0.385} \times \frac{2800.0}{0.146} \times \sqrt{\frac{10.0}{1304173.0}}} = \sqrt{18.0} = 4.2$$

HK Live time (days)	1,625
HK Fiducial Vol. (ktonnes) $[\rho_{HK}]$	560.0
Efficiency of detecting ALPs $[\epsilon_{HK}]$	0.122
HK background count (after cuts) $[B_{HK}]$	1,304,173

Table 6.14: Summary of estimates for the sensitivity of HK to ALPs. These values are scaled from SK-I.

6.13 Other ALP searches

There are several searches for ALPs such as Axion Dark Matter Experiment (ADMX) [87] looking for relic axions, CERN Axion Solar Telescope (CAST) [73] looking for solar ALPs [59]. Cavity microwave experiments such as ADMX

have been developed to search for the resonant conversion of ALPs into photons, within a high-Q factor microwave cavity with a very strong magnetic field threaded through it. The resonance frequency of the lowest TM mode is slowly swept while the cavity output is monitored for excess power. This excess power could be attributed to resonant ALP conversions [88][89][90]. Cavity experiments probe very low ALP masses and are only sensitive to $g_{A\gamma}$ coupling via ALP decay or the Primakoff effect. They use the coupling between an ALP field, Φ_a and the electromagnetic tensor such that:

$$\mathcal{L} = -\frac{1}{4}g_a\gamma\gamma\Phi_a\epsilon_{\mu\nu\alpha\beta}F^{\mu\nu}F^{\alpha\beta} = -g_{a\gamma\gamma}\Phi_a\vec{B}\cdot\vec{E} \quad (6.30)$$

These type of experiments probe a very different region of phase space compared to the ALP searches with LUN experiments (see figure 6.22).



Figure 6.20: Image of the CAST experiment taken from <http://cast.web.cern.ch/CAST/CAST.php>

The CAST experiment is also searching for the conversion of solar ALPs into photons, in the presence of a significant magnetic field ($\sim 9\text{T}$) [91]. CAST uses a prototype magnet for CERN's LHC dipole magnet, looking for ALP conversion to photons inside the magnet. This process would be observed through the coupling of a virtual photon, producing a real photon via Primakoff effect, where the photon's energy is equal to the ALP's total energy [92] (see figure 6.21).



Figure 6.21: *Left:* is the Feynman diagram of the ALP-photon coupling and *Right:* is the Feynman diagram via a triangle loop can carry electromagnetic and PQ charge. This is one of the main detection modes within the CAST experiment

The CAST experiment is very sensitive to the non-hadronic models of solar ALPs, and has the best limit on non-hadronic ALPs at low masses $m_a \leq 10$ meV. Non-hadronic models can produce ALPs via the electron coupling to ALPs and are detected by in CAST via two-photon coupling (given in figure 6.21) [93]. This results in a combined ALP- γ and ALP- e^- limit of:

$$|g_{A\gamma} \times g_{Ae}| \leq 8.1 \times 10^{-23} \text{GeV}^{-1} \quad (95\% \text{ c.l.}) \quad (6.31)$$

Another approach is employed by the BGO collaboration [77]. The BGO experiment is an array of $\text{Bi}_4\text{Ge}_3\text{O}_{12}$ (BGO) scintillating bolometers containing 1.65kg of Bi [77]. The scintillation light produced by particle interactions within the BGO detector is monitored with an auxiliary bolometer made of high-purity germanium. Solar ALPs interact with the BGO detector via the axioelectric effect where $Z_{\text{Bi}} = 83$ for Bismuth. BGO placed an upper limit on the number of AE events, $S_{lim} = 2.44$ [77]. From equation 5.7, the cross section for the AE interaction of ALPs, $\sigma_{Ae} \propto g_{Ae}^2$ and gives a limit of $|g_{3AN} \times g_{Ae}|$ [77]:

$$|g_{3AN} \times g_{Ae}| \leq 1.9 \times 10^{-10} \quad (90\% \text{ c.l.}) \quad [\text{unitless}] \quad (6.32)$$

6.14 Conclusion

This chapter has explored the potential of SNO+ improving the current upper limits on ALP couplings to matter, during the unloaded scintillator phase via IP interaction of ALPs and Te-loaded scintillator phases via the IP, CCA and AE interactions of ALPs. The potential of other LUN experiments, such as Super Kamiokande, has also been explored and the limits for different types of ALP couplings to matter are summarised in the following sections.

6.14.1 Limits for $|g_{3AN} \times g_{Ae}|$

Liquid scintillator detectors have a better energy resolution, whereas the water Cherenkov detectors can apply a powerful directional cut on the Compton conversion of ALPs. In scintillator, both the electron and γ particles produced in CCA have a higher light yield per MeV in water.

The backgrounds in scintillator and water experiments are both dominated by internal Th concentrations (from ^{208}Tl decays) and solar neutrinos. However, the concentration of Thorium is lower in scintillator because it is easier to purify. A dedicated ALP detector could either be a liquid scintillator or water Cherenkov detector, which can either capitalise on a higher light yield per MeV with lower radiopurity levels or the power directional cut applied in water (but only for CCA interactions).

Borexino currently has the best published limit on $|g_{3AN} \times g_{Ae}|$ with CCA. This can be slightly improved by using 5 years of SNO+ Te-loaded scintillator. Hyper Kamiokande could also potentially improve upon the current limit by an order of magnitude, if a low trigger threshold (below 5.0 MeV) can be achieved.

BGO currently has the best limits on $|g_{3AN} \times g_{Ae}|$ with AE. This could be significantly improved with 5 years of SNO+ Te-loaded phase (see figure 6.23). SNO+ has a significantly larger fiducial volume than the BGO bolometer (with only around 8kg of BGO). The summary of all experiments and their limit setting potential for $|g_{3AN} \times g_{Ae}|$ is given in table 6.15.

Figure 6.22 depicts the parameter space of g_{Ae} and $|g_{3AN} \times g_{Ae}|$ against ALP mass m_A for CCA. There are several different experiments that can place constraints for ALPs, which are given in [71]. Only a small number of experiments probe the parameter space relevant for the GUT and hadronic models. Dark matter experiments such as CoGeNT and CDMS have some sensitivity to ALP masses between $10^2 - 10^3$ eV, but the LUN experiments can probe parameter space at higher ALP masses. SK can improve on the current limits set by Borexino. This is only possible if a directional cut can be placed on CCA events that removes any isotropic backgrounds by an order of magnitude. SK-I has a better limit than Borexino because it has an exposure ~ 100 kTonne-yrs, compared to the 0.146 kTonne-yrs exposure in Borexino. This can be further improved with a full analysis of SK data across all the phases in combination.

Experiment	ALP efficiency	$ g_{Ae} \times g_{3AN} $ (CCA)	$ g_{Ae} \times g_{3AN} $ (AE)
Borexino	0.385 [71]	5.5 [71]	-
SNO+ Water Phase (6 months) ^{*1}	0.384	9.0	-
SNO+ Scintillator Phase (6 months) ^{*2}	0.86	4.2	-
SNO+ Te-Scintillator Phase (5 years) [*]	0.41	3.3	700
BGO Bolometer	0.59 [77]	-	19,000 [77]
SNO (Phase I & II)	0.384	5.3 ^{**}	-
Super Kamiokande (SK-I)	0.243	2.1 ^{**}	-
Hyper Kamiokande (5MeV Threshold) [*]	0.122	1.3 ^{**}	-

Table 6.15: Sensitivity to $|g_{3AN} \times g_{Ae}|$ (in units of 10^{-13}) for $m_A \leq 1$ MeV and the detection efficiency of ALPs from different experiments. Experiments indicated with * are proposed experiments that have yet to take data. The limits with ** are estimates that are implied from the measured backgrounds and have an estimated efficiency relative to Borexino. ¹See Appendix B for the calculation of the SNO+ Water (6 months) limit. ² See Appendix C for the calculation of the SNO+ Scintillator Phase (6 months) limit

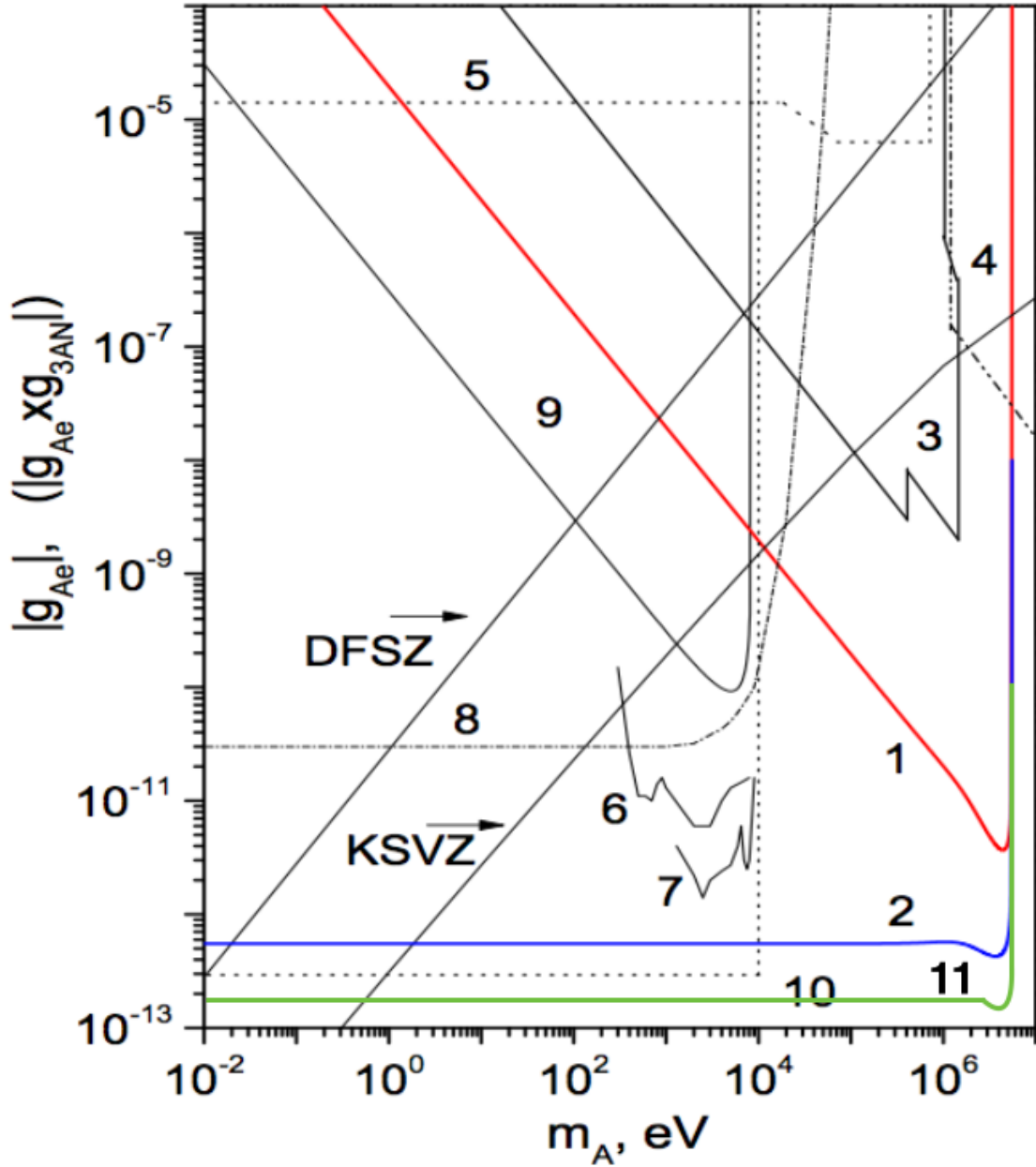


Figure 6.22: The limits on g_{Ae} coupling constant obtained by 1 - Borexino [71], 2 for $|g_{3AN} \times g_{Ae}|$ from Borexino [71], 3- reactor experiments [94][95] and solar experiments [96][97], 4- beam dump experiments [98][99], 5- ortho-positronium decay [100], 6- CoGeNT [101], 7- CDMS [102], 8- solar axion luminosity [103], 9-resonance absorption [104], 10 (dashed line)- red giant stars [105], 11- current work using SK-I data as a best limit on $|g_{3AN} \times g_{Ae}|$. Note that this has been adapted from figure 6 in [71].

Figure 6.23 depicts the $g_{A\gamma}$ and $|g_{A\gamma} \times g_{3AN}|$ against the ALP mass m_A for the AE effect. Experiments included in figure 6.23 constrain parameter space for the GUT and hadronic models.

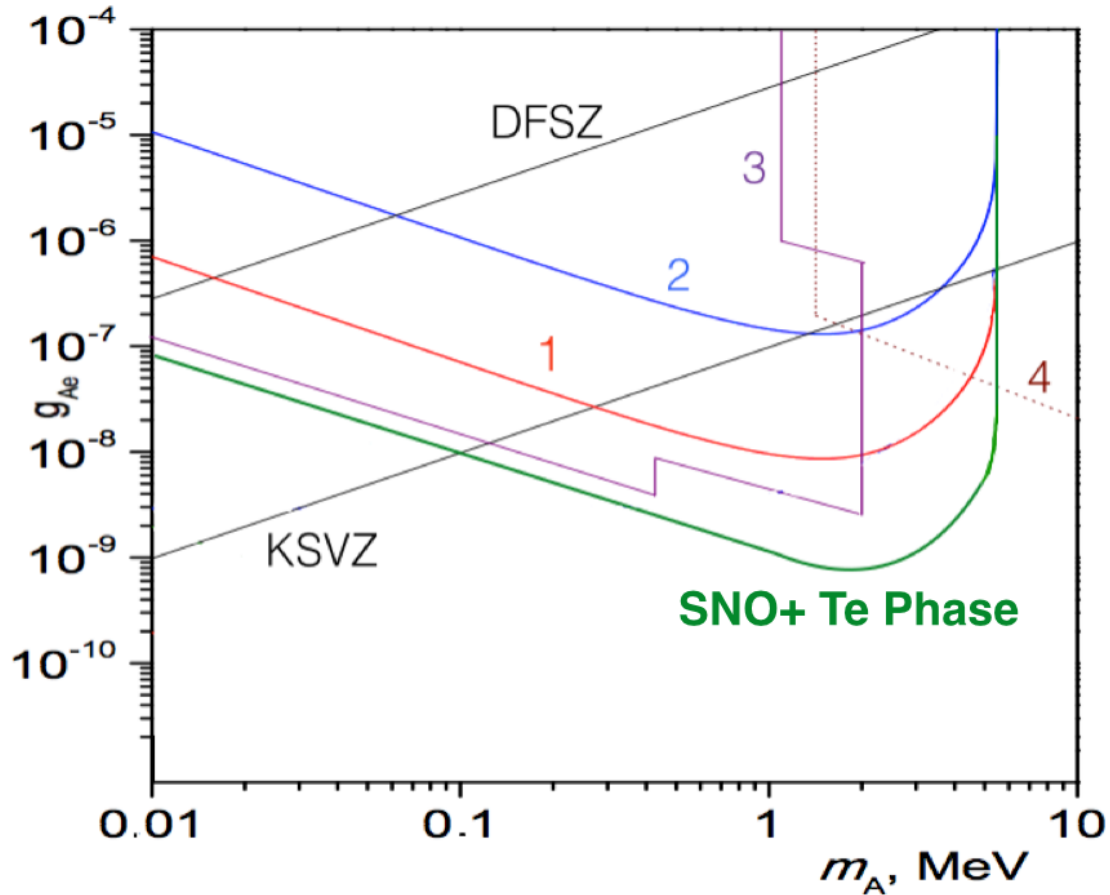


Figure 6.23: Limits on ALP-electron coupling with the axio-electric effect. 1- 8kg of BGO bolometer[59], 2- BGO scintillator[77], 3- solar and reactor experiments, 4-beam dump experiments. The limits for 0.5% of Te-loading for 5 yrs of SNO+ Te phase are included. This figure has been adapted from [59].

6.14.2 Limits for $|g_{3AN} \times g_{A\gamma}|$

The inverse Primakoff interaction of ALPs does not conserve directional information, which means large water Cherenkov detectors have poor sensitivity to $|g_{A\gamma} \times g_{3AN}|$. Borexino is currently the best limit on $|g_{A\gamma} \times g_{3AN}|$, but a loading of only 0.5% of Tellurium into SNO+ for a 5 year period can improve the best limit

by an order of magnitude.

Loading large isotopes into liquid scintillator based experiments is advantageous, because the cross section for inverse Primakoff has a Z^2 dependence. By loading Tellurium ($Z=52$) into the SNO+ scintillator, the sensitivity to $|g_{A\gamma} \times g_{3AN}|$ is improved. Table 6.16 gives a summary of the limits on $|g_{A\gamma} \times g_{3AN}|$ for different phases of SNO+ compared against Borexino.

Figure 6.24 depicts the parameter space of $g_{A\gamma}$ and $|g_{A\gamma} \times g_{3AN}|$ against ALP mass m_A for a generalised ALP. There are several different types of experiments that are sensitive to ALPs in the parameter space relevant for hadronic and GUT models. Specifically, helioscopes such as CAST have sensitivity to low mass ALPs but LUN experiments have sensitivity to ALPs with masses between 0.5 – 5.0 MeV.

Experiment	ALP Efficiency	$ g_{3AN} \times g_{A\gamma} $	$m_A \times g_{A\gamma} $
Borexino	0.385	4.6	1.7
SNO+ Scint. Phase (6 months)*	0.72	3.4	1.2
SNO+ Te Phase (5 years)*	0.71	2.9	1.6

Table 6.16: Sensitivity to $|g_{A\gamma} \times g_{3AN}|$ (in units of $10^{-11} \text{ GeV}^{-11}$), $m_A \times |g_{A\gamma}|$ (in units of 10^{-12}) and the detection efficiency of ALPs for different experiments. Experiments indicated with * are proposed experiments that have yet to take data.

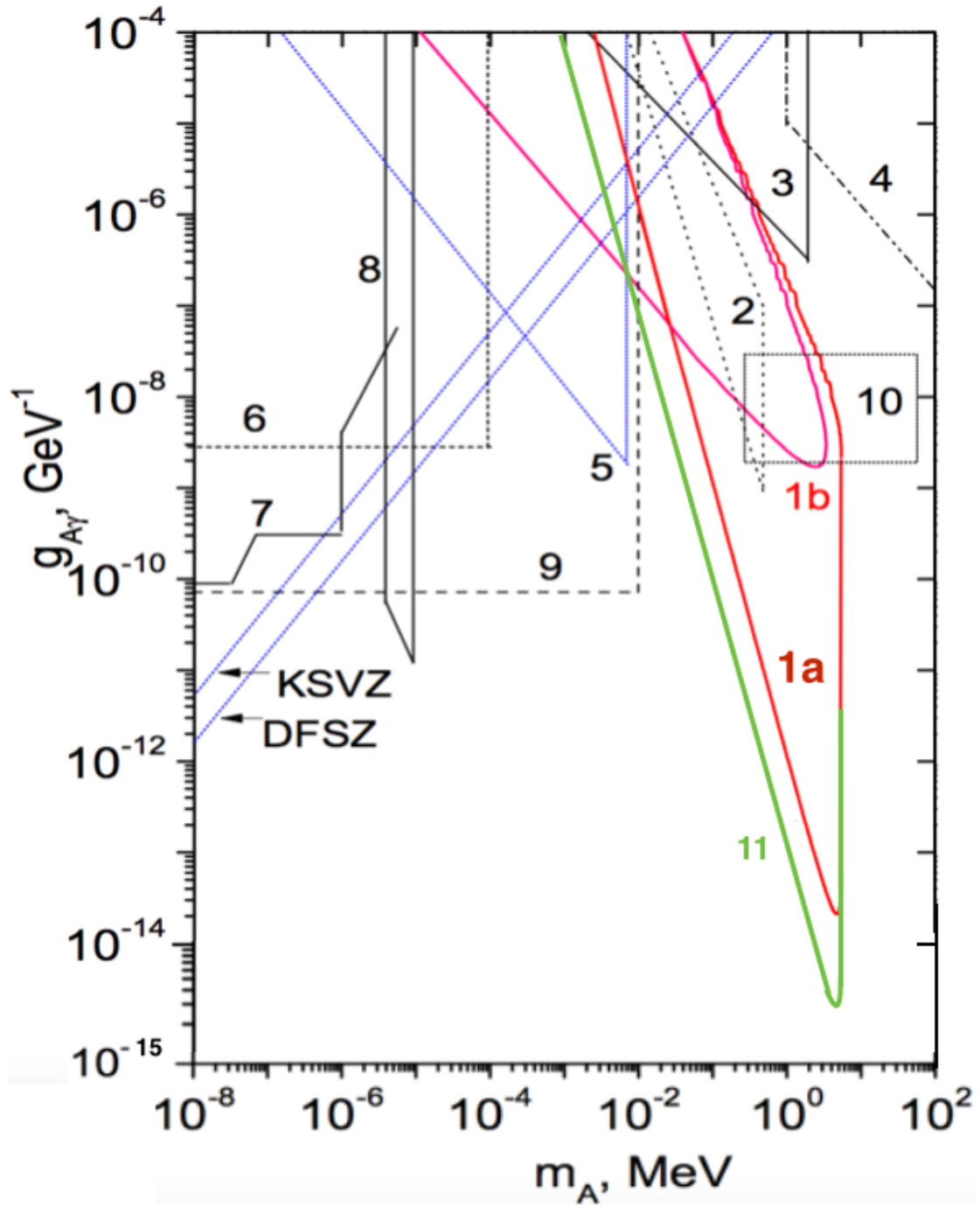


Figure 6.24: The limits on $g_{A\gamma}$ coupling constant obtained by 1a,1b - Borexino [71], 2- CTF [96] 1, 3- reactor experiments [95] and solar experiments [96][97], 4- beam dump experiments [98][99], 5-resonance absorption [104], 6- solar axions conversion in crystals [106][107][108], 7- CAST and Tokyo Helioscope [109][110][111], 8- telescopes [112][113][114], 9-HB Stars [105], 10- expectation region from heavy axion models [115][116][117], 11 - limit set by 5 years of 0.5% Te-loaded scintillator in SNO+. Note that this has been adapted from figure 7 in [71].

7

Supernova neutrinos in SNO+

“Still waiting around for a supernova on SNO+?”

– Oxford students at CERN

Current and proposed neutrino experiments have ushered in a new age of astrophysics: neutrino astronomy. Neutrinos are very difficult to detect, as they have a minute cross section at kinetic energies \sim MeV-GeV. Yet, it is this characteristic that makes them a valuable probe to study a rare astrophysical signal, the core-collapse of supernovae (SN) originating from the Galaxy¹. During the core-collapse of a supernova and its resulting explosion, around 99% of the gravitational binding energy of the progenitor star is carried away by neutrinos with kinetic energies of $\mathcal{O}(10 \text{ MeV})$ [3]. Neutrinos can emerge from the very high densities, within a collapsing star, not only providing an insight to the explosion mechanism, but also insight into neutrino-neutrino interactions, which are only possible to achieve at such high densities.

During the core-collapse, the interior of a supernova is so dense that it is opaque to neutrinos. These neutrinos experience significant matter oscillations at high

¹Hyper Kamiokande, a proposed upgrade to the Super Kamiokande experiment, may be sensitive to supernova neutrinos from the Andromeda Galaxy [86]

number densities and undergo neutrino-neutrino forward scattering effects [3][32]. The neutrino physics driving this effect upon the flavour composition is described in section 2.5.

SNO+ is a multi-purpose, 0.78 kTonne scale detector with a low energy threshold, suitable for measuring the low energy signals during the arrival of a burst of supernova neutrinos. This is a mixture of different flavours of neutrinos (and anti-neutrinos), which interact predominantly via inverse beta decay (IBD) and proton elastic scattering (PES) interactions within the SNO+ detector. For a given supernova explosion, the burst of neutrinos produced in the explosion precedes the arrival of light by $\mathcal{O}(\text{hours})$ and is expected to last for up to 10 seconds[32]. This allows an alert to be given to the astronomical community of an incoming supernova event via the SNEWS network.

All SN neutrino signals discussed in this chapter assume a SN originating at a distance of 10 kPc away (the Galaxy is approximately 30 kPc wide). This chapter is structured into three core parts: the physics of supernovae in sections 7.1 and 7.2, the detection of supernova neutrinos in SNO+ (including a discussion on external backgrounds) and the potential sensitivity to the neutrino mass hierarchy is given in sections 7.3 to 7.5 respectively. An extraction of the number of PES events with artificial data is given in section 7.6.

7.1 The physics of supernovae

Supernova are generated either from the core collapse of a star or the accretion of a white dwarf within a binary system. This thesis will focus on neutrinos produced as the result of a core collapse supernova. Based on the observed absorption lines of SN, they are historically classified into two broad groups: Type II with hydrogen

lines in the emission spectra and Type II without. Type I supernovae are further classified into: Type Ia, 1b and 1c.

7.1.1 Type Ia

Type Ia supernovae occur within a binary system of two stars, where one of the stars is a white dwarf. White dwarfs are supported against gravity by electron degeneracy pressure as opposed to thermal pressure in main sequence stars. As material from the other star is accreted onto the white dwarf, the star comes to within 1% of the Chandrasekhar mass limit. White dwarfs have too high a metallicity to undergo expansion cooling, thus igniting fusion of heavy elements and generating a type Ia supernova [118].

7.1.2 Type Ib/c

The original classifications for supernova were determined by their lack of hydrogen absorption lines, as opposed to the underlying physics that drives the explosion. Type Ib/c are both triggered by core collapse, as opposed to accretion, and lack the absorption line of silicon that is present in Type Ia supernovae. These stars are thought to have lost most of their outer envelope of lighter elements such as hydrogen (Type Ib) and also helium (Type Ic) from strong stellar winds [119].

7.1.3 Type II

Type II supernovae occur in stars that have a mass between 8 and 50 solar masses [120]. The core collapse of a single star is triggered after the exhaustion of all available fuel. Depending on the mass of the star and its metallicity, the implosion either produces a complete gravitational collapse into a black hole or a supernova explosion.

7.1.4 Core collapse supernovae

Core collapse occurs for a Type Ib/c and Type II supernova. It arises as the gravitational pressure of a star overcomes the thermal pressure generated via fusion within the star. As a star runs out of hydrogen fuel to burn, it starts to burn heavier elements such as helium, carbon and progressively heavier elements until it reaches iron. The fusion of iron is not energetically favourable and leads to the formation of a characteristic ‘onion-shell’ of elements, with iron at the centre and lighter elements as you move progressively outwards (see figure 7.1) [121].

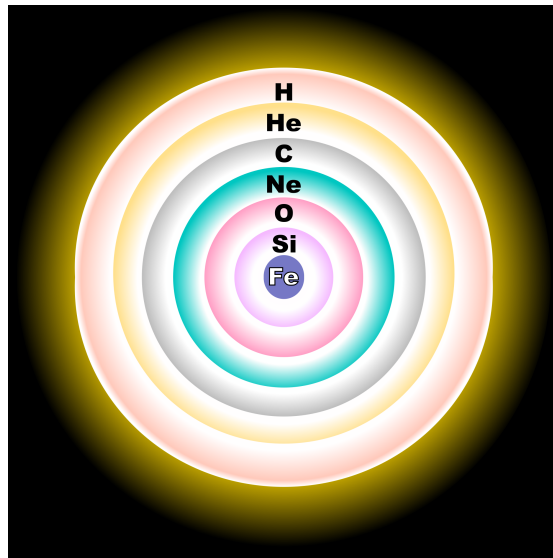


Figure 7.1: A diagram of a massive star before collapse. This image taken from https://www.physics.rutgers.edu/analyze/wiki/cc_supernovae.html

The central iron core is inert and is only prevented from collapse by electron degeneracy pressure. The maximum mass of the iron core is determined by the Chandrasekhar limit, above this limit the core collapses in on itself as the electron degeneracy pressure is no longer large enough to support the surrounding envelope of matter. The high temperatures and pressures in the core start to melt down some of the iron nuclei into helium via photodissociation, removing more energy needed to maintain the pressure required to slow down the core collapse [121]. The core becomes so dense that it traps neutrinos at mass densities $> \mathcal{O}(10^{12}) \text{ g cm}^{-3}$.

At these densities, the timescale between successive scatters becomes larger than the timescale of core collapse [121]. As the inner core reaches mass densities of $\mathcal{O}(10^{14}) \text{ g cm}^{-3}$, short range nuclear forces sharply halt the collapse of the inner core. Any falling material rebounds generating a shockwave through the outer core [121]. This shockwave is stalled by further photodissociation and neutrino production from electron-positron annihilation. However a few milliseconds after the bounce, a proto-neutron star (PNS) with a radius of about 30km remains at the core of the star. This PNS starts to accrete mass at 0.1 solar masses per second [121]. At this point there are two possibilities: formation of a black hole or supernova explosion. If the PNS does not become a black hole, the dissociation of nuclei provides free proton targets for electron capture producing a huge amount of electron neutrinos from the neutronisation of the core. The PNS is now supported by neutron degeneracy and can only cool via neutrino pair-production and diffusive loss of neutrinos. After $\sim 10\text{s}$, a large fraction of the energy in the core is radiated away as neutrinos become transparent to the PNS.

7.2 Neutrino mass hierarchy with SN

In a core-collapse supernova, neutrinos may interact within the SN envelope via collective oscillation effects induced by neutrino-neutrino forward scattering[3]. This type of interaction arises from the large densities during the stellar collapse, whilst the PNS is still opaque to neutrinos at densities $> 10^{14} \text{ g cm}^{-3}$. It is proposed [3][32] that these neutrino self-interactions (described in section 2.5) dramatically change the flavour composition of supernova neutrinos. The initial spectrum is expected to be dominated by electron neutrinos, produced by inverse beta decay and electron capture, in the collapsing star. In the inverted mass hierarchy of neutrinos, the flavour evolution due to neutrino self-interactions may produce a distinct ‘spectral swap’ between the flux of electron neutrinos (ν_e) and

the flux of all neutrino flavours (ν_x) [32]. For both neutrino and anti-neutrinos, the ‘spectral swapping’ is given in figure 7.2, which depicts the effect on the initial $\bar{\nu}_x/\nu_x$ and $\bar{\nu}_e/\nu_e$ spectra [31].

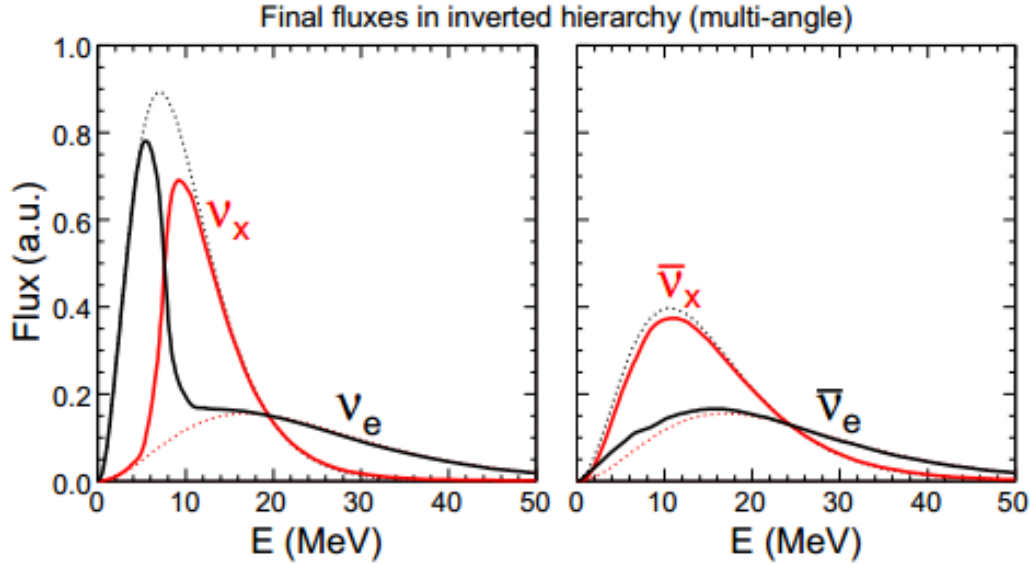


Figure 7.2: The flux of supernova neutrinos against the neutrino energy. **Left:** Indicates the spectral swapping between ν_x and ν_e and **right:** indicates the spectral swapping between $\bar{\nu}_x$ and $\bar{\nu}_e$ due to neutrino-neutrino forward scattering within the SN envelope. Dotted lines represent the original fluxes of neutrinos in a SN without any self-interaction effects applied. Solid lines represent the supernova neutrino fluxes with self-interaction effects applied. This figure is taken directly from figure 8 in [31].

For the neutrino case, the peak of the ν_e is shifted to lower energies and the ν_x peaks is shifted to lower energies with a much sharper peak. The IBD interaction can be used to observe the $\bar{\nu}_e$ flux and the combination of ν_x and $\bar{\nu}_x$ is observed by the PES interaction. The simultaneous measurement of both $\bar{\nu}_e$ and $\nu_x/\bar{\nu}_x$ fluxes via IBD and PES interactions respectively is unique to SNO+.

The flux distribution of $\nu_x/\bar{\nu}_x$ combined relative to $\bar{\nu}_e$ could give a strong indication of the inverted mass hierarchy of neutrinos. Thus, one of the aims of this thesis is to demonstrate how well the number of PES events can be measured in SNO+. The following sections will explain the expected types of events from

a burst of supernova neutrinos with a focus on IBD and PES interactions. The average thermalised energy of electron neutrinos, $\langle E_{\nu_e} \rangle = 18.0$ MeV, an average thermalised energy of non-electron neutrino flavours, $\langle E_{\nu_x} \rangle = 20.0$ MeV and a supernova at 10 kPc away from Earth is assumed throughout this thesis.

7.3 Supernova neutrinos in SNO+

The SN neutrino burst of SN 1987A was observed by Kamiokande-II[122], Baksan [123] and IMB [124]. SN 1987A occurred within the Large Magellanic Cloud, a satellite galaxy of the Milky Way, at distance of ~ 50 kPc and a total of 24 events were observed, predominantly via inverse beta decay (IBD) [125]. IBD is a prominent interaction of supernova neutrinos in neutrino detectors, which measures the anti-electron neutrino flux. The main interactions of SN neutrinos are given in table 7.1, where PES has the highest number of expected interactions closely followed by IBD in unloaded and loaded scintillator phases of SNO+. The water phase has no PES events, because the visible energy of PES events in a water Cherenkov detector is below the energy trigger threshold.

Type of SN event	Water phase	Scintillator/Te phase
IBD	19 ^a	101 ^a
ES + ¹² C	33 ^a	27 ^a
PES	N/A	247 ^a
Total	52	375

Table 7.1: Estimated number of events within the 10 seconds of a supernova at 10 kPc with $\langle E_{\nu_x} \rangle = 20.0$ MeV and $\langle E_{\nu_e} \rangle = 18.0$ MeV. This table assumes a 100 % trigger efficiency [126].

7.3.1 Inverse beta decay (IBD)

IBD occurs when an electron neutrino interacts with a proton, producing a positron and neutron:

$$\bar{\nu}_e + p \rightarrow e^+ + n \quad (7.1)$$

This interaction produces at least 1.8 MeV of visible energy in SNO+ scintillator phases, because the positron produces a prompt signal from the deposition of kinetic energy and the e^+e^- annihilation. Additionally, a delayed signal is produced by the neutron, as it is captured on a nucleus within the detector medium. The capture nucleus de-excites producing a γ -ray $\mathcal{O}(100\mu\text{s})$ later as given in figure 7.3.

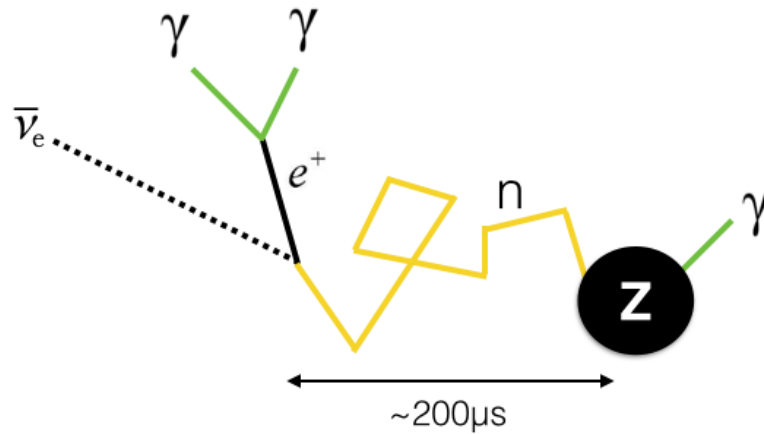


Figure 7.3: Diagram of the IBD interaction in SNO+. The incoming anti-electron neutrino scatters off a proton, producing a positron and a neutron. The positron almost immediately annihilates, whilst the neutron scatters within the scintillator before being captured on a nucleus.

In SNO+, neutron capture from IBD predominantly occurs on hydrogen within the scintillator molecules, producing a delayed γ -ray at 2.223 MeV between 200 - 260 μs after the prompt e^+ signal. Whilst the cross section for neutron capture on carbon is lower than hydrogen, around 1% of thermalised neutrons are captured on ^{12}C , releasing a γ -ray of 4.945 MeV.

7.3.2 Inelastic scattering off ^{12}C

Neutrinos of any flavour, ν_x can inelastically scatter off ^{12}C nuclei within the SNO+ scintillator via:



where $^{12}\text{C}^*$ is an excited state of ^{12}C producing a prompt γ -ray with 15.11 MeV of energy. A large burst of events at ~ 15 MeV would be strong evidence for the arrival of a supernova and acts as a key trigger signal for the SNEWS network [127].

7.3.3 Electron elastic scattering (νES)

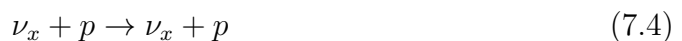
All flavours of neutrinos can elastically scatter off electrons, but with higher cross section for ν_e , at the kinetic energies of supernova neutrinos via:



νES has a lower cross section than IBD. Since this is a purely leptonic process, the cross section is known to a high level of precision within the Standard Model. This interaction has no coincidence tagging method that can be applied in scintillator to distinguish it from backgrounds or other supernova neutrino signals.

7.3.4 Proton-neutrino elastic scattering (PES)

Proton-neutrino elastic scattering is the neutral current interaction with the largest number of events in SNO+ [3]:



The proton is highly quenched and the light yield is reduced due to non-radiative deposition of energy in the detector medium. The rate of IBD events only indicates the flux of anti-electron neutrinos, whereas the rate of PES events indicates the flux of all flavours of neutrino and anti-neutrino. SNO+ should be uniquely placed to get the best measurement of this signal, because it has a low incidence of cosmic muons (~ 3 per hour), can observe the recoiling protons in scintillator and has a sufficiently low energy trigger threshold. Large water Cherenkov experiments, such as Super Kamiokande, are capable of observing IBD events but don't have a low enough energy trigger threshold to observe PES events.

7.4 PES flux in SNO+

The number of proton-neutrino elastic scattering interactions, during a SN burst, is determined by the number of free protons within the liquid scintillator. Protons with kinetic energies less than 2 MeV are highly quenched, thus following the formalism given in [3], the number of protons per MeV of visible energy dN/dT' is given as:

$$\frac{dN}{dT'} = \frac{N_p}{dT'/dT} \int_{E_{min}}^{\infty} dE \frac{dF}{dE} \frac{d\sigma}{dT}(E) \quad (7.5)$$

where T' is the visible energy of the proton, T is the kinetic energy of the proton, E is the energy of the neutrino, dF/dE is the total neutrino fluence and $d\sigma/dT$ is the proton-neutrino elastic scattering cross section. A neutrino of energy E can produce a recoil energy between 0 and $T_{max} = 2E^2/m_p$, where m_p is the proton mass and the minimum neutrino energy for such an event is $E_{min} = \sqrt{m_p T/2}$

The neutrino fluence for each neutrino flavour α , at a given distance d is dis-

tributed in energy [3]:

$$\frac{dF}{dE} = \sum_{\alpha} \frac{dF_{\alpha}}{dE} = \frac{1}{4\pi d^2} \sum_{\alpha} \frac{\epsilon_{\alpha}}{\langle E_{\alpha} \rangle} \frac{d\varphi_{\alpha}}{dE} \quad (7.6)$$

where $d\varphi_{\alpha}/dE$ is a normalised Keil Parametrization [128] for the neutrino spectrum:

$$\frac{dF_{\alpha}}{dE} = \frac{2.35 \times 10^{13} \epsilon_{\alpha}}{\text{cm}^2 \text{MeV}} \frac{E^3}{d^2 \langle E_{\alpha} \rangle^5} \exp\left(\frac{4E}{\langle E_{\alpha} \rangle}\right) \quad (7.7)$$

where ϵ_{α} is the total energy output of neutrino flavour α and given in units of 10^{52} ergs. Throughout this thesis, the average thermalised energy of the neutrino $\langle E_{\alpha} \rangle$ is taken as 12 MeV for ν_e , 15 MeV for $\bar{\nu}_e$ and 18 MeV for the 4 other flavours represented by ν_x respectively.

The differential cross section, $d\sigma/dT$ for a neutrino of energy E to produce a proton recoil of kinetic energy T , to zeroth order in E/m_p is given by [3]:

$$\frac{d\sigma}{dT} = \frac{G_F^2 m_p}{\pi} \left[\left(1 - \frac{m_p T}{2E^2}\right) c_v^2 + \left(1 + \frac{m_p T}{2E^2}\right) c_a^2 \right] \quad (7.8)$$

where T and E are in MeV and $m_p = 938\text{MeV}$, $c_v = 0.04$ and $c_a = 1.27/2$ [3]. Where c_v and c_a are the vector and axial neutral-current coupling constants between the exchanged Z^0 boson and proton.

In SNO+, the proton energy is measured by counting the number of photons detected (Nhits) within a SNO+ event. The calibration of the Nhits to energy is better understood for electrons and γ -rays compared to protons, because radioactive calibration sources such as ^{90}Y (for electrons) and ^{16}N (for γ -rays) with known decay energies can be placed into the scintillator. For SNO+, the proton energy deposition and quenching model has been measured by Belina von Krosigk [15], using small samples of LAB and Te-loaded LAB in a proton beam.

The SNO+ scintillator consists of linear alkyl benzene (LAB) as the main component, with a wavelength shifter 2,5-diphenyloxazole (PPO) as a primary fluor [10]. As charged particles (such as protons or electrons) travel through the scintillator, they ionize and excite surrounding scintillator molecules. Some of the kinetic energy deposited in the scintillator is observed as LAB molecules de-excite producing photons with a wavelength ~ 300 nm, but some energy from the excited LAB molecules is non-radiatively transferred to PPO, which then reemits light of wavelengths between 350-450 nm. This wavelength range is optimal for the photocathode response of the SNO+ PMTs [10]. The type of particle depositing energy in LAB determines how much visible energy is lost to non-radiative processes and thus quenched. The quenching model for a general charged particle in scintillator is given by Birk's law [129]:

$$\frac{dT'}{dT} = \frac{1}{1 + k_b \langle dT/dx \rangle} \quad (7.9)$$

where $\langle dT/dx \rangle$ is the energy loss and k_b is birk's constant. Protons produce slightly later light than electrons and it could be possible to make a time residual based cut, in order to separate proton-like events from electron-like events, but this is beyond the scope of this thesis.

7.5 Backgrounds to PES events

The rate of PES events in SNO+, during a burst of supernova neutrinos, is a unique measurement that can be made by large, deep, liquid scintillators like SNO+. Before exploring the extraction of PES events, the background to this signal needs to be understood. Internal backgrounds occur within the scintillator cocktail, whereas external backgrounds are decays from the outer material of

SNO+ that reconstruct within the AV volume. Muons also occur at less than 3 per hour, within the SNO+ detector and, thus, no muon events or muon-activated backgrounds are considered. PES events deposit between 0.1 and 1.0 MeV of visible energy within the scintillator cocktail. This section identifies the relevant backgrounds, which are then added to an artificial PES signal extraction given in section 7.6. The total number of PES events is extracted using the procedure described in section 7.6.

7.5.1 Internal backgrounds to PES events

The carbon molecules in the SNO+ scintillator contains a natural amount of ^{14}C , which undergoes a beta decay with an endpoint of 0.156 MeV and has a half-life of 5,730 years. In 0.8kTonnes of scintillator, this equates to $\mathcal{O}(10^2)$ decays per second, assuming a concentration of ^{14}C in Borexino [16] of 1.94×10^{-18} g/g in the LAB. There are many different radioactive decays in SNO+, but only the decays with very high rates > 1 decay per second in the entire detector (regardless of energy trigger threshold) are included in table 7.2.

Background	Rate (Hz)	Expected decay count in 10s
^{14}C	4.08×10^9	1,292.9
^{210}Bi	2.03×10^8	64.3
^{210}Po	1.93×10^8	61.1

Table 7.2: Summary of high rate internal backgrounds between 0.1 - 1.0 MeV [16], assuming conservative estimates on the $^{210}\text{Po}/^{210}\text{Bi}$ decays from Lead leaching and ^{14}C concentration of Borexino.

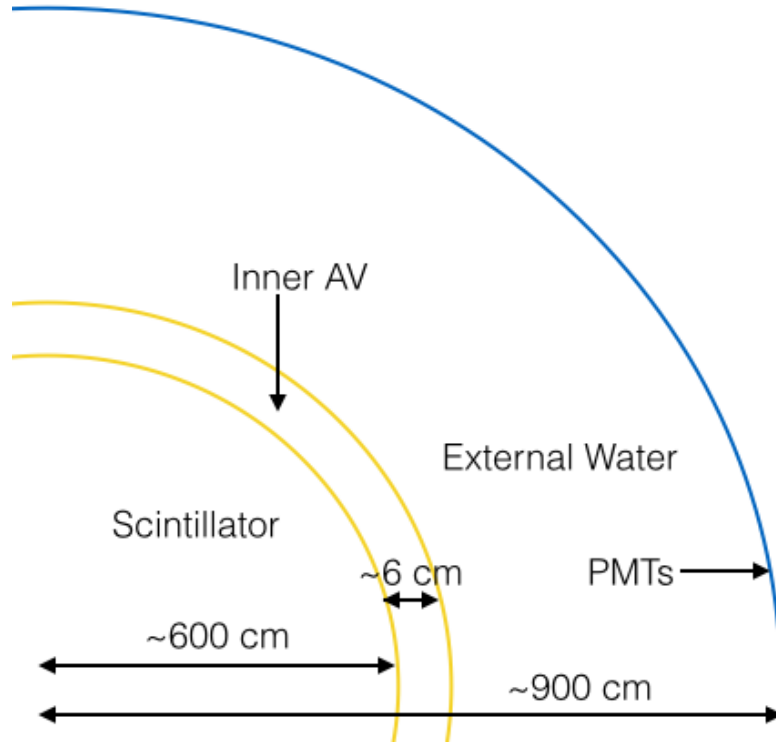


Figure 7.4: Diagram of sources of SNO+ external backgrounds. The AV is placed at the centre of the SNO+ detector. The thickness of the AV is ~ 5 cm and it has a radius of ~ 600 cm. The PMTs are placed on the PSUP at ~ 900 cm from the centre of the AV.

Since the completion of SNO, the inner AV has been exposed to mine air, during the commissioning of SNO+, which contains a concentration of ^{222}Rn and builds up within the inner AV (see figure 7.4) [10]. The ^{210}Pb daughter from ^{222}Rn , in the inner AV, can leech into the scintillator and decay to either ^{210}Po or ^{210}Bi . During the first 6 months of scintillator phase, 2.03×10^8 events of ^{210}Po and 1.93×10^8 events of ^{210}Bi per year are expected [16]. These conservative estimates on the rates are assumed throughout this thesis. Pile-up events from combinations of different radioactive backgrounds, occurring in coincidence can also form a background to PES events.

7.5.2 External backgrounds to PES signal

There are many different external backgrounds in SNO+, but only the external backgrounds from ^{222}Rn daughters, which haven't leached into the scintillator, can affect the PES measurement. No leaching is assumed for the external background estimation in order to calculate the most conservative estimate of external backgrounds. Table 7.3 gives the expected number of decays in SNO+ in a 10s window, where the vast majority of these decays reconstruct at energies too low to trigger the SNO+ detector or are completely missed by the SNO+ trigger.

Background	Rate (Hz)	Expected decay count in 10s)
^{210}Bi (AV)	3.63×10^{10}	11,502.7
^{210}Po (AV)	3.63×10^{10}	11,502.7
^{210}Pb (AV)	3.63×10^{10}	11,502.7

Table 7.3: Summary of high rate external backgrounds between 0.1 - 1.0 MeV [16], after trigger efficiencies have been taken into account.

One of the ^{222}Rn daughters, ^{210}Bi , has a beta-decay with an endpoint of 1.1 MeV. Electrons from ^{210}Bi decays have a small probability of travelling into the scintillator and reconstructing within the fiducial volume for a supernova analysis. Only a small fraction of ^{210}Bi decays in the inner AV can reconstruct within the fiducial volume because the outgoing electron from the decay has no preferred direction.

Figure 7.5 depicts the reconstructed energy against the reconstructed position R/R_{AV} , where R_{AV} is the radius of the AV. Approximately 200 Bismuth decays reconstruct very close to the AV, at values of $(R/R_{AV})^3 > 0.9$, which corresponds to $\sim 2\%$ of ^{210}Bi decays. An even smaller fraction, $< 0.1\%$ of outgoing electrons from a ^{210}Bi decay, reconstruct at $R < 5500$ mm (equivalent to $(R/R_{AV})^3 < 0.77$).

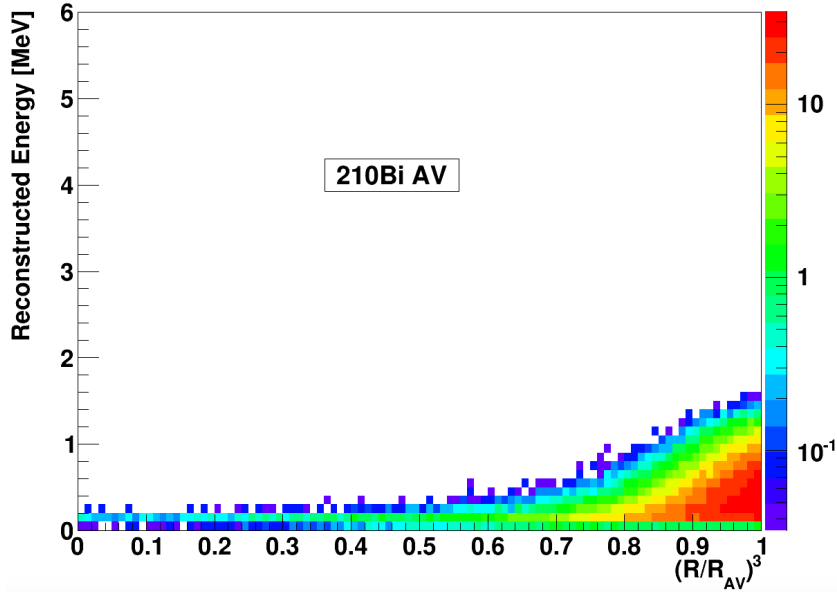


Figure 7.5: 2D histogram of ^{210}Bi decays in 10s from the AV, where R is the reconstructed position and $R_{AV} = 6005$ mm is the radius of the AV. For reference, the expected fiducial volume for $0\nu\beta\beta$ of 3500 mm with $(R/R_{AV})^3 = 0.2$ and for ALPs of 5500 mm with $(R/R_{AV})^3 = 0.77$.

^{210}Po decays, from the inner AV, also originate from Radon daughters within the AV material. ^{210}Po is a decay that produces a mono-energetic α -particle with a kinetic energy of 5.4 MeV. α -particles are heavily quenched in scintillator, because they are a highly ionising particle and deposit a large fraction of their energy non-radiatively. These events produce a visible energy of ~ 0.45 MeV in scintillator.

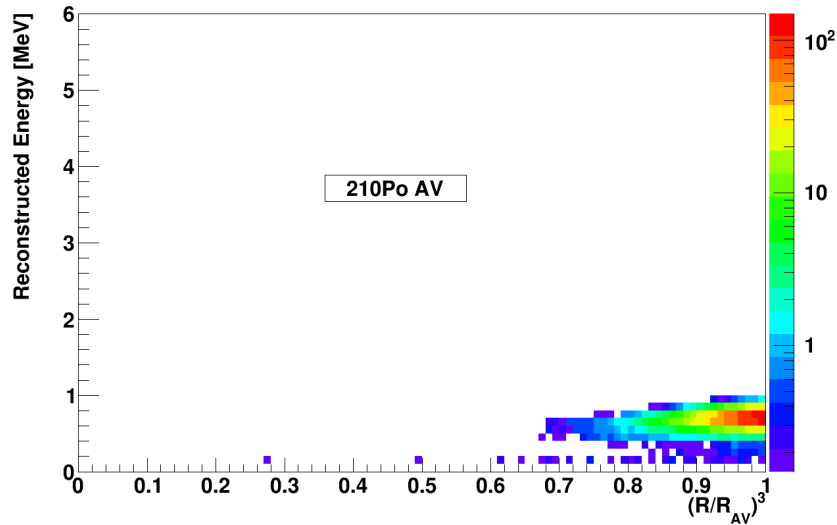


Figure 7.6: 2D histogram of ^{210}Po decays in 10s from the AV, where R is the reconstructed position and $R_{AV} = 6005$ mm is the radius of the AV. For reference, the expected fiducial volume for $0\nu\beta\beta$ of 3500 mm with $(R/R_{AV})^3 = 0.2$ and for ALPs of 5500 mm with $(R/R_{AV})^3 = 0.77$.

Figure 7.6 is equivalent to figure 7.5 but for ^{210}Po decays. The distribution of the reconstructed energy is centred at ~ 0.6 MeV, implying a quenching factor of ~ 10 with almost no events reconstructing at $R < 5100$ mm. Despite having the same rate as ^{210}Bi decays, an α -particle from a ^{210}Po decay with 5.4 MeV travels, on average, a much shorter distance into the scintillator compared to an electron from a ^{210}Bi decay.

In order to reduce external backgrounds, a fiducial volume choice of $(R/R_{AV})^3 = 0.77$ is made for supernova analysis in the remainder of this thesis. This maximises the signal from supernova without a significant contribution from external backgrounds. External backgrounds have a very distinctive time residual, compared to events originating from within the scintillator, and could be further reduced with timing based cuts.

7.6 PES signal extraction

PES events have an energy range from around 0.1 MeV to 1.1 MeV (see figure 7.7) against backgrounds from ^{14}C within the scintillator, ^{210}Po and ^{210}Bi from Pb leaching from the AV. PES events cannot be distinguished from backgrounds on an event-by-event basis. This section outlines a procedure, using simulated data, to extract the number of PES events from a total energy distribution within 10s of a SN burst and after applying a fiducial volume cut of 5.5m to remove external backgrounds. IBD events are not included in the PES extraction, because these events have a visible energy greater than 2.0 MeV. Assuming that bin in the energy distribution are independent and identically distributed observations, the maximum likelihood technique is the most powerful method for parameter estimation [130]. This section describes how a potential PES signal could be extracted and the validity of this extraction.

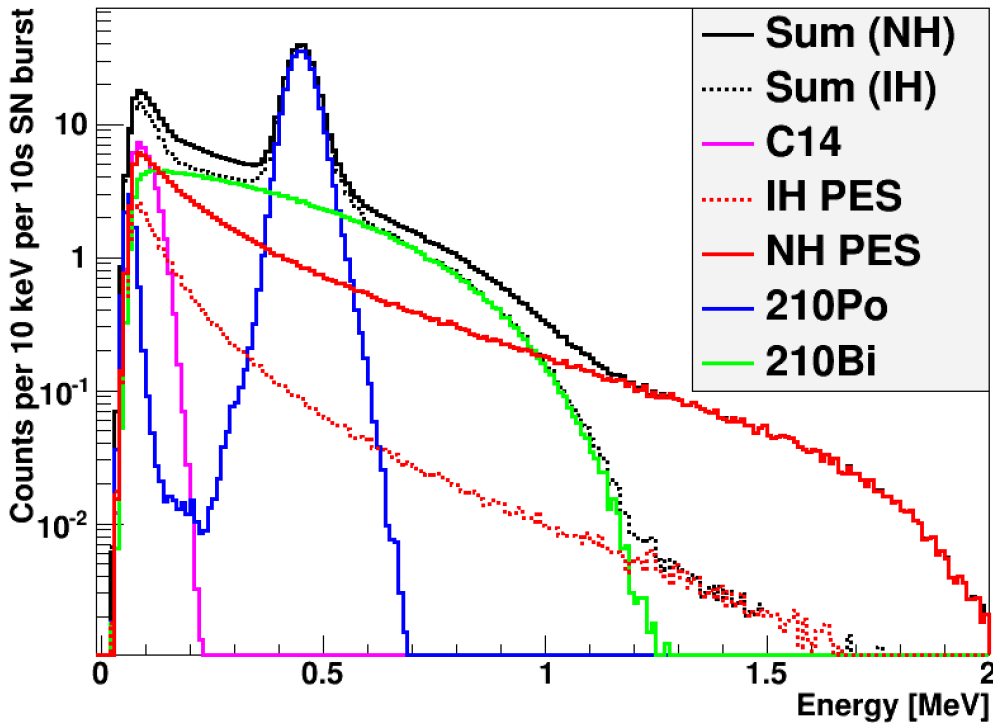


Figure 7.7: Visible energy distribution for PES events in normal (NH) and inverted (IH) mass hierarchies for neutrinos against with internal backgrounds occurring at rates greater than 10 Hz.

The expectation value for the i -th bin $\nu_i(\vec{\theta})$ for an observed number of events, n_{tot} is given as:

$$\nu_i(\vec{\theta}) = n_{\text{tot}} \int_{x_i^{\min}}^{x_i^{\max}} p(x; \vec{\theta}) dx \quad (7.10)$$

where x_i^{\min} and x_i^{\max} are the bin limits, $p(x; \vec{\theta})$ is the PDF (probability distribution function) of PES signal plus backgrounds, $\vec{n} = (n_1, \dots, n_N)$ is the vector of observed entries and $\vec{\nu} = (\nu_1, \dots, \nu_N)$ is the expected entries for N bins and parameterised as:

$$\vec{\theta} = \{N_{14C}, N_{210\text{Bi}}, N_{210\text{Po}}, N_{\text{PES}}, \{\text{PDFs}\}\} \quad (7.11)$$

containing the total number of events from all different species and the set of PDFs of PES and each background calculated from MC simulations. The joint pdf can be used to build a **likelihood function** $\mathcal{L}(\vec{\theta})$ across all bins in the histogram:

$$\mathcal{L}(\vec{\theta}) \propto f_{\text{joint}}(\vec{n}, \vec{\nu}(\vec{\theta})) \quad (7.12)$$

This assumes each bin is an independent event and that the height of the i -th bin follows a Poisson distribution with mean of ν_i and the value of $\vec{\theta}$ which maximises the likelihood function $\mathcal{L}(\vec{\theta})$ is chosen as the best estimator of $\vec{\theta}$. However, it is computationally easier to calculate the logarithm of the likelihood ℓ and yields:

$$\begin{aligned} \ell &= \log [\mathcal{L}(\vec{\theta})] \\ \ell &= \sum_{i=1}^N n_i \log \nu_i(\vec{\theta}) \end{aligned} \quad (7.13)$$

where additive terms not depending on the parameters have been dropped. But, the total number of events n_{tot} is actually Poisson distributed around a true mean of ν_{tot} [130]. Thus, the joint pdf is multiplied by a Poisson probability of observing

n_{tot} events, with an expected number of ν_{tot} events, becoming [130]:

$$f_{\text{joint}}(\vec{n}, \vec{\nu}) = \prod_{i=1}^N \frac{\nu_i^{n_i}}{n_i!} e^{-\nu_i} \quad (7.14)$$

where $\nu_{\text{tot}} = \sum_{i=1}^N \nu_i$, $n_{\text{tot}} = \sum_{i=1}^N n_i$, the expected number of events in each bin ν_i depends on both the model $\vec{\theta}$ and the expected total number of events ν_{tot} and equation 7.10 becomes:

$$\nu_i(\vec{\theta}, \nu_{\text{tot}}) = \nu_{\text{tot}} \int_{x_i^{\text{min}}}^{x_i^{\text{max}}} f(x; \vec{\theta}) dx \quad (7.15)$$

Taking the logarithm of the joint pdf in equation 7.14 gives the **extended log-likelihood function**, $\ell(\vec{\theta}, \nu_{\text{tot}})$ for the case of binned data [130]:

$$\ell(\vec{\theta}, \nu_{\text{tot}}) = -\nu_{\text{tot}} + \sum_{i=1}^N n_i \log \left[\nu_i(\vec{\theta}, \nu_{\text{tot}}) \right] \quad (7.16)$$

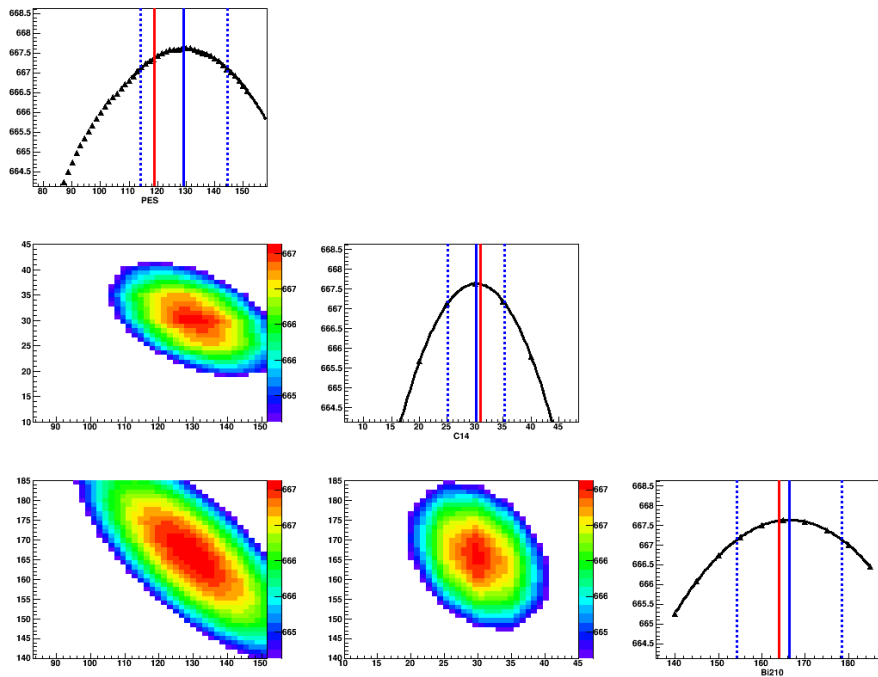
The **log-likelihood space** can be built by choosing different combinations of the number of events for each species and calculating the likelihood using a grid search. The **principle of maximum likelihood** states that the combination of $\{N_{14\text{C}}, N_{210\text{Bi}}, N_{210\text{Po}}, N_{\text{PES}}\}$ that maximises the likelihood is the most likely description of the observed data.

The Poisson distribution of the rates of ^{210}Po , ^{210}Bi and ^{14}C , in a 10s window without supernova neutrinos, can be measured during the running of SNO+. These distributions can be multiplied by the likelihood space, in order to constrain the likelihood space. This reduces the size of the likelihood space and the number of local maxima, making it easier to computationally identify the ‘true’ global maxima. This is called ‘constraining’ the likelihood. This calculation is equivalent to an addition in log-likelihood space, where the constrained log-likelihood $\ell_{\text{con.}}(\vec{\theta})$ is

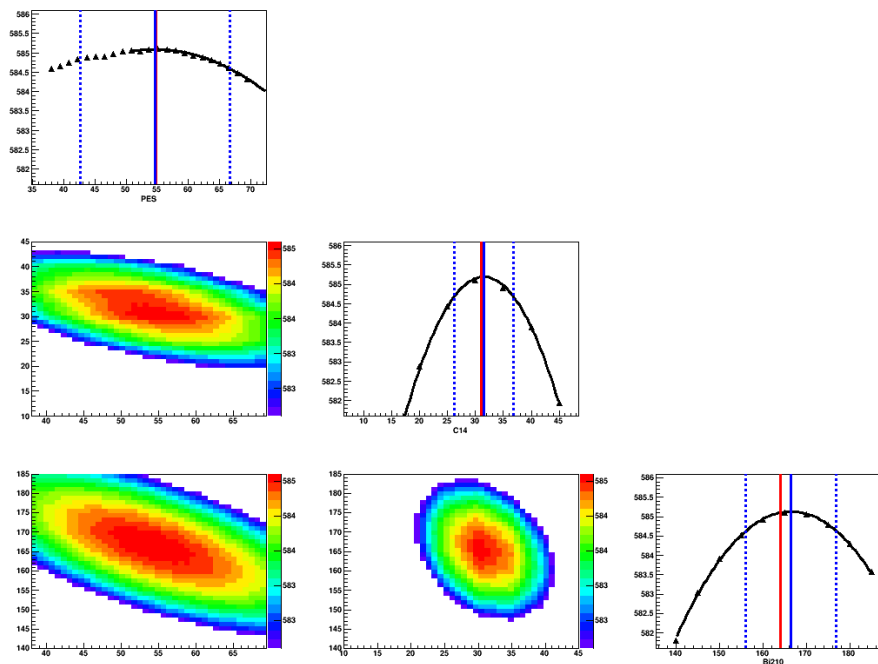
given as:

$$\ell_{\text{con.}}(\vec{\theta}) = \ell(\vec{\theta}) + \log[\text{Poi}(\lambda_{210\text{Po}})] + \log[\text{Poi}(\lambda_{210\text{Bi}})] + \log[\text{Poi}(\lambda_{14\text{C}})] \quad (7.17)$$

Since SNO+ has not seen a supernova, a simulated set of experiments have been performed by randomly sampling a number of events from the PDF of each event type: PES, ^{210}Po , ^{210}Bi and ^{14}C . The number of ^{210}Po , ^{210}Bi and ^{14}C events is given in table 7.2 and the number of PES events is determined by the SN distance (away from Earth) and the choice of neutrino mass hierarchy. The procedure for extracting the maximum likelihood involves calculating the likelihood for all combinations of the ^{210}Bi , ^{14}C and PES events between 1 - 500 events (in integer increments), where the number of ^{210}Po is restricted by the total number of observed events less the fitted number of ^{210}Bi , ^{14}C and PES events. For each type of event, a likelihood space is calculated by marginalising over all other event types, in order to find the maximum marginalised likelihood of that event. Figure 7.8 depicts an example of marginalised likelihoods for ^{210}Bi , ^{14}C and PES events for the inverted and normal hierarchies, in subfigures 7.8a and 7.8b respectively.



(a) Inverted hierarchy



(b) Normal hierarchy

Figure 7.8: For each subfigure, **top**: marginalised likelihood of PES, **middle left**: 2D marginalised likelihood for ^{14}C and PES, **middle right**: marginalised likelihood of ^{14}C , **bottom left**: 2D marginalised likelihood for ^{210}Bi and PES, **bottom middle**: 2D marginalised likelihood for ^{210}Bi and ^{14}C and **bottom right**: marginalised likelihood for ^{210}Bi . The red lines are the true number of events, the blue is the fitted number of events and the dashed blue lines are the extraction error on the fitted number of events.

The marginalised likelihood functions in figure 7.8 include the true event rates (in red), the fitted event rates (in solid blue) and the standard deviation (in dashed blue) for PES, ^{14}C and ^{210}Bi events. The fitted event rate is extracted by finding the maximum value of the marginalised likelihood for each species. But, the standard deviation is extracted graphically and using the Rao-Cramer-Frechet (RCF) inequality. The RCF inequality gives a lower bound on an estimator's variance, in this case the maximum likelihood estimator of events of type k , $\mathbf{n}_k^{\hat{\max}}$ and its variance $\hat{\sigma}_{\mathbf{n}_k^{\hat{\max}}}^2$ has a bound [130]:

$$\hat{\sigma}_{\mathbf{n}_k^{\hat{\max}}}^2 \geq \left(1.0 + \frac{\partial b}{\partial n_k}\right)^2 \bigg/ E \left[-\frac{\partial^2 \ell}{\partial n_k^2} \right] \quad (7.18)$$

where $b = E[n_k] - n_k$ is the statistical bias. Assuming there is no statistical bias in the fit and evaluating the second derivative at $\mathbf{n}_k^{\hat{\max}}$, equation 7.18 reduces to [130]:

$$\hat{\sigma}_{\mathbf{n}_k^{\hat{\max}}}^2 = \left(-1 \bigg/ \frac{\partial^2 \ell}{\partial n_k^2} \right) \bigg|_{n_k = \mathbf{n}_k^{\hat{\max}}} \quad (7.19)$$

The variance on the fitted number of events of species k can be extracted graphically with a Taylor series expansion about $\mathbf{n}_k^{\hat{\max}}$:

$$\ell(n_k) = \ell(\mathbf{n}_k^{\hat{\max}}) + \left[\frac{\partial \ell}{\partial n_k} \right]_{n_k = \mathbf{n}_k^{\hat{\max}}} (n_k - \mathbf{n}_k^{\hat{\max}}) + \frac{1}{2!} \left[\frac{\partial^2 \ell}{\partial^2 n_k} \right]_{n_k = \mathbf{n}_k^{\hat{\max}}} (n_k - \mathbf{n}_k^{\hat{\max}})^2 + \dots \quad (7.20)$$

By the definition of the maximum likelihood, $\ell(\mathbf{n}_k^{\hat{\max}}) = \ell_{max}$, has a first derivative equal to zero. Thus, equation 7.20 can be combined with equation 7.19 to give the likelihood as a function of $\mathbf{n}_k^{\hat{\max}}$:

$$\ell(n_k) = \ell_{max} - \frac{(n_k - \mathbf{n}_k^{\hat{\max}})^2}{2\hat{\sigma}_{\mathbf{n}_k^{\hat{\max}}}^2} \quad (7.21)$$

which can be re-written as:

$$\ell(n_k \pm \hat{\sigma}_{\mathbf{n}_k^{\hat{\max}}}) = \ell_{max} - \frac{1}{2} \quad (7.22)$$

Equation 7.22 shows that a quadratic expansion about the maximum likelihood value of $\mathbf{n}_k^{\hat{\max}}$ can give an approximate estimate of the standard deviation. Thus, the standard deviation of $\mathbf{n}_k^{\hat{\max}}$ can be approximately given as a reduction of 1/2 from the maximum likelihood value. The maximum likelihood estimation procedure, described above, relies upon the likelihood function being approximately gaussian, such that the log-likelihood can be expanded as a quadratic about the maximum likelihood estimator and the standard deviation can be estimated. As a cross check, the marginalised log-likelihood for all species of events is fitted to a quadratic curve. If the $\tilde{\chi}^2/\text{DOF}$, where DOF is the degrees of freedom is between $0.7 < \tilde{\chi}^2/\text{DOF} < 1.3$, the fit is accepted and considered a valid quadratic function in log-likelihood space.

Figure 7.8 also includes the 2D marginalised likelihood distributions, which indicate the correlation between the extractions of different backgrounds. The PES and ^{210}Bi events are negatively correlated, because the PDF for PES events is peaked at around the same energy as the ^{210}B PDF (see figure 7.7). An increase/decrease in the number of events between 0.1 and 0.4 MeV could be attributed to either an increase in PES events or ^{210}Bi events. Since the total number of events is constrained, a choice of $\vec{\theta}$ with more PES events will have less ^{210}Bi events. A similar argument can be made between PES events and ^{14}C events. An increase in events at around 0.1 MeV is much more likely to be due to an increase in ^{14}C events rather than ^{210}Bi events.

An estimation of n_k using only one trial experiment may produce a statistical

fluctuation. Thus, 100 simulated experiments (for both the IH and NH cases separately) are performed at different SN distances. The average $\mathbf{n}_k^{\hat{\max}}$ and average $\hat{\sigma}_{\mathbf{n}_k^{\hat{\max}}}$ are taken from 100 simulated experiments, and figure 7.9 depicts the estimated number of PES events for both mass hierarchies in LAB and 0.5% Te-loaded LAB.

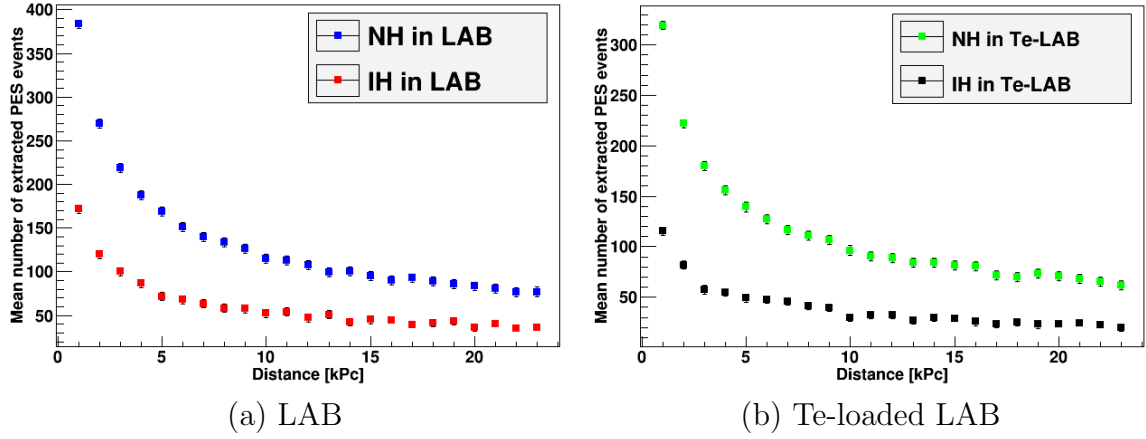


Figure 7.9: Average $\mathbf{n}_k^{\hat{\max}}$ and $\hat{\sigma}_{\mathbf{n}_k^{\hat{\max}}}$ over 100 trial experiments for PES events. The $\tilde{\chi}^2/\text{DOF}$ values, with $\text{DOF} = 22$, for this figure is given as (a) NH LAB ($\tilde{\chi}^2/\text{DOF} = 0.87$), IH LAB ($\tilde{\chi}^2/\text{DOF} = 0.96$) (b) NH Te-LAB ($\tilde{\chi}^2/\text{DOF} = 0.93$), IH Te-LAB ($\tilde{\chi}^2/\text{DOF} = 0.90$). This was repeated for 100 trial experiments per distance.

There is a distinguishable difference between the expected number of PES events in the inverted and normal mass hierarchies in figure 7.9. This difference becomes larger for SN at closer distances, as this corresponds to a greater flux of supernova neutrinos. The difference between IH and NH arises due to the spectral swapping, which yields a difference in the ν_x fluence, using the SN explosion model given in [31]. It is important to note that the total number of events is also affected by the SNO+ trigger threshold and throughout this thesis a trigger threshold of 0.1 MeV is assumed. A discussion on the systematics for this signal extraction is given in section 7.6.4.

The optical properties of Te-loaded LAB give a lower light yield than LAB. This is

equivalent to a reduction in the energy resolution. In te-loaded LAB, the energy resolution is reduced and smears a fraction of the PES PDF below the trigger threshold. In both LAB and Te-loaded LAB, there are more PES events in the normal hierarchy than the inverted hierarchy. This arises because the spectral swapping described by [31], shifts the shape of ν_x to lower energies in the inverted hierarchy, where as this isn't predicted to occur if neutrinos are subject to the normal mass hierarchy.

7.6.1 Verification of PES extraction

In order to test the signal extraction procedure, the bias and the pull are defined:

$$\begin{aligned} Bias &= \frac{N_{\text{fit}} - N_{\text{true}}}{N_{\text{true}}} \\ Pull &= \frac{N_{\text{fit}} - N_{\text{true}}}{\sigma_{\text{fit}}} \end{aligned} \tag{7.23}$$

where N_{fit} is the fitted number of events in the maximum likelihood procedure, N_{true} is the true number of events in the artificial data and σ_{fit} is the statistical uncertainty on the fitted number of events. The bias is the fraction shift of the fitted value from the true value and the pull is the significance of any statistical bias in the fitting procedure. For an unbiased PES extraction, the bias and pull should be a Gaussian distribution with a mean of zero. If the statistical uncertainty of the fit is correct, then the pull should have a Gaussian distribution with a width of 1.0. One of the requirements for applying the RCF inequality, in equation 7.19, is no statistical bias in the maximum likelihood estimation of the number of observable PES events. It is important to note that a supernova, at a small distance in the normal hierarchy has a much larger flux than the other fits.

Figure 7.10 depicts the mean bias for PES events in IH/NH and LAB/Te-loaded

LAB. The distribution of the bias is expected to be a Gaussian centred around 0 with a standard deviation of 1 and the $\tilde{\chi}^2/\text{DOF}$ for $\text{DOF} = 22$ is consistent with this expectation for all fits.

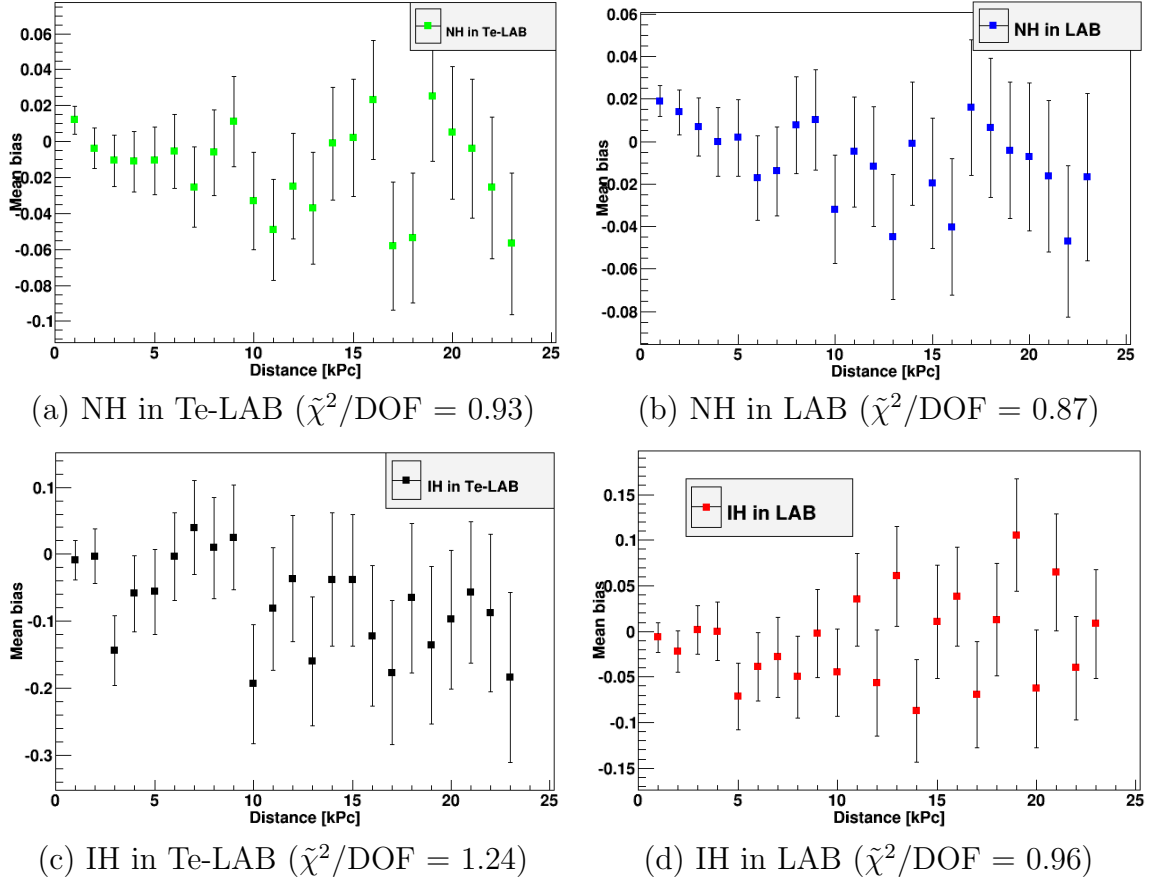


Figure 7.10: Mean bias of PES extraction for supernova at different distances with $\tilde{\chi}^2/\text{DOF}$ for $\text{DOF} = 22$

The mean pulls are given in figure 7.11. The pulls are a test to see if the distribution can be represented with a Gaussian distribution with a standard deviation of 1. In the normal hierarchy, are centred around zero with widths close to 1.0. The $\tilde{\chi}^2/\text{DOF}$ is again consistent with this hypothesis as the value of $\tilde{\chi}^2/\text{DOF}$ is between $0.5 < \tilde{\chi}^2/\text{DOF} < 1.5$ for all fits.

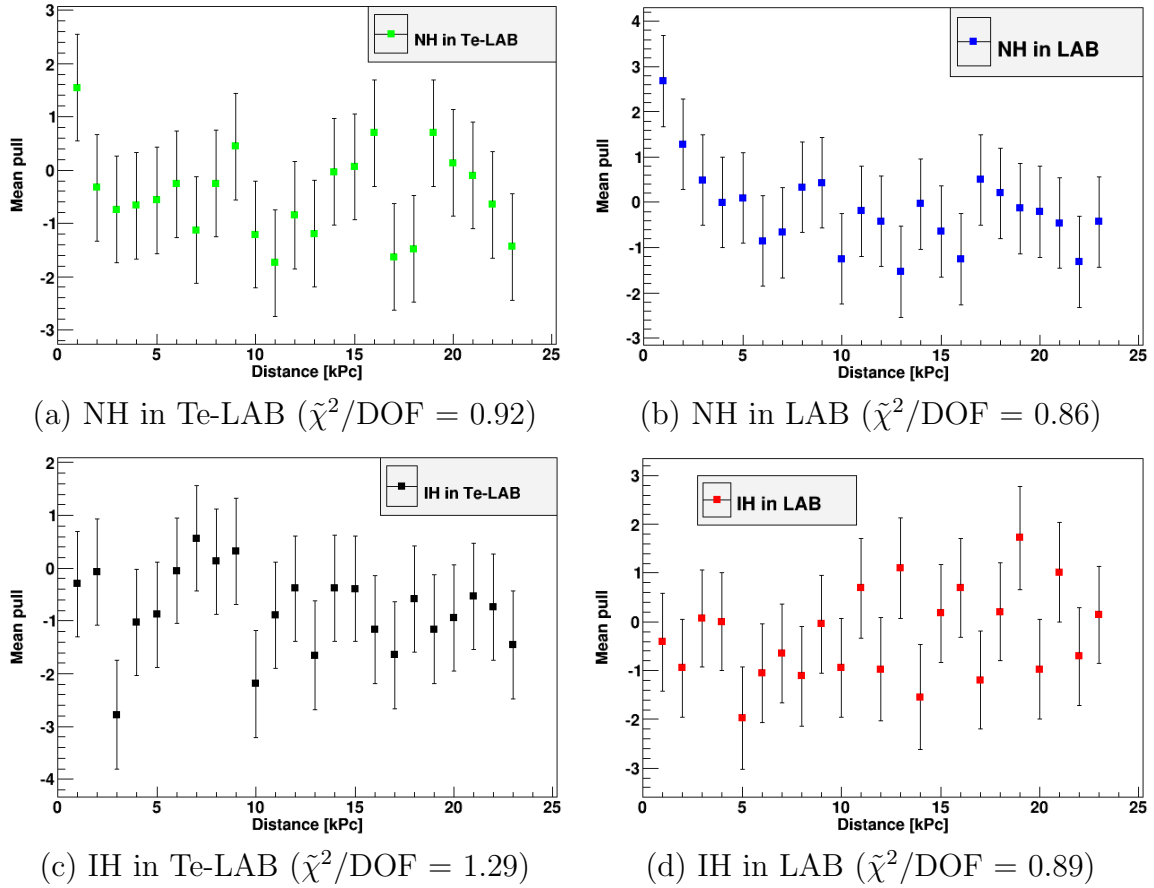


Figure 7.11: Mean pull of PES extraction for supernova at different distances with $\tilde{\chi}^2/\text{DOF}$ for $\text{DOF} = 22$

7.6.2 Ratio of PES to IBD events

The total number of PES events, measured during a SN burst would itself not be sufficient evidence to distinguish between the inverted and normal mass hierarchies. The ratio of IBD to PES events is a more powerful measurement for making a potential distinction between the inverted and normal mass hierarchies. There are many systematics in the model given in [31], which could affect the overall ν_x flux as well as systematics in the SNO+ response to protons. However, the spectral swapping would result in a dramatic change in the $\bar{\nu}_e$ and ν_x flux. Since SNO+ is uniquely capable of measuring the number of IBD and PES event simultaneously, the ratio of $\bar{\nu}_e/\nu_x$ can be constrained via the ratio of IBD/PES events.

IBD events can also be extracted above background events, because there are no high rate backgrounds at energies above 2.0 MeV and tagged by their delayed capture off nuclei. IBD events produce a prompt signal of at least 1.0 MeV, due to positron annihilation plus the kinetic energy of the positron, followed by a delayed ($\sim 100\text{s } \mu\text{s}$) capture of the IBD neutron on a nucleus. The IBD tagging efficiency has been measured for Borexino, a similar liquid scintillator experiment Borexino, which has an IBD tagging efficiency of $(85 \pm 1)\%$ [131]. This IBD tagging efficiency is assumed for SNO+ throughout this thesis.

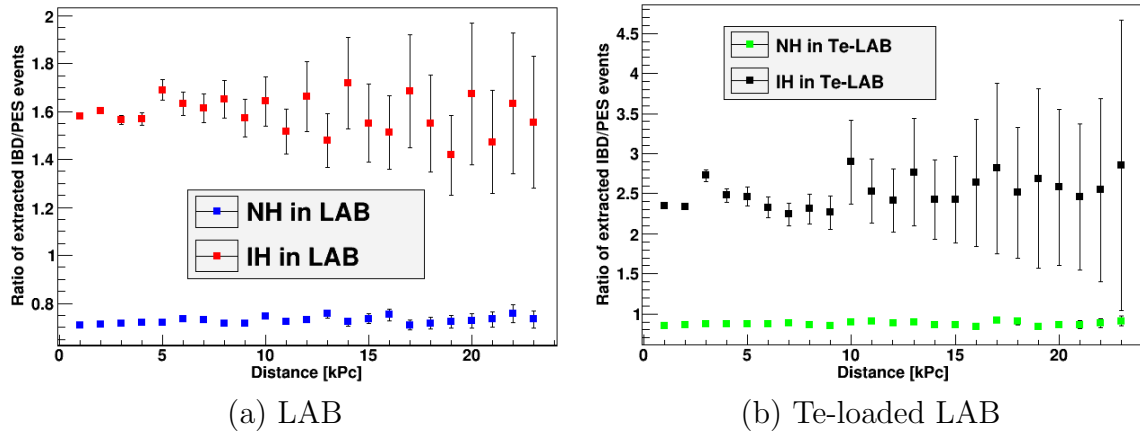


Figure 7.12: Extracted ratio of IBD to PES events for the normal and inverted mass hierarchies.

Figure 7.12 depicts the ratio of IBD to PES event in SNO+, errors from the IBD tagging and PES estimation are propagated into an overall error on the IBD/PES ratio. The ratio of IBD to PES events is smaller in the normal hierarchy, because the ν_x flux distribution is greater than in the inverted hierarchy at higher energies and thus, generates more PES events. The error on the ratio is larger, for the inverted hierarchy, because there are a smaller number of PES events and a higher uncertainty in the PES extraction. The total number of IBD events is the same in both mass hierarchies, because any change in the shape of the $\bar{\nu}_e$ flux distribution, doesn't shift IBD interaction below the trigger threshold. An

observation of spectral swapping, with a supernova at less than 5 kPC, would support the inverted mass hierarchy of neutrinos.

7.6.3 Systematic uncertainties

The ratio of IBD to PES events determines the sensitivity of SNO+ to the neutrino mass hierarchy from neutrinos originating from a supernova. This measurement has several systematic uncertainties associated with both the PES and IBD signal, which are discussed in this section. Any uncertainty in the underlying supernova dynamics model, which may affect the overall PES measurement, is discussed separately in section 7.6.4.

Energy resolution

Energy resolution significantly affects the extracted number of PES events, because a reduction in the energy resolution is equivalent to smearing the PDFs given in figure 7.7. The shape of the PES and background energy PDFs drives the effectiveness of the maximum likelihood estimation and a smearing of these PDFs reduces distinct features in each PDF, making it more difficult to distinguish key features. The energy resolution of SNO+ is approximately the square root of the number of PMTs hit (Nhits), in LAB the light yield is approximately 600 Nhits per MeV. Thus, at 0.1 MeV this is equivalent to 60 Nhits, giving an expected energy resolution of $\sim 13\%$. At energies just above the SNO+ trigger threshold, the majority of events are ^{14}C β -decay events, which have an endpoint of 0.154 MeV. It could be possible to compare the energy distribution close to the trigger threshold against the expected distribution of ^{14}C decay events and use this to estimate of the energy resolution at low energy. This can also be used to verify any bias in the energy reconstruction just above the SNO+ trigger threshold.

Nature of ^{210}Bi and ^{210}Po decays in SNO+

The rate of ^{210}Bi and ^{210}Po decays within the scintillator is determined by the rate of ^{210}Pb leeching from the AV into the SNO+ detector. It is also assumed, throughout this thesis, that these decays are homogeneously distributed throughout the detector. The homogeneity of these events should be tested, otherwise the rate of $^{210}\text{Bi}/^{210}\text{Po}$ decays could be overestimated and bias the maximum likelihood fit. The rate of $^{210}\text{Bi}/^{210}\text{Po}$ decays is used to constrain the likelihood space affects and the maximum likelihood estimation: a smaller uncertainty in these decay spectra will improve the constraints and reduce the estimation uncertainty; a larger uncertainty will reduce the constraints and increase the estimation uncertainty. The rate of $^{210}\text{Bi}/^{210}\text{Po}$ decays will also be cross-checked via radio-assays of LAB extracted from the AV [132].

Quenching model of protons in SNO+

The visible energy distribution of PES events is very sensitive to the quenching model (given in equation 7.9) and the light yield of protons, which are quenched by a factor of ~ 10 . The current quenching model for LAB and Te-loaded LAB has been verified by Belina von Krosigk [15], using a proton accelerator to fire protons at LAB and Te-loaded LAB targets. But the proton response is highly sensitive upon the scintillator cocktail and these measurements would have to be repeated with the finalised Te-loaded scintillator.

Pile-up model

In-window pile-up occurs when two or more types of event occur within the same trigger window. The SNO+ trigger window is ~ 440 ns long and thus it is possible for different combinations of events to ‘pile-up’ in the same event window. Pile-up events affect the measured energy distribution between 0.1 and 2.0 MeV and will increase the uncertainty in the statistical fit from the maximum likelihood proce-

dure. The rate of pile-up, within a 10s, is likely to be very small. The pile-up from the Borexino experiment between 0.1 - 1.0 MeV was less than 100 events per day [133]. But this will also need to be verified, during the SNO+ unloaded and Te-loaded scintillator phases.

7.6.4 Supernova model uncertainties

There are many uncertainties in the supernova core collapse model given in [31], which define the total flux of neutrinos, the energy distribution of $\nu_x/\bar{\nu}_e$ and the mechanics of spectral swapping, in the inverted mass hierarchy, are beyond the scope of this thesis. The dominant systematics are the average thermalised neutrino energy [31] and the total neutrino flux of a galactic supernova, which would be constrained by astronomical observations of the luminosity and distance. The average thermalised energy of the supernova neutrinos, $\langle E_{\nu_x} \rangle$ determines the shape of the ν_x flux. The total expected number of PES events, as a function of SNO+ trigger threshold, is given in figure 7.13. For a 0.1 MeV threshold, between 220 and 270 events expected (a difference of around 20% depending on $\langle E_{\nu_x} \rangle$).

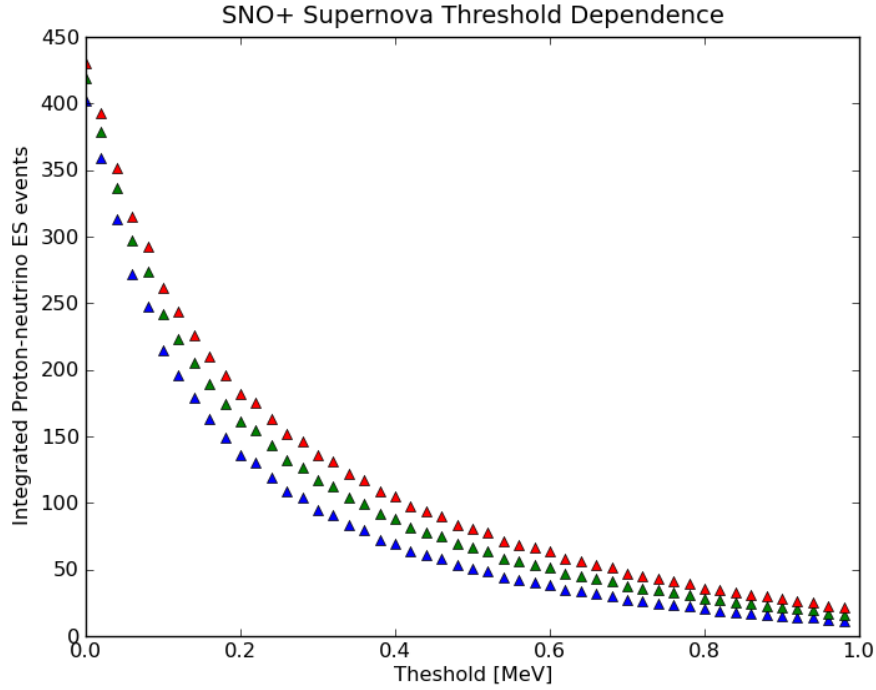


Figure 7.13: The expected number of SN neutrinos in SNO+ for different energy trigger thresholds. **Red** corresponds to $\langle E_{\nu_x} \rangle = 20$ MeV, **green** corresponds to $\langle E_{\nu_x} \rangle = 18.0$ MeV and **blue** corresponds to $\langle E_{\nu_x} \rangle = 15.0$ MeV

7.7 Conclusion

SNO+ should be capable of extracting a good estimate on the number of PES and IBD events, during a burst of supernova neutrinos lasting for ~ 10 s, with a fiducial volume of 5.5m and a trigger threshold of 0.1 MeV. The constrained, extended maximum likelihood procedure, described in this chapter, can be used to extract a PES signal from conservative estimates on the rates of internal ^{210}Bi , ^{210}Po and ^{14}C decays. Depending on the supernova model and given a sufficient neutrino flux, the measurement of the ratio of IBD/PES events would give evidence for a neutrino mass hierarchy in the supernova explosion model from [31].

8

Conclusion

SNO+ should be capable of measuring two types of rare astrophysical signal: ALPs originating from the Sun and the ratio of PES/IBD events from a burst of supernova neutrinos, originating from supernova core collapse at distances up to 20 kPc away from the Earth. ALPs are a proposed pseudo-scalar particle that could explain a fraction of the observed dark matter within the Universe. The axio-electric effect, inverse Primakoff effect and Compton scattering of ALPs have been simulated and validated within the SNO+ simulation framework. During the unloaded and Te-loaded scintillator phases of SNO+, the dominant external backgrounds from ^{208}Tl decays in the AV, outer water and PMTs, can be mitigated by taking a fiducial volume cut of $R < 5500$ mm. The dominant internal backgrounds to ALPs are ^{208}Tl decays and solar neutrinos. The internal ^{208}Tl backgrounds could be mitigated by a timing based discrimination, if the concentration of Thorium, is significantly higher when the SNO+ detector is fully commissioned.

Due to the large size and lower muon flux relative to Borexino, SNO+ will be able to set improved bounds on ALP couplings after 6 months of unloaded scintillator phase. SNO+ will predominantly operate in the Te-loaded scintillator phase and will be able to improve the sensitivity of ALP coupling to electrons, by an

order of magnitude above the limit set by BGO, giving a limit of:

$$|g_{Ae} \times g_{3AN}| < 0.7 \times 10^{-11} \quad (8.1)$$

via the axio-electric effect and after 5 years of Te-loaded scintillator. The loading of Tellurium into SNO+ is crucial for this interaction, because the AE cross section is enhanced by Z^5 with $Z_{\text{Te}} = 52$. SNO+ will also be able to improve the current limit of the ALP-photon coupling, by an order of magnitude above the limit set by Borexino, giving limit of :

$$|g_{A\gamma} \times g_{3AN}| < 2.9 \times 10^{-11} \text{ GeV}^{-1} \quad (8.2)$$

via the inverse Primakoff effect and after 5 years of Te-loaded scintillator.

It has also been shown that large water Cherenkov detectors may have significant potential to limit the ALP coupling to electrons via the Compton conversion of ALPs. Despite the lower light yield and higher concentration of Thorium in water Cherenkov detectors, the direction of CCA events can be reconstructed relative to the Sun. A directional cut, in SNO+ water phase, could reduce the background levels by an order of magnitude, whilst keeping $\sim 80\%$ of the CCA signal. This gives SNO+ water phase an ALP-electron coupling sensitivity comparable to Borexino, but is particularly exciting for several other large water Cherenkov experiments. It could set a limit of the ALP coupling to electrons, which is an order of magnitude better than the current Borexino limit, assuming a trigger threshold at visible energies > 4.5 MeV. This enhances the prospects for Large Underground Neutrino (LUN) experiments, such as SNO+ and Super Kamiokande, but also highlights the different strategies for ALP analysis in water Cherenkov and liquid scintillator experiments loaded with high Z isotopes, such as Tellurium in SNO+

The observation of a 10s burst of supernova neutrinos is one of the physics goals of SNO+. These neutrinos are composed of a mixture of electron, tau and muon neutrinos. SNO+ is uniquely sensitive to all the flux of all flavours of neutrino (ν_x), via the proton elastic scattering (PES) interaction, due to the relatively low energy trigger threshold. It has been shown that the PES signal can be extracted, within a 10s event window, against conservative estimates of the rates of ^{210}Bi , ^{210}Po and ^{14}C decays and assuming a SNO+ trigger threshold of 0.1 MeV.

The extraction of a simulated PES signal was performed using a constrained, extended maximum likelihood method, where the biases and pulls of 100 artificial experiments were used to verify the performance of such an extraction. It is also possible to extract IBD events within the scintillator phase and thus, make the measurement of the ratio of PES/IBD events, which was used to calculate the $\nu_x/\bar{\nu}_e$ flux ratio. In the Fogli *et al.* [31] supernova core collapse model, if neutrinos follow the inverted mass hierarchy, the ν_x and $\bar{\nu}_e$ flux distributions are predicted to dramatically ‘swap’ due to neutrino-neutrino forward scattering. SNO+ could potentially observe this effect, for a core collapse supernova at distances less than 20 kPc away from the Earth. This has been explored for the unloaded scintillator phase of SNO+, but is applicable to the Te-loaded scintillator phase with a small reduction in the energy resolution.

This thesis also outlines my contribution to the commissioning of the DAQ and SMELLIE systems. It describes the commissioning work that I have completed, in order to prepare the SNO+ experiment for data taking and scattering calibration. For the DAQ, this involved implementing the database records for all the hardware in the SNO+ experiment and updating the monitoring systems. For SMELLIE, this involved implementing the SMELLIE software and the integration

with the DAQ. The analysis of SMELLIE data from the December 2014 SNO+ runs, demonstrate that laser light is being injected into the detector, the SMELLIE system has been successfully integrated into the DAQ and is prepared for taking scattering calibration measurements once SNO+ is fully commissioned.

Appendix A

Statistical limit setting technique for ALPs

This section describes the technique used for setting Bayesian limits on ALP couplings. The upper limit on the number of ALP events, S_{events} is given as:

$$S_{events} = \Phi_A \sigma N T \epsilon \leq S_{90\%} \quad (\text{A.1})$$

where σ is the cross section for a particular ALP interaction, N is the number of targets (e.g. number of electrons or nuclei targets), T is the measurement time (in seconds), ϵ is the detection efficiency of a given ALP interaction and $S_{90\%}$ is the 90% confidence limit on the number of events observed. The ALP coupling to nucleons (g_{3AN}) is included in Φ_A and the ALP coupling to either electrons (g_{Ae}) or photons ($g_{A\gamma}$) is included in the cross section such that:

$$|g_{3AN}^2 \times g_{A\gamma, Ae}^2| \propto \left(\frac{S_{90\%}}{N T \epsilon} \right)^{\frac{1}{2}} \quad (\text{A.2})$$

The number of targets, exposure time and detection efficiency for ALPs are either quoted or calculated for a given experiment. The $S_{90\%}$ limit is calculated

throughout this study using the O'Helene method [134] where:

$$\frac{\int_{0.0}^{S_{90\%}} (s+b)^n \times e^{-(s+b)}/n!}{\int_{0.0}^{\infty} (s+b)^n \times e^{-(s+b)}/n!} = 0.9 \quad (\text{A.3})$$

with an observed signal (s), an expected background level (b) and an observed number of events (n). $S_{90\%}$ is the 90% Bayesian confidence limit with a Uniform prior. Equation A.3 can be reduced [135], using the lower incomplete gamma function Γ_{LIC} and gamma function Γ :

$$\begin{aligned} \Gamma(t) &= \int_0^{\infty} x^{t-1} \exp^{-x} dx \\ \Gamma_{\text{LIC}}(s, x) &= \int_0^x t^{s-1} \exp^{-t} dt \end{aligned} \quad (\text{A.4})$$

such that:

$$\frac{\Gamma_{\text{LIC}}(n+1)(S_{90\%}+b) - \Gamma_{\text{LIC}}(n+1)(b)}{\Gamma(n+1) - \Gamma_{\text{LIC}}(n+1)(b)} = 0.9 \quad (\text{A.5})$$

for all complex numbers, except the non-positive integers.

In lieu of access to the full simulation and data for other experiments, an estimate of the ALP coupling sensitivity relative to Borexino is given as:

$$\frac{\text{Experiment X}}{\text{Borexino}} = \sqrt{\frac{\epsilon_X}{\epsilon_{\text{BOR}}} \times \frac{\rho_X}{\rho_{\text{BOR}}} \times \sqrt{\frac{B_{\text{BOR}}}{B_X}}} \quad (\text{A.6})$$

where $\epsilon_{X,\text{BOR}}$ is the ALP detection efficiency of experiment X and Borexino respectively, $\rho_{X,\text{BOR}}$ is the exposure time of the experiment in kTonne-yrs and $B_{X,\text{BOR}}$ is the number of backgrounds. Borexino is currently the only large neutrino experiment to publish results on all ALP couplings and is used as a benchmark throughout this thesis. Large neutrino experiments looking to set upper limits on ALP couplings, are not only sensitive to g_{Ae} or $g_{A\gamma}$, but must account for the solar ALP production.

Appendix B

ALP detection in SNO+ water phase

The CCA interaction for ALPs corresponds to > 3.5 MeV electron equivalent energy deposited within SNO+ water phase and can capitalise on the directional information maintained by the Compton conversion of ALPs.

There are relatively few backgrounds, at energies greater than 3.5 MeV in SNO+ water phase. With the exception of solar neutrinos (or ^8B neutrinos), backgrounds are predominantly isotropic and a directional cut of $\cos(\theta_{\text{sun}}) > 0.8$ reduces these backgrounds by an order of magnitude (whilst maintaining $\sim 80\%$ of signal events). These backgrounds are predominantly naturally occurring amounts of Uranium and Thorium, which are present within the water. The dominant decay observed from Thorium chain, originates from ^{208}Tl decay, which produced β particles up to an energy of 1.8 MeV and associated gammas with energies at around 2.6 MeV. The dominant decay in the Th chain, a β decay with an endpoint of 3.3MeV with associated gammas.

Backgrounds	Interactions per year	Source
Solar (after oscillations)	678	SNO B8 Paper
Bi214 (Internal)	1.24×10^7	SNO+ Backgrounds [81]
Bi214 (HDR)	4.06×10^7	SNO+ Backgrounds [81]
Bi214 (AV)	1.29×10^6	SNO+ Backgrounds [81]
Tl208 (Internal)	1.46×10^5	SNO+ Backgrounds [81]
Tl208 (HDR)	2.32×10^6	SNO+ Backgrounds [81]
Tl208 (AV)	1.50×10^6	SNO+ Backgrounds [81]
Reactor (after oscillations)	110	I.Coulter PhD Thesis [2]

Table B.1: Estimated backgrounds levels for the SNO+ water phase compared to the H₂O shielding and D₂O internal backgrounds from the SNO experiment

External Backgrounds originate from Uranium and Thorium present within the Acrylic vessel (AV), Hold Down Ropes (HDR), the outer water shielding and U/Th within the glass of the PMTs. External background events are decays, which have reconstructed within the fiducial volume, despite originating from outside the AV. The solar background originates from the measured flux of solar neutrinos, which will be detected within the water loaded detector. Reactor neutrino backgrounds originate from the neutrino flux of reactors located within ~ 100 km's of the SNO+ detector, which also includes a small component of geoneutrinos.

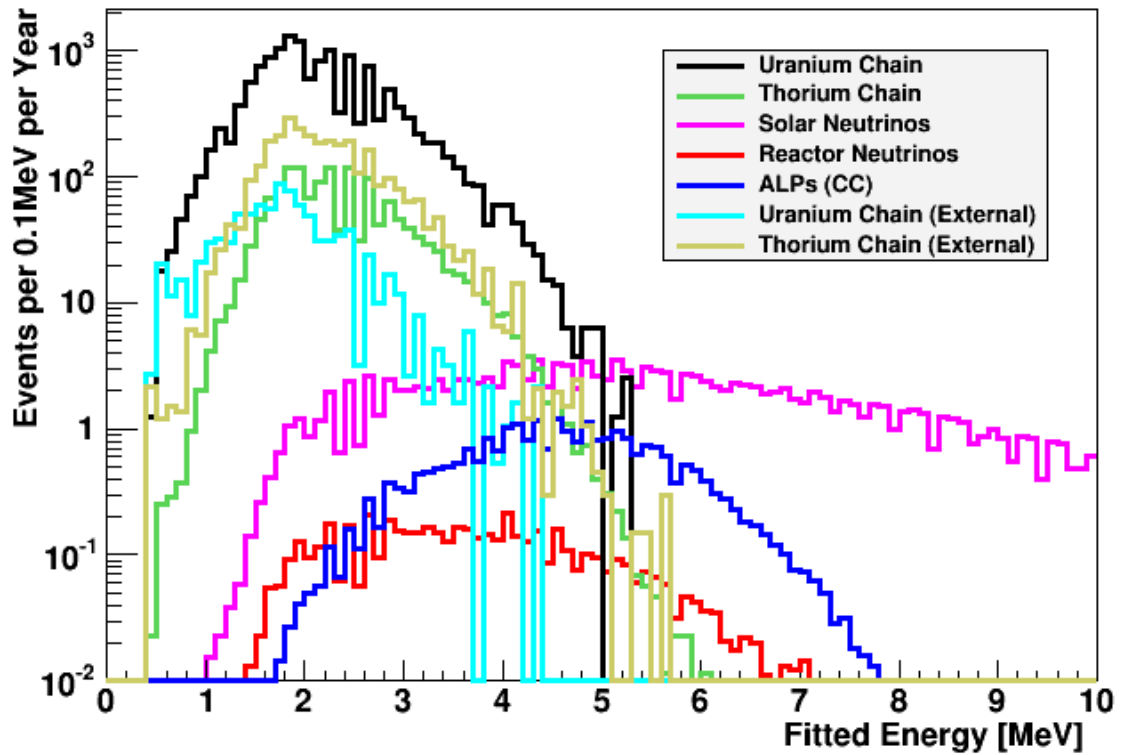


Figure B.1: Estimated number of observed backgrounds for SNO+ in water phase for 1 year, after a Fiducial volume cut of 5.5m and a directional cut of $\cos(\theta_{\text{int}}) > 0.8$ used for ALP analysis. There is a significant reduction in any isotropic background due to an angle of $\cos(\theta_{\text{int}}) > 0.8$. The ALP signal is normalised to the 30 ALP events per year, which is approximately the current limit set by Borexino.

Backgrounds (per year)	4.5 - 7.0 MeV	5.5 - 9.0 MeV	6.0 - 9.0 MeV
Solar	63.9	60.7	48.0
Tl208 (AV)	6.1	0.0	0.0
Tl208 (HDR)	0.0	0.0	0.0
Tl208 (Internal)	5.8	0.1	0.0
Bi214 (HDR)	0.0	0.0	0.0
Bi214 (AV)	1.4	0.0	0.0
Bi214 (Internal)	40.3	0.0	0.0
Reactor	0.4	0.2	0.1
Total	117.9	60.9	48.1

Table B.2: Expected background counts to an ALP signal after a fiducial volume cut of 5.5m and a directional cut of $\cos(\theta_{\text{int}}) > 0.8$

Considering the ALP flux, we can equate the ALP interaction (S) as:

$$S = \Phi_{\nu pp} \left(\frac{\omega_A}{\omega_\gamma} \right) \sigma_{ALP} N_t T \epsilon \quad (\text{B.1})$$

where σ_{ALP} is the cross section of a given ALP interaction such as Compton conversion interaction. $\Phi_{\nu pp}$ is the flux of pp neutrinos at the Earth, $\frac{\omega_A}{\omega_\gamma}$ is the ratio of M1 magnetic nuclear transition with axion production against γ production, N_t is the number of electron targets, T is the exposure time (in seconds) and ϵ is the signal efficiency for ALPs. Using analysis performed in [71], we can reduce equation 5.6 for 6 months of SNO+ water using:

- $N_e = 2.33 \times 10^{32}$ electrons
- $T(6 \text{ Months}) = 1.58 \times 10^7$ s

Using the O'Helene method [134], the limit than SNO+ can set on $|g_{Ae} \times g_{3AN}|$ is dependent upon the actual background measurement that will be taken within a given energy window. For example, a 1σ background fluctuation upwards would reduce our limit setting capabilities, whereas a 1σ fluctuation downwards would improve our upper limit on ALP couplings.

In lieu of SNO+ water data, an ensemble of experiments for an expected background is given in figure B.2. The median of each of these distributions is chosen due to the skewness of the distribution. Thus, the SNO+ limit of 6 months of water using an energy window between 4.5-7.0 MeV:

$$|g_{Ae} \times g_{3AN}| \leq 1.3 \times 10^{-12} \quad (\text{B.2})$$

which is comparable to the Borexino [71] limit of $|g_{Ae} \times g_{3AN}| \leq 5.5 \times 10^{-13}$.

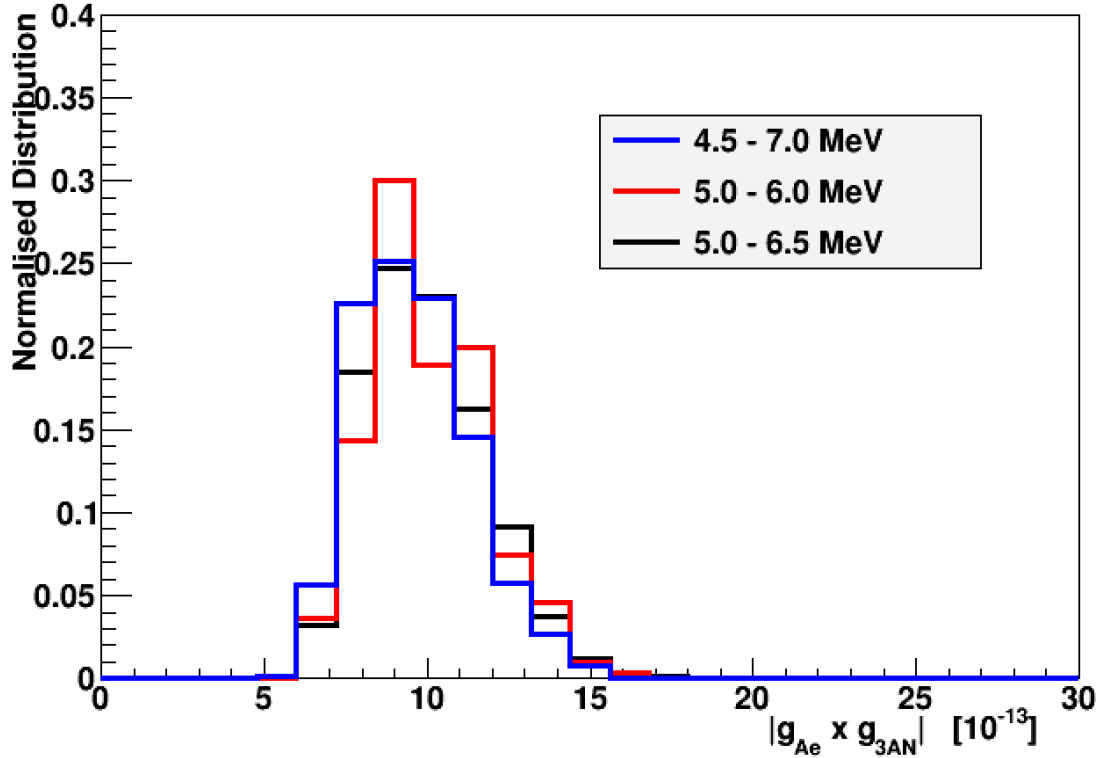


Figure B.2: Ensemble of 1000 different potential measurements of $|g_{Ae} \times g_{3AN}|$, for 6 months of SNO+ water phase. A statistical ensemble of observed events (n) applied to equation A.5 are calculated from a Poisson fluctuation about the expected background rate.

Energy Window (MeV)	Efficiency	Expetd Bkg.	$ g_{Ae} \times g_{3AN} [10^{-13}]$
4.5 - 7.0	0.3	117.9	12.7
5.0 - 6.0	0.15	75.7	14.4
5.0 - 6.5	0.18	98.4	14.4

Table B.3: Median values taken from statistical ensemble from figure B.2 for one year of SNO+ water phase

Appendix C

$|g_{Ae} \times g_{3AN}|$ in SNO+ scintillator phase

Taking a fiducial volume cut of 5.5m for SNO+ Water Phase and running for 6 Months gives approximately 0.35 kTonne-yrs exposure. Borexino over its entire live-time had approximately an exposure of 0.146kTonne-yrs with around 10 background events in the energy window. Thus, the expected relative sensitivity of SNO+ (6 Months of Scintillator) to Borexino is:

$$\frac{\text{SNO+ (6 Months of Scintillator)}}{\text{Borexino}} \sim \sqrt{\frac{0.35}{0.146}} \times \sqrt{\frac{10}{55}} = \sqrt{1.02} = 1.0 \quad (\text{C.1})$$

Thus an *a priori* estimate, for 6 Months of SNO+ scintillator phase, is $|g_{Ae} \times g_{3AN}| \leq 5.4 \times 10^{-13}$

Energy Window (MeV)	Efficiency	Expctd Bkg.	$ g_{Ae} \times g_{3AN} $
5.1 - 5.7	0.71	40	4.8
5.0 - 6.0	0.73	57	5.6
5.4 - 6.0	0.45	25	5.4

Table C.1: Median values taken from the statistical ensemble of the Compton conversion of ALPs in figure C.2. The additional energy window cuts between 5.0-6.0 MeV and 5.0-6.5 MeV have been included for completeness. The units of $|g_{Ae} \times g_{3AN}|$ are 10^{-13} .

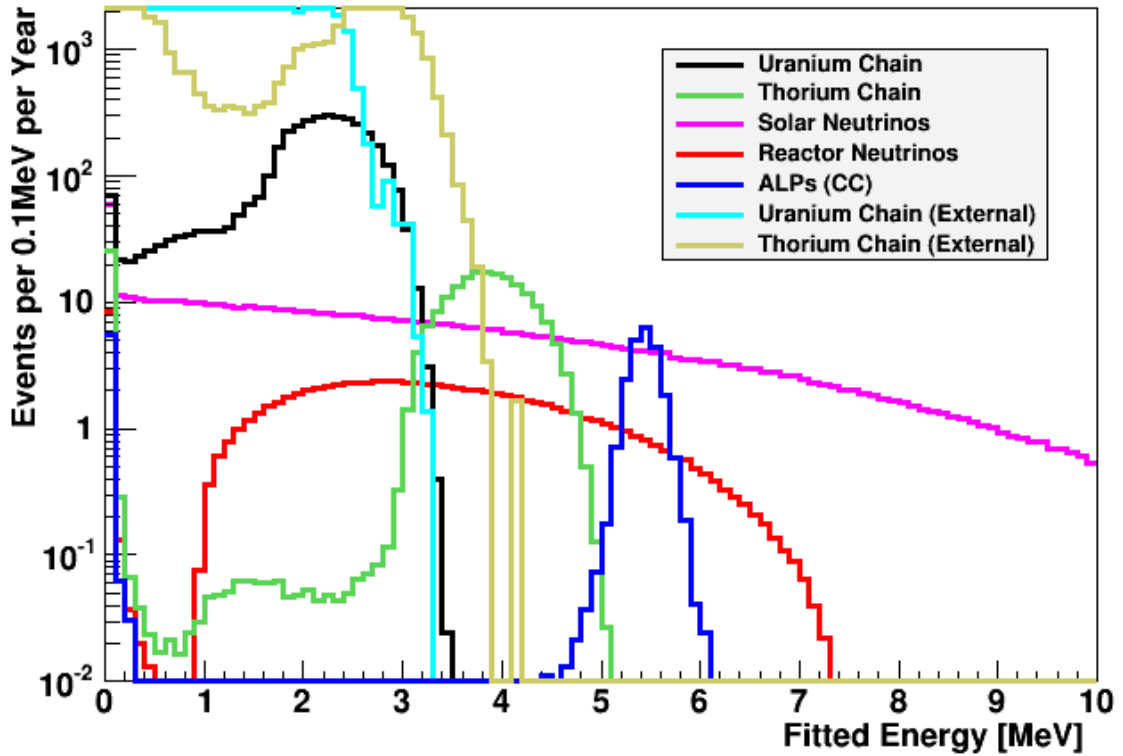


Figure C.1: Estimated number of observed backgrounds for SNO+ in scintillator phase for 1 year, after a Fiducial volume cut of 5.5m. This includes the ALP energy spectrum for the Compton conversion of axions originating from the sun.

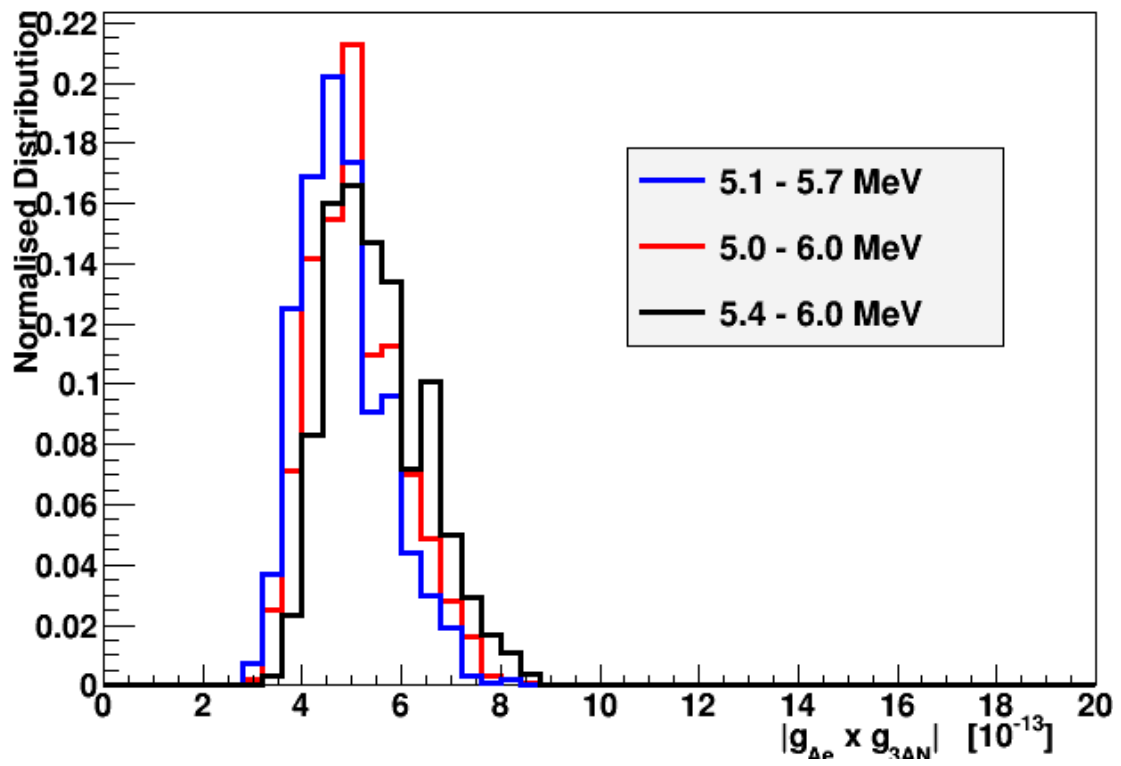


Figure C.2: Ensemble of 1000 different potential measurements of $|g_{Ae} \times g_{3AN}|$, where the number of observed events is a Poisson fluctuation of the expected background rate.

Figure C.1 shows the energy spectrum of the backgrounds and Compton conversion of ALPs in one year of SNO+. Taking table C.1 gives $|g_{Ae} \times g_{3AN}| \leq 5.4 \times 10^{-13}$ with a 5.4 - 6.0 MeV energy window. This energy window is chosen because it approximately represents the 1σ region around the peak of the energy distribution of Compton conversion of ALPs.

Appendix D

Distinct ALP signals in SNO+ water phase

The majority of the predicted ALP signals are very difficult to distinguish between other physics events on an event by event basis. The Compton conversion of an ALP produces an electron (typically $\sim 2.5\text{MeV}$) and a γ (typically $\sim 3\text{MeV}$). The electron produces a Cherenkov cone, which has a much higher light yield than the γ -ray in water. The γ -ray has to Compton scatter and produce an electron of around 1MeV , just above the Cherenkov threshold, in order to produce visible light. This produces a secondary vertex, with a secondary Cherenkov cone and could provide a very distinct signal of ALP interactions in the SNO+ detector.

In order to achieve any form of 'double' Cherenkov fitting algorithm, there must be a sufficient fraction of PMTs observing photons outside the reconstructed Cherenkov cone, which are above the detector noise. If a significant fraction of the PMT hits are outside the cone, it may be possible to observe a 'double' Cherenkov cone from subsequent Compton scattering of the γ particle.

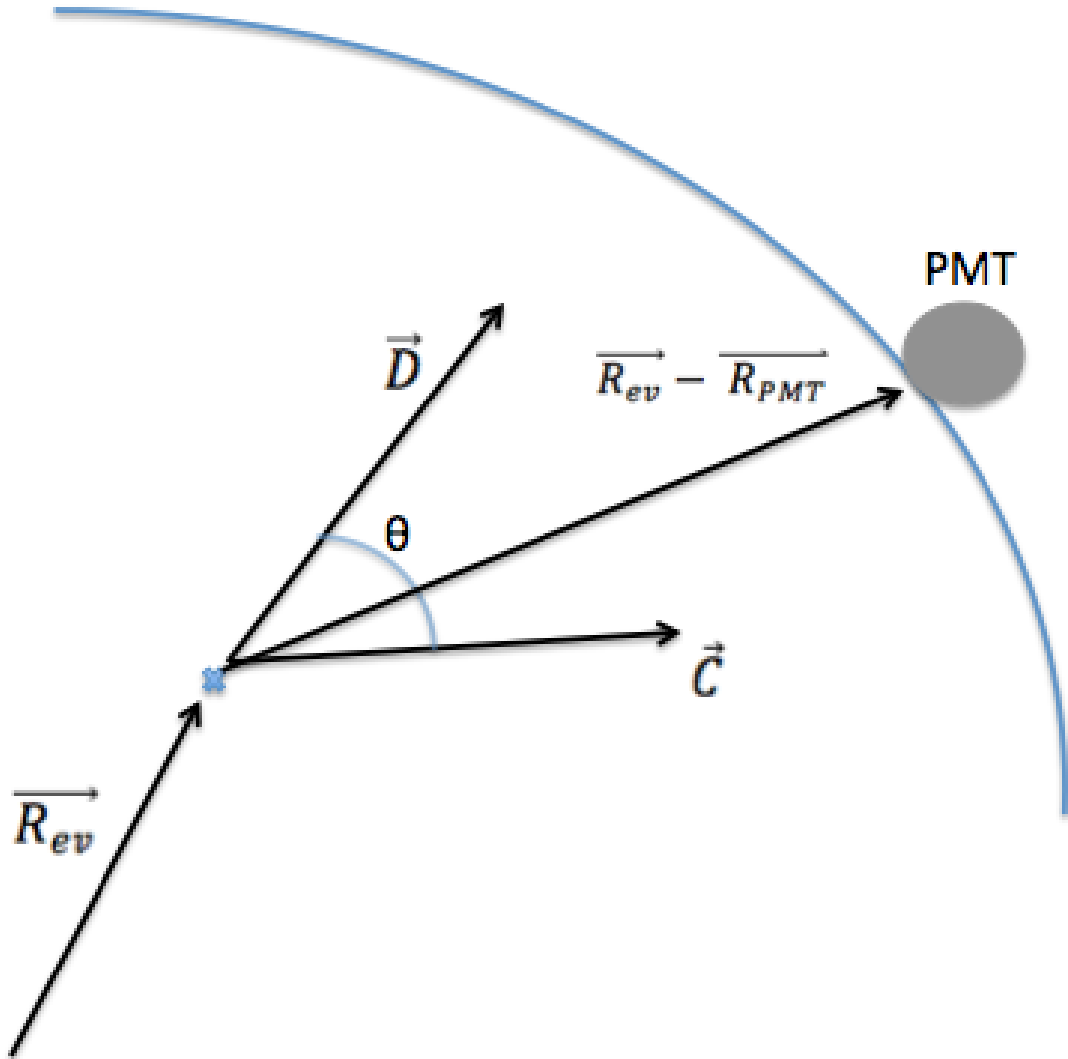


Figure D.1: Description of how to spot PMTs contained within an additional, weak Cherenkov ring

Figure D.1 illustrates how searches for an extra Cherenkov cone could be statistically performed. In figure D.1, $\hat{\mathbf{R}}_{ev}$ is the unit event position vector, $\hat{\mathbf{R}}_{PMT}$ is the unit PMT position vector, $\hat{\mathbf{D}}$ is the reconstructed direction unit vector, θ is the Cherenkov angle between $\hat{\mathbf{D}}$ and $\hat{\mathbf{C}}$, where $\hat{\mathbf{C}}$ is the unit vector representing the largest Cherenkov opening angle with respect to $\hat{\mathbf{D}}$ such that:

$$(\hat{\mathbf{R}}_{ev} - \hat{\mathbf{R}}_{PMT}) \cdot \hat{\mathbf{D}} < \hat{\mathbf{C}} \cdot \hat{\mathbf{D}} \quad (\text{D.1})$$

If the statement in equation D.1 is true, for a given PMT vector, then the a given PMT is considered to be within the Cherenkov cone of the event. Otherwise that PMT is considered to be outside. By taking all of the triggered PMTs for each event, the fraction of PMTs within the cone as a total of all triggered PMTs can be calculated.

Figure D.2 shows the histogram of the fraction of PMTs hit outside the Cherenkov cone for a set of 2.5MeV electrons against a set of Compton conversion ALP events.

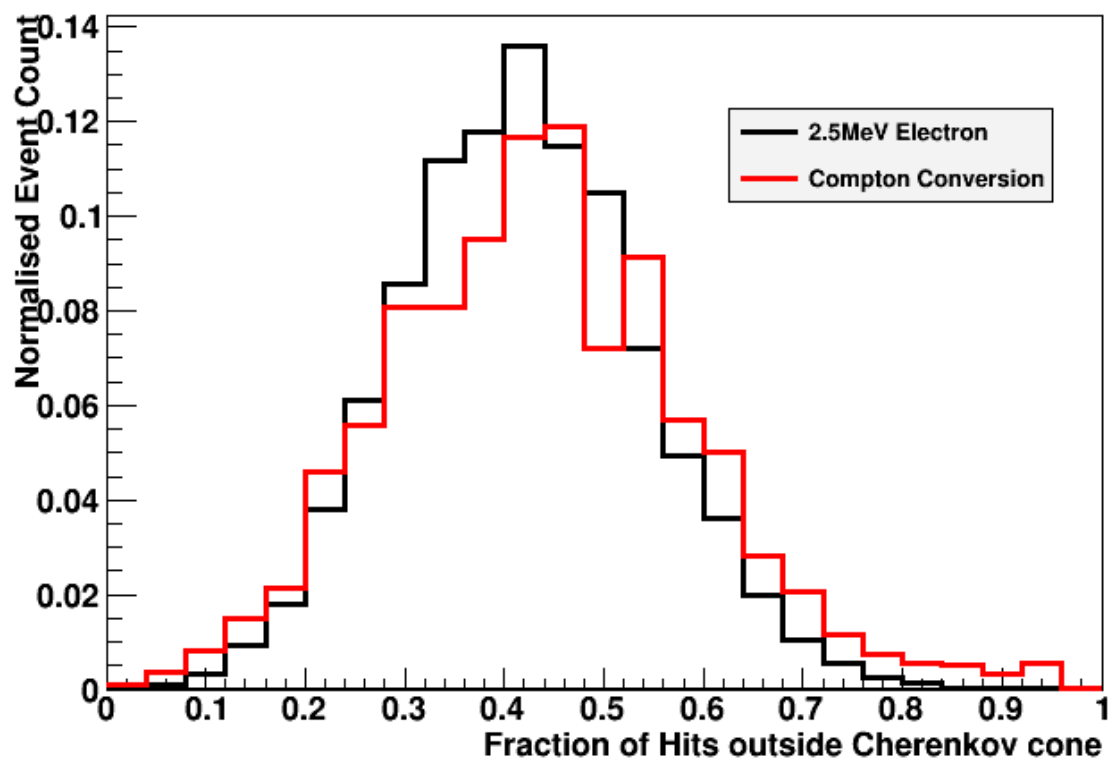


Figure D.2: Fraction of PMT hits outside the Cherenkov cone for electron events (black) and Compton conversion of ALPs (red). This shows that a separation between these two types of events would be very difficult to achieve. Both sets of data were randomly generated across the entire detector with a random direction.

Figure D.2 is a simplified picture because there is a continuum (see figure 5.2) of how energy is distributed between the electron and γ particle from the Compton conversion of an ALP. Strictly, this should compare a continuum of energy, however there is a broad tail of Compton conversion events that have more than 80% of

the PMT hits outside of the reconstructed Cherenkov cone. This could arise due to a significant fraction of the ALPs energy transferred to the γ particle with an immediate Compton scatter of an electron possibly combined with a specific geometry.

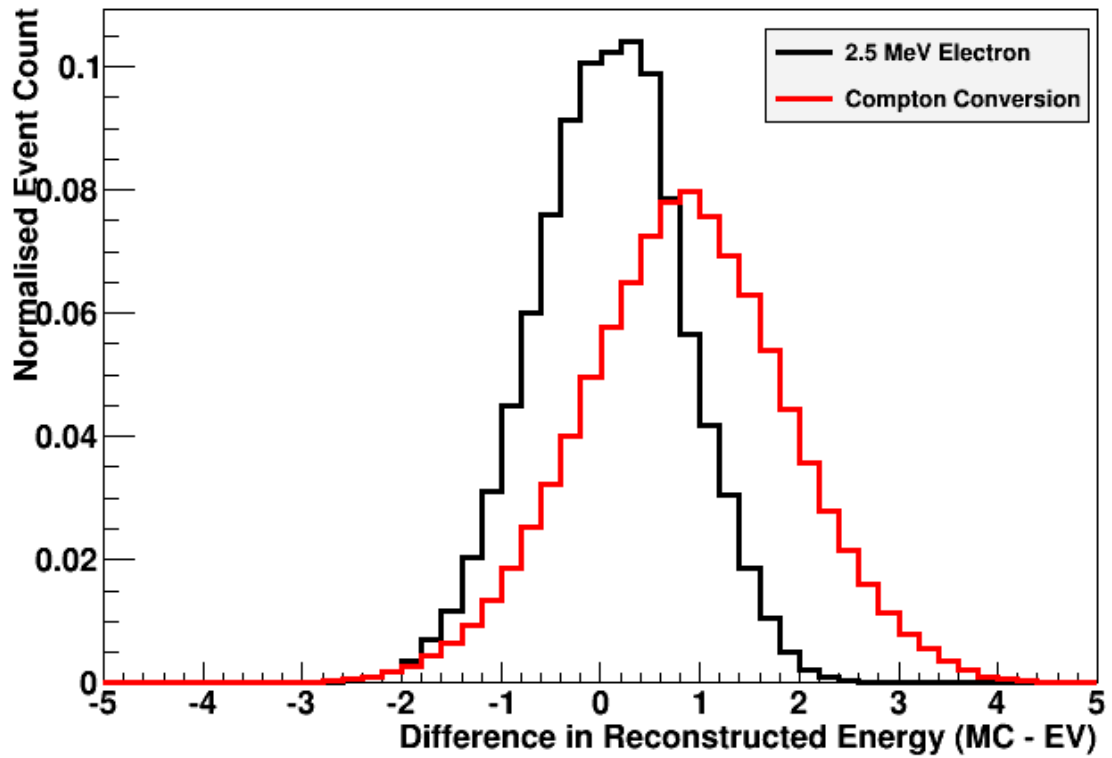


Figure D.3: Difference between the total MC kinetic energy and reconstructed energy for electrons at 2.5 MeV against Compton conversion interactions in water.

Appendix E

$\Delta\mathcal{L}$ cut for ALPs

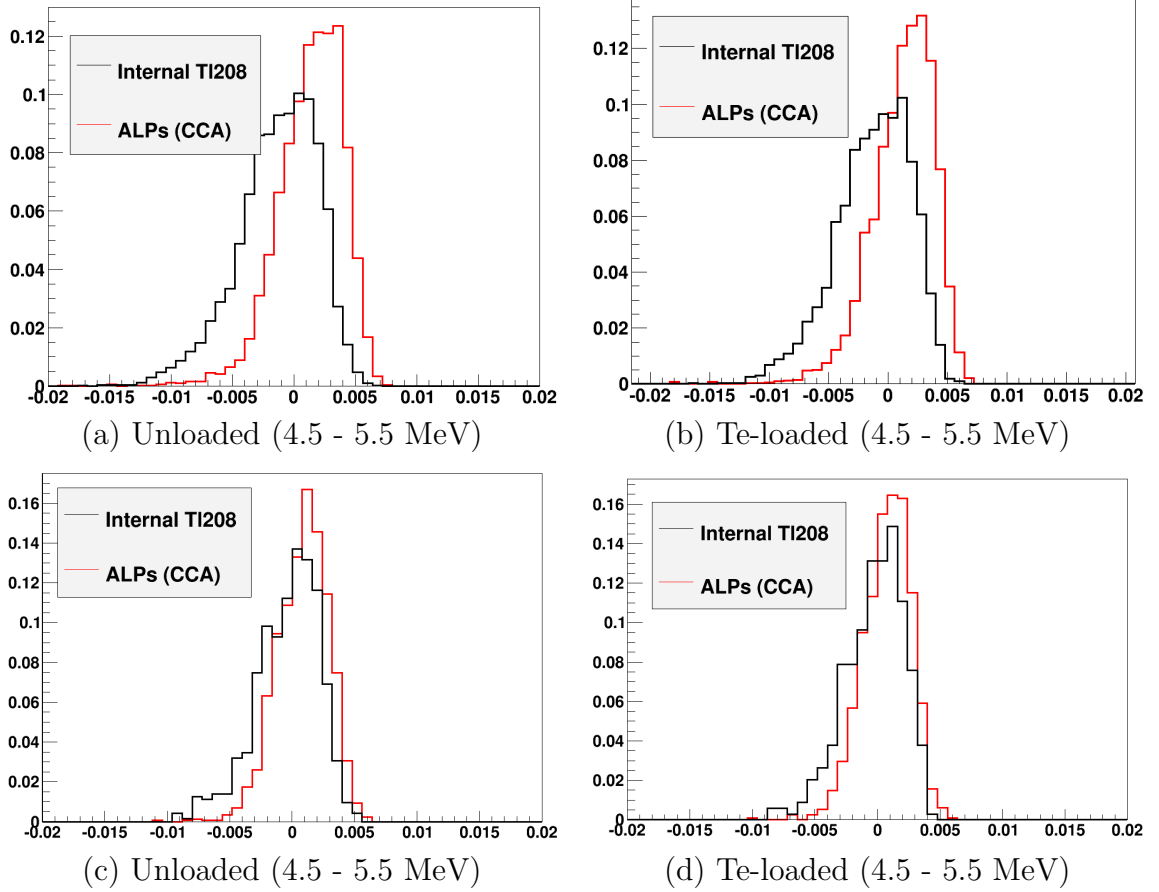


Figure E.1: Distributions of $\Delta\mathcal{L}$ for ALPs in unloaded scintillator

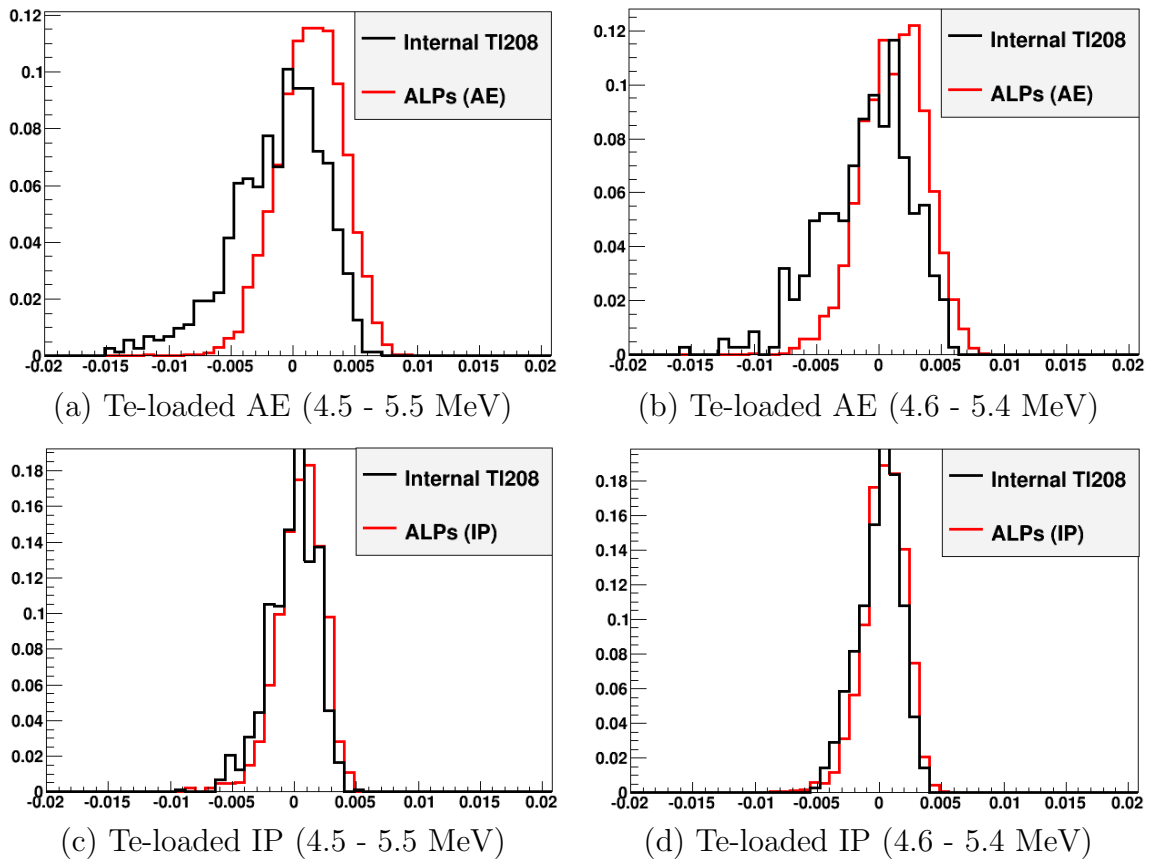


Figure E.2: Distributions of $\Delta\mathcal{L}$ for ALPs in Te-loaded scintillator

Bibliography

- [1] J. Boger. *et al. Nucl. Instrum. Meth.* **449** no. 172-207, (2000) .
- [2] I. Coulter, *Modelling and reconstruction of events in SNO+ related to future searches for lepton and baryon number violation.* PhD thesis, Oxford University (Balliol College), 2013.
- [3] B.Dasgupta and J. Beacom *Physical Review D* **83** no. 113006, (2011) .
- [4] M. Schmaker *Nucl. Phys. (Proc. Supl.)* **229-232** (2012) 547.
- [5] R. A. et al., “The calibration system for the photomultiplier array of the sno+ experiment,” *Journal of Instrumentation* **10** (2015) .
- [6] I. Coulter, “Smellie and amellie,” *SNO+ Internal Document* **1344-v1** (2012) .
- [7] S. Peeters, “Calibration overview,” *SNO+ Internal Doc-1614* (2012) .
- [8] S. Agostinelli, “Geant4 - a simulation toolkit,” *Nucl. Instrum. Meth.* **506** (2003) .
- [9] I. Coulter, “Modelling and reconstruction of events in sno+ related to future searches for lepton and baryon number violation,” *Oxford University PhD Thesis* (2013) .
- [10] S. Andringa *et al.*, “Current status and future prospects of the sno+ experiment,” *Adv. High En. Phys.* (2015) .

-
- [11] A. Wright *et al.*, “Tellurium loading downselect background information document,” *SNO+ Internal Document 3505-v1* (2015) .
- [12] Alfonso *et al.* *Phys. Rev. Lett.* **115** (2015) .
- [13] S. Nilenky and C. Giunti, “Neutrinoless double-beta decay: A brief review,” *Modern Physics Letters A* **27** no. 1230015, (2012) .
- [14] S. Woosley and T. Janka *Nature. Phys.* (2005) 147–154.
- [15] B. Krosigk, “Measurement of proton and α -particle quenching in lab based scintillators and determination of spectral sensitivities to measurement of proton and alpha-particle quenching in lab based scintillators and determination of spectral sensitivities to supernova neutrinos in the sno+ detector,” *Thesis* (2015) .
- [16] M. Chen *et al.*, “Expected radioactive backgrounds in sno+,” *Internal SNO+ Document* (2015) .
- [17] S. N. Ahmed *et al.* *Phys. Rev. Lett.* **92** no. 10, (2004) .
- [18] T. Araki *et al.* *Phys. Rev. Lett.* **96** no. 10, (2006) .
- [19] H. Back *et al.* *Phys. Lett. B* **563** (2003) .
- [20] C. Cowan *et al.*, “Detection of the free neutrino: a confirmation,” *Science* **124** (1956) .
- [21] R. Davies *et al.*, “Search for neutrinos from the sun,” *Phys. Rev. Lett.* **20** (1968) .
- [22] J. Hosaka *et al.*, “Solar neutrino measurements in Super-Kamiokande-I,” *Physical Review D - Particles, Fields, Gravitation and Cosmology* **73** (2006) .

- [23] M. Bergevin *et al.*, “Combined Analysis of all Three Phases of Solar Neutrino Data from the Sudbury Neutrino Observatory,” *Phys. Rev. C* **88** (2013) 1–27, [arXiv:arXiv:1109.0763v1](#).
- [24] K. Hagiwara *et al.* *Phys. Rev. D* **66** no. 010001, (2002) .
- [25] K. Olive *et al.*, “2014 review of particle physics,” *Chin. Phys. C* **38** (2014) .
- [26] I. Cholis and D. Hopper, “On the origin of icecube’s pev neutrinos,” *Journal of Cosmology and Astroparticle Physics* **030** (2013) .
- [27] M. Aartsen *et al.*, “First observation of pev-energy neutrinos with icecube,” *Phys. Rev. Lett.* **111** no. 021103, (2013) .
- [28] C. Spiering, “Towards high-energy neutrino astronomy,” *Europ. Phys. J. H* **37** no. 3, (2012) .
- [29] L. Wolfenstein *Phys. Rev. D* **17** no. 2369, (1978) .
- [30] S. Mikheyev and A. Smirnov *Sov. J. Nucl. Phys.* **42** no. 913, (1985) .
- [31] G. Fogli *et al.* *Journal of Cosmology and Astroparticle Physics* **12010** (2007) .
- [32] B. Dasgupta *et al.* *Phys. Rev. Lett.* **101** (2008) .
- [33] J. Pantaleone, “Neutrino oscillations at high densities,” *Phys. Lett. B* **287** (1992) .
- [34] J. Gomez-Cadena *et al.*, “The search for neutrinoless double beta decay,” *Riv. Nuovo Cim.* **35** (2011) .
- [35] E. Majorana, “Theory of the symmetry of electrons and positrons,” .
- [36] W. Furry, “On transition probabilities in double beta- disintegration,” *Phys. Rev.* **56** (1939) .

-
- [37] K. Zuber, “Neutrino physics,” *CRC Press* (2012) .
- [38] F. Boehm and P. Vogel, “Physics of massive neutrinos.,” *University of Cambridge Press* (1992) .
- [39] S. Biller *Private Communication* (2016) .
- [40] K. Alfonso *et al.*, “Search for neutrinoless double beta decay of ^{130}Te with Cuore-0 ,” *Phys. Rev. Lett.* **115** (2015) .
- [41] A. Gando *et al.*, “Limit on neutrinoless double beta decay of ^{136}Xe from the first phase of kamland-zen and comparison with the positive claim in ^{76}Ge ,” *Phys. Rev. Lett.* **110** (2013) .
- [42] M. Auger *et al.*, “Search for neutrinoless double-beta decay in ^{136}Xe with EXO-200 ,” *Phys. Rev. Lett.* **109** (2012) .
- [43] B. Mong *et al.*, “Spectroscopy of Ba and Ba^+ deposits in solid xenon for barium tagging in NEXO ,” *Phys. Rev. A* **91** (2015) .
- [44] A. Gando *et al.*, “Search for majorana neutrinos near the inverted mass hierarchy region with kamland-zen,” *Submitted to NIM* (2016) .
- [45] J. Klein *et al.*, “The sno trigger system,” *SNO+ Internal Document 827-v1* (1997) .
- [46] K. Majumdar, “On the measurement of optical scattering and studies of background rejection in the sno^+ detector,” *Oxford University PhD Thesis* (2015) .
- [47] E. Gamma *et al.*, “Design patterns: Elements of reusable object-oriented software,” .
- [48] R. Wentk, “Cocoa: Volume 5 of developer reference apple developer series,” *J. Wiley and Sons* .

- [49] N. Gagnon *Private Communication* (2015) .
- [50] N. McCauley, “Producing a background free data set for measurement of the charge current flux and day-night asymmetry at the sudbury neutrino observatory,” .
- [51] “Ni daqmx,” 2015.
<http://sine.ni.com/nips/cds/view/p/lang/en/nid/209795>.
- [52] P. GmbH, “Ldg series picosecond pulsed diode laser heads,” 2014. <http://www.picoquant.com/products/category/picosecond-pulsed-driver>.
- [53] L. C. U. Ltd., “Fiber optic switch operation manual,” *Private Communication* (2009) .
- [54] K. Majumdar, “On the measurement of optical scattering and studies of background rejection in the sno+ detector,” *Thesis* (2015) .
- [55] Hamamatsu, “Metal package pmt photosensor modules h10720/h10721 series,” 2014. http://www.hamamatsu.com/resources/pdf/etd/m-h10720_h10721e.pdf.
- [56] G. Keiser, *Optical Fibre Communications*. McGraw-Hill, 2000.
- [57] Fibredyne, “Variable fiber optic in-line attenuators,” 2015.
<http://www.fiberdyne.com/products/inlineatten.html>.
- [58] L. U. Ltd., “Lemo b series connectors.” <http://www.lemo.co.uk/index.php/product-range/connector-range#b-series-keyed-standard>.
- [59] P. W. Graham, I. G. Irastorza, S. K. Lamoreaux, A. Lindner, and K. A. van Bibber, “Experimental Searches for the Axion and Axion-Like Particles,” *Annual Review of Nuclear and Particle Science* **65** no. 1, (2015)

150807173859001. <http://www.annualreviews.org/doi/abs/10.1146/annurev-nucl-102014-022120>.
- [60] R. D. Peccei and H. R. Quinn, “CP conservation in the presence of pseudoparticles,” *Physical Review Letters* **38** no. 25, (1977) 1440–1443.
- [61] S. Weinberg, “A New Light Boson?,” *Physical Review Letters* **40** no. 4, (1978) 223.
<http://journals.aps.org/prl/pdf/10.1103/PhysRevLett.38.1440>.
- [62] F. Wilczek, “Problem of Strong P and T Invariance in the Presence of Instantons,” *Phys. Rev. Lett.* **40** no. 5, (1978) 279–282.
<http://journals.aps.org/prl/pdf/10.1103/PhysRevLett.40.279>.
- [63] K. Nakamura, K. Hagiwara, K. Hikasa, Particle, Data, and Group, “Review of Particle Physics,” *Journal of Physics G: Nuclear and Particle Physics* **37** no. 7A, (2010) 075021.
<http://iopscience.iop.org/0954-3899/37/7A/075021/fulltext/>.
- [64] J. E. Kim, “Weak-interaction singlet and strong CP invariance,” *Physical Review Letters* **43** no. 2, (1979) 103–107.
- [65] M. Shifman, A. Vainshtein, and V. Zakharov, “Can confinement ensure natural CP invariance of strong interactions?,” *Nuclear Physics B* **166** no. 3, (1980) 493–506.
- [66] Dine, M., Fishchler, W. and Srednicki, M., “A simple Solution to the Strong CP Problem,” *Physics Letters* **104** no. 3, (1981) 4, [arXiv:0110178 \[hep-ph\]](https://arxiv.org/abs/hep-ph/0110178). <http://arxiv.org/abs/hep-ph/0110178>.
- [67] A. Zhitnitskii *Sov. J. Nucl. Phys.* **31** no. 260, (1980) .

- [68] D. Hopper and T. Tait, “Neutralinos in an extension of the minimal supersymmetric standard model as the source of the pamele positron excess,” *Phys. Rev. D.* **80** (2009) .
- [69] S. Andreas and A. Ringwald, “Status of sub-gev hidden particle seaches,” *6th Patras Workshop on Axions, WIMPs and WISPs* (2010) .
- [70] K. Baker *et al.*, “The quest for axions and other new light particles,” *Ann. Phys. (Berlin)* **525** (2013) .
- [71] G. Bellini. *et al.*, “Search for solar axions produced in the $p(d,He^3)\alpha$ reaction with Borexino detector,” *Physical Review D - Particles, Fields, Gravitation and Cosmology* **85** (2012) 1–11, [arXiv:arXiv:1203.6258v1](https://arxiv.org/abs/1203.6258v1).
- [72] K. van Bibber and G. Carosi, “Status of the admx and admx-hf experiments,” *8th Patras Workshop on Axions, WIMPS and WISPs* (2012) .
- [73] M. Arik *et al.*, “Search for solar axions by the cern axion solar telescope with 3he buffer gas: Closing the hot dark matter gap,” *Phys. Rev. Lett.* **112** (2014) .
- [74] A. Zhitnitskii and Y. Skovpen *Yad. Fiz.* **29b** no. 995, (1979) .
- [75] W. C. Haxton *et al.*, “Search for axions from the 1115-keV transition of ^{65}Cu ,” *Phys. Rev. D.* **37** no. 3, (1988) .
- [76] T. Donnelly *et al.*, “Do axions exist?,” *Physical Review D* **18** no. 5, (1978) .
- [77] A. Derbin *et al.*, “Search for axioelectric effect of solar axions using BGO scintillating bolometer,” [arXiv:1405.3782](https://arxiv.org/abs/1405.3782).
<http://arxiv.org/abs/1405.3782>.

- [78] F. Avignone *et al.*, “Search for axions from the 1115-keV transition of ^{65}Cu ,” *Phys. Rev. D.* **37** no. 3, (1988) .
- [79] A. V. Derbin, A. S. Kayunov, and V. N. Muratova, “Search for Solar Axions Produced in the $p + d$ to $^3\text{He} + A$ Reaction,” [arXiv:1007.3387](https://arxiv.org/abs/1007.3387).
<http://arxiv.org/abs/1007.3387>.
- [80] G. Raffelt and L. Stodolsky, “New particles from nuclear reactions in the sun,” *Physics Letters B* **119** no. 4-6, (1982) 323–327.
- [81] V. Lozza *et al.*, “Expected radioactive backgrounds in sno+,”.
- [82] A. Ljubcic *et al.*, “Search for hadronic axions using axioelectric effect,” *Phys. Lett. B* **143** (2004) .
- [83] B. Aharmim *et al.*, “Low-energy-threshold analysis of the Phase I and Phase II data sets of the Sudbury Neutrino Observatory,” *Physical Review C* **81** (2010) 1–49.
- [84] T. Mori *et al.*, “Status of super-kamiokande gadolinium project,” *Nucl. Instrum. Meth.* (2013) .
- [85] C. Arpesella *et al.*, “Direct measurement of the ^7Be solar neutrino flux with 192 days of borexino data,” *Phys. Rev. Lett.* **101** no. 091302, (2008) .
- [86] K. Abe *et al.*, “Letter of Intent: The Hyper-Kamiokande Experiment,” [arXiv:arXiv:1109.3262v1](https://arxiv.org/abs/1109.3262v1).
- [87] A. Wagner *et al.*, “Search for hidden sector photons with the admx detector,” *Phys. Rev. Lett.* (2010) .
- [88] P. Sikivie, “Detection rates for invisible-axion searches,” *Physical Review D* **32** no. 11, (1985) 2988–2991.

- [89] C. Hagmann *et al.*, “Results from a search of cosmic axions,” *Physical Review D* **42** no. 4, (1990) .
- [90] S. DePanfilis *et al.*, “Limits on the Abundance and Coupling of Cosmic Axions,” *Physical Review Letters* **59** no. 7, (1987) 839–842.
<http://journals.aps.org/prl/pdf/10.1103/PhysRevLett.59.839>.
- [91] J. Vogel *et al.*, “Search for Solar Axions with the CAST-Experiment,” *Astroparticle, Particle and Space Physics, Detectors and Medical Physics Applications - Proceedings of the 10th Conference* (2008) 282–286.
http://eproceedings.worldscinet.com/9789812819093/9789812819093_0049.html.
- [92] B. Beltran *et al.*, “Search for solar axions: the CAST experiment at CERN,” arXiv:0507007 [hep-ex].
<http://arxiv.org/abs/hep-ex/0507007>.
- [93] K. Barth *et al.*, “CAST constraints on the axion-electron coupling,” *Journal of Cosmology and Astroparticle Physics* **05** (2013) .
- [94] M. Altmann *et al.* *Z. Phys.* **C28** no. 221, (1995) .
- [95] H. Chang *et al.* *Physical Review D* **75** no. 052004, (2007) .
- [96] G. Bellini. *et al.* *Europ. Phys. J.* **61** no. C54, (2008) .
- [97] A. Derbin, A. Kayunov, and V. Muratova *Bull. Tus. Acad. Sci. Phys.* **74** no. 805, (2010) .
- [98] A. Konaka *et al.* *Phys. Rev. Lett.* **57** no. 659, (1986) .
- [99] J.D.Bjorken *et al.* *Physical Review D* **38** no. 3375, (1988) .
- [100] S.Asai *et al.* *Phys. Rev. Lett.* **66** no. 2440, (1991) .

-
- [101] C. aalseth *et al.* *Phys. Rev. Lett.* **101** no. 251301, (2008) .
- [102] Z. Ahmed *et al.* *Phys. Rev. Lett.* **103** no. 141802, (2009) .
- [103] P. Gondolo and G. Raffelt *Phys. Rev. D.* **79** no. 107301, (2009) .
- [104] A. Derbin *et al.* *Phys. Rev. D.* **83** no. 023505, (2011) .
- [105] G. Raffelt *Lect. Notes Phys.* **51** no. 741, (2008) .
- [106] F. Avignone *et al.* *Nucl. Phys. (Proc. Supl.)* **72** no. 176, (1999) .
- [107] R. Bernabei *et al.* *Phys. Lett. B* **6** no. 515, (2001) .
- [108] A. Morales *et al.* *Astropart. Phys.* **16** no. 325, (2002) .
- [109] K. Zioutas *et al.* *Phys. Rev. Lett.* **94** no. 121301, (2005) .
- [110] E. Arik *et al.* *JCAP0902* **008** (2009) .
- [111] Y. Inoue *et al.* *Phys. Lett. B* **668** no. 98, (2008) .
- [112] M. Bershadsky, M. Ressel, and M. Turner *Phys. Rev. Lett.* **66** no. 1398, (1991) .
- [113] M. Ressel *Phys. Rev. D.* **66** no. 3001, (1991) .
- [114] D. Grin *et al.* *Phys. Rev. D.* **75** no. 105018, (2007) .
- [115] Z. Berezhiani, L. Gianfagna, and M. Guannotti *Phys. Lett. B* **500** no. 286, (2001) .
- [116] Z. Berezhiani and A. Drago *Phys. Lett. B* **473** no. 281, (2000) .
- [117] L. J. Hall and T. Watari *Phys. Rev. D.* **70** no. 115001, (2004) .
- [118] W. Hillebrandt and J. Niemeyer, “Type Ia supernova explosion models,” *Ann. Rev. Astron. Astrophys.* **38** (2000) .

-
- [119] A. Heger *et al.*, “How massive single stars end their life,” *Astrophys. Journal* **591** (2003) .
- [120] A. Mirizzi *et al.*, “Supernova neutrinos: Productions, oscillations and detection,” *Il Nuovo Cimento* (2015) .
- [121] S. Woosley and T. Janka, “The physics of core-collapse supernovae,” *Nature. Phys.* **1** (2005) .
- [122] K.Hirata *et al.*, “Observation of a neutrino burst from the supernova sn1987a,” *Phys. Rev. Lett.* **58** (1987) .
- [123] E.N.Alexeyev *et al.*, “Detection of the neutrino signal from sn1987a in the lmc using the inr baksan underground scintillation telescope,” *Phys. Lett. B* **205** (1988) .
- [124] C. Bratton *et al.*, “Neutrinos from sn1987a in the imb detector,” *Nucl. Instrum. Meth.* **264** (1988) .
- [125] W. Arnett *et al.*, “Supernova 1987a,” *Ann. Rev. Astron. Astrophys.* **27** (1989) .
- [126] S. Korte, “Simulating supernova physics at sno+,” *Master’s thesis* (2009) .
- [127] L. Cavalli, “Rapid identification of supernova at sno+,” *Oxford University Masters Thesis* (2015) .
- [128] M.T.Keil *et al.* *Astrophys. Journal* **590** no. 971, (2003) .
- [129] J.B.Birks, “The theory and practice of scintillation counting,” *Pergamon Press* (1967) .
- [130] G. Cowan, *Statistical Data Analysis*. Oxford Science Publications, 1998.

-
- [131] G. Bellini. *et al.*, “Observation of geo-neutrinos,” *Phys. Lett. B* **687** (2010) .
- [132] J. Rumleskie, “Evaluating sno+ backgrounds through ^{222}Rn assays and the simulation of $^{13}\text{C}(\alpha, n)^{16}\text{O}$ reactions during the water phase,” *Laurentian University* (2015) .
- [133] S. Zavatarelli *et al.*, “Recent results from borexino and the first real time measure of solar pp neutrinos,” *Nucl. and Particle Physics Proceedings* **273** (2016) .
- [134] O.Helene *Nucl. Instrum. Meth.* **212** (1983) .
- [135] J. Dunger, “Private communication.”